



# The physics of lightning

Joseph R. Dwyer<sup>a,\*</sup>, Martin A. Uman<sup>b</sup>

<sup>a</sup> Department of Physics and Space Sciences, Florida Institute of Technology, Melbourne, FL 32901, USA

<sup>b</sup> Department of Electrical and Computer Engineering, University of Florida, Gainesville, FL 32611, USA



## ARTICLE INFO

### Article history:

Accepted 25 September 2013

Available online 9 October 2013

editor: M.P. Kamionkowski

## ABSTRACT

Despite being one of the most familiar and widely recognized natural phenomena, lightning remains relatively poorly understood. Even the most basic questions of how lightning is initiated inside thunderclouds and how it then propagates for many tens of kilometers have only begun to be addressed. In the past, progress was hampered by the unpredictable and transient nature of lightning and the difficulties in making direct measurements inside thunderstorms, but advances in instrumentation, remote sensing methods, and rocket-triggered lightning experiments are now providing new insights into the physics of lightning. Furthermore, the recent discoveries of intense bursts of X-rays and gamma-rays associated with thunderstorms and lightning illustrate that new and interesting physics is still being discovered in our atmosphere. The study of lightning and related phenomena involves the synthesis of many branches of physics, from atmospheric physics to plasma physics to quantum electrodynamics, and provides a plethora of challenging unsolved problems. In this review, we provide an introduction to the physics of lightning with the goal of providing interested researchers a useful resource for starting work in this fascinating field.

© 2013 Elsevier B.V. All rights reserved.

## Contents

1. Introduction.....	148
1.1. Overview .....	148
1.2. History .....	149
1.3. Phenomenology and terminology .....	149
1.4. Experimental techniques .....	156
1.5. The top ten questions in lightning research .....	156
2. Conventional discharges.....	157
2.1. Overview .....	157
2.2. The microphysics of conventional discharges .....	158
2.3. Electrical breakdown.....	162
2.4. Corona discharges.....	163
3. The lightning initiation problem.....	163
3.1. Overview .....	163
3.2. Thunderstorm and lightning phenomenology related to lightning initiation.....	164
3.2.1. Thunderstorm charge structure.....	164
3.2.2. Lightning initiation locations.....	165
3.2.3. Preliminary breakdown.....	165

\* Corresponding author. Tel.: +1 321 674 7208; fax: +1 321 674 7482.  
E-mail address: [jdwyer@fit.edu](mailto:jdwyer@fit.edu) (J.R. Dwyer).

3.3.	Electric field measurements inside thunderclouds .....	167
3.4.	Localized field enhancements from hydrometeors .....	168
3.5.	Laboratory measurements of corona from hydrometeors .....	169
3.6.	Modeling streamer initiation and propagation .....	170
3.7.	Runaway electrons and lightning initiation.....	171
4.	Lightning propagation .....	172
4.1.	Overview .....	172
4.2.	Negative stepped leaders and dart-stepped leaders .....	173
4.3.	Positive “stepped” leaders .....	183
5.	High energy atmospheric physics .....	187
5.1.	Introduction .....	187
5.2.	Introduction to runaway electron physics .....	188
5.2.1.	Wilson runaway electrons .....	188
5.2.2.	Thermal runaway electron production .....	189
5.2.3.	Relativistic runaway electron avalanches (RREAs).....	190
5.2.4.	Relativistic feedback mechanism .....	190
5.3.	Observations of energetic radiation produced within our atmosphere .....	192
5.3.1.	X-ray observations of lightning .....	192
5.3.2.	X-ray observations of long laboratory sparks .....	198
5.3.3.	Gamma-ray glows from thunderclouds .....	199
5.3.4.	Terrestrial gamma-ray flashes (TGFs) .....	201
5.3.5.	Radio observations of TGFs .....	203
5.3.6.	Terrestrial electron beams (TEBs).....	205
5.3.7.	Neutrons.....	208
5.4.	Theory and modeling.....	208
5.4.1.	RREA propagation .....	208
5.4.2.	Detailed runaway electron physics .....	210
5.4.3.	Runaway electron energy spectrum.....	211
5.4.4.	Relativistic feedback calculations .....	212
5.4.5.	Comparison of runaway electron mechanisms .....	214
5.4.6.	Electric currents .....	216
5.4.7.	Radio frequency emissions .....	217
5.4.8.	TGF models.....	218
5.4.9.	Results of the relativistic feedback discharge model .....	219
5.4.10.	RREAs and cosmic-ray air showers.....	221
5.4.11.	Runaway electrons and field enhancements .....	223
6.	Compact cloud discharges (CIDs).....	224
6.1.	Introduction .....	224
6.2.	Trans-ionospheric pulse pairs (TIPPs) .....	226
6.3.	CID optical emissions .....	226
6.4.	CID association with thunderclouds meteorology .....	227
6.5.	RREA models of CIDs.....	227
7.	Transient luminous events (TLEs) .....	227
7.1.	Sprites and halos .....	227
7.2.	Elves .....	230
7.3.	Blue starters blue jets, and gigantic jets .....	230
8.	Concluding remarks .....	231
	Acknowledgments .....	231
	References.....	231

## 1. Introduction

### 1.1. Overview

Lightning is the most impressive, commonly-experienced geophysical phenomenon. It produces the brightest light and the loudest sound commonly occurring on Earth. Since lightning has been seen by virtually everyone (there are 30–100 cloud and cloud-to-ground lightning discharges per second worldwide; that is, roughly 9 million discharges per day worldwide, or  $6 \text{ km}^{-2} \text{ yr}^{-1}$  averaged over the Earth), one might think that lightning is very well understood. That is not the case. Lightning's seemingly random occurrence in space and time and the wide range of its significant time variation, from tens of nanoseconds for many individual processes to almost a second for the total discharge, and its obscuration by the thundercloud producing it makes lightning particularly difficult to study. Nevertheless, more than a century of measurement has produced a relatively complete picture of the phenomenology of lightning. A detailed understanding of the physics, involving mathematical modeling, has lagged behind. The joint lightning research team from the Florida Institute of Technology and the University of Florida, under the direction of this paper's authors, have compiled a list of the

ten most important unanswered questions about lightning. These serve as guides to our own research effort, and we hope they will act as motivation to prospective lightning researchers. The questions are given in the final section, Section 1.5, of this Introduction. First, we present a short review of the history, phenomenology, and terminology of lightning, presented as background with which to view both the ten questions in Section 1.5 and the research in progress to answer them. Some perspective on the history of lightning research can be obtained from a sequential look at the following monographs: Malan [1]; Schonland [2]; Uman [3,4]; Rakov and Uman [5]. Additional information can be found in Refs. [6–8].

## 1.2. History

Lightning research can be considered to have begun with Benjamin Franklin. In 1746 he began his laboratory experiments with electricity, made possible by (1) a familiarity with the frictional charge-separation mechanism occurring when dissimilar materials are rubbed together and (2) the invention earlier that year of the Leyden jar, a capacitor to store electrical charge. In 1749 Franklin described the similarities between lightning and the laboratory sparks he had created, and in 1750 he published the design of an experiment involving vertical metal rods insulated from the Earth intended to prove that lightning was electrical. That experiment was first performed successfully in France in May 1752. Soon after, sometime in the summer of 1752, Franklin flew his famous kite. Among Franklin's many accomplishments was his measurement showing that the major charge in the lower part of a thunderstorm was negative, his laboratory experiments having led him to define the sign of electrical charge. Details of Franklin's electrical experiments can be found in Dibner [9] and Cohen [10,11].

Following Franklin there was little significant progress in understanding lightning until the late nineteenth century when photography and spectroscopy became available as diagnostic techniques. The early history of lightning photography and spectroscopy is reviewed by Uman [12]. Investigators in England, Germany, and the United States used time-resolved photographic techniques to identify the individual "strokes" that comprise a lightning discharge to ground and the "leader process" that precedes first strokes. The invention of the double-lens streak camera in 1900 by Boys [13] in England made possible the pioneering advances in our understanding of the main aspects of the phenomenology of cloud-to-ground lightning by Schonland, Malan, and co-workers in South Africa in the 1930s and thereafter [14]. In the "Boys" streak camera, film moves continuously behind one lens in one horizontal direction and behind the other lens in the opposite direction so luminous events occurring at different times are displaced horizontally in different directions on the two pieces of film.

The first lightning current measurements were made by Pockels [15–17] in Germany. He analyzed the residual magnetic field induced in basalt rock in the Earth by nearby lightning currents and by doing so was able to estimate the values of those currents.

The modern era in lightning research can be dated to Wilson [18,19] in England, the same individual who received a Nobel Prize for his invention of the cloud chamber to track high-energy particles. Wilson used remote, ground-based electric field measurements to estimate both the charge structure in the thunderstorm and the individual charge involved in the lightning discharge. Contributions to our present understanding of lightning have come from researchers throughout the world and cover the time period from Wilson's work to the present. Most notable prior to 1970 was the high-speed photographic and correlated electric field measurements of the South African group under Schonland, as noted above, and the work of Berger and colleagues (e.g., [20,21]) in Switzerland in measuring lightning currents on instrumented towers.

The period from about 1970 to the present has been particularly active and productive for lightning research, in part due (1) to the development of new techniques of data taking and analysis involving high-speed tape recording before about 1990 and direct 10 ns-scale digitization and storage under computer control of analog electromagnetic (from ELF to optical to gamma radiation) signals after about 1990, and (2) to the motivation provided by lightning damage to aircraft, spacecraft, and sensitive ground-based installations because of the vulnerability of modern low-voltage solid-state electronics, including computers, to lightning currents and electromagnetic fields. Prior to about 1970, much of the practical motivation for lightning research came from the need to adequately protect power utility distribution and transmission lines.

After about 1975 and continuing to the present, the use of rocket-and-wire triggered lightning from natural thunderstorms became a widespread technique to study various aspects of lightning. Triggered lightning research, discussed further in Section 1.3, is a major part of the present authors' research and has been or is being employed in the US, France, Brazil, Japan, and China.

It was only about 20 years ago that Transient Luminous Events (TLEs) (red Sprites of various types, Sprite halos, blue starters, blue jets, gigantic jets, and Elves) were discovered to occur in the rarified air above thundercloud tops; and only about 10 years ago that it was found that high-energy phenomena (runaway electrons, X-rays, and gamma rays including the Terrestrial Gamma Ray Flashes (TGFs) observed on orbiting satellites) are produced by both thunderclouds and lightning. The relatively-recently discovered TLEs and high-energy phenomena are presently the subject of intensive research, and are further defined in Section 1.3. High energy lightning and thunderstorm phenomena are discussed in detail in Sections 4–6.

## 1.3. Phenomenology and terminology

Lightning can be defined as a very long electrical spark, "very long" meaning greater than about 1 km. Most lightning is generated in thunderstorms and is characterized by a length of 5–10 km, at the extreme over 100 km (see Section 4.1). In a thunderstorm, the primary charge transfer process is thought to involve collisions between (1) soft hail (graupel) particles

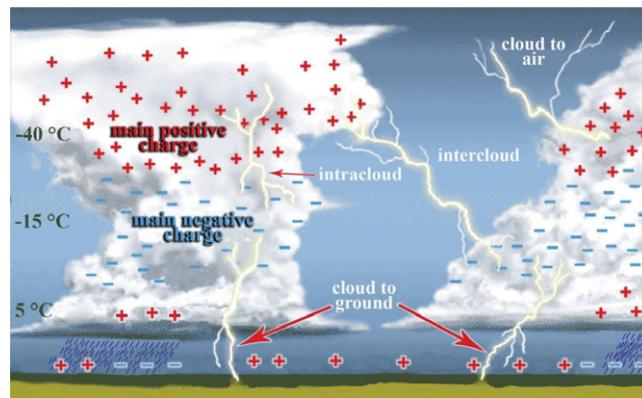


**Fig. 1.1.** The charge structure of two simple isolated thunderclouds and some of the locations where the lightning can occur.  
Source: Adapted from Ref. [489].

that are heavy enough to fall or remain stationary in the thunderstorm's updrafts and (2) small crystals of ice that are light enough to be carried upward in those updrafts, all in the presence of super-cooled (unfrozen, but colder than 0 °C) water droplets. To produce the primary thundercloud charges that have been inferred from ground-based and balloon measurements of cloud electric fields, these ice-hail interactions must take place at altitudes where the temperature is considerably colder than freezing, generally –10 °C to –20 °C. After charge has been transferred between the colliding ice and hail particles, the positively charged ice crystals are carried further upward in updrafts to the top part of the thundercloud, to an altitude near 10 km above sea level in temperate summer storms; while the negatively charged hail resides at an altitude of 6–8 km. Thus, the idealized primary charge structure of an isolated, mature thundercloud consists of many tens of Coulombs of positive charge in its upper portions and a more or less equal negative charge in its lower levels. In a typical thundercloud, a small positive charge is also found below the main negative charge, at altitudes where the temperature is near or warmer than freezing. There are a variety of mechanisms that have been suggested to produce this lower positive charge including corona discharge emanating from the ground and collisions between different types of precipitation particles at temperatures warmer than 0 °C.

The idealized thundercloud charge structure discussed above is illustrated in Fig. 1.1 along with the potential locations of some different types of lightning discharges. Note that while the two main charge centers are labeled, the small positive charge region residing below the main negative charge is not labeled, for lack of space. Note also that, again for lack of space, upward lightning from ground-based objects (discussion given later) is not illustrated in Fig. 1.1; nor is cloud-to-ground lightning from either of the two positive charge regions; nor cloud-to-air discharges from other charge regions than the main positive; nor intracloud lightning between the main negative charge center and the small positive charge below it. The charge structure in a thunderstorm is actually more complex than shown in Fig. 1.1, varies from storm to storm, and is occasionally very much different from the structure illustrated, even sometimes up-side-down with the main positive charge on the bottom and the main negative charge on top. Further, the two isolated thunderclouds illustrated in Fig. 1.1 may comprise a portion of many contiguous and interacting storm "cells" that comprise larger storm systems. To read more about cloud charge and cloud charging, the reader is referred to the book by MacGorman and Rust [22] and the references found therein.

A typical small thunderstorm system produces a lightning flash to ground every 20–30 s for 40–60 min and covers an area of typically 100–300 km<sup>2</sup> (roughly a circle on the ground with a radius between 6 and 10 km). Large storm systems can produce more than one flash to ground each second over areas a hundred times larger or even more.

All lightning discharges can be divided into two categories: (1) those that bridge the gap between the cloud charge and the Earth and (2) those that do not. The latter group as a whole is referred to as "cloud discharges" and accounts for the majority of all lightning discharges. As illustrated in Fig. 1.1, cloud discharges that occur totally within a single cloud (or "cell") are called intracloud lightning (thought to be the most common cloud lightning and the most common of all the forms of lightning); those that occur between clouds are called intercloud lightning (less common than intracloud lightning); and those that occur between one of the cloud charge regions and the surrounding air are called cloud-to-air lightning.

The terms "lightning flash", "lightning discharge", and "lightning" are used interchangeably in the literature to describe either cloud lightning or cloud-to-ground lightning, generally the whole event lasting about 0.5 s. There are four types of lightning flashes that occur between the cloud and ground. The four types, illustrated separately in Fig. 1.2a-d, are distinguished from each other by the sign of the electrical charge carried in the initial "leader" and by the direction of propagation of that leader. Fig. 1.2a, c show flashes referred to as downward lightning; Fig. 1.2b, d depict upward lightning. About 90% of cloud-to-ground lightning flashes are initiated by a negatively-charged, downward-propagating leader, as shown in Fig. 1.2a, and result in the lowering of negative charge from the main negative charge region in the middle part of the cloud to the ground. About 10% of cloud-to-ground lightning flashes are initiated by a positively-charged, downward-propagating leader, as shown in Fig. 1.2c, and results in the lowering of positive charge from the cloud to the ground, either

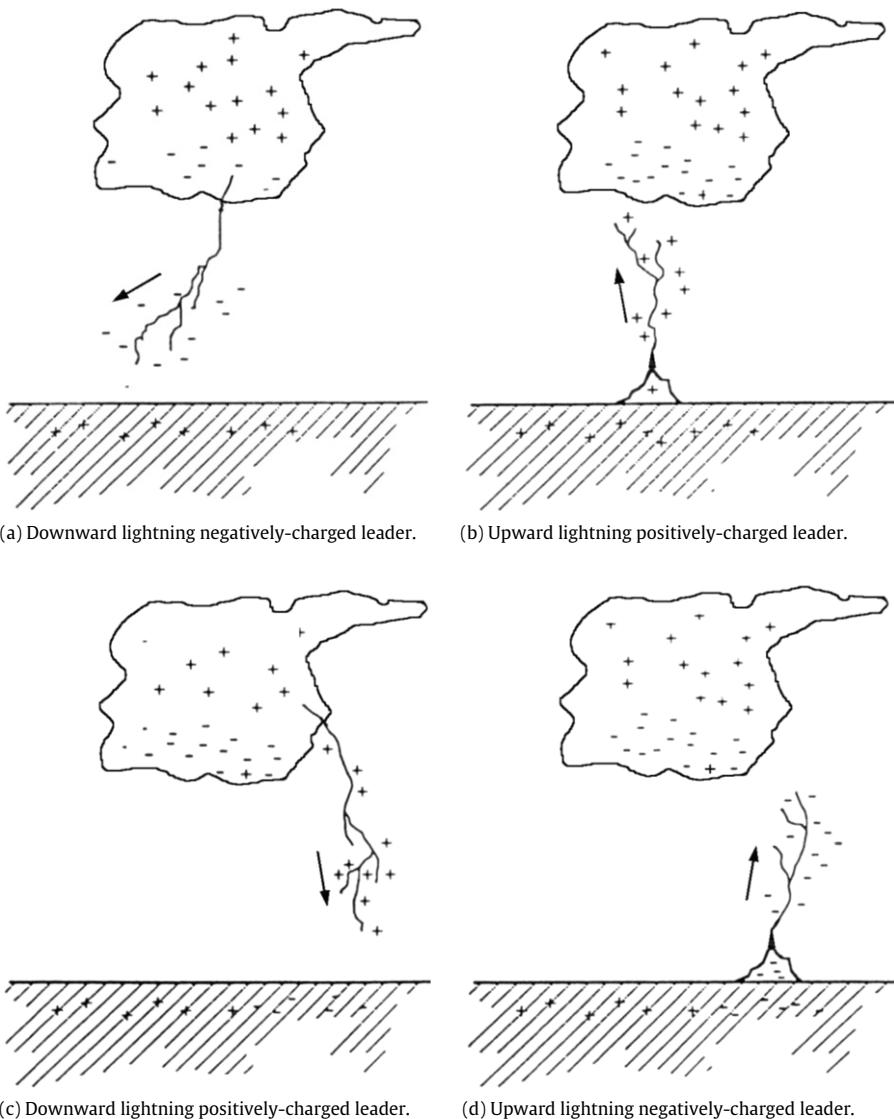


**Fig. 1.2.** The four types of cloud-to-ground lightning flashes as defined from the direction of leader propagation and the charge on the initiating leader. Source: Adapted from Berger [490].

from the upper or lower positive charge regions. The remaining two types of cloud-to-ground (actually ground-to-cloud) lightning discharges (Fig. 1.2b, d) are relatively uncommon and are upward initiated from mountaintops, tall man-made towers, or other tall objects, towards the cloud charge regions. Note that the branching shown in Fig. 1.2b, d is upward, in the direction of propagation of the initiating discharge, whereas in the downward lightning of Fig. 1.2a, c the branching is downward, again in the direction of the propagating, initiating “leader”, from the cloud charge to the Earth.

The most common cloud-to-ground discharge, downward lightning carrying negative charge, may well begin as a local discharge between the bottom of the main negative charge region and the small lower positive charge region beneath it (see Fig. 1.1). This local discharge would serve to provide free electrons previously immobilized by virtue of their attachment to hail and other heavy particles. Because of the electron’s small mass, free electrons are extremely mobile (they move easily when exposed to an electric field) compared to the heavier ionized air atoms or molecules, or to charged hail, ice, or water particles which are essentially stationary on the time scale of lightning. Hence free electrons are the primary contributor to the lightning current. In negative cloud-to-ground lightning, the free electrons over-run the lower positive charge region, neutralizing a significant fraction of its small positive charge, and then continue their trip toward ground. The physical mechanism for moving the negative charge to Earth is a propagating electrical discharge called the “stepped leader”. Prior to observations of the overall electric field change and electric field pulses associated with the stepped leader propagation near ground, there are often larger electric field pulses associated with a “preliminary” or “initial” breakdown in the cloud charge

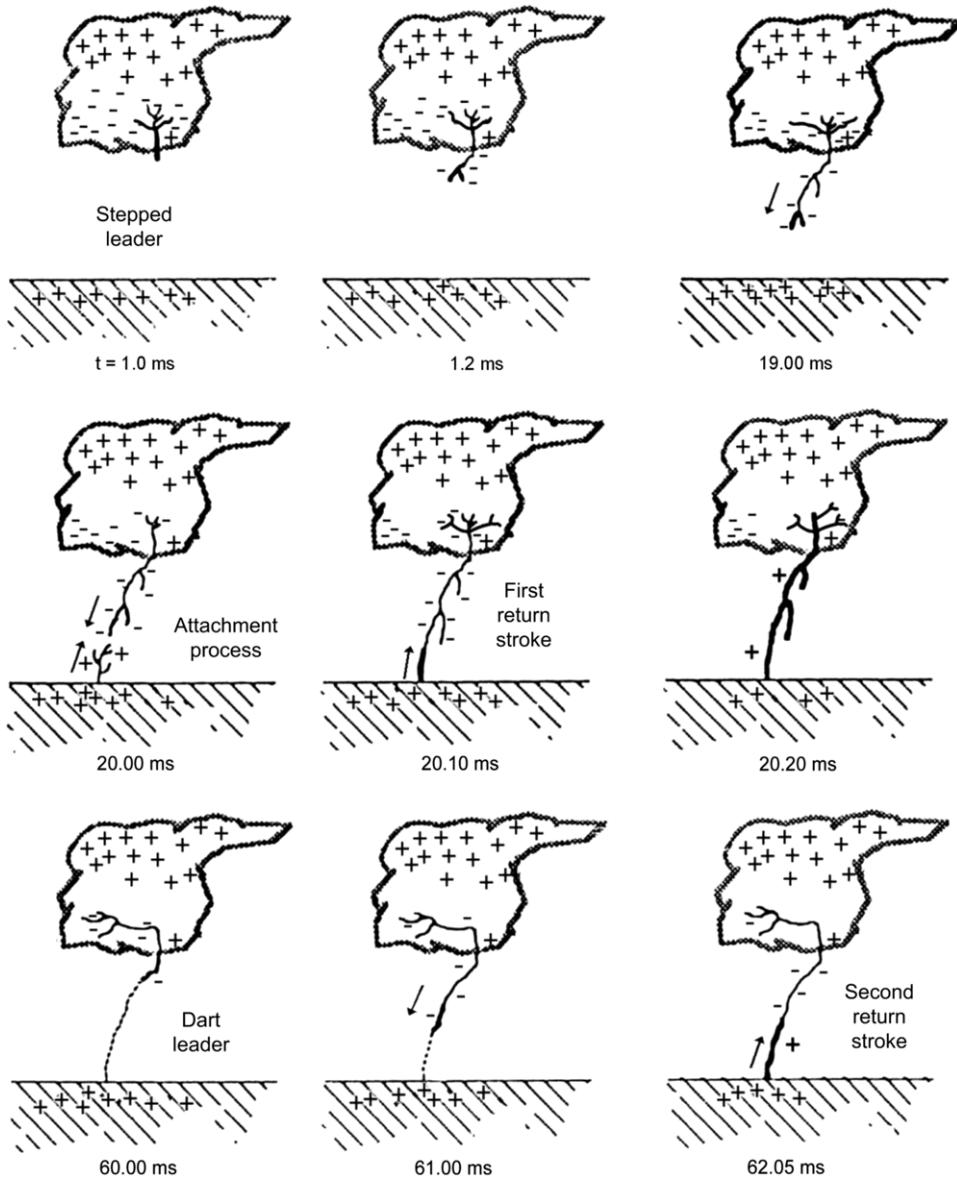


**Fig. 1.3.** A drawing depicting the development of a negative cloud-to-ground lightning flash, the most common type of cloud-to-ground lightning. The time-scale is given in milliseconds from the first electrical breakdown processes in the cloud.

Source: Adapted from Uman [4].

region, as discussed further in Sections 3.2.3 and 4.1. Salient aspects of the negative cloud-to-ground flash are illustrated in Fig. 1.3.

The stepped leader's movement from cloud to ground is not continuous, but rather it moves downward in discrete luminous segments of tens of meters length, then pauses, then moves another "step", and so on. In Fig. 1.3 the luminous steps appear as darkened tips on the less-luminous leader channel extending downward from the cloud. Each luminous leader step appears in a microsecond or less. Studying and understanding the physics of negative step formation is an important aspect of modern lightning research, as discussed in detail in Section 4.2. The time between luminous steps is about  $50 \mu\text{s}$  when the stepped leader is far above the ground (and below the cloud base) and less, near  $10 \mu\text{s}$ , when it is near the ground. The downward-propagating stepped leader branches downward, as noted earlier. Negative charge (free electrons) is more-or-less continuously lowered from the main negative charge region in the middle of the cloud (Fig. 1.1) into the leader channel. The average downward speed of the bottom of the stepped leader during its trip toward ground is about  $2 \times 10^5 \text{ m s}^{-1}$  so the trip between the cloud charge and ground takes about 20 ms. A typical stepped leader has about 5 C of negative charge distributed over its length, or about  $10^{-3} \text{ C/m}$ , when it is near ground. In order to establish this charge on the leader channel an average current of about 100–200 Amperes must flow during the whole leader process. The pulsed currents involved in

generating the leader steps have a peak current of the order of 1000 Amperes and microsecond duration. Each negative leader step produces a pulse of visible light, a pulse of radio-frequency energy, and a pulse of X-rays, primarily in the 200 keV range. The luminous diameter of the stepped leader has been measured photographically to be between 1 and 10 m. It is thought, however, that most of the stepped-leader current flows down a narrow conducting core a few centimeters in diameter at the center of the observed leader. The large photographed diameter is probably due to a luminous “corona”, a low-level, non-thermalized electrical discharge made up of a multitude of “corona streamers” surrounding the conducting core.

When the stepped leader is near the ground, its relatively large negative charge induces (attracts) concentrated positive charge on the conducting Earth beneath it and especially on objects projecting above the Earth's surface. When the electric field intensity near ground from these charges becomes large enough, upward-going, positively-charged electrical discharges from the ground or from grounded objects will be initiated, as illustrated in Fig. 1.3 at 20.00 ms. One of these upward-going discharges will contact a branch of the downward-moving leader, thereby determining the lightning strike-point and the primary lightning current path (channel) between cloud and ground. Understanding the “attachment process” is critical to the proper design of lightning protection systems. Unfortunately, the attachment process is sufficiently complex and variable that it has not been possible to gain more than a relatively crude understanding of it. Hence, number 3 of the top ten questions given in Section 1.5.

When a downward-moving, negatively-charged leader branch and an upward-moving, positively-charged leader connect, negative charge near the bottom of the leader channel moves violently (increasing the ionization level of the leader channel) downward into the Earth, causing large currents to flow at ground and causing the channel near ground to become very luminous. Since electrical signals have a maximum speed of  $3 \times 10^8 \text{ m s}^{-1}$  – the “speed of light” – the leader channel above ground has no way of knowing for a short time that the leader bottom has been connected to ground and has become highly luminous and highly electrically conducting. The channel luminosity and current, in a process termed the first “return stroke”, propagate continuously up the channel and out (down) the branches of the leader channel at a speed typically between one-third and one-half the speed of light, as illustrated in Fig. 1.3 at times 20.10 and 20.20 ms. Even though the return stroke's high current and high luminosity move upward on the main channel, electrons at all points in the main channel always move downward and, as noted earlier, represent the primary components of the current. Electrons flow up the channel branches toward the main channel while the return stroke traverses the branches in the outward and downward direction. Eventually, some milliseconds after the return stroke is initiated, the several Coulombs of negative electric charge which were resident on the stepped leader all flow into the ground. Additional current may also flow to ground directly from the cloud charge region once the return stroke has reached it.

The return stroke produces the bright channel of high temperature air that we commonly observe. The maximum return stroke temperature is near 30,000 °C. We usually do not see the preceding, dimmer, downward-moving stepped leader with our eyes, but it has been well recorded with high-speed film streak cameras and high-speed video cameras. One reason we do not visually detect the stepped leader preceding a first return stroke is apparently because the eye cannot resolve the time interval between the formation of the weakly luminous leader and the explosive illumination of the leader channel by the return stroke, 10 ms or less depending on the height. Further, the human eye also cannot respond quickly enough to resolve the upward propagation of the return stroke, and thus it appears as if all points on the return stroke channel become bright simultaneously. The return stroke impulsively heats the current-carrying air which then expands and thereby produces most of the thunder we hear. That thunder, a sound wave, originates as an outward propagating shock wave and is a shock wave to 10 m to 100 m from the expanding return stroke channel.

After the first stroke current has ceased to flow, the lightning flash may end, in which case the discharge is called a single-stroke flash. About 80% of flashes that lower negative charge in temperate regions contain more than one stroke, usually three to five. The individual strokes are typically separated by 40 or 50 ms. Strokes subsequent to the first (called “subsequent strokes”) are initiated only if additional negative charge is made available to the upper portion of the previous stroke channel in a time less than about 100 ms from the cessation of the current of the previous stroke. When this additional charge is available, a continuously propagating leader (as opposed to a stepped leader), known as a “dart leader”, moves down the defunct return stroke channel, again depositing negative charge from the negative charge region along the channel length, as illustrated in Fig. 1.3 at 60.00 and 61.00 ms. The dart leader thus sets the stage for the second (or any subsequent) return stroke. The dart leader's earthward trip takes a few milliseconds. To high speed cameras the dart leader appears as a luminous section of channel tens of meters in length which travels smoothly earthward at about 1/30 the speed of light (about  $10^7 \text{ m s}^{-1}$ ). The dart leader generally deposits somewhat less charge, perhaps a tenth as much, along its path than does the stepped leader, with the result that subsequent return strokes generally lower less charge to ground and have smaller peak currents than first strokes.

First stroke currents are typically near 30 kA, while subsequent stroke peak currents are typically 10–15 kA. First stroke current risetimes are a few microseconds, likely influenced by the attachment process, while subsequent stroke risetimes are faster, of the order of 0.1 μs.

The first return stroke in a negative cloud-to-ground flash appears to be strongly branched downward because the return stroke follows the path and branches of the previous stepped leader. Dart leaders generally follow only the main channel of the previous stroke and hence subsequent return strokes generally exhibit little branching. There are types of leaders preceding subsequent return strokes that are intermediate between the stepped leader and the dart leader. In fact, there may be a more or less continuum of leader features between pure stepped leaders and pure dart leaders. Dart leaders propagating

down the remains of more-decayed (either older or subjected to more wind turbulence) or less-well-conditioned return stroke channels may at some point begin to exhibit stepping, either within the confines of those channels of warm, low-density air or by leaving those channels and propagating into virgin air, in either case becoming dart-stepped leaders or chaotic dart leaders, the latter characterized by especially noisy radio frequency (RF) emission and copious X-ray emission. Because some of the dart-stepped leaders form new paths to ground, one-third to one-half of all cloud-to-ground lightning flashes contact the Earth in more than one location.

A typical cloud-to-ground discharge lowers about 30 C of negative charge from the main negative charge region of the cloud ([Fig. 1.1](#)) to the Earth. This charge is transferred in some tenths of a second by the several strokes and any “continuing current” which may flow from the cloud-charge source to ground after a stroke. Most continuing current follows subsequent strokes. Half of all flashes contain at least one continuing current interval exceeding about 40 ms. The time between strokes which follow the same channel can be as long as tenths of a second if a continuing current flows from the cloud charge into the channel after a given stroke. Apparently, the channel is receptive to a new dart leader only after all current, including continuing current, has terminated. While the leader-return stroke process transfers charge to ground in two steps (charge is put on the leader channel from the cloud charge, from the top down, and then is discharged to ground from the channel bottom upward), the continuing current represents a relatively steady charge flow between the main negative charge region and ground.

As noted earlier, about 10% of cloud-to-ground flashes are initiated by downward-moving stepped leaders that lower positive charge ([Fig. 1.2c](#)), either from the main upper positive charge region of the cloud or from the small lower positive charge region ([Fig. 1.1](#)). The steps of positive stepped leaders are typically less distinct optically than the steps of negative stepped leaders if, indeed, there are steps at all. More discussion of the optical characteristics of positive leaders is found in Section 4.3. Positive return strokes can exhibit currents at the ground whose peak value can exceed 300 kA, considerably larger than for negative strokes whose peak currents rarely exceed 100 kA. Nevertheless, median positive peak currents are similar to median negative peak currents, near 30 kA. Positive discharges usually exhibit only one return stroke, and that stroke is almost always followed by a relatively long period of continuing current. The overall charge transfer in positive flashes can considerably exceed that in negative flashes. Although positive flashes are less common than negative flashes, the potentially large peak current and potentially large charge transfer of the positive flashes make them a special hazard that must be taken into account when designing lightning protection.

In upward lightning ([Fig. 1.2b, d](#)), the first leader propagates from ground to cloud but does not initiate an observable return stroke or return-stroke-like process when it reaches the cloud charge. Rather, the upward leader primarily provides a connection between the cloud charge region and the ground. After that connection is made and the initial current has ceased to flow, “subsequent strokes”, initiated by downward-moving dart leaders from the cloud charge and having the same characteristics as strokes following the first stroke in cloud-to-ground lightning may occur. About half of all upward flashes exhibit such subsequent return strokes. Natural upward lightning is similar to the upward lightning that can be artificially initiated (triggered) from natural thunderstorms using the rocket-and-wire technique, noted earlier and discussed in the next paragraph. The reason that the upward first leader in both natural upward and triggered lightning does not produce a detectable downward return stroke is likely because there is no well-defined region of vastly different electrical potential in the cloud from that of the leader, as there is in the case of the downward leader of negative potential  $10^7$ – $10^8$  V striking the well-conducting zero-electrical-potential Earth. For more information regarding the physics of all types of cloud and cloud-to-ground lightning, the reader is referred to the books by Uman [[4](#)], and Rakov and Uman [[5](#)].

Lightning can be artificially initiated (triggered) from natural thunderstorms via the rocket-and-wire technique, either with a grounded wire towed upward for a few hundred meters by a small rocket (classical triggering) or with an ungrounded wire (altitude triggering) of a few hundred meter length whose bottom is raised 100 m or so above ground. Triggered-lightning has been and is a major subject of study as part of modern lightning research because of its accessibility and its similarity to aspects of all types of natural lightning. At the University of Florida and Florida Institute of Technology lightning research facility in north-central Florida, the International Center for Lightning Research and Testing (ICLRT), we trigger 20–30 lightning flashes per summer, and have triggered over 400 total.

The mechanisms of classical rocket-and-wire triggering are shown in [Fig. 1.4](#) in a sequence of 6 panels, increasing in time from left to right. Typically, when the rocket has lifted the trailing wire (in all ICLRT studies the conducting wire has been unspooled from the rocket) to a height of several hundred meters in a time of 2 or 3 s, electrical breakdown occurs at the top of the wire. For a several-hundred-meter length of vertical, grounded, conducting wire, the ambient electric field at and above the wire top from the negative cloud charge overhead is enhanced to a level sufficient to launch an upward propagating, positively-charged leader (UPL) from the wire top toward the negative cloud charge. At some point, not well defined, the UPL transitions to an “initial continuous current” (ICC) of some hundreds of amperes flowing for tenths of a second. The triggering wire, 0.2 mm diameter Kevlar-covered copper, generally explodes or melts after 10 ms or so of current flow, during the propagation of the upward positive leader. See [Fig. 1.9](#) for an example of the path followed by the triggered lightning UPL and ICC as determined from the location of VHF radiation sources. When the ICC ceases to flow, the flash may end, or, more preferably for lightning research, a negative dart leader (or dart-stepped or chaotic dart) may traverse the defunct ICC channel in a downward direction from cloud charge to ground, followed by the propagation of a return stroke from the ground up the negatively-charged leader channel, an essentially identical sequence to subsequent strokes in natural lightning.

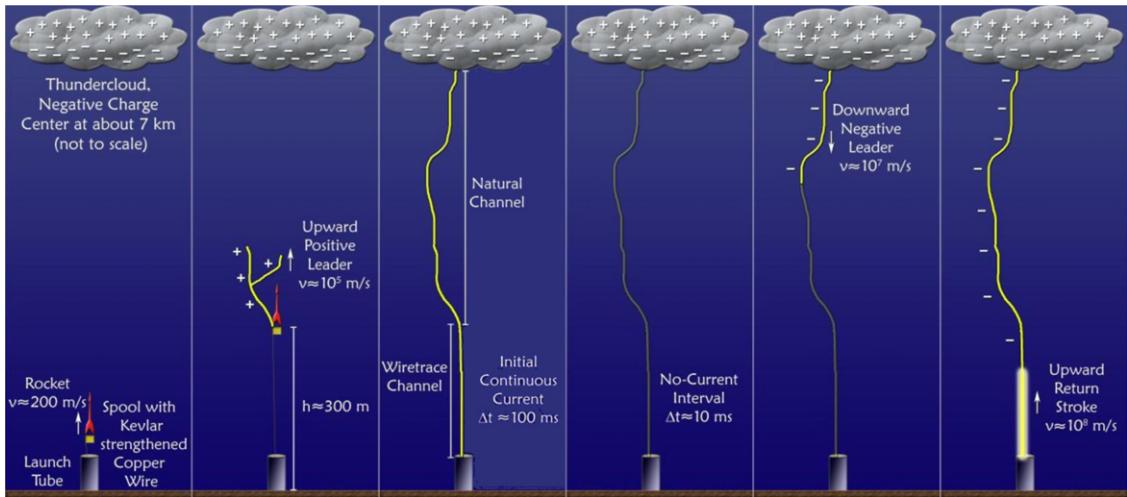


**Fig. 1.4.** Processes involved in the artificial initiation of lightning by rocket-and-wire triggering. Drawing by J. Schoene. Source: Adapted from Uman [491].

Rocket-triggered lightning has many features in common with upward-initiated lightning from tall structures. In rocket-triggered lightning, the several hundred meters of vertical, grounded, conducting wire carried aloft by the rocket provides the same function as the tall, stationary, conducting structure. In both cases, an upward-moving leader from the grounded object is followed by an ICC; and these two processes replace the downward-moving stepped leader and upward-moving first return stroke of natural lightning. In both cases, there may or may not be dart leader/return stroke sequences that follow the ICC, sequences present in about half of both natural and triggered upward-initiated flashes. The fundamental difference between the two cases is that the initiating electric field for rocket triggering must be relatively high and steady (e.g.,  $20 \text{ kV m}^{-1}$  at 500 m altitude) whereas the initiating field for a stationary tall structure is thought to be either a rapid electric field change of about the same magnitude caused by an overhead cloud discharge or nearby ground flash, or a high, relatively steady field.

The preceding discussion addressed the triggering of lightning using a grounded wire, so-called “classical” triggering. “Altitude” triggering, triggering with an ungrounded wire, has much less probability of success, but, when successful, produces a stepped leader from the bottom on the ungrounded wire, simulating well the stepped leader of natural lightning. A detailed discussion of classical and altitude rocket-triggered lightning and other prospective types of artificially-initiated lightning, such as laser triggered, is found in Chapter 7 of Rakov and Uman [5].

We briefly discuss now so-called Compact Intracloud Discharges (CIDs), considered in more detail in Section 6. CIDs are discharges of short vertical length, probably less than 1 km, high in the cloud that produce relatively large narrow bipolar radio pulses accompanied by copious VHF radiation and little visible light. Although most CIDs appear as isolated events, CIDs are sometimes followed by normal IC lightning and so are considered a type of preliminary breakdown pulse. Other types of preliminary breakdown pulses are discussed in Sections 3.2.3 and 4.1.

We now list the general types of Transient Luminous Events (TLEs) that occur between cloud tops and the lower ionosphere at about 90 km. Each type has several subtypes. “Sprites” are electrical discharges that occur when relatively large cloud charges are discharged to Earth by lightning, generally positive lightning, transiently increasing the electric field between cloud tops and the ionosphere. “Jets” (blue starters, blue jets, gigantic jets) are upward-going lightning from high-altitude cloud charge into the low density air above cloud tops, gigantic jets reaching all the way to the ionosphere, and blue jet starters going upward only a kilometer or so. “Elves” are the circularly-expanding luminous reaction of the lower ionosphere when cloud-to-ground lightning’s radiated electromagnetic fields strike it. “Sprite halos” are horizontal ionization caps, sometimes appearing above Sprites. The halos have sometimes been misidentified in the literature as Elves. TLEs are further discussed in Section 7.

Terrestrial Gamma-Ray Flashes (TGFs), discussed in detail in Sections 5.3.4 and 5.4.8, are bursts of X-ray and gamma rays usually of less than 1 ms total duration with energies of individual photons reaching tens of MeV. They represent one class of high energy phenomena that are associated with thunderstorms and lightning. TGFs have been observed primarily on orbiting satellites and are associated with the leaders of certain cloud discharges that occur near the tops of thunderclouds. TGFs have been reported only twice on the ground, both times at the authors’ research facility [23,24], and once in a research aircraft [25].

Finally, we say a few words about “ball lightning”, the subject of question 10 in Section 1.5. Further discussion of this mysterious phenomenon is outside the scope of the present review. There are almost 5000 published eyewitness reports of ball lightning, and many published theories, none of the theories being completely satisfactory [26–28]. Hill et al. [28] used triggered lightning to reproduce the conditions of several leading theories of ball lightning, with limited success in producing

ball lightning but perhaps generating some of its relatives. The most commonly reported ball lightning observation is of an orange-to-grapefruit-size glowing sphere which is usually red, orange, or yellow in color with luminosity about as bright as a 60 W light bulb. Larger and smaller spheres are also observed. Ball lightning typically has a duration of a few seconds, during which time it generally moves horizontally (it does not rise as would hot air) and then decays either slowly and silently or abruptly and explosively. Its luminosity is reported to be roughly constant until it extinguishes. It is most often seen spatially close to and just after the occurrence of a cloud-to-ground lightning flash. There are a significant number of credible reports of ball lightning occurring within metal (aluminum) aircraft, both commercial and military. Ball lightning, or a similar phenomenon, has been also reported to be generated from high-power electrical equipment such as battery-bank switches.

#### 1.4. Experimental techniques

It is of value to examine the various experimental tools that are used to study lightning since modeling and understanding of lightning processes depend on the adequacy of the experimental data characterizing those processes. We can perhaps best provide a general view of lightning experimental science by describing the equipment that has been assembled at our own research facility, the ICLRT located on an Army National Guard Base 45 km northeast of the University of Florida campus in Gainesville.

A schematic drawing of the ICLRT site is shown in Fig. 1.5. The ICLRT was founded in 1994, occupies about one square kilometer of flat land, and has its military airspace controlled for launching rockets to trigger lightning. A photograph of one of the two triggering facilities at the ICLRT is shown in Fig. 1.6 and one of the 26 instrumentation sites arrayed over the 1 km<sup>2</sup> is shown in Fig. 1.7. As noted earlier, about 400 lightning flashes have been triggered at the ICLRT to date. Experimental facilities at the ICLRT include two time of arrival (TOA) networks for locating lightning sources in 3D over the ICLRT, the individual networks being composed of ten electric-field-derivative ( $dE/dt$ ) antennas and ten co-located X-ray detectors (eight plastic detectors and two Lanthanum Bromide X-ray detectors), a nine sensor electric field measurement network (bandwidths from near DC to 15 MHz), the TERA network (TERA stands for Thunderstorm Energetic Radiation Array) of 45 NaI detectors, triggered lightning current measurements in the range from 1 mA to 60 kA, a seven-station Lightning Mapping Array (LMA) network employing the TOA technique to map lightning VHF sources near 70 MHz to about 12 km in altitude and about 25 km in radius, a 30 pixel imaging X-ray camera containing 30 unshielded NaI detectors aimed slightly above the rocket launcher, and an X-ray spectrometer composed of seven NaI detectors with varying degrees of aluminum, steel and lead shielding. The LMA sources for a natural cloud-to-ground discharge preceded by an intracloud flash, both occurring near the ICLRT, are shown in Fig. 1.8. The LMA sources for the initial stage of a triggered lightning flash at the ICLRT are shown in Fig. 1.9. The  $dE/dt$  and X-ray time-of-arrival networks each use 10 separate sensors from the 26 instrumentation sites, connected together with nanosecond timing resulting in meter-scale location accuracy for both X-ray pulses and  $dE/dt$  pulses within about 1 km<sup>3</sup>. The ICLRT photographic setup for optically recording lightning includes eight Nikon digital still cameras that take continuous sequential 5 s time exposures from different locations, five Canon high-definition (HD) video cameras, one Phantom v711 high-speed camera (100  $\mu$ s frame rate), one Phantom v7.3 high-speed camera (100  $\mu$ s frame rate), one Photron SA1 high-speed camera (3.3  $\mu$ s frame rate), and one Cordin 550 high-speed camera (0.25  $\mu$ s frame rate). During the Summers of 2012 and 2013, the University of Oklahoma (OU) operated both a dual polarization C-Band radar and an X-band radar from approximately 11 km south of the ICLRT in Keystone Heights in order to record the cloud hydrometer characteristics over the ICLRT. Additionally, during Summers of 2012 and 2013 visiting scientists operated time-resolved spectrometers, photometers, and streak cameras from the Optical Building 200 m from the main triggering site (see Figs. 1.5 and 1.6); and in 2013 a team from NSSL launched electric field and precipitation probing balloons into overhead storms at the ICLRT.

#### 1.5. The top ten questions in lightning research

Given below is our subjective view of the top ten questions in lightning research.

1. By what physical mechanism or mechanisms is lightning initiated in the thundercloud? What is the maximum cloud electric field magnitude and over what volume of the cloud? What, if any, high energy processes (runaway electrons, X-rays, gamma rays) are involved in lightning initiation and how? What is the role of various forms of ice and water in lightning initiation?
2. What physical mechanisms govern the propagation of the different types of lightning leaders (negative stepped, first positive, negative dart, negative dart-stepped, negative dart-chaotic) between cloud and ground and the leaders inside the cloud?
3. What is the physical mechanism of leader attachment to elevated objects on the ground and to the flat ground? What are the characteristics of upward connecting leaders from those objects or from the ground?
4. What is the physics of compact intra-cloud discharges (CIDs) (that produce a narrow bipolar wideband electric field pulse, a narrow bipolar event or NBE, apparently multiple-reflecting propagating waves within 1 km height, and copious HF and VHF radiation)? How are CIDs related to other types of preliminary breakdown pulses? Are CIDs related to the Terrestrial Gamma-Ray Flashes (TGFs) observed on orbiting satellites or to the Transient Luminous Events (TLEs) photographed above cloud tops, particularly to so-called “gigantic jets”?

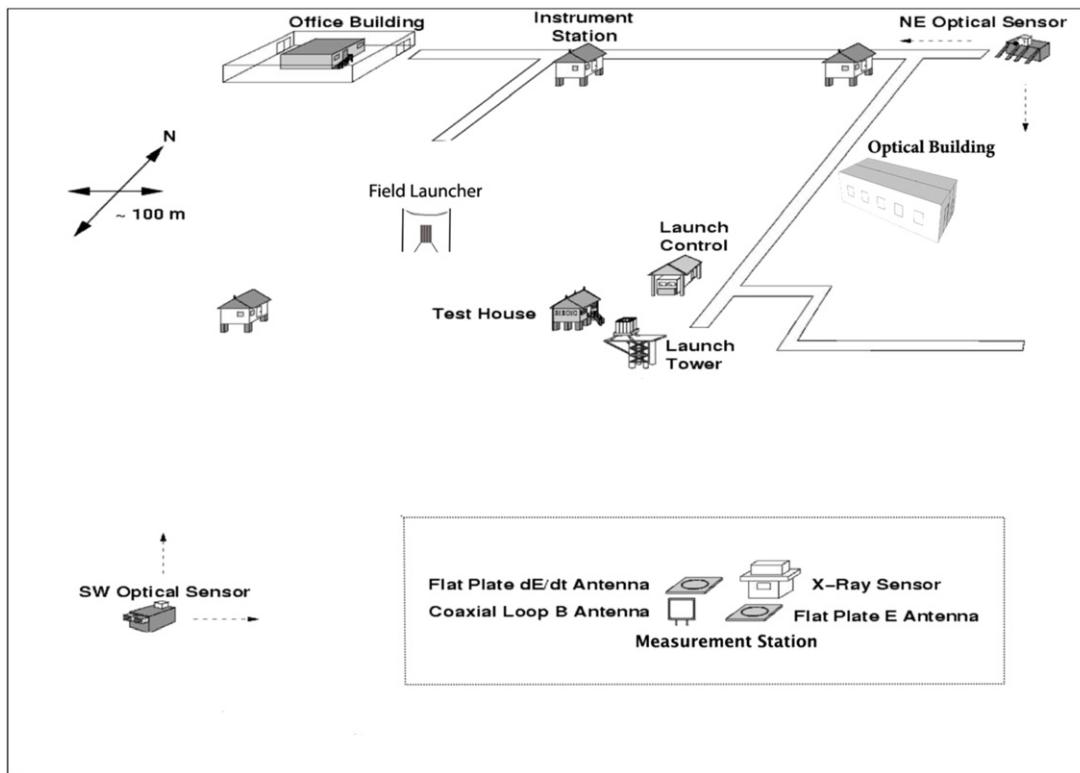


**Fig. 1.5.** A drawing of the layout of structures on one square kilometer of the International Center for Lightning Research and Testing (ICLRT) at Camp Blanding. Some of the structures are shown in the photograph of Fig. 1.6. The compliment of instruments shown in the box at the bottom of the drawing is found at 26 locations across the site, all connected by fiber optics to Launch Control and the Office Trailer. One such instrumentation site is shown in Fig. 1.7.

Source: Courtesy, J.D. Hill.

5. By what physical mechanisms do lightning leaders emit pulses of X-rays? Do the X-rays play a role in lightning propagation? By what mechanism do thunderclouds generate relatively-steady internal X-rays? Do X-rays and other high energy radiation affect cloud electrification and play a role in lightning initiation?
6. By what physical mechanisms are Terrestrial Gamma-Ray Flashes (TGFs) produced? Do TGFs pose a hazard to individuals in aircraft?
7. How do cloud-to-ground and intra-cloud lightning affect the upper atmosphere and ionosphere? What are the physics of the Transient Luminous Events (TLEs), “Sprites”, “jets”, and “elves”? What is the energy input into the ionosphere/magnetosphere from lightning?
8. How exactly does rocket-and-wire (“classical” with a grounded wire and “altitude” with a floating wire) triggering of lightning work? Are there other possible and practical triggering techniques such as laser triggering? Can triggering reduce or eliminate the local occurrence of natural lightning?
9. What are the power and energy of the component processes of lightning flashes and how are they distributed among electromagnetic processes (DC to light), thermal processes, mechanical (acoustic) processes, and relativistic (high energy) processes (runaway electrons, runaway positrons, X-ray, and gamma rays)?
10. What is the physics of ball lightning? Is there more than one type of ball lightning?

Questions 1, 2, 4, 5, 6, and 7 will be addressed directly in the following sections of this paper: Section 3. The Lightning Initiation Problem; Section 4. Lightning Propagation; Section 5. High-Energy Atmospheric Physics; Section 6. CIDs; and Section 7. TLEs.

## 2. Conventional discharges

### 2.1. Overview

Conventional discharges in a gas such as air involve the propagation of free low-energy (few eV) electrons and ions and should be distinguished from discharges that involve runaway electrons in the keV to multi-MeV range. These high-energy discharges will be discussed in detail in Section 5.

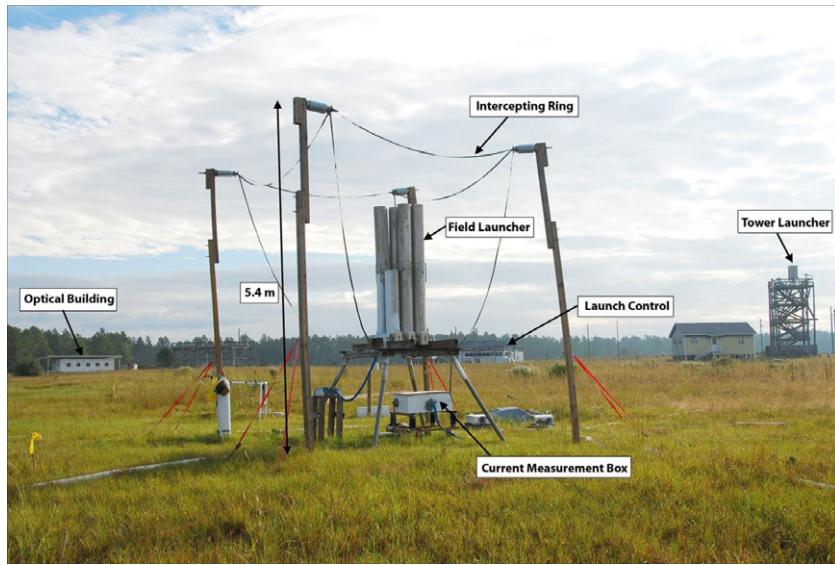


**Fig. 1.6.** A photograph showing ground-based (Field) and Tower rocket launchers, Launch Control, and the Optical Building at the International Center for Lightning Research and Testing (ICLRT) at Camp Blanding. About 100 electromagnetic and optical measurements are arrayed around the research area of the ICLRT.

Source: Courtesy, J.D. Hill.



**Fig. 1.7.** Color photograph of one of the ICLRT instrumentation sites with the Tower Launcher and Launch Control in the background.

Source: Courtesy, J.D. Hill.

## 2.2. The microphysics of conventional discharges

When an electron-positive ion pair is created in air in the presence of an applied electric field, the free, low-energy electron and the ion both move under the influence of the field. In air, the low-energy electrons quickly attach to oxygen via either 2-body or 3-body attachment processes, forming negative ions. The electron attachment time,  $\tau_a$ , is a function of the electric field strength and the air density. At sea-level  $\tau_a$  has values between about  $8 \times 10^{-8}$  s and  $1.4 \times 10^{-7}$  s, depending upon the electric field strength. At higher altitudes,  $\tau_a$  increases more quickly than the air density decreases because of the 3-body electron attachment. For example, at thunderstorm altitudes,  $\tau_a$  is usually on the order of about  $10^{-6}$  s.

Before the electrons attach, they experience multiple scatters with air molecules, resulting in a constant average velocity,  $\vec{v}_e = -\mu_e \vec{E}$ , known as the drift velocity, where  $\mu_e$  is the mobility of the electrons. Similarly, ions also drift in the electric field, but at a much lower speeds due to their larger masses and hence smaller mobilities. The positive and negative ions have drift velocities given by  $\vec{v}_{\pm} = \pm \mu_{\pm} \vec{E}$ , where the mobilities of the ions in dry air are  $\mu_+ = (1.4 \times 10^{-4} \text{ m}^2/\text{V s})/n_{air}$

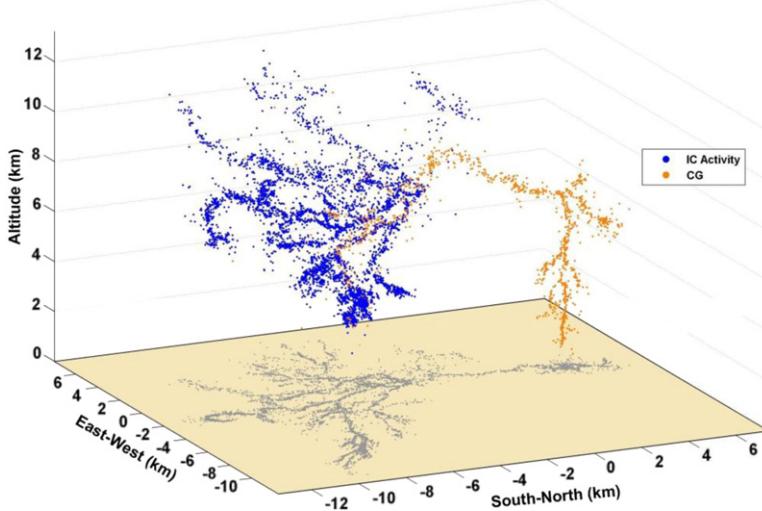


**Fig. 1.8.** LMA sources from a “Bolt-from-the-Blue” flash. The flash began as an intracloud discharge between the negative midlevel charge region and the positive upper charge region (see Fig. 1.1). Following extensive intracloud activity (colored blue), a cloud-to-ground flash occurred, initiated by the stepped leader whose VHF source locations are shown in orange. The ICLRT is located at the origin of the plot.  
Source: Courtesy, J. Pilkey.

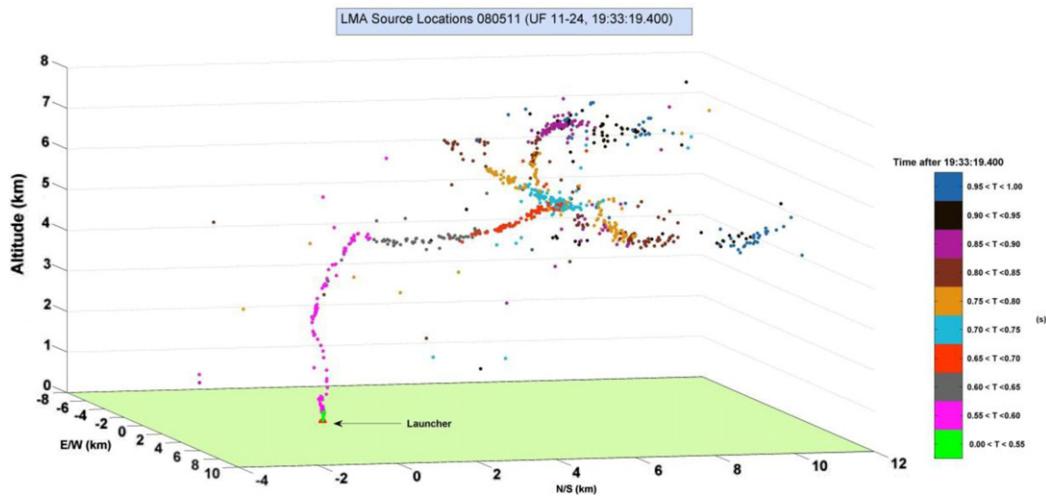


**Fig. 1.9.** LMA source locations for the initial stage (IS) of rocket-and-wire lightning UF 11–24 that occurred on August 5, 2011. The bright green sources are associated with successive electrical breakdowns (the so-called precursor pulses) at the top of the upward-moving triggering wire and occur during 550 ms of the roughly 2 s wire launch. The time of the LMA sources during the IS, including the precursor pulses, are color coded on the right.  
Source: Adapted from Hill et al. [492].

and  $\mu_- = (2.1 \times 10^{-4} \text{ m}^2/\text{V s})/n_{\text{air}}$  [29], and  $n_{\text{air}}$  is the air density relative to that at sea-level at standard conditions (1 atm pressure and a temperature of 0 °C), i.e.,  $n_{\text{air}} = N_{\text{air}}/N_{\text{STP}}$ , with  $N_{\text{air}}$  the number density of air molecules. At the electric fields of interest, unlike the ions, the electron's mobility,  $\mu_e$ , is sensitive to the electric field strength, having sea-level values between about 0.3 m<sup>2</sup>/(V s) and 0.04 m<sup>2</sup>/(V s), depending upon the electric field. However, if we consider, instead, the same reduced electric field,  $E/n_{\text{air}}$ , then  $\mu_e$  scales simply with air density as 1/ $n_{\text{air}}$ . More precise values of the attachment rates and mobilities are found, for instance, using data from Refs. [30,31].

As the electric field is increased, the average energy of the drifting electrons also increases. At high enough fields, a fraction of the electron velocity distribution will have energies sufficient to ionize air, predominantly due to the impact of the electrons with the air molecules, thus generating additional electrons along with the original ones. These secondary electrons may also ionize air, creating more electrons. This growth in the number of electrons competes with the loss of electrons due to attachment. For small electric fields, where the attachment rate is larger than the ionization rate, without an external ionization source, the number of free electrons quickly declines. As the field strength is increased, however,

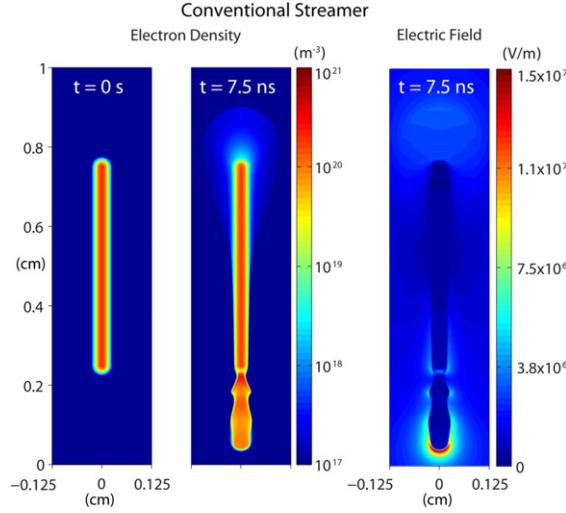


**Fig. 2.1.** Cross-sectional views of a numerical simulation of the electron density and electric field of a positive streamer at sea-level, initiated from a conductive region ( $t = 0$  s). The positive streamer propagates downward at the bottom of the figure. No negative streamer is initiated at the top of the column in this simulation.

Source: Figure reprinted with permission from [37].

© 2012, by the American Physical Society.

the ionization rate increases rapidly, surpassing the attachment rate at about  $E_k = 3 \times 10^6 \text{ V/m} \times n_{\text{air}}$  [32], called the conventional breakdown field. Note that this field scales linearly with air density, so at higher altitudes in the atmosphere the breakdown field is lower than at sea level. Above  $E_k$ , the number of electrons grows exponentially with time and distance, forming an avalanche of low-energy electrons. Of course, for the avalanche to be initiated there must be at least one free, low-energy “seed” electron. Such seed electrons may be supplied by background radiation such as from atmospheric cosmic-rays and natural radioactivity as well as from ultra-violet light.

The densities of the low-energy electrons and positive and negative ions,  $n_e$ ,  $n_p$  and  $n_n$ , may be found using the following coupled equations (e.g., [30,31,33]):

$$\frac{\partial n_e}{\partial t} + \vec{\nabla} \cdot (\vec{v}_e n_e) - \vec{\nabla} \cdot (\hat{D}_e \cdot \vec{\nabla} n_e) = S_e + n_e v_e (\alpha_e - \eta) - \beta_{ep} n_e n_p; \quad (2.1)$$

$$\frac{\partial n_p}{\partial t} + \vec{\nabla} \cdot (\vec{v}_p n_p) = S_e + n_e v_e \alpha_e - \beta_{ep} n_e n_p - \beta_{np} n_n n_p; \quad (2.2)$$

$$\frac{\partial n_n}{\partial t} + \vec{\nabla} \cdot (\vec{v}_n n_n) = n_e v_e \eta - \beta_{np} n_n n_p, \quad (2.3)$$

where  $S_e$  is the source of new ionization;  $\alpha_e$  is the number of ionizing collisions per unit length, and  $\eta$  is the number of electron attachments per unit length. The parameter  $\alpha_e$  is called the first Townsend coefficient, and  $\eta = (v_e \tau_a)^{-1}$  is called the attachment coefficient, and both depend upon the electric field strength and the air density [34].  $\beta_{ep}$  is the rate (per second) of electron-ion recombination.  $\beta_{np}$  is the rate (per second) of ion-ion recombination, and  $\hat{D}_e$  is the low-energy electron diffusion tensor. In Eqs. (2.2) and (2.3) the diffusion terms for the ions could be included, similar to Eq. (2.1) for the electrons. However, for most cases of interest for electrical discharges in strong electric fields, the diffusion term is small compared with the drift velocity term (2nd term on left).

Eqs. (2.1)–(2.3) are often combined with Poisson’s equation for the electrostatic potential.

$$\nabla^2 \varphi = -\frac{e}{\epsilon_0} (n_p - n_e - n_n). \quad (2.4)$$

The electric field is then calculated, allowing the various coefficients in Eqs. (2.1)–(2.3) to be found. These coupled equations are usually solved numerically. Examples of such calculations are shown in Fig. 2.1.

As an example, let us consider avalanche multiplication from a single electron injected at the origin. For simplicity, we shall consider a uniform electric field in the  $-z$  direction and low enough electron and ion densities so that we may ignore recombination. In Eqs. (2.1)–(2.3), the combination of the velocity times the density is the convective flux, e.g.,  $\vec{F}_e = \vec{v}_e n_e$ . If we ignore the effects of diffusion, the total number of electrons passing through the plane at position  $z$  is then given by [35]

$$N_e(z) = \int_{-\infty}^{\infty} \int_{-\infty}^{\infty} \int_{-\infty}^{\infty} F_e(x, y, z, t) dx dy dt. \quad (2.5)$$

Integrating Eq. (2.1) as in Eq. (2.5) (and dropping the diffusion term) gives

$$\frac{dN_e}{dz} - N_e(\alpha_e - \eta) = \delta(z), \quad (2.6)$$

where  $\delta(z)$  is the Dirac delta function, describing the injection of one electron at the origin

For a uniform electric field both  $\alpha_e$  and  $\eta$  are constant, and so Eq. (2.6) may be integrated directly to give

$$n_e = \exp((\alpha_e - \eta)z), \quad (2.7)$$

the number of low-energy electrons in an avalanche at position  $z$  initiated by one seed electron. For strong electric fields,  $E > E_k$ , the avalanche given by Eq. (2.7) can rapidly grow on sub-millimeter length scales.

If the number of electrons in the avalanche grows sufficiently large, the polarization of the medium due to the separation of the electrons and the positive ions that trail behind can enhance the field at the front of the avalanche, increasing the amount of avalanche multiplication at the tip. In this way, a self-propagating structure called a negative “streamer” may form, which allows the avalanche to propagate into lower ambient fields, since the streamer carries the high field needed for avalanche multiplication with it as it moves. Raether [36] estimated that about  $10^8$  electrons in the avalanche are needed to create a streamer.

Similarly, positive streamers may propagate in the opposite direction of the electron avalanche. For a positive streamer, electron avalanches move towards the column of positive ions. These avalanches create more positive ions, which extends the channel and hence the streamer in the direction of the electric field. Fig. 2.1 shows numerical simulations of the low-energy electron density and electric field strength for a positive streamer initiated by a conductive region, representing for example a long hydrometeor [37]. In the figure, the electric field is directed downward, and so the electron avalanches move upward. The positive streamer can be seen as a downward extension of the conductive region. No corresponding upward extension is produced, indicating that no negative streamer was created.

It is known that positive streamers can propagate in lower ambient electric fields than negative streamers ( $\sim 5 \times 10^5$  V/m versus  $\sim 1 \times 10^6$  V/m at sea level for positive and negative streamers, respectively), and so positive streamers are often created before negative streamers [33]. Phelps and Griffiths [38] performed laboratory experiments in which positive streamers propagated in a parallel plate geometry with different air pressures and humidities. The experiments used dark adapted eyes to determine the minimum field required for positive streamers to cross a gap (usually 12 cm). It was found that the critical field for propagation,  $E_s$ , was about  $5 \times 10^5$  V/m at sea-level. Furthermore, the critical field depended linearly on the water vapor pressures from 0 to 30 mbar with values of  $E_s$  between  $4 \times 10^5$  V/m and  $6 \times 10^5$  V/m at  $T = 25^\circ\text{C}$ . They also found that the critical field decreased approximately as the 1.5 power of the dry air pressure. As an example, for the mid-level of a thunderstorm ( $P = 300$  mbar and  $T = -14^\circ\text{C}$ ), they found the critical field for positive streamer propagation is about  $1 \times 10^5$  V/m. For fields at or just above the critical field, the streamer propagation speed is on the order of  $10^5$  m/s. Because the free electrons quickly attach to air, the conductivity of the streamer is only significant for a few cm behind the tip. As a result, such streamers will not transport large amount of charge large distances. However, as the electric field is increased, the speed of the streamers and the charges at the tips also increase, resulting in longer conducting columns behind the tip.

As a streamer propagates through a strong electric field, the charge that accumulates at its tip may become sufficiently large that the streamer splits into two or more streamers. The process may repeat many times, producing a branched network of positive and/or negative streamers. If the currents produced by the streamers are large, the streamers may also heat the air, which increases the conductively, allowing more current to flow, which causes more heating, and so on. This instability tends to constrict the current along a narrow hot channel. Specifically, above about 1500 K, the conductivity of air greatly increases, due to the rapid detachment of electrons from negative ions [39]. Gallimberti [40] hypothesized that as the temperature increases, the energy initially transferred into the vibrational states of nitrogen molecules by the current flow through cold air is transferred to translational energy states causing the temperature of the channel to rise quickly. At high electron densities and temperatures, thermalization occurs and impact ionization between ions and neutrals becomes important. Such hot (heated to 5000 K or more) narrow channels are often called “leaders”.

Without the presence of a metal electrode to supply an external current (no such electrode is present inside thunderclouds) it is challenging to understand how the so-called streamer to leader transition actually occurs. For laboratory sparks, it is observed that multiple streamers emitted from a small region of a metal electrode have a high enough current density to heat the electrode and the nearby air (see Sections 4.2 and 4.3). For thunderclouds, without metal electrodes, it is not clear how this process happens. In order to create and maintain a hot channel, the energy from the electrostatic field must be concentrated into a much smaller volume, where the heating occurs. This may happen via the creation of an extended streamer network, with many streamers feeding their current into a narrow channel, although this idea has not yet been validated either experimentally or theoretically for the thunderstorm environment.

It is known that leaders may themselves propagate by producing large electric fields at their tips, these large fields generating streamers that move out into the space in front of the leader. These streamers deliver current to the leader, keeping it hot and allowing it to propagate. The space in front of the leader is called the streamer zone [41]. It is observed that negative leaders propagate in a stepwise fashion (Section 1.3). For the leader to move forward, a leader segment in the

space in front of the old leader channel, called a space leader, develops out of the preceding corona streamers. The space leader propagates backwards until it connects to the old leader channel forming a longer channel. When the space leader and old channel come in contact, there is a rush of current that brings the old and new segments to the same electric potential. When this current wave hits the end of the new leader segment, a burst of streamers propagates out in front of the new tip, called the corona flash. A new space leader then forms in front of the new tip and the cycle repeats. This process is discussed further in Section 4.2. For natural cloud-to-ground lightning, the stepped leader lengths apparently range from a few meters near ground up to perhaps a few hundred meters in the cloud [42] (see also Sections 1.3 and 4.2). It is not understood exactly how or why negative leaders propagate in this stepped manner. In particular, it is not clear how the space leaders form and why they form so far out in front of the old leader channel.

Another type of electrical discharge occurring between metal electrodes that does not involve hot leaders or arcs is the so-called Townsend discharge [43,44]. For the Townsend discharge, positive ions and ultra-violet (UV) photons produced by the electrons in an avalanche may interact with the cathode (negative electrode) or air, producing more free electrons and thus secondary avalanches. These avalanches may, in turn, generate more ions or UV photons and the process continues. This mechanism forms a positive feedback cycle allowing the production of avalanches to be self-sustaining. The parameter that describes the Townsend feedback rate is called the second Townsend coefficient,  $\gamma_T$ , the probability per avalanche electron of creating a new seed electron in one feedback cycle. If we multiply the Townsend coefficient by the total number of electrons in the avalanche,  $\gamma_T N_e^{total}$ , we get the number of new seed electrons in one feedback cycle per seed electron in the previous cycle. When  $\gamma_T N_e^{total} > 1$ , the generation of seed electrons, and hence avalanche electrons, is self-sustaining, with an ever increasing number of electrons generated with each feedback cycle. For a self-sustaining Townsend discharge, the number of avalanches may increase exponentially. In this case, eventually, the number of electrons and hence the conductivity of the air increases to the point where the field collapses, ending the discharge. Some authors distinguish between a Townsend discharge that is self-sustaining and one that is not, calling the former a Townsend breakdown and the later a Townsend discharge or, alternatively, a dark discharge. To complicate matters further, for gas-filled particle detectors, the Townsend discharge mechanism is also called a Geiger mechanism, i.e., as in a Geiger counter. In this paper, because the underlying mechanism is the same in all cases, we shall refer to any discharge that results from low-energy feedback processes as a Townsend discharge, regardless of whether or not it is self-sustaining.

### 2.3. Electrical breakdown

An “electrical breakdown” is usually considered to be a self-sustaining discharge that produces a rapid increase in the electrical conductivity that results in the collapse of the electric field. Electrical breakdown is an internal state of the system and so it is not sensitive to external influences such as external sources of ionizing radiation. The more general term “electrical discharge”, in addition to describing an electrical breakdown, also describes processes that are not self-sustaining and so may depend upon external influences. Electrical discharges may also describe slower processes such as leakage currents that relax the electric field over a long period of time.

As discussed above, air usually breaks down at electric fields that exceed the conventional breakdown field:  $E_k = 3 \times 10^6 \text{ V/m} \times n_{air}$ . In non-uniform air gaps, it is not always necessary for the field to exceed the breakdown field for all location in the gap, but for a conventional breakdown to begin, the field must exceed this value in at least one location in the gap. Furthermore, there is no single way that air breaks down. Often a narrow, hot channel is formed, through which large currents flow. Such a channel may be called a spark, an arc, a leader or a stroke, depending on the situation. Although small gaps may discharge without a hot channel (e.g., via a Townsend discharge), for kilometer scale discharges, such as occurs with lightning, a hot channel is usually (although not always) thought to be required. This is because the fast attachment of free electrons in air causes the conductivity to rapidly decrease, making it difficult for currents to flow over large distances. An alternative method for generating large scale currents is via the relativistic feedback discharge mechanism. Relativistic feedback discharges, which are discussed in Sections 5.2.4, 5.4.4 and 5.4.9, do not involve hot channels and so are quite different from normal lightning.

Normal lightning is known to propagate by forming a hot leader channel (Section 4). Leaders are highly conductive and so transfer charge from one part of the cloud to another, between clouds and the surrounding air, between clouds, and between the cloud and the ground. When leaders connect to the Earth (or conducting electrodes for laboratory sparks), large currents will flow, further heating the channel and forming a hot, bright arc. In particular, when the leader contacts the ground, a short circuit is created between the cloud and the ground with a very large potential difference between the leader tip and the Earth. The upward rush of current, typically with tens of thousands of Amps, is called the return stroke, the brightest part of the lightning flash, as discussed previously in Section 1.3. Similar fast processes within the cloud, connecting various charge regions, are called “recoil streamers” (an unfortunate name since they are not really streamers) or K-changes [45].

Leader networks have been measured to extend within thunderstorm systems over 100 km (Section 4.1), which is quite amazing considering that each leader segment is roughly as wide as a human finger. In order for the leaders to propagate, they must generate high enough electric fields at their tips to break down the air in front of them. The electric current that results must then feed into the leader channel, keeping the channel hot and transferring new charge to the tip. The physics of how the leader channel is maintained over large distances has only begun to be addressed.

## 2.4. Corona discharges

A corona discharge, or corona, is defined to be a localized discharge, consisting of electron avalanches and/or streamers, that does not result in electrical breakdown with other objects. St. Elmo's fire, seen in the dark on sharp surfaces of aircraft and the masts of ships, is an example of corona. Corona discharges are important when considering discharges associated with water and ice particles (hydrometeors) inside thunderclouds (see Section 3).

Corona discharges come in a variety of types, which depend upon the polarity of the discharge: For negative discharges these include Trichel pulses, negative glow discharges, and propagating negative streamers [46]. Trichel pulses are due to a Townsend discharge with positive ions (and UV photons) interacting with the cathode (e.g., the negative hydrometeor surface) to produce an increasing number of secondary avalanches. The discharge is eventually quenched when the space charge produced by the negative ions becomes sufficiently large to locally reduce the electric field. Only after the ions have drifted away, clearing out the space charge, can another Trichel pulse form. The repetition rate of Trichel pulses can be quite large, reaching  $10^6 \text{ s}^{-1}$ . For larger applied electric fields, the negative space charge is created far enough away from the cathode that the Townsend discharge is not completely quenched and a steady state glow-like discharge occurs. For even stronger applied fields, negative streamers can form and propagate away from the cathode. However, because of the mutual repulsion of the electrons and the fact that they often propagate into lower fields after their formation, the negative streamers tend to be weaker than the positive ones.

For positive discharges, corona starts with short duration pulses, called onset streamers, or burst pulses. The positive streamers propagate by accumulating positive space charge (positive ions) near their tip, which enhances the electric field, permitting more avalanche multiplication. As electron avalanches propagate towards the tip, they produce UV photons that cause secondary avalanches that also move towards the tip (Townsend discharge in the air surrounding the tip). The accumulated positive charge from the avalanches extends the high field region further away from the anode (e.g., the positive electrode or hydrometeor surface), allowing the streamer structure to propagate in the direction opposite to the electron motion. The pulsed nature of the onset streamers comes from the accumulation of space charge near the anode surface, which inhibits further streamer development until the positive ions drift away. For larger applied electric fields, the space charge distribution causes a steady state discharge, with no pulses, often called a positive glow that inhibits further streamer production. The avalanche multiplication for the glow occurs near the anode, between the surface and the negative space charge layer. As the applied field is increased further, vigorous pulses of streamers, called breakdown streamers occur, which for laboratory experiments, results in the spark breakdown of the gap [47].

## 3. The lightning initiation problem

### 3.1. Overview

The problem of how lightning is initiated inside thunderclouds is not only one of the biggest unsolved problems in lightning physics; it is also probably one of the biggest mysteries in the atmospheric sciences. At the heart of the problem is the fact that decades of electric field measurements made directly inside thunderclouds have failed to find electric field strengths large enough to make a spark (according to our current understanding), even when the effects of reduced air density and the presence of water and ice particles are taken into account. And yet we routinely see very large sparks being made inside thunderclouds in the form of lightning. This suggests that there is either something wrong with our measurements or there is something wrong with our understanding of how electrical discharges occur in the thunderstorm environment. When we consider how much we know about complex and exotic astrophysical objects half way across the universe, it is quite amazing that we do not understand the basics of how something as common as lightning gets started in clouds just a few miles above our heads.

Let us begin by defining precisely what we mean by lightning initiation. We define lightning initiation inside thunderclouds as the processes that lead up to the creation of a propagating hot leader channel. Sometimes that “leader” channel is called an initial breakdown or preliminary breakdown channel to distinguish its properties from those of leaders in air below the cloud, as noted in Section 4.1. To understand lightning initiation, we wish to understand both the details of the microphysical discharge processes that produce the leader and the processes within the thundercloud that create the large electric fields needed for lightning to begin. Once the leader is created inside the thundercloud then the problem becomes that of lightning propagation, which itself is rather poorly understood (see Section 4).

Of key importance to the problem of lightning initiation is determining what electric field is required at a given altitude for a lightning leader to form. Presumably this involves the heating of air by streamers, but, as discussed in Section 2, it is not well understood exactly how this occurs [48]. Stipulating that streamers must be present in order to create a leader channel, just the presence of streamers does not guarantee that a leader will form, since streamers often propagate without producing significant heating of the air. For electric fields just above the minimum field required for continuous propagation, called the critical field,  $E_s$  [38], the streamers are weak and propagate at relatively slow speeds. This means that after a few centimeters the streamers become electrically isolated from their point of origin due to electron attachment to air. For stronger fields, the streamers generate more charge at their tips and propagate faster, increasing the conductivity and length of the channel behind. As the charge at the tip builds, the streamers also branch, allowing multiple channels to

supply current back to the original channel, increasing the amount of heating (see Section 2). The electric field at which the intensification, speed, and branching of streamers becomes large enough to heat a channel segment to several thousand Kelvin is not known, but it must have a sea level equivalent field somewhere between the positive streamer critical field of 300–500 kV/m and the conventional breakdown field of 3000 kV/m. Because the streamer-to-leader transition probably occurs at field strengths above the fields required for other important processes, such as streamer initiation from ice and water particles, and streamer and leader propagation, if the field is large enough for the streamer-to-leader transition to occur, then it seems likely that lightning will also occur. As a result, we suggest that the streamer-to-leader transition field may be viewed as the true lightning initiation field.

There seems to be a broad consensus that the field needed to initiate lightning is much larger than the maximum fields observed inside thunderclouds. For example, Ref. [49] quotes a streamer to leader transition field of  $2 \times 10^6$  V/m. Since this field is several times larger than the largest thunderstorm fields measured, models have been developed to help the thunderstorm locally enhance the electric field so that lightning may initiate. However, there appears to be little experimental or theoretical justification for such a large streamer-to-leader transition field. If the required field is, in fact, smaller, then perhaps the ambient thunderstorm fields developed through normal charging are large enough to initiate lightning without assistance from other mechanisms.

Assuming that the predominate view expressed in the literature is correct and the observed thunderstorm fields are too small to initiate lightning, we may divide the main hypotheses about lightning initiation into three types: (1) The electric field somewhere within the thundercloud is really much larger than measured. (2) Lightning is created via streamer initiation from liquid or ice particles, called hydrometeors. (3) Energetic runaway electrons (see Section 5) play a role in lightning initiation. These three ideas are actually related. For example, if the runaway electron production (hypothesis 3) is playing a role in lightning initiation, it is probably by locally enhancing the electric field to large values (hypothesis 1) whereby streamers may be initiated from hydrometeors (hypothesis 2). Alternatively, it may be possible that the collective effect of many streamers (hypothesis 2) locally enhances the electric field (hypothesis 1) to the point where lightning is initiated. Finally, it is possible that thundercloud charging, all by itself, can produce isolated pockets with high electric field (hypothesis 1), e.g., via charged eddies produced by turbulence within the thundercloud [50], allowing the air to break down and lightning to form with the help of hydrometeors (hypothesis 2) or possibly even without hydrometeors present.

### 3.2. Thunderstorm and lightning phenomenology related to lightning initiation

#### 3.2.1. Thunderstorm charge structure

The simplest picture of the charge structure of thunderstorms is the standard tripole model, which contains a main negative, main positive and a lower positive charge center [51], also illustrated in Fig. 1.1 (also see Section 1.3). Representative charge values are  $-40\text{ C}$ ,  $+40\text{ C}$  and  $+3\text{ C}$ , respectively. In addition to the three charge centers in the standard tripole model, there is often a fourth significant charge region called the upper screening layer, which is negatively charged. (Actually, there is some amount of screening charge all around the cloud.) This layer is due to the higher conductivity of the clear air outside the cloud, especially in the stratosphere above the storm. This higher conductivity expels the field lines produced by the thunderstorm charges, forming the screening layer, similar to the surface charges induced on a metal conductor embedded in an external electric field. The main negative charge center is found in a relatively narrow temperature range, generally thought to be between  $-10$  and  $-25^\circ\text{C}$ , regardless of the height of the ground below the storm, where the cloud contains both ice and super-cooled water [52–54]. Both of these ingredients are thought to be necessary for the so-called non-inductive charging mechanism to operate [55]. For summer time thunderstorms in Florida and New Mexico, these temperatures occur roughly between 6 and 8 km above sea level. For Japanese wintertime storms, the negative charge center also occurs at about the same temperature range, but because the atmosphere is cooler, these temperatures occur at much lower altitudes, e.g., 2 km above sea-level [56]. The main positive charge region is usually more diffuse than the main negative charge layer and resides in the upper parts of the cloud. Depending upon the height of the thunderstorm, the upper positive charge can range between about 8–15 km in summertime storms, and has an altitude thickness of a few km in wintertime storms. The lower positive region is located below the main negative charge layer and the bottom of the visible cloud, e.g., above 2 km altitude for summertime thunderstorms in Florida.

Using a series of balloon soundings of mesoscale convection systems (MCSs), isolated supercell storms and air-mass thunderstorms, Stolzenburg et al. [57–59] found that within the updraft region ( $>1\text{ m/s}$ ) the vertical electric field profiles were relatively smooth and conformed to the basic tripole plus upper negative screening layer model described above (see Fig. 3.1). They also found that the height of the main negative charge region correlated well with the updraft speed. This can be understood by the fact that in regions with vigorous updrafts, the larger graupel particles that acquire negative charge via the non-inductive charge mechanism can be elevated to higher parts of the cloud by the updrafts [60,61]. Outside the updraft region, but still within the region of convection, Stolzenburg et al. reported that there were typically at least six distinct charge regions, with larger peak fields and more rapid changes between polarities with altitude. They also found that charge regions tended to be horizontally stratified with horizontal extents often much larger than the vertical extents.

In contrast to the picture described above, some storms are found to have inverted charge structures (lower main positive and upper main negative) [62]. In addition, lightning has been observed to deposit or re-arrange charge within storms, and

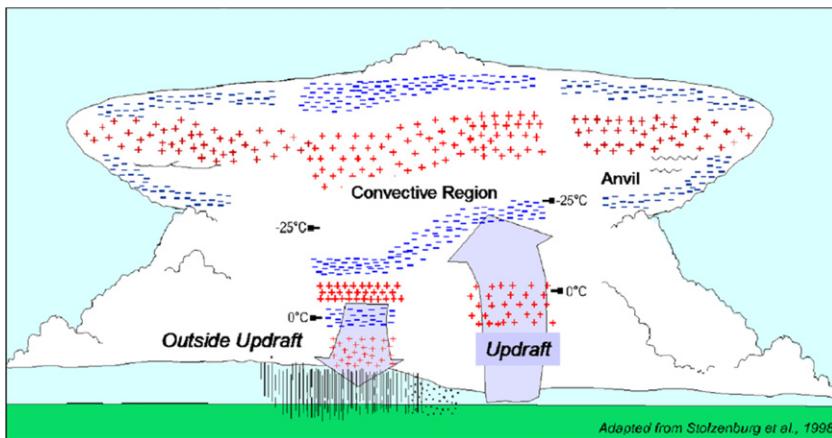


**Fig. 3.1.** Conceptual model of an isolated, mature thunderstorm. The diagram is based upon the balloon soundings through different clouds by Stolzenburg, Marshall and collaborators. The region with upward convection has the four charge regions described by the standard tripole model plus the upper screening layer. Regions with at least six charge regions are found outside the updraft region.

Source: Figure from Ref. [61].

the charge structures can evolve throughout the life of the storm, complicating the picture. Altogether, the charge structure and hence the electric fields of thunderstorms are complex, depending upon time, location and the type of storm. As a result, since in situ electric field measurements only sample a small part of the storm, by no means giving a complete picture of the electric field environment, care should be taken when interpreting the observations using a specific model of the charge structure.

### 3.2.2. Lightning initiation locations

Just as there is no single charge structure of thunderstorms, there is no single lightning initiation location, although some patterns have been observed. Proctor [63] used the first 6–10 VHF source locations of lightning in South Africa to calculate the distributions of 773 intra-cloud and cloud-to-ground lightning initiation heights. The distribution appeared to be bimodal with broad peaks near 5 km and 9 km. The temperature ranges were roughly 0 to  $-10^{\circ}\text{C}$  for the lower peak and  $-25$  to  $-35^{\circ}\text{C}$  for the upper peak. When the data were separated into 221 CG and 559 IC flashes, the CG flashes were found to fall almost entirely in the lower part of the distribution centered near 5 km. In contrast, the IC lightning followed the same bimodal distribution as all lightning, with a slight propensity for the higher initiation location. Based upon the temperatures, and given that most CG lightning has a negative polarity, it is reasonable to assume that most CG lightning initiates near the main negative charge region. It is expected that the lightning would not start in the centers of the charge regions, but instead at the edges, where the electric fields are larger, likely maximum. For lightning that initiates between the main negative and the lower positive, the negative branch propagates downward. If the lower positive charge is not large, it would provide an insufficient potential barrier to prevent the lightning from continuing on towards the ground, becoming CG lightning [64]. In contrast, if the lower positive charge is large enough to prevent the further downward propagation, then the flash would just neutralize itself in the positive charge and remain an IC lightning [64]. On the other hand, lightning that initiates between the main negative and main positive or between the main positive and the upper screening layer, might be expected to usually remain within the cloud in the form of IC lightning. Indeed, LMA and VHF interferometer data often show IC lightning initiating between the main negative and main positive charge centers, vertically crossing the gap and the branching horizontally through the two main charge regions [65]. Sometimes CG lightning can also appear as a minor branch in an extensive IC flash, and so the distinction between IC and CG flashes is not always clear cut. Finally, it is significant that about half of all lightning observed by Proctor was found to initiate at temperatures below  $-25^{\circ}\text{C}$  with some initiating at temperatures below  $-40^{\circ}\text{C}$ . It is unlikely that liquid hydrometeors would exist at those cold temperatures [66], making lightning initiation mechanism that rely on liquid raindrops unlikely in those regions of the storm.

### 3.2.3. Preliminary breakdown

There is a considerable amount of lightning literature on preliminary breakdown of lightning, also called initial breakdown, which usually refers to the first radio frequency pulses or electric field deflections detected in association with a lightning flash [67]. These observations are most likely detecting the early stage of the formation of the leader or pre-leader channel in the cloud. In this section we discuss preliminary breakdown in the context of lightning initiation. In Section 4.1, preliminary breakdown is discussed in terms of lightning propagation.

The discussion of preliminary breakdown is often divided into preliminary breakdown of CG flashes and IC flashes. For CG flashes, preliminary breakdown, which usually lasts a few ms, describes the IC lightning activity that occurs before the leader exits the cloud on the way to the ground. Preliminary breakdown pulses are observed to be large bipolar pulses, often as large as the pulses generated by lightning return strokes, which typically have currents in the tens of kA range. Krider et al. [68] recorded RF radiation between 3 and 295 MHz in coincidence with each bipolar pulse, indicating that the process involved in the bipolar pulses also involves the breakdown of virgin air, i.e., streamer type breakdown [69]. Baharudin et al. [70] investigated 1685 negative CG lightning flashes from 39 thunderstorms by simultaneously recording the slow electric field, fast electric field and narrowband radiation field (3 and 30 MHz). They found that the start of the slow field change was 1.4–6.47 ms (arithmetic mean) after the first preliminary breakdown pulse, showing that significant charge motion always followed the start of the preliminary breakdown.

Usually, the preliminary breakdown pulses will disappear before the leader exits the cloud followed by a period with few and small pulses. Once the leader exits the cloud and approaches the ground the pulses intensify again becoming normal stepped leader pulses, which are usually much smaller than the preliminary breakdown pulses (see Fig. 4.2). For IC lightning, the preliminary breakdown usually lasts tens to hundreds of microseconds and often occurs during the so-called early stage when the leader is bridging the gap between the main negative and main positive charge regions. These sometimes large bipolar pulses, usually have several fast unipolar pulses superimposed on the initial rise. Weidman and Krider [71] found that the large pulses have a full width of 63  $\mu$ s and a mean duration of 780  $\mu$ s, a value similar to the earlier results of Kitagawa and Brooks [72]. The initial breakdown pulses for IC lightning are usually about a factor of two longer and the pulse separated by a factor of a few larger than for CG lightning [73]. Coleman et al. [64] used LMA and electric field data to study lightning propagation and interpreted their results in terms of a negative potential well between the main negative and lower positive charge centers. They found that the presence of such a well alters the downward propagation of the leader, causing horizontal branching within the well. They also concluded that CG flashes have a period of preliminary breakdown if and only if there is such a potential well between the lightning initiation altitude and the ground.

It is often suggested that preliminary breakdown pulses are a form of negative leader stepping similar to that seen during negative stepped leader propagation near the ground. However, radio pulses produced by stepped leaders near the ground look quite different from preliminary breakdown pulses. Stepped leader pulses near the ground are usually unipolar, smaller in amplitude and more regular, with a pulse spacing of 10–50  $\mu$ s (see Fig. 4.2). In contrast, the preliminary breakdown pulses are bipolar, appear more irregularly, are much larger – comparable to return stroke pulse amplitudes – and have much longer spacing between pulses. If initial breakdown pulses are produced by a leader stepping processes, then it is natural to infer that the step size is measured in hundreds of meters rather than the tens of meters as seen near the ground (see Section 4.1). As for the bipolar shape of the pulses, since the electromagnetic radiation field is being measured, such pulses are always bipolar, since they are proportional to the derivative of the current moment (see Eqs. (5.38) and (5.39)). Because all electrical currents have a beginning and an end, the derivative of the current will always have one sign in the beginning and the opposite sign in the end. The polarity and the shape of the radiation pulse, will depend upon the sign of the current pulses and the how quickly the current rises and then decreases (e.g., see Fig. 4.7). For the pulses from stepped leaders near the ground, the current pulse occurs when the old and new (space leader) segment come in contact. This produces a rush of current to establish an equipotential along the conductive channel. The radio pulse is really bipolar but appears unipolar because the leader channel is long and has a high conductivity, allowing the current pulse to propagate a long distance up the old channel before it decays. In contrast, for the preliminary breakdown pulses inside the cloud, the pulses appear more bipolar because the rise-time of the current is comparable to the fall-time and the channel carrying the current is probably shorter. The longer step length may partially be explained by the lower air pressure at thundercloud altitudes, assuming step length scales inversely with density, although this explanation is not entirely satisfactory, since it is not known how or why leaders step.

Narrow bipolar pulses (NBEs) are another type of initial breakdown pulse (e.g., see Fig. 6.1) [74]. These are large, often isolated, single bipolar pulses, which typically have durations of 10–30  $\mu$ s. The initial rise of the pulse is often very fast, on the order of 1  $\mu$ s. NBEs are unique since the sferic (LF and VLF) radio pulse, which is produced by a large current moment, is observed to occur simultaneously with the HF and VHF signals caused by breakdown activity, giving the impression that the NBEs “suddenly appear from nowhere”. NBEs, which are also called compact intracloud discharges, are quite mysterious and will be discussed in more detail in Section 6.

Finally, there may be multiple breakdown events within the cloud with only one of them eventually producing the CG lightning flash. For example, Krehbiel et al. [75] using eight station electric field measurements to infer the locations of the breakdown events associated with the start of CG lightning, found a horizontal extent of several km prior to the development of the leader that propagated down to the ground. Using VHF-band radar in East Georgia USSR, Mazur [76] recorded rapidly occurring small scale discharges, with an average duration of 12.5 ms, within a narrow (1–2 km) region inside the most electrically active part of a thunderstorm. Mazur proposed that these quasi-stable discharges were long sparks (tens to hundreds of meters) produced by the lightning triggering mechanism inside the storm. Since these discharges had a maximum occurrence rate of about 200/min, which was more frequent than the maximum lightning flash density of the storm, Mazur concluded that not all long sparks created within the thunderstorm lead to the formation of lightning and that most remained confined to the lightning initiation region, which he then inferred also had a length of 10–100 m (also see Section 4.1 and Ref. [5]).

### 3.3. Electric field measurements inside thunderclouds

Knowledge of the electric fields inside thunderclouds is key to understanding how lightning is initiated, since it provides the framework on which models may be constructed. Unfortunately, measuring the electric field is difficult for several reasons: (1) Thunderstorms are a large and violent environment, which makes it challenging to make *in situ* measurements; e.g., it is dangerous to fly aircraft into thunderclouds and difficult (and sometimes dangerous) to launch balloons into thunderstorms. It is also challenging to position and launch rockets into active thunderstorms. Furthermore, the large volume of thunderclouds makes it unlikely that a balloon, aircraft or rocket will traverse the regions with the highest field, which may be relatively small. (2) The thunderstorm fields often change rapidly, on the time scale of seconds, and so even jet aircraft will only sample a small part of the cloud before the field changes. This is especially problematic for calculations involving runaway electrons, since they depend on both the magnitude of the electric field and the total potential difference in the high field region. (3) Finally, some lightning initiation models postulate that lightning forms from small (few mm sized) water droplets or ice. Placing a large (sometimes wet) object, such as balloon, aircraft or rocket, could artificially discharge the thundercloud before the field has a chance to build up to the point where lightning might be naturally initiated. In other words, the act of observing the system may substantially perturb it.

When considering the electric field strength observations, it is important to know what altitude the observation was made, since the breakdown field scales linearly with the air density. For example, a field of 700 kV/m, which is only about 1/5 the conventional breakdown field,  $E_k$ , near the ground, may be above  $E_k$  near the tops of thunderclouds. Unfortunately, many discussions of the electric field observations that appear in the literature do not report the exact altitude or the air density at the time of the observations and so are difficult to interpret. A standard way of reporting the electric field, which takes out the air density dependence, is the reduced electric field,  $E/N_{air}$ , or equivalently  $E/n_{air}$ , where  $N_{air}$  is the number density of air molecules and  $n_{air}$  is the density of air relative to that at sea level at standard conditions. In this paper, we shall use an exponential altitude dependence of the air density,  $n_{air} = \exp(-z/H)$ , with the scale-height  $H = 8.5$  km. The reduced field,  $E/N_{air}$ , is commonly given in units of Townsends 1 Td =  $10^{-21}$  V m<sup>2</sup>. Alternatively,  $E/n_{air}$ , in units of V/m, is called the sea-level equivalent (SLE) field. The breakdown field at all altitudes has the same sea-level equivalent field of about  $3 \times 10^6$  V/m, equal to 110 Td.

In the following, we present a sample of maximum electric field strengths recorded inside thunderclouds. These maximum fields are also summarized in Table 3.1. When considering the electric field strengths presented below, in addition to the conventional breakdown field, the values should also be compared with the positive streamer critical field for propagation, which has sea-level equivalent values between about  $3 \times 10^5$  V/m and  $6 \times 10^5$  V/m depending upon the altitude and humidity [38], and the runaway electron avalanche threshold field, which has a sea-level equivalent value of  $2.84 \times 10^5$  V/m [77,78]. The latter will be discussed further in Section 5.

Gunn [79] made aircraft measurements at an altitude of 3.9 km and found a maximum electric field of  $3.4 \times 10^5$  V/m just before lightning struck (sea-level equivalent field,  $E_{SLE} = 5.4 \times 10^5$  V/m). The average maximum field was  $1.3 \times 10^5$  V/m ( $E_{SLE} = 2.1 \times 10^5$  V/m) for 9 different storms with the most intense field near the 0 °C level. Winn and Moore [80] made sounding rocket measurements of the electric field component perpendicular to the long axis of the rocket and found fields were commonly  $1.0 \times 10^4$  V/m and occasionally reached  $6.0 \times 10^4$  V/m at about 5.5 km ( $E_{SLE} = 1.9 \times 10^4$  V/m and  $1.1 \times 10^5$  V/m, respectively). Winn et al. [81] reported a rocket measurement of the horizontal electric field of  $4.0 \times 10^5$  V/m at 6 km ( $E_{SLE} = 8.1 \times 10^5$  V/m). In another flight they recorded a field of up to  $1.0 \times 10^6$  V/m at about 6 km ( $E_{SLE} = 2.0 \times 10^6$  V/m), although they did question whether this observation was reliable, since it should have created a very large field near the rocket that should have initiated corona streamers. Overall, they concluded that *in situ* fields of  $4.0 \times 10^5$  V/m do exist, with the highest fields near 5–6 km. These results agree with those of Gunn [79], who found a similar high field near the same location. Using a balloon sounding, Winn et al. [82] reported maximum electric fields in excess of  $1.4 \times 10^5$  V/m near 5.7 km ( $E_{SLE} = 2.7 \times 10^5$  V/m). Similarly, Weber et al. [83] measured fields in excess of  $1.0 \times 10^5$  V/m at 8 km ( $E_{SLE} = 2.6 \times 10^5$  V/m), although the balloon used was experiencing corona at the time, adding uncertainty to the measurement. Fitzgerald [84] reported F-100F aircraft observations in central Florida and found a maximum vertical field of  $1.2 \times 10^5$  V/m at an altitude of 8.8 km, with  $5.0 \times 10^4$  V/m being a more typical maximum field at that altitude ( $E_{SLE} = 3.4 \times 10^5$  V/m and  $1.4 \times 10^5$  V/m, respectively). Fitzgerald also recorded horizontal fields with typical values of about  $2.5 \times 10^4$  V/m at 8.8 km, which is roughly consistent with typical horizontal fields recorded by Winn et al. [81] using rocket soundings. They also recorded a rapid increase of the field to about  $5.0 \times 10^4$  V/m when the balloon was above 10 km, suggesting that lightning deposited negative charge below and to the side of the balloon, demonstrating that lightning may deposit significant charge within the thundercloud, increasing the field in some circumstances. Other electric field measurements inside thunderclouds include ([54,85,86], also see Ref. [87]).

Marshall, Stolzenburg and collaborators conducted a large number of balloon soundings through various thunderstorm types in different locations, e.g., see summaries in Refs. [61,88]. It was found that the maximum electric fields during the soundings were usually less than the runaway electron avalanche threshold,  $E_{th}$ , and when the fields exceeded this threshold lightning would often initiate [61,89,90]. This result has been interpreted as evidence that runaway breakdown is playing a role in lightning initiation [89]. However, care should be taken with interpreting these observations, since the runaway electron avalanche threshold is also close to the positive streamer critical field at thunderstorm altitudes. In addition, runaway electron avalanches may help discharge the large scale electric field, keeping it near the threshold value. As a

**Table 3.1**

Maximum electric fields observed inside thunderclouds.

Reference	Type of measurement	Maximum electric field (kV/m)	Altitude of maximum electric field (km)	Sea-level equivalent electric field (kV/m)
Gunn [79]	Aircraft	340	3.93	540
Winn and Moore [80]	Rocket	60	5.5	110
Winn et al. [81]	Rocket	400	6	810
Winn et al. [82]	Balloon	1000	6	2000
Weber et al. [83]	Balloon	100	8	260
Fitzgerald [84]	Aircraft	120	8.8	340
Stolzenburg et al. [91] (i)	Balloon	78.7	11.5 <sup>e</sup>	309 <sup>e</sup>
Stolzenburg et al. [91] (ii)	Balloon	115	8.4	310
Stolzenburg et al. [91] (iii)	Balloon	245 <sup>e</sup>	8.4	665 <sup>e</sup>
Stolzenburg et al. [91] (iv)	Balloon	97.5	10.1	327
Stolzenburg et al. [91] (v)	Balloon	118.6	8.6	331
Stolzenburg et al. [91] (vi)	Balloon	135.9	7.6	336
Stolzenburg et al. [91] (vii)	Balloon	79.0	13.1	376
Stolzenburg et al. [91] (viii)	Balloon	87.9	13.0	413
Stolzenburg et al. [91] (ix)	Balloon	135.2	10.0	445
Stolzenburg et al. [91] (x)	Balloon	127.0	13.4	626
Stolzenburg et al. [91] (xi)	Balloon	195	12.2 <sup>e</sup>	833 <sup>e</sup>
Stolzenburg et al. [91] (xii)	Balloon	220 <sup>e,s</sup>	12.1 <sup>e</sup>	929 <sup>e</sup>

<sup>e</sup> Estimated values.<sup>s</sup> Measurement was saturated.

result, the fact that the field often approached the runaway electron avalanche threshold may have more to do with the difficulty in exceeding that field value over large distances than with the initiation of lightning.

Stolzenburg et al. [91] examined electric fields measured by 250 balloon sounding and found that 9 were adversely affected (ascent stopped, data ended, or instrument burned or charred) by lightning. These nine soundings were interpreted as ending near the lightning flash initiation point. By examining the electric fields just before the initiation of the lightning, they found that the fields often increased to very large values over a short time period. For instance, seven cases had rapid field increases (rates of increase  $11\text{--}100 \text{ kV m}^{-1} \text{ s}^{-1}$ ) in the few seconds before the flash, and for three cases the maximum field occurred 3 s or more before the flash. This is seen in the examples shown in Fig. 3.2. In one additional sounding, which was not affected by the lightning, the field exceeded the runaway avalanche threshold more than 38 s before lightning was initiated 2 km from the balloon as determined by LMA measurements. This last measurement shows that having the field reach or exceed the runaway avalanche threshold is not always sufficient to initiate lightning.

### 3.4. Localized field enhancements from hydrometeors

The presence of hydrometeors may reduce the required ambient electric field for electrical breakdown by locally enhancing the fields near the surface of the hydrometeors, both due to charges on the particles and polarization of the water or ice. Hydrometeors, which are defined to be liquid or ice particles, include both small cloud droplets and cloud ice particles as well as larger particles with appreciable fall speed ( $>0.3 \text{ m/s}$ ) called precipitation. For most of the discussion of lightning initiation in this paper, the hydrometeors being considered will be in the category of precipitation. However, we shall follow the standard convention of simply referring to them as hydrometeors.

Charges on individual hydrometeors have been measured to occasionally reach about 400 pC. For instance, observations of the charges on particles in the 1–3 mm diameter range inside thunderclouds found charge magnitudes between 10 and 200 pC with a few particles having charges in the 200–400 pC range [92]; see Ref. [22] for a discussion of other observations. There is a maximum charge that a rain drop can have, called the Rayleigh limit, before the electrostatic force exceeds the surface tension of the drop, causing it to break apart. Although droplets measured within thunderstorms generally have charges much less than the Rayleigh limit, it is conceivable that some droplets have charges that approach this limit. The Rayleigh limit charge depends on the droplet radius,  $a$ , as  $q_{Ra} \propto a^{3/2}$  [93], and so larger droplets are capable of holding more charge. However, since the maximum field is proportional to  $a^{-2}$ , the surface field can be greater on smaller droplets. The electric fields at the surface of the hydrometeors, due to their charges, could conceivably surpass the local breakdown field at thundercloud altitudes. For uncharged hydrometeors, a spherical water or ice particle will also polarize in an electric field, reducing the electric field inside the particle and increasing the field just outside by up to a factor of three. Therefore, an ambient field of 1/3 the breakdown field will result in the breakdown field near the surface of the hydrometeor. However, exceeding the breakdown field near the surface of the hydrometeor does not automatically ensure that electrical breakdown over a large scale will occur. This is because the field drops off rapidly with distance away from the particle, i.e.,  $E \propto (a/r)^2$  and  $E \propto (a/r)^3$ , for a charged and uncharged cases, respectively. For typical thunderstorm rain droplets,  $a$  is equal to a millimeter or two. The fall off is even more rapidly for the fields near the points of ice shards.

Because the field required for the inception of an electrical discharge near the surface of a hydrometeor is less than the field required for streamer formation, it is possible that the field near the hydrometeor will discharge before streamers can form. Falling charged droplets can develop instabilities, generating sharp points that result in large fields in a very small

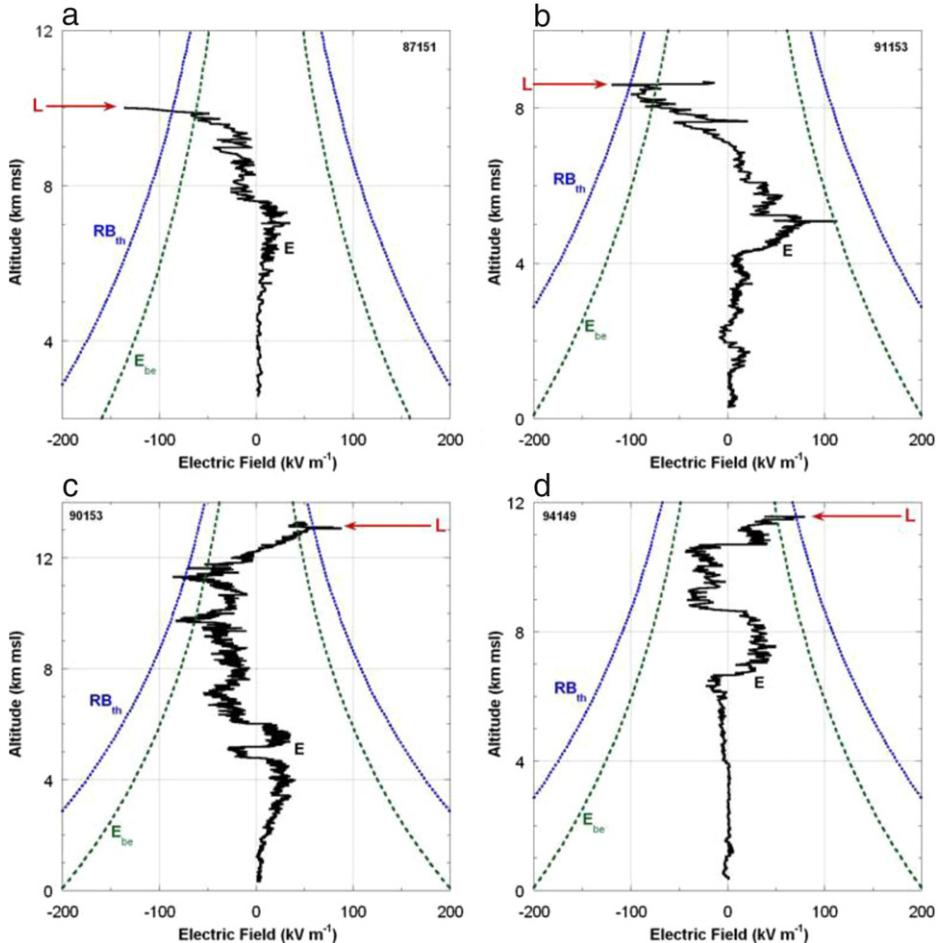


**Fig. 3.2.** Four balloon soundings from Ref. [91]. For all 4 soundings the electric field strength rapidly increased, beginning a few seconds before the lightning, shown as red arrows. Also shown are the runaway electron avalanche threshold (labeled  $RB_{th}$ ) and the so-called breakeven threshold for runaway electron propagation (labeled  $E_{be}$ ), both as a function of altitude (see Section 5 for definitions of each). In each sounding the electric field data stopped at the time of the flash. Panel (a) is sounding (vii) in Table 3.1; (b) is sounding (iv); (c) is sounding (vi); and (d) is sounding (i). After recovery, the electric field meter for panel (d) was found to have burn marks and charred components.

region near the points. These points can produce corona that reduces the charge on the droplet [94]. In addition, Liu et al. [95] used numerical simulations to investigated the inception of corona (Townsend discharge threshold) from positively charged spherical hydrometeors of a radius of 1 mm at atmospheric pressure and found that the onset surface field needed is about 2.75 times the conventional breakdown threshold field. In humid air (a gas mixture of dry air and water vapor), they found that a stronger field is required for the corona onset, and the effect of humidity is stronger for large hydrometeors. Once the corona discharge began, the discharge current could remove all the charge on the hydrometeor in about 10 ms.

### 3.5. Laboratory measurements of corona from hydrometeors

There have been several attempts to measure discharges from hydrometeors in laboratories. Macky [96] found that discharges could be initiated by falling water droplets in uniform fields as low as  $8.0 \times 10^5$  V/m at sea-level pressures. Dawson [97] and Richard and Dawson [94] studied the corona emissions and instabilities of falling liquid raindrops at their terminal velocities in an electric field. They found that the droplets form points at their upper surfaces from which corona was emitted, resulting in a change in the net charge on the drops. They observed no mass loss associated with the instability. They also found threshold fields for corona of  $5.5 \times 10^5$  V/m and  $9.5 \times 10^5$  V/m at sea-level pressures for charged and uncharged droplets, respectively. Crabb and Latham [98] did experiments with colliding liquid drops and found that sea-level fields as low as  $2.5 \times 10^5$  V/m were needed to initiate corona. Blyth et al. [99] carried out similar experiments to those of Crabb and Latham, considering colliding droplets at different temperatures and droplets colliding with ice. They concluded that collisions of water droplets could indeed generate corona during thunderstorm conditions through the creation of long liquid filaments.

Griffiths and Latham [47] performed laboratory experiments from ice particles and found that corona starts with a positive discharge of regularly spaced onset streamer pulses, produced at a rate of  $1.6 \times 10^3 \text{ s}^{-1}$ . These streamers would either terminate in the air of the gap or at the negative electrode. The electric field threshold for onset streamers varied with pressure, temperature, and shape of the ice particles, but was as low as about  $3.5 \times 10^5 \text{ V/m}$  at 500 mb pressure and  $T = -12^\circ\text{C}$ . As the electric field was increased, the current also increased until a positive glow-like discharge began, at which point the current suddenly decreased. As the field was increased further, the current in the glow-like discharge continued to increase until breakdown streamers were emitted and the gap sparked at roughly  $6 \times 10^5 \text{ V/m}$ . Griffiths and Latham concluded the onset fields for corona emission from ice in the central regions of thunderclouds are probably in the range of  $4-5 \times 10^5 \text{ V/m}$ . They also noted the importance of the conductivity of the ice for maintaining the discharge, which depended upon temperature, with higher onset fields occurring at lower temperatures. They also noted that the streamers emitted by the ice particles continued to grow as they traversed the 1 cm gap in their experiment. For thunderstorm condition with no nearby electrodes, it is reasonable that the streamers would continue to strengthen and eventually branch. It is interesting to point out that although strong electric fields were applied to ice particles for long periods of time, resulting in both burst pulses and glow-like discharges along with accompanying negative discharges, the gap did not break down, despite the presence of nearby electrodes until the field reached a sea-level equivalent field of about  $1.2 \times 10^6 \text{ V/m}$  or about  $0.4E_k$ . As a result, at least for laboratory experiments, vigorous corona from hydrometeors does not guarantee that a spark breakdown will occur. Griffiths [100] performed additional experiments with charged ice particles, similar to Griffiths and Latham, and used the results to estimate that charges on ice particles could reduce the initiation threshold of lightning by about 10%–20%.

Even stipulating that streamers can be created, the combined action of many streamers from a large number of hydrometeors may discharge the electric field in that region of the thundercloud rather than initiating lightning. Griffiths and Latham [47] measured discharge currents created by the corona from ice particles on the order of micro-amps, well before spark breakdown occurred. A majority of streamers initiated by hydrometeors probably fail to form hot leader channels [100], instead resulting in an increased conductivity and larger leakage currents in some volume, thus discharging the electric field and inhibiting lightning formation. As pointed out by Dawson and Duff [101], the observations of radio frequency noise from thunderclouds prior to lightning indicates that corona emission without the initiation of lightning probably happens quite often [102,103].

Loeb [104] hypothesized that a collection of positively charged raindrops, carried by an updraft towards a negative charge center, could initiate positive streamers that propagate upward and outward towards the negative charge. This conical shaped region produces negative charge at the origin of the streamers, initiating more positive streamers from the droplets below. The result is a funneling of positive charge upward with the negative stem of the funnel moving downward. Eventually the field at the bottom stem reaches very large values, allowing conventional breakdown to occur. The idea of positive streamers producing a propagating region that intensifies the electric field was also studies for charged rain columns [101,105], although the validity of this model has been questioned since it would require an unrealistically large number of droplets [49]. Griffiths and Phelps [106] performed numerical calculations on a variation of Loeb's hypothesis: that a network of positive streamers, initiated by a hydrometeor, could form a conical discharge region that leads to the enhancement of the field at the boundary. They suggested that several overlapping streamer discharge regions could combine to enhance the field to values that exceed the conventional breakdown field. Presumably such a large field would facilitate lightning initiation, although this final step has not yet been modeled. In those models, the role of the hydrometeors and the streamers they produce is not to directly initiate lightning but rather to locally enhance the field so that it reaches the breakdown field over a meter scale region. An assumption in these model is that thundercloud electrification processes could not achieve this strong electric field alone and the thundercloud requires some help getting the field to the point where lightning can form.

Alternatively, Peterson et al. [107] suggested a two-step process in which runaway electron avalanches followed by streamers enhance the field to the point where lightning could initiated, i.e., via a process similar to space leader formation in front of negative stepped leaders. Finally, Nguyen and Michnowski [108] modeled lightning initiation as a series of breakdown events between a chain of closely spaced hydrometeors. In this model and all other models that involve the production of streamers by hydrometeors, the number of large hydrometeors in the high field region of the thunderstorm is important, since it is these hydrometeors that initiate the streamers. Unfortunately, the likelihood of a region of the storm having sufficient numbers of the necessary hydrometeors for lightning initiation is not known.

### 3.6. Modeling streamer initiation and propagation

A variety of models have been developed to study properties of corona initiation from hydrometeors (e.g., [95,109–111]) and streamer propagation (e.g., [37,112–117]). In particular, Liu et al. [95] modeled the initiation of a positive streamer from the positive end of an ionization column, representing an elongated hydrometeor (see Fig. 2.1), and found that fields of  $0.5E_k$  ( $1.5 \times 10^6 \text{ V/m}$  at sea-level) were sufficient for positive streamer initiation, but found that no negative streamers appeared from the other end, even for applied fields that approached the breakdown field. Schroeder, Baker and Latham [118] modeled streamers from colliding raindrops and found that fields as low as  $2 \times 10^5 \text{ V/m}$  at 500 mb pressure were needed. Since  $2 \times 10^5 \text{ V/m}$  at 500 mb pressure is also about the minimum field needed for positive streamer propagation, according to this model, this would be the minimum required field for lightning initiation at that altitude. It is doubtful, however, that the colliding raindrop model could account for lightning initiation at higher and colder parts of the cloud where it is

completely glaciated. For ice particles, Solomon et al. [110] surveyed the literature and concluded that positive streamers required ambient fields of about  $6 \times 10^5$  V/m at 500 mb for temperatures greater than  $-18^\circ\text{C}$ .

Bazelyan and Raizer [119] compared numerical models of streamer propagation in a uniform field [112] with laboratory experiments of the critical field,  $E_s$ , for steady state streamer propagation. While the laboratory measurements found  $E_s = 5 \times 10^5$  V/m at sea-level, the simulations found  $8 \times 10^5$  V/m. Since the simulations agreed well with experiments for non-uniform field, Bazelyan and Raizer questioned whether the experimental data on  $E_s$  were interpreted correctly. However, Liu et al. [37] found a critical field of  $5 \times 10^5$  V/m, in line with laboratory experiments.

### 3.7. Runaway electrons and lightning initiation

The threshold electric field for relativistic runaway electron avalanche (RREA) multiplication is  $E_{th} = 2.84 \times 10^5$  V/m  $\times n_{air}$  [77,78] (also see Section 5). Another field that is often cited in the literature is the so-called breakeven field  $E_b = 2.18 \times 10^5$  V/m  $\times n_{air}$  [120]. The breakeven field is the electric field strength at which the rate of energy gain from the field is equal to the rate of energy loss (mostly due to ionization of the air) for an electron moving directly along the field line. However, because of elastic scattering, electrons never travel in a straight path along the field line, and so  $E_b$  underestimates the field necessary to generate runaway electrons. Monte Carlo simulations have shown that for fields above  $E_{th}$ , the number of runaway electrons will increase exponentially with distance. There has been a persistent misconception appearing in the literature that once the RREA threshold is reached, then electrical breakdown will automatically ensue, i.e., runaway breakdown will occur. Perhaps one reason for this misconception is that often the conventional breakdown field only needs to be exceeded over a very small region (e.g., over a mm scale) in order to produce a spark breakdown of a gap. In reality, the conventional breakdown field needs to be exceeded over a large enough distance for significant low-energy avalanche multiplication to occur. Because the low-energy avalanche lengths can be quite small, this condition is often met for electrodes in laboratory experiments and fingers approaching doorknobs after a walk across a carpet.

Similarly for RREAs, in order to generate a significant number of runaway electrons, not only does the field need to exceed  $E_{th}$ , it needs to do so over many avalanche lengths. As will be discussed in Section 5, the RREA avalanche length depends upon the field strength and the air density, but can be on the order of roughly 100 m inside the electrified regions of thunderstorms. For example, a sea-level equivalent field of  $4 \times 10^5$  V/m will produce a RREA avalanche length of 120 m at 6 km altitude. Clearly, as can be seen in Table 3.1, the maximum thundercloud electric fields do sometimes exceed  $E_{th}$  by a substantial amount. However, what is not clear from the electric field data, given that the fields often change rapidly with time, is whether or not the electric fields exceed  $E_{th}$  over a large enough distance to produce a significant number of runaway electrons to the point where the conductivity of the cloud is affected.

Marshall et al. [92] made in situ balloon measurements and inferred the field at 5.77 km reached  $1.87 \times 10^5$  V/m with a vertical depth of about 1 km. This would give a RREA multiplication factor of about 650. In other words, for every seed particle from atmospheric cosmic rays [121], there would be 650 additional relativistic runaway electrons traversing the end of the avalanche region. Such an enhancement in the flux of energetic particles will certainly increase the electrical conductivity in that part of the cloud, but considering that these energetic electrons are produced over a large volume, it is not obvious that they would do more than introduce an additional leakage current that would either help counter balance the charging or gradually discharge the thundercloud.

On the other hand, there are several encouraging facts for proponents of the importance of runaway electron physics for understanding thunderclouds and lightning. Firstly, the electric fields needed to produce runaway electron avalanches have been shown to be relatively common inside thunderclouds, both from the direct measurements of the field discussed above and the frequent observations of gamma-ray glows from thunderclouds. Indeed, the amount of RREA multiplication inferred by the Marshall et al. [92] observations should produce a significant enhancement of the gamma-ray flux from the cloud. Such enhancement of the gamma-ray fluxes are routinely seen on the ground, and inside and near thunderclouds (see Section 5.3.3), suggesting that significant amounts of RREA are common and so extended regions with field above the RREA threshold are also common. Furthermore, the gamma-ray glows often occur before lightning and terminate at the time of the lightning, indicating the high field regions that produce the gamma-ray glows are the same as the high field regions subsequently discharged by lightning. Second, even if the RREAs do not directly result in lightning initiation, the impact they have on the conductivity of the cloud may be important, since it will compete with the charging processes, affecting the charge structure of the storm—a topic important to understanding lightning initiation. Indeed, the results of Marshall et al., showing that the maximum fields are often below  $E_{th}$ , may be hinting that it is difficult for thunderclouds to produce large electric fields above  $E_{th}$  over a large volume because of the rapid increase in conductivity due to runaway electron production. Third, an avalanche multiplication of 650, as found above, is not far below the amount of avalanche multiplication needed for relativistic feedback effects to become important (see Sections 5.2.4, 5.4.4 and 5.4.9). The relativistic feedback mechanism is analogous to the Townsend discharge (breakdown), allowing the production of runaway electrons to become self-sustaining and producing explosive growths in the number of energetic electrons and gamma-rays. This mechanism may explain the bright bursts of gamma-ray seen from space, called Terrestrial Gamma-ray Flashes (TGFs). Even if a TGF is not produced, the relativistic feedback mechanism may still dramatically increase the conductivity of the thundercloud and produce bright, long lasting gamma-ray glows. Finally, RREA production, with or without feedback effects, may generate a region with a large enough conductivity to discharge one part of the thundercloud, while enhancing the field in other parts. At the end of

Section 5, in Section 5.4.11, we will discuss further two possible lightning initiation mechanisms involving runaway electrons enhancing the electric field in this way.

## 4. Lightning propagation

### 4.1. Overview

As a consequence of the lightning initiation processes discussed in Section 3, one or more thermally-ionized, centimeter-diameter conducting channels are formed within or near a region of cloud charge. Those conducting channels subsequently elongate in the ambient electric field. Many researchers (e.g., [122]) have argued that the stage of the negative cloud-to-ground flash immediately after initiation and before the few tens-of-milliseconds duration of the stepped leader (Sections 1.3 and 4.2) is a separate process from the stepped leader, a process called “initial breakdown” or “preliminary breakdown”, as defined above in Section 3.2.3. This process is identified by its relatively large, bipolar electric field “preliminary breakdown pulses”, these being up to an order of magnitude larger in both amplitude and width than the unipolar electric field pulses radiated by the stepped leader when it is near ground. [For more details, see the review in Sections 4.3 and 4.4 of Ref. [123].] The preliminary breakdown pulses may be associated with the optically-measured  $\beta$  stepped leaders that Schonland [14] described from streak camera (Section 1.2) measurements as stepped leaders initially having higher propagation speed and longer step lengths than the  $\alpha$  (apparently normal) leaders that follow below (e.g., [124,125]). It is also possible that the preliminary breakdown pulses should be considered part of the lightning initiation process (see Section 3.2.3 above). Proctor et al. [126] treat all propagating processes before the first return stroke as the stepped-leader since the character of the 355 MHz radiation used in their time-of-arrival (TOA) system to locate VHF sources did not change over that period. However, Rustan et al. [127] and Rhodes and Krehbiel [128], using different VHF systems (a 30–50 MHz TOA system and 274 MHz interferometer, respectively), reported that there were differences between the later stepped leader radiation and the radiation from earlier process. Rakov and Uman [5] conclude from their review of the literature on both preliminary breakdown and stepped leaders in negative cloud-to-ground flashes that the preliminary breakdown process can be viewed as involving a sequence of channels extending in more-or-less random directions from the cloud charge source, one of which evolves into the stepped leader to ground. Very recently, Stolzenburg et al. [129], Karunaratne et al. [130], and Bitzer et al. [131] have provided data on the length, speed, and starting height of preliminary breakdown pulses in both cloud and cloud-to-ground discharges from time-of-arrival measurements on the electric field pulses and from high-speed video imaging (at about 50,000 frames per second) of the first luminosity. Stolzenburg et al. [129], using high-speed video, imaged linear luminous channel segments of 20–100  $\mu$ s duration, coincident with cloud-to-ground preliminary breakdown electric field pulses, advancing downward for a few hundred meters at initial estimated speeds of  $4\text{--}18 \times 10^5$  m s<sup>-1</sup> over the first few hundred microseconds, with speeds then decreasing. The initial speeds are at the upper end of normal below-the-cloud-base stepped leader speeds, the higher speeds being consistent with streak-camera photographic measurements of the so-called  $\beta$  stepped leaders described by Schonland [14]. Stolzenburg et al. [129] found that sequential preliminary breakdown luminosity sequences repeatedly illuminated the same path away from the location of the initial light.

In addition to being observed in negative cloud-to-ground flashes, preliminary breakdown electric field pulse trains (of opposite polarity to the negative trains) precede positive stepped leaders in positive cloud-to-ground flashes [e.g., [132] and references therein]. Schumann et al. [132] found a mean positive pulse train duration of 3.1 ms and a mean time of 157 ms between the positive pulse train and the initiation of the return stroke for 80 single-stroke positive flashes.

**Fig. 1.2a, c** illustrate initial leaders in cloud-to-ground flashes from negative and positive cloud charge sources, respectively. A more detailed illustration of the common downward-moving negative stepped leader in cloud-to-ground lightning is given in **Fig. 1.3**. Initial leaders in upward flashes of each polarity are shown in **Fig. 1.2b, d**. All of the initial leaders propagate many kilometers through virgin air, and it is the behavior of these virgin-air leaders on which we will primarily concentrate. We will also examine some aspects of dart-stepped leaders, those leaders which traverse the upper portion of defunct return stroke channels as continuously-moving dart leaders and then, in the lower portion, deviate from those channels or trace through their remains as stepped leaders (Section 1.3). It is quite remarkable that initial leaders of the type shown in **Fig. 1.2** and those initiating cloud discharges can propagate virtually limitless distances through seemingly clear air and/or cloud hydrometeors. Leaders of “Bolts from the Blue” (see **Fig. 1.8**), which can be of either negative or positive polarity [e.g., [133,134]], commonly propagate more than 10 km through clear air from their cloud charge source and strike ground many kilometers away from the side of the thundercloud. The record length observed for leader propagation may be the 150 km through a frontal system determined by radar reflected off the conducting leader channel [135]. As leaders extend, they draw their energy from the collapse of the electric field along their propagation path. Since there are no fixed-potential, highly-conducting electrodes (like the Earth) within the cloud, the leader elongation must be bidirectional, although, depending on the environment (e.g., atmospheric pressure, local charge density, hydrometeors present), the different ends of the leader (of different polarities) may exhibit different characteristics: branch more and/or elongate slower or less. The illustrations in **Fig. 1.2a, c** do not show the development of the upper, opposite-polarity end of the leader, rather treating it as part of the charge source feeding the leader current, but the illustration in **Fig. 1.3** shows some development of the upper, in-cloud portion of the negative stepped leader. The leader propagation properties in the

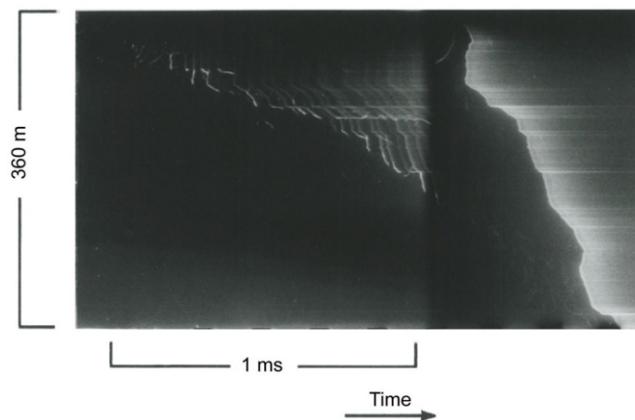


**Fig. 4.1.** Streak-camera photograph of a downward negative stepped leader within 360 m of ground. Time advances from left to right. The left part of the photograph was overexposed in the reproduction process in order to enhance the intensity of the early portion of the leader image.  
Source: Adapted from Berger and Vogelsanger [139].

cloud may well be different from those properties in clear air outside (usually beneath) the cloud, perhaps as a result of the decreased air density with altitude or the presence of hydrometeors in the cloud, as implied above in reference to Schonland's  $\alpha$  and  $\beta$  stepped leaders. Winn et al. [136] observed, with an instrumented balloon and an LMA, a negative stepped leader at 8–9 km altitude exhibiting step lengths of 50–600 m and times between steps of a millisecond or so, consistent with other data on the characteristics of negative leaders relatively high in the cloud [e.g., [72,137]].

#### 4.2. Negative stepped leaders and dart-stepped leaders

The negative stepped leader propagates, as indicated by its name, by way of a stepping process, each step extending the length of the leader channel. Meter-length spark-formation experiments in the laboratory provide information pertinent to the lightning step process, the laboratory step process having been studied with better time and spatial resolution than the natural lightning step process.

First we review general background information on average stepped leader speed and duration (averaged over both the steps and the time between steps), and on the individual leader step lengths and inter-step time. The distances to individual leader steps and their lengths in the earlier streak photographic and photoelectric experiments were often subject to significant measurement error because they were estimated, for example, from thunder ranging on the return stroke or from knowledge of the cloud base height. Additional length (and speed) errors occurred from the lack of knowledge of leader step orientation relative to the vertical. Recent measurements [e.g., [138]] use multiple-station  $dE/dt$  time-of-arrival techniques to accurately locate individual leader steps.

Schonland [14], using streak photography, reported that average two-dimensional speeds for 60 of the most common  $\alpha$ -type stepped leaders in South Africa were between  $0.8 \times 10^5$  and  $8.0 \times 10^5$  m s $^{-1}$  in the bottom 2–3 km of the channel. Schonland [14] also estimated that the minimum average three-dimensional stepped leader speed was about  $1 \times 10^5$  m s $^{-1}$ . Berger and Vogelsanger [139], also using streak cameras, found that average vertical speeds for 14 stepped leaders in Switzerland ranged from  $0.9 \times 10^5$  to  $4.4 \times 10^5$  m s $^{-1}$  in the final 1.3 km above ground; and four stepped leaders terminating on their instrumented towers had speeds between  $1.9 \times 10^5$ – $2.2 \times 10^5$  m s $^{-1}$  over the bottom 100 m of the channel. A streak camera photograph of a negative stepped leader from Berger and Vogelsanger [139] is given in Fig. 4.1. Chen et al. [140], who used the ALPS photoelectric imaging system [141], reported on two downward negative stepped leaders, one of which exhibited an average speed ranging from  $4.5 \times 10^5$  to  $1.1 \times 10^6$  m s $^{-1}$  (mean value  $7.3 \times 10^5$  m s $^{-1}$ ) between the heights of 367 and 1620 m above ground, and the other from  $4.9 \times 10^5$  to  $5.8 \times 10^5$  m s $^{-1}$  between 33 and 102 m. Proctor et al. [126], using the VHF TOA lightning-channel imaging system noted in Section 4.1, measured channel extension speeds for 66 stepped leaders ranging from  $3 \times 10^4$  to  $4.2 \times 10^5$  m s $^{-1}$  with a median value of  $1.3 \times 10^5$  m s $^{-1}$ . Shao et al. [142], using a VHF interferometer, found that stepped leaders to ground progressed at a typical speed of  $2 \times 10^5$  m s $^{-1}$ .

The estimated duration of the stepped leader from measured stepped-leader electric field waveforms is some tens of milliseconds [143]. Rakov and Uman [144] found a geometric-mean leader duration of 35 ms for 71 stepped leaders in Florida. Using this latter value of leader duration and assuming a reasonable average stepped-leader speed of  $2 \times 10^5$  m s $^{-1}$  (see above), they estimated an average channel length of 7 km for Florida stepped leaders.

The lengths of the individual steps in stepped leaders were reported by Schonland [14] to vary from 10 to 200 m and the interstep intervals to range from 40 to 100  $\mu$ s. Both the step lengths and their brightness were reported to increase as the leader speed increased. Berger and Vogelsanger [139] reported step lengths between 3 and 50 m and interstep intervals between 29 and 52  $\mu$ s. According to Schonland [14], the leader steps showed increased average speed and step brightness as

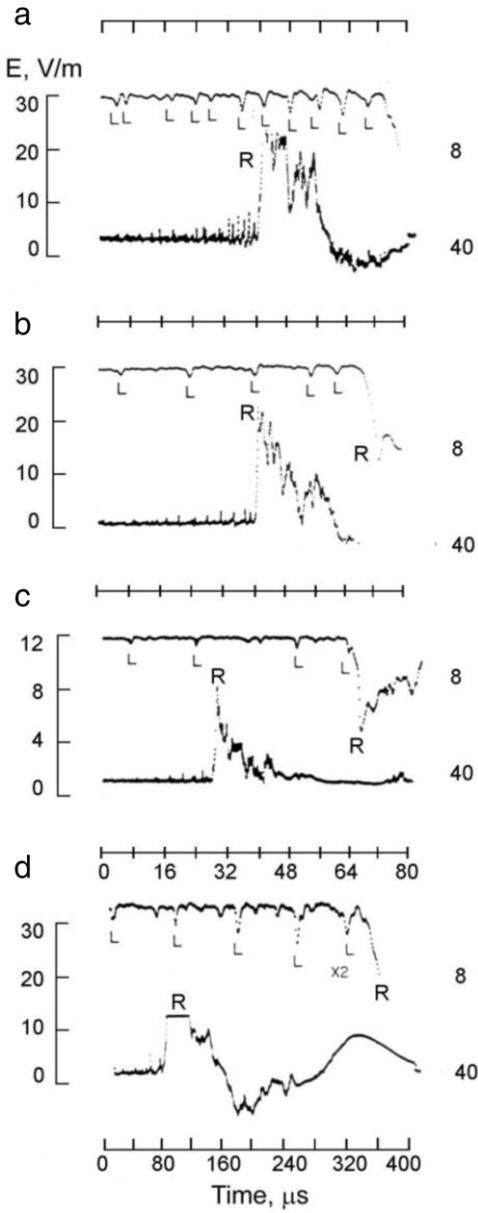


**Fig. 4.2.** Electric field waveforms produced by four negative first strokes in Florida at distances of some tens of kilometers. Each record is displayed on two time scales, 8  $\mu$ s per division (upper trace) and 40  $\mu$ s per division (lower trace), the two traces being inverted with respect to each other. Note that the abrupt return-stroke transitions (clipped in the lower trace of Fig. 4.2d), labeled R, are preceded by small pulses characteristic of leader steps, each labeled L. The vertical scale is shown on the left (this is to be reduced by a factor of 2 for the 8  $\mu$ s per division (upper) trace in Fig. 4.2d).

Source: Adapted from Krider et al. [147].

the ground was approached. Chen et al. [140] observed two downward negative stepped leaders using the ALPS photoelectric imaging system. For one of these leaders, the step length ranged between 7.9 and 20 m for heights between 367 and 1620 m, and the interstep interval ranged from 5 to 50  $\mu$ s. For the other leader, the step length was about 8.5 m between 33 and 102 m, and the interstep interval ranged from 18 to 21  $\mu$ s.

Beasley et al. [145] were the first to demonstrate the correspondence between individual leader-step light pulses and the corresponding electric field pulses. They examined leader light pulses from an approximately 12-m-high channel section about 80 m above ground and electric field pulses, both occurring 50–100  $\mu$ s before the first return-stroke. Both light and electric field pulses in the three Florida flashes studied occurred at time intervals of 5–20  $\mu$ s. Thus, most electric field pulses reported within some hundreds of microseconds of the first return stroke [e.g., [124,138,146–149]] are likely to be associated with the luminous-step-formation process near ground. Examples of step electric field pulses are given in Fig. 4.2, and examples of step electric field derivative pulses are shown in Figs. 4.3a and 4.3b.

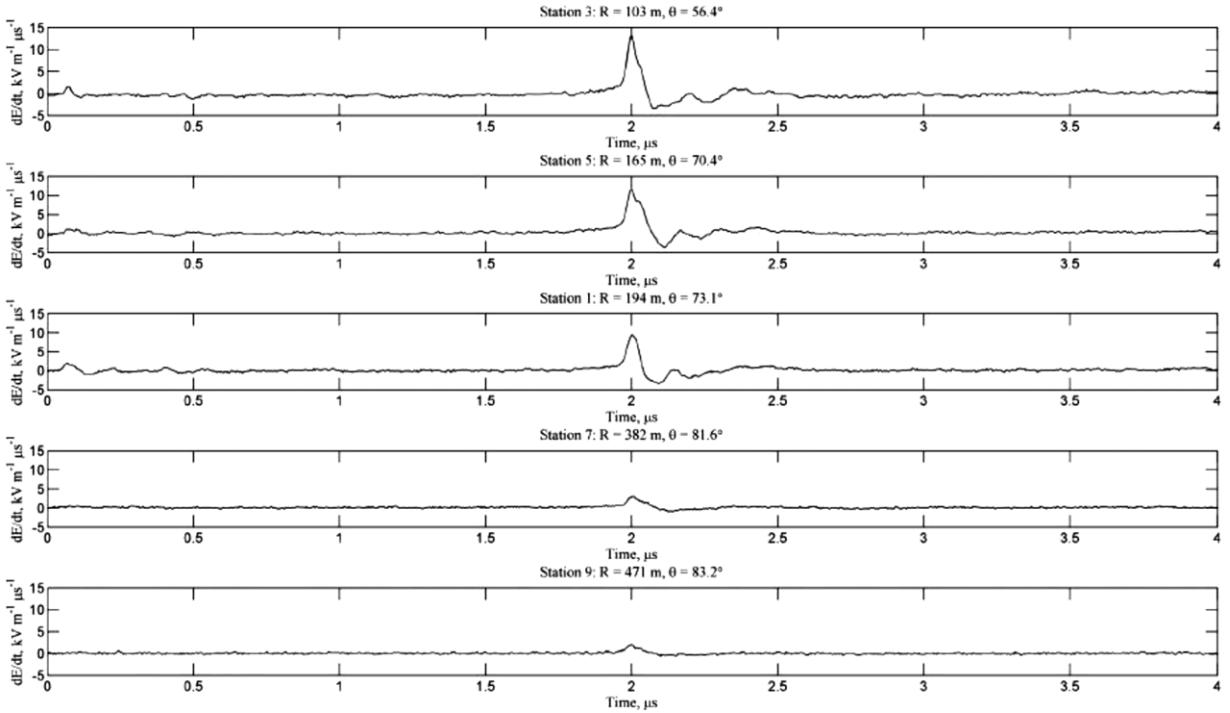


**Fig. 4.3a.** A characteristic leader-step  $dE/dt$  waveform observed at five different locations on ground at the ICLRT. Step distance and the angle between a downward vertical from the step and a line to the measurement station ( $0^\circ$  signifies a station below the step) are given.  
Source: Adapted from Howard et al. [138].

Chen et al. [140], using the ALPS photoelectric imaging system, reported that zero-to-peak risetimes of luminosity associated with steps for one leader ranged from 0.5 to 3.5  $\mu\text{s}$ , with mean value 1.7  $\mu\text{s}$ , and for another leader ranged from 0.6 to 1.2  $\mu\text{s}$ . From earlier photographic and photoelectric measurements, the luminosity of the step was found to rise to peak in about 1  $\mu\text{s}$  and fall to half this peak in roughly the same time [14, 145, 150, 151]. These values might be affected by the scattering of the step light by aerosol or cloud particles. If a step becomes luminous in 1  $\mu\text{s}$  or less and has an assumed length of 50 m or less, the rate with which this luminosity fills the step (a process that is unresolved by ordinary streak cameras) is in excess of  $5 \times 10^7 \text{ m s}^{-1}$  [150, 152].

Wang et al. [153], using ALPS to observe triggered lightning with 30 m spatial resolution, found that the luminosity pulses formed at the dart-stepped leader tip propagated upward at a mean speed  $6.7 \times 10^7 \text{ m s}^{-1}$  and exhibited a decrease in peak amplitude to about 10% of the original luminosity value within the first 50 m. The spatial resolution of 30 m was insufficient to resolve the step-formation process. Hill et al. [154] have confirmed the presence of the upward-propagating wave in natural negative step formation using high speed video (3.3  $\mu\text{s}$  frame integration time), as discussed later.

As noted by many researchers [e.g., [124]], the step electric field peak amplitudes increase as the stepped leader approaches ground. The last stepped-leader pulse is generally the largest, and its peak, on average, is about 0.1 of the return-stroke pulse peak [147]. Krider et al. [147] found that the 10%–90% risetimes of the individual step electric field waveforms are on average 0.2–0.3  $\mu\text{s}$  and the half-peak width is typically 0.4–0.5  $\mu\text{s}$ , for waveforms that propagate across tens of kilometers of salt water where the distortion of the waveforms due to ground propagation effects is minimal. Weidman and Krider [155] reported that the 10%–90% risetimes of individual step pulse fields had a mean of 90 ns, again when the propagation paths were over salt water. Krider et al. [156] reported the mean peak of  $dE/dt$  (the time derivative of the electric field) for a step waveform, range-normalized to 100 km via the inverse distance relation characteristic of radiation fields, was  $13 \text{ V m}^{-1} \mu\text{s}^{-1}$  (17 values) and the mean half-peak width (a measure of the risetime of E) was 69 ns (eight values). Willett and Krider [157] found that the mean half-peak width of  $dE/dt$  was 54 ns for 114 stepped-leader pulses, and 64 ns for 24 dart-stepped leader pulses. From measurements of the step electric field pulses Krider et al. [147], using a simple transmission line model (an un-attenuated current pulse propagating upward from the bottom of the leader step with a speed near  $10^8 \text{ m s}^{-1}$ ), inferred a peak step current close to the ground of at least 2–8 kA, a maximum rate-of-change of step current of  $6\text{--}24 \text{ kA } \mu\text{s}^{-1}$ , and a minimum charge involved in the formation of a step of  $(1\text{--}4) \times 10^{-3} \text{ C}$ . Many additional details of the fine structure of leader electric field wave shapes over salt water are given by Murray et al. [158].

Leader step electrical parameters similar to those given above have been found via measurements of steps at accurately-known close distances, from tens to hundreds of meters, by Howard et al. [138] who used a TOA system to locate the leader step via its  $dE/dt$  pulse radiation (see Figs. 4.3a and 4.3b). They found a mean value of half-peak width for the  $dE/dt$  pulse of 33.5 ns for 69 very close leader steps, about half the value of Willett and Krider [157] whose waveforms propagated over tens

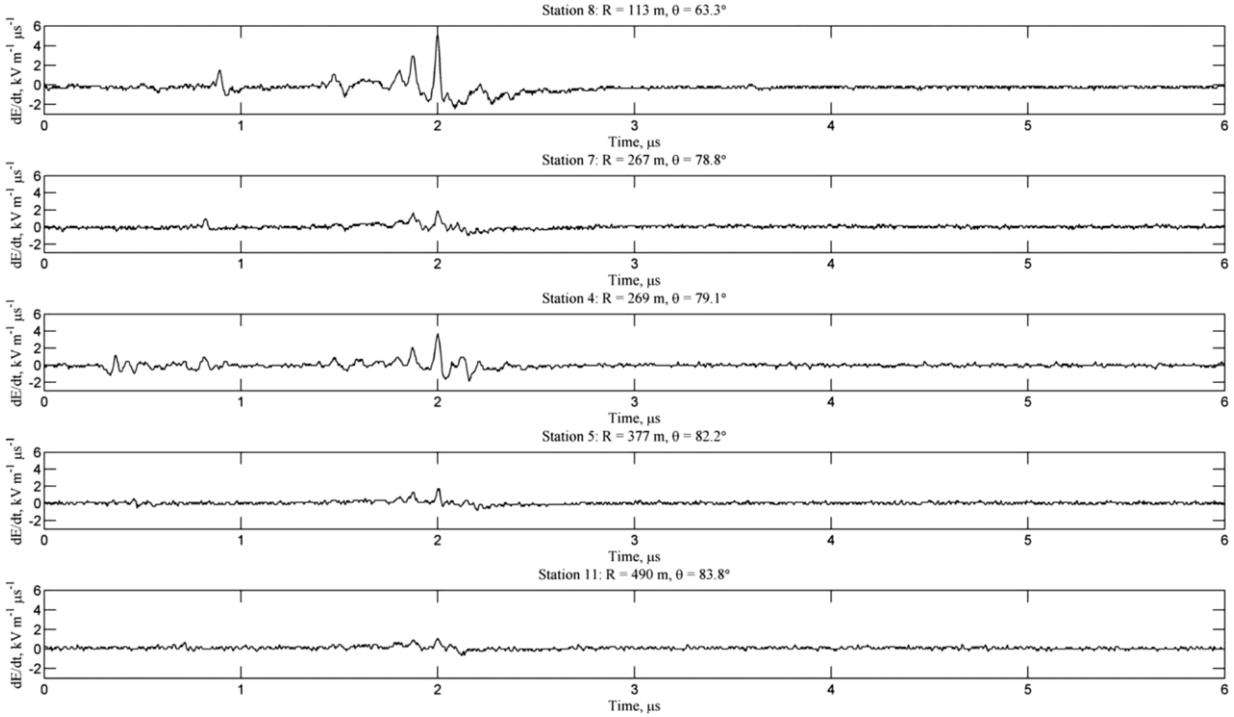


**Fig. 4.3b.** A more complex leader step  $dE/dt$  waveform than in Fig. 4.3a. Step distance and the angle between a downward vertical from the step and a line to the measurement station ( $0^\circ$  signifies a station below the step) is given.

Source: Adapted from Howard et al. [138].

of kilometers of salt water. For 103 leader steps, Howard et al. [138] found a mean peak  $dE/dt$  of  $7.4 \text{ V m}^{-1} \mu\text{s}^{-1}$  normalized to 100 km, as opposed to Krider et al. [156]'s  $13 \text{ V m}^{-1} \mu\text{s}^{-1}$  viewed over tens of kilometers of salt water and also normalized to 100 km, although Howard et al. [138] state that, because of system calibration issues and the line-of-sight of the close steps being non-perpendicular to the step, their measurement may underestimate the actual value by a factor of 1.2 to 2.

In one of the few instances where lightning streak photographs showed evidence of the corona or corona streamers commonly seen in laboratory high voltage discharges and recently observed in natural lightning leaders with high speed video (both discussed next), Schonland et al. [150] reported that for one downward negative stepped leader there was faint luminosity extending downward about 30 m below the bottom of a bright step, the last one seen in the streak photograph before the occurrence of the return stroke. They also noted “a similar effect, but to a much smaller extent” in a few other steps of this leader. Berger [20], also using streak photography, reported two cases of a brush-like corona occurring ahead of the upward-moving negatively-charged leader tip in upward lightning from an instrumented tower (Fig. 1.2d). In one case, the extent of the visible corona was estimated to be at least 3 m. It appeared that corona developed in less than the 5  $\mu\text{s}$  resolution of the streak camera, essentially simultaneously with the formation of each step; that is, the corona did not appear to develop continuously between steps [159]. No corona at the tip of downward negative leaders or at the tip of either upward or downward positive leaders (the positive leaders show less distinct, if any, steps, as we shall discuss in Section 4.3) was reported by Berger [20]. Idone [160] gives a near-ultraviolet streak photograph showing a “diffuse, hemispherical corona brush” extending over a distance of about 5–10 m above the bright steps of one upward-moving positive leader in altitude-triggered lightning. He states that he observed the “corona brush” in almost all of his near-ultraviolet recordings of positive leaders but not in the two recordings of negative leaders in altitude-triggered lightning imaged with the same system. Corona and corona streamers associated with negative leader steps were first clearly observed by Biagi et al. [161,162] using high speed video and will be considered below. But before we examine the most recent information on natural stepped-leader step formation and step properties, it is instructive to look at experiments on long laboratory sparks since those experiments provide a framework and terminology by which to examine lightning step formation.

Laboratory spark gaps several meters in length with applied voltages on the order of megavolts have been used to study leader stepping mechanisms by optically time-resolving the spark leader process with photoelectric streak photography and simultaneously measuring the electrode current and voltage. Fig. 4.4 shows Biagi et al. [162]’s adaptation of the description by Gorin et al. [163] of a negative leader propagating via stepping from a negative rod to a ground plane across a 6 m gap. Three to five leader steps were typically involved. Stepping of the type described by Gorin et al. [163] apparently occurs only for gaps longer than 2 m [e.g., [164,165]]. Rakov and Uman [5], in their Fig. 4.25, show a schematic similar to Fig. 4.4 but it is labeled differently. The diagram in Fig. 4.4a illustrates the “streamer zone” of a negative laboratory leader several microseconds after its initiation from the high-voltage electrode: (1) the primary leader channel that grows from

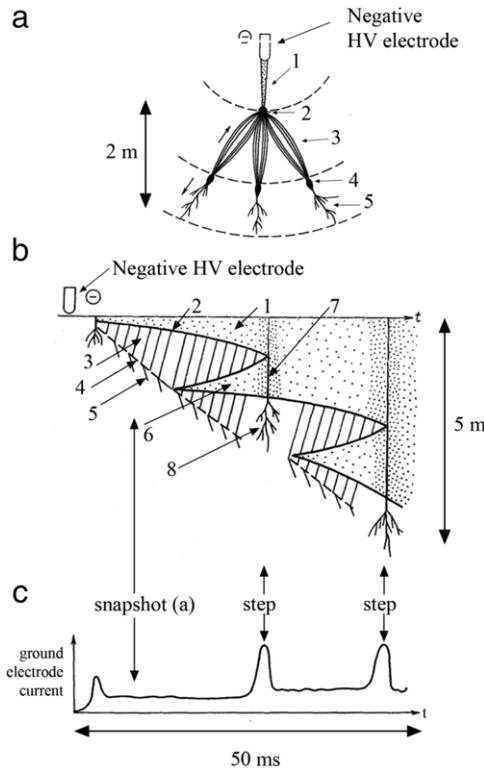


**Fig. 4.4.** (a) A diagram (snapshot) showing the streamer zone structure ahead of a negative leader tip, (b) a space–time diagram of negative leader development with time increasing from left to right over  $50 \mu\text{s}$ , and (c) the corresponding current in the ground electrode.  
Source: Diagrams are adapted from Gorin et al. [163] and Biagi et al. [162].

the negative high-voltage electrode, (2) the leader tip, (3) positive streamers (filamentary channels of low conductivity), (4) space stems, and (5) negative streamers emanating from the space stems. The streamer zone apparently extends from the primary leader channel intermittently [164]. Fig. 4.4b depicts negative leader development in time from left to right, as interpreted from the streak photographic observations, with electrode current shown below (Fig. 4.4c on the same time scale). The numbers (1) through (5) on Fig. 4.4b designate the same phenomena as on Fig. 4.4a. The leader tip develops quasi-continuously down curve (2) in Fig. 4.4b, with the luminous “space stem” moving along the negatively sloped dashed line labeled (4). The space stem eventually thermalizes and becomes a space leader (6) that develops bidirectionally. When the positive end (top) of the space leader merges with the negative leader tip (at 7), the higher potential of the leader channel is transferred to the negative end (bottom) of the space leader, followed by a burst of negative corona or corona streamers (8). As we shall discuss later in this section and in Section 5.2.2, it may well be the electric fields of these negative streamers that are the source of the runaway electrons that produce the X-rays associated with the step process in natural lightning. When the space leader contacts the primary leader above it, current and luminosity waves travel up the leader channel, completing the leader step process. The spark propagation continues in the corona created at (8) with the development of a new space stem that initiates the next leader step. Current pulses in the grounded electrode are associated with each step, as shown in Fig. 4.4c. Reports by other researchers (e.g., [33,165–168]) confirm the general description of negative laboratory leader step formation given above. For gaps greater than about 2 m, space stems also sometimes occur in parallel (i.e., two separated horizontally at about the same distance from the primary leader) and/or in series (i.e., one beneath the other) (e.g., [165,166]).

Measurements by Biagi et al. [161,162] on triggered lightning and Hill et al. [154] on natural lightning confirm that natural lightning strokes form in the same general way as negative laboratory leader steps: via the formation of a luminous “space stem” in the corona processes some meters below the primary leader tip, followed by the elongation of the space stem in both directions as a “space leader” which connects to the leader tip above, forming a new step.

Biagi et al. [161] reported imaging two space stems that were associated with a dart-stepped leader in a triggered lightning flash, the first observations of space stems outside of the high voltage laboratory. One space stem was 4 m in length and was observed at a height of 250 m above ground. The other space stem, depicted with a 20  $\mu\text{s}$  frame integration time in Biagi et al. [161] and reproduced in Fig. 4.5, was significantly more luminous than the surrounding corona streamers, was about 2 m in length, and formed about 5 m below the downward negative dart-stepped leader tip and about 5 m above the upward positive connecting leader from ground. While Biagi et al. [161] referred to these two luminous channel

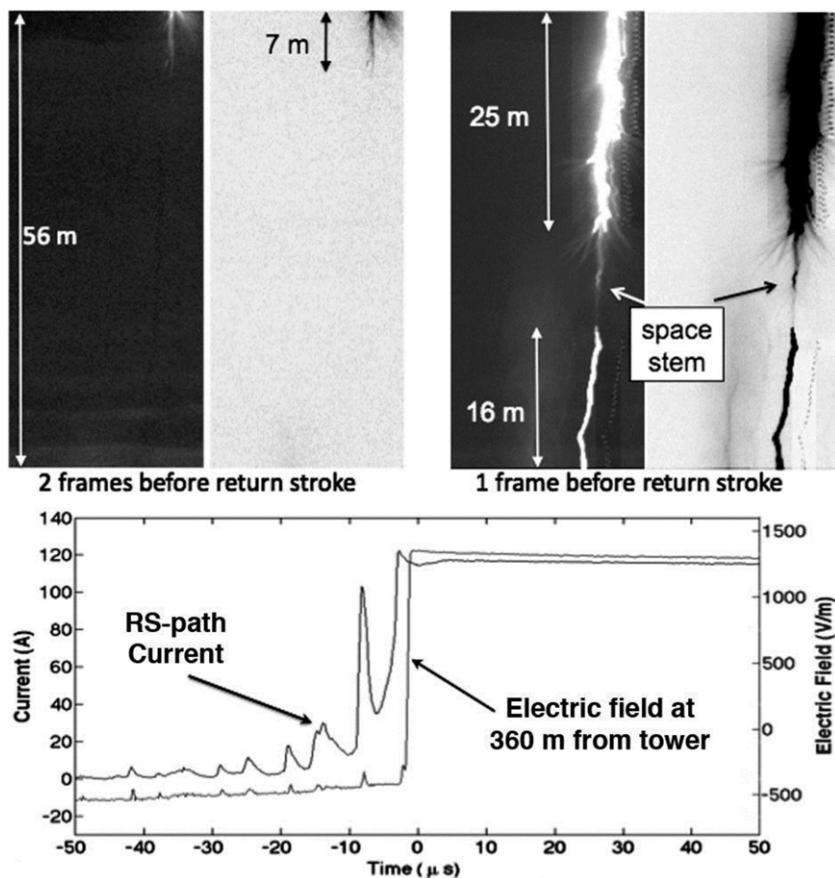


**Fig. 4.5.** An enhanced and enlarged view of the two  $20\ \mu\text{s}$  video frames (and their negatives) (top) before return stroke 8 of a triggered lightning flash at the ICLRT along with (bottom)  $100\ \mu\text{s}$  of electric field and current centered on return stroke 8. The current and electric field both saturated before the return stroke.

Source: Adapted from Biagi et al. [161].

segments as space stems, they might more accurately be called space leaders, space leaders being the expanding, more spatially developed, and more luminous version of the preceding space stem.

As a continuation of the work of Biagi et al. [161,162] presented 10 high-speed video images that depict the bottom  $150\ \text{m}$  of a downward negative, dart-stepped leader in a triggered flash. The dart-stepped leader extended downward at an average speed between  $2.7 \times 10^6$  and  $3.4 \times 10^6\ \text{m s}^{-1}$ . The video data were recorded at 240 kiloframes per second ( $4.7\ \mu\text{s}$  frame integration time), along with correlated measurements of the X-ray emission observed at  $50\ \text{m}$ , electric field derivative ( $dE/dt$ ) measured at  $80\ \text{m}$ , and the rocket-launch-tower current measured beneath the leader. Figs. 4.6a and 4.6b illustrate the observations of Biagi et al. [162]. They observed discrete segments of secondary channel that exhibited luminosity greater than that of the surrounding corona streamers and were distinctly separate and beneath the downward-extending leader channel. These segments appear similar to the space stems or space leaders that had been imaged in long negative laboratory sparks.

Hill et al. [154] recorded high-speed video images of eight branches of a natural lightning stepped leader at a frame rate of 300 kiloframes per second (kfps) ( $3.33\ \mu\text{s}$  frame integration time), representing the first published observations of space stems/leaders associated with natural stepped leaders. Sixteen occurrences of space stems/leaders were imaged in 14 different frames at various distances ahead of the descending leader tip. Eighty-two steps were imaged altogether. The stepped leader exhibited characteristics similar to those observed in both dart-stepped leaders in triggered lightning and in long laboratory sparks. In most cases, the space stem/leader in one frame connects to the leader tip above in the subsequent frame, extending the leader channel. Thus, the  $3.33\ \mu\text{s}$  time resolution is not sufficient to resolve the actual connection process. Most connections are associated with significant isolated brightening of the space/stem leader and the connection region, followed by frames of upward propagating re-illumination of the existing leader channel. Assuming the leader to be  $1\ \text{km}$  distant (the possible range was  $700\ \text{m}$ – $2\ \text{km}$ , which changes the calculated vertical length measurements proportionally), Hill et al. [154] measured the 16 space stems/leaders to be on average  $3.9\ \text{m}$  in length and separated from the previous leader channel tip by an average distance of  $2.1\ \text{m}$ . For the 82 steps, interstep intervals were on average  $16.4\ \mu\text{s}$  and step lengths on average were  $5.2\ \text{m}$ . The measured statistics for natural stepped leader space stem/leader length

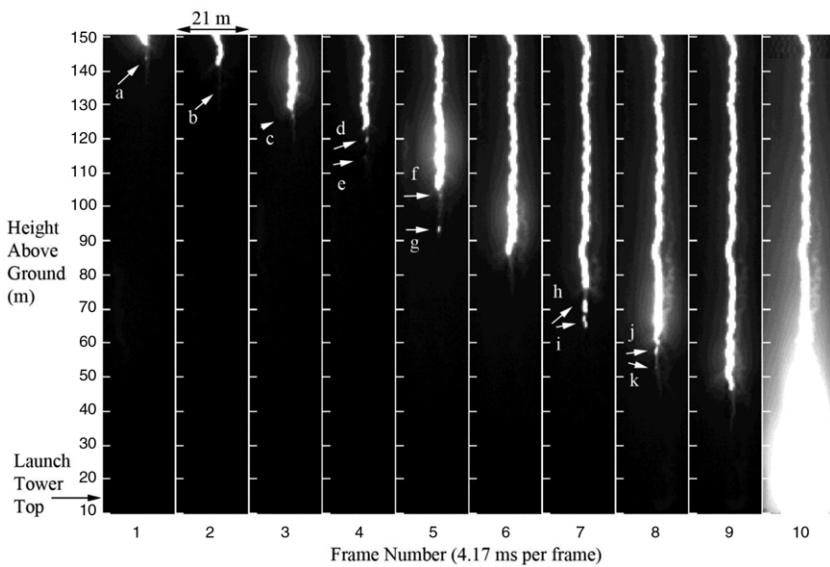


**Fig. 4.6a.** Ten high-speed video frames (240 kfps, 4.17  $\mu$ s per frame) depicting a dart-stepped leader in triggered lightning at the ICLRT developing from 150 m height to ground during a time of 41.7  $\mu$ s. The top of the launch tower is 14 m above ground. The white arrows point to the luminous segments that formed separately from and below the downward-extending leader channel (some of them are too faint to be seen in this reproduction, but are readily identifiable in the original frames). The return stroke began during frame 10.

Source: Adapted from Biagi et al. [162].

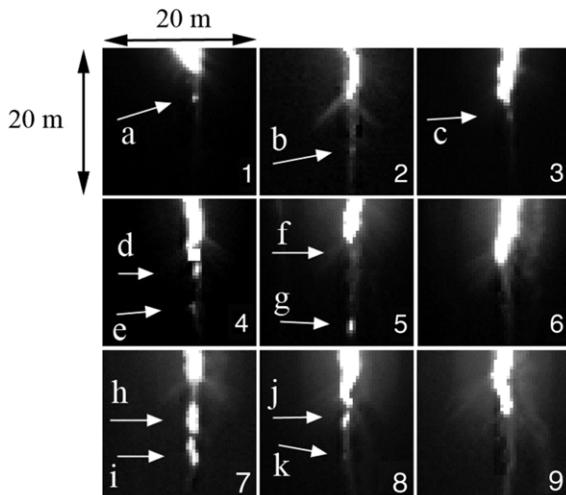


**Fig. 4.6b.** The bottom 20 m of the downward-extending leader channel in the first nine frames in Fig. 4.6a, shown expanded and contrast-enhanced. Each image shows about 20 m  $\times$  20 m. The white arrows correspond to those in Fig. 4.6a and point to the luminous segments of interest.

Source: Adapted from Biagi et al. [162].

and separation from the previous leader channel tip given by Hill et al. [154] are in relatively good agreement with those obtained by Biagi et al. [162] for a dart-stepped leader preceding a rocket-triggered lightning return stroke at a range of 430 m. Biagi et al. [162] reported space stem/leader lengths ranging from 1 to 4 m and separations from the leader channel ranging from 1 to 10 m.

Hill et al. [154]'s measured interstep intervals and step lengths for the natural stepped leader are, in general, shorter in duration and length than previously reported interstep intervals and step lengths obtained earlier using streak cameras. From examination of published streak photographs, Hill et al. [154] argue that step lengths from streak photographs could have been overestimated by recording on film not only the length of the newly-formed section of leader channel, but the superposition of the newly-formed section and the luminosity wave that travels back up the leader channel after step formation (see discussion in next paragraph), since the upward propagating luminosity wave often exhibits luminosity comparable to that of the leader tip for some tens of meters up the existing channel. As noted earlier, most prior optical studies of leader propagation used techniques such as thunder ranging and cloud-base height estimation to determine

vertical scales and the distance to a given leader channel. The inherent errors in these lightning location techniques likely contribute to the relatively wide range of values in the literature for step length, between 3 and 200 m. Finally, Hill et al.'s measured average step leader propagation speeds, assuming a range of 1 km, are in good agreement with those of Schonland et al. [150] and Schonland [14], on the upper boundary of those measured by Berger [20], and on the lower boundary of those measured by Chen et al. [140].

Hill et al. [154] measured a minimum average velocity of about  $10^7$  m/s for the upward propagating luminosity wave following steps in natural lightning, a minimum value due to the necessary assumption that the propagation observed in a video frame took place during the full 3.33  $\mu$ s frame. As noted earlier, Wang et al. [153], using the ALPS photodiode system, measured the lengths of the upward propagating luminosity waves following step formation in triggered lightning and reported that in the bottom 400 m of a dart-stepped leader those lengths were from several tens of meters to more than 200 m and the speeds of the upward propagating waves were from  $1.9 \times 10^7$  to  $1.0 \times 10^8$  m  $\text{s}^{-1}$ , with an average value of about  $6.7 \times 10^7$  m  $\text{s}^{-1}$ , not unlike the speed of a return stroke.

In addition to the optical measurements just discussed, which must be an order of magnitude faster in order to adequately resolve optical step formation (that is, must be sub-microsecond-scale), both electric field and X-ray emission measurements associated with leader stepping contribute to the overall picture of the leader step process. Earlier we summarized the existing data on step electric field and electric field derivative measurements, those having been made with sufficient time resolution to resolve all the salient features of the waveforms. Next we look further at the most recent leader electric field measurement and associated modeling of Howard et al. [138]. Then we look at the issue of X-ray emission from the step process. Again, laboratory measurements of X-ray emission associated with meter-length high-voltage sparks provide valuable clues to the natural lightning X-ray emission.

As noted earlier, individual leader-step locations were accurately determined by Howard et al. [138] with a  $dE/dt$  TOA system. Example waveforms are given in Figs. 4.3a and 4.3b. The more complex waveform, Fig. 4.3b, likely contains in its initial smaller pulses information on the space stem/space leader process. The leader-step field derivative is typically a bipolar pulse with a sharp initial half-cycle of the same polarity as that of the return stroke, followed by an opposite polarity overshoot that decays relatively slowly to background level. A "clean" version of this waveform is found in Fig. 4.3a. The opposite polarity overshoot (that part associated with the electrostatic field, the initial peak being primarily radiation field) increases in amplitude relative to the initial peak and becomes dominant as range decreases. The initial peak is often preceded by a "slow front", similar to the slow front that precedes the fast transition to peak in first return stroke  $dE/dt$  and  $E$  waveforms. The slow front, which is apparent in the modeled current (see below) as well as in the electric field and field derivative, may well be related to the space stem/leader process, the initial formation of the step, prior to the primary step current. The overall step-field  $dE/dt$  waveform duration is typically less than 1  $\mu$ s.

From modeling  $dE/dt$  pulses of the type shown in Fig. 4.3a (the modeled currents were propagated upward at  $1.5 \times 10^8$  m  $\text{s}^{-1}$  from the bottom of the step, with their amplitudes decaying exponentially with a decay height constant of 25 m, and their shapes adjusted until they matched the multiple-station  $dE/dt$  measurements), Howard et al. [138] determined the properties of two step leader currents vs. time. They use one of these currents to calculate leader step  $E$  and  $dE/dt$  vs. time as a function of source range and height, the results being in good agreement with their overall observations. One of the derived step currents with the corresponding measured  $dE/dt$  and the calculated  $E$  and  $dE/dt$  predicted to be associated with that current are given in Figs. 4.7 and 4.8, respectively. The two modeled current waveforms had maximum rates of current rise-to-peak near  $100$  kA  $\mu\text{s}^{-1}$ , peak currents in the 5–7 kA range, current half-peak widths of about 300 ns, and charge transfers of about  $3 \times 10^{-3}$  C, similar to the values estimated by Krider et al. [147] from distant lightning except for Howard et al.'s much faster current rate of rise. The modeled currents were from the simple, "clean" bipolar  $dE/dt$  step waveform. For the more complex step waveforms with multiple  $dE/dt$  pulses, as shown in Fig. 4.3b and in some of the waveforms in Fig. 4.10, the modeling would likely need to consist of more than one current wave moving upward and, ideally, would take account of the effect of space stems/leaders in forming the step.

Recently, ground-based X-ray sensors have provided new insights and raised new questions about the physics of leader propagation. As will be discussed in detail in Section 5.3.1, it has been shown that both stepped and dart leaders (including dart-stepped leaders and chaotic dart leaders [169]) produce X-ray emission as they descend towards the ground [170–173]. Further, the production of X-rays in stepped leaders has been shown to be directly associated with the step formation process [173], as illustrated in Fig. 4.9. Note that the shape of the close, overhead leader step waveforms in Fig. 4.9 match those predicted in Fig. 4.8. For both stepped and dart leaders, the emissions were first observed when the leaders were several hundred meters above ground, terminated near the time of the return stroke, and were composed of multiple, brief bursts of X-rays in the 30–250 keV range, with each burst typically lasting less than 1  $\mu$ s [172,173]. Howard et al. [174] were the first to report that there was both a close spatial and temporal association between the sources of the X-rays and causative leader step electric field change, and that this relationship was similar for both a stepped leader in a natural flash and a dart-stepped leader in a rocket-triggered flash. The X-rays are radiated just after the  $dE/dt$  peak (see below). The similarities of the X-ray emissions from different types of leaders imply a common physical mechanism in all downward negative leaders and further imply that dart leaders, which are generally viewed as moving continuously, may well involve some degree of stepping. The mechanism by which leaders produce X-rays likely involves the acceleration of high-energy electrons, so-called runaway electrons, under the influence of strong electric fields [120]. One of the currently favored models in the so-called thermal (or cold) runaway electron mechanism [172,175,176], which does not require an external source of energetic seed particles nor a strong electric field that extends for some tens to hundreds of meters in

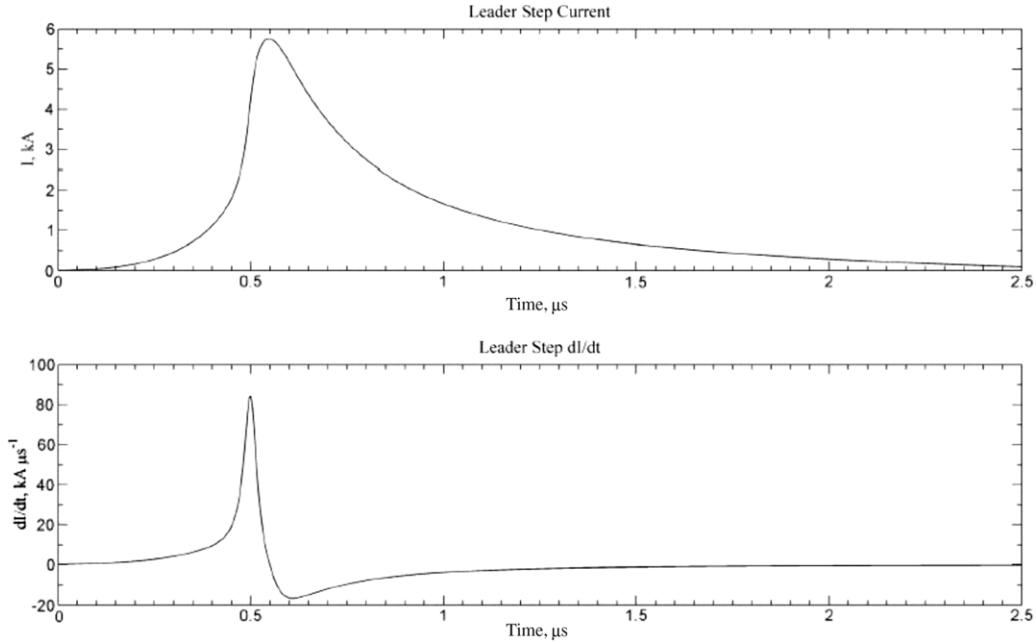


**Fig. 4.7.** Current and current derivative waveforms used in modeling a typical stepped leader step.  
Source: Adapted from Howard et al. [138].

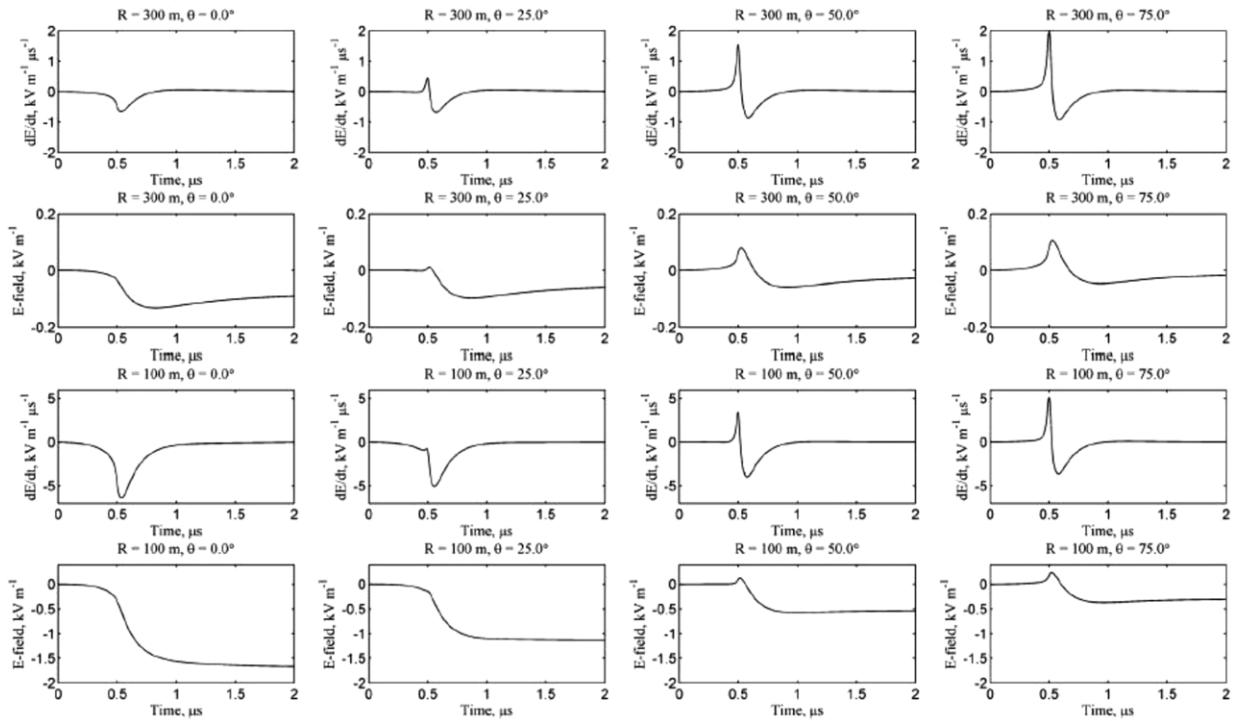


**Fig. 4.8.** Modeled electric fields and field derivatives using the current and current derivative of Fig. 4.9. The current front was assumed to propagate upward with a speed of  $1.5 \times 10^8 \text{ m s}^{-1}$ , and the amplitude of the current waveform was assumed to decay exponentially with a decay constant of 25 m. The first and second rows show leader-step  $dE/dt$  and E-field waveforms, respectively, for various angles (see Figs. 4.3a and 4.3b) at a range of 300 m. The third and fourth rows show waveforms for various angles at a range of 100 m. The vertical scales for the 100 m and 300 m calculations are different.  
Source: Adapted from Howard et al. [138].

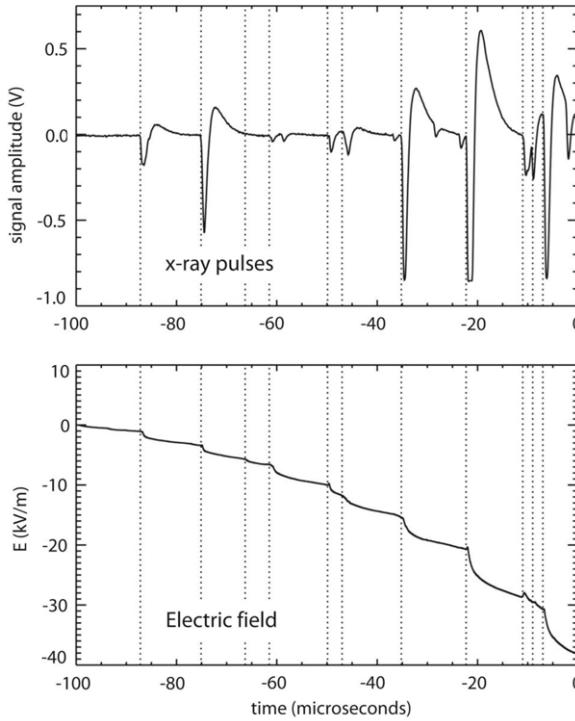


**Fig. 4.9.** X-rays (top panel) and electric field (integrated  $dE/dt$ ) waveforms (bottom panel) for a natural cloud-to-ground lightning flash. The lightning struck within 50 m of the electric field antenna and about 260 m from the X-ray detector. Time zero in the plot corresponds to the beginning of the return stroke. The start times of the eleven final steps are denoted by vertical dotted lines.

Source: Adapted from Dwyer et al. [173].

space, as does the Relativistic Runaway Electron Avalanche (RREA) mechanism [177,178]. However, the thermal runaway model does require the electric field near the step formation to approach values equivalent to near 30 MV/m at standard air conditions, approximately 10 times the electric field required for conventional breakdown. The fields are presumably found at negative streamer tips (e.g., [176,179,180]). Laboratory spark measurements inform this issue, as described later.

An example of correlated leader-step electric field derivative and X-ray emission waveforms from co-located sensors is given in Fig. 4.10, from data in Hill [181]. From Hill's data and the earlier data of Howard et al. [174], it can be concluded that the primary X-ray emission associated with the step process follows the  $dE/dt$  pulse associated with the step process by 10 ns to a few  $\mu$ s, and hence a reasonable inference is that the X-rays are emitted by the negative corona streamers propagated downward beneath the space leader just after it has connected with the primary leader above to form a new step. Hill [181] has located the X-ray sources and associated  $dE/dt$  sources in 3-D via TOA techniques with a location error of about 1 m for dart-stepped leader steps in both natural and triggered lightning. For two triggered lightning dart-stepped leaders, X-ray sources were emitted from locations separated from the locations of the associated  $dE/dt$  pulse peaks by average distances of 22.7 m and 29 m, respectively. The X-ray sources occurred beneath the  $dE/dt$  sources in 88% of the cases. X-rays were emitted from 20 ns to 2.16  $\mu$ s following the  $dE/dt$  pulse peaks, with average temporal separations of 150 ns and 290 ns, respectively, for the two triggered lightning events. For one natural lightning dart-stepped leader, X-ray sources were emitted an average total distance of 39.2 m from the associated  $dE/dt$  pulse peak, and occurred beneath the location of the  $dE/dt$  source in 86% of the cases. The X-rays were emitted from 10 ns to 1.76  $\mu$ s following the  $dE/dt$  pulse peak with an average temporal separation of 280 ns. In each of the three events, the altitude displacement between the  $dE/dt$  and X-ray sources dominated the total separation, accounting for 90%, 63%, and 72%, respectively, of the total separation. X-ray sources were distributed randomly in the lateral directions about the lightning channel in each event. For the triggered lightning events, X-rays were located from 2.5 to 83.5  $\mu$ s prior to the return stroke at altitudes ranging from 24 to 336 m. For the natural lightning event, X-rays were located from 40.4 to 222.3  $\mu$ s prior to the return stroke at altitudes ranging from 99 to 394 m. Cumulatively, 67% of the located X-ray sources occurred between 60 and 280 m in altitude.

We now examine X-ray emission from meter-length, megavolt laboratory sparks. Unfortunately, X-ray emission has not been studied in a spark long enough, over about 2 m [e.g., [164,165]], to generate steps via space stems, but we can gain insight into the physical process generating the X-rays, apparently negative corona streamers (see Section 5.3.2 for additional discussion). The first solid evidence that X-rays were produced by long high voltage sparks in sea-level air was reported by Dwyer et al. [182]. The X-rays were in the 30–150 keV range and were very similar in characteristics to those from lightning, arriving in discrete bursts less than 0.5  $\mu$ s in duration either when the voltage across the gap was maximum or was in the

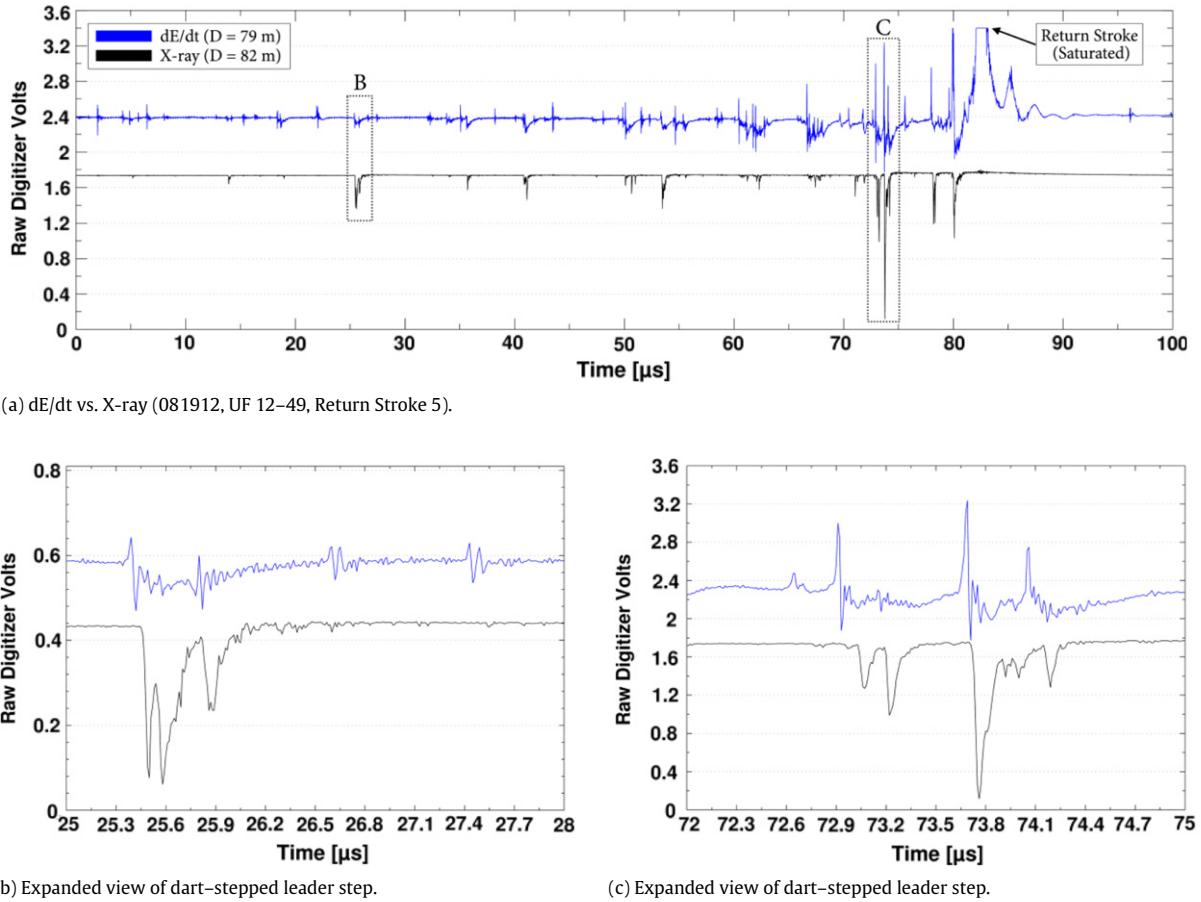


**Fig. 4.10.** Correlated electric field derivative and x-radiation from a dart-stepped leader in triggered lightning at the ICLRT.  
Source: Adapted from Hill [181].

process of collapse. In the most recent laboratory measurements, van Deursen et al. [183], in a follow-on experiment to the experiment of Kochkin et al. [184], reported that “negative streamers were a necessary and sufficient condition” for X-ray production and that most X-rays produced in their studies of long laboratory sparks of either polarity occurred as negative and positive streamers approached each other from the opposite electrodes. The characteristic X-ray energy emitted from streamers in their 1 MV gap was about 200 keV. Other pertinent laboratory spark/X-rays studies are reported by Dwyer et al. [185], Nguyen et al. [186], Rahman et al. [187], Nguyen et al. [188], and March and Montanya [189]. More about this in Section 5.3.2.

#### 4.3. Positive “stepped” leaders

Positive leaders have been much less studied than the negative leaders discussed in Section 4.2. There are several reasons. First, positive flashes to ground are much less frequent than negative flashes (Section 1.3); second, positive leaders are much less luminous than negative leaders making streak photography inefficient [21]; and third, positive leaders emit much less VHF radiation than negative leaders making problematic the tracking of positive leader propagation via LMAs or interferometers [e.g., [190,191]]. Positive flashes to ground are often, if not usually, preceded by cloud discharges with durations of the order of hundreds of milliseconds [133,192–194], suggesting that a positive flash to ground may often be just a branch of an extensive cloud discharge. While negative initial leaders apparently always propagate by intermittent stepping, positive leaders can either step or move in a more continuous or pulsing fashion. When positive leaders do step, the stepping mechanism is different from that discussed for negative stepped leaders in Section 4.2. Initial positive leader electric field waveforms sometime show pulses similar to those of negative stepped leaders (Fig. 4.2) and sometimes do not.

Free electrons move away from (diverge from, are repelled by) the negative leader tip, whereas in the case of a positive leader the free electrons move toward (converge on) the leader tip producing ionization in the high electric field near the tip. The result is that the formation of ionization via corona streamers in the vicinity of the positive leader tip requires less leader tip voltage and less overall electric field magnitude than for the negative leader. While the propagation of the two

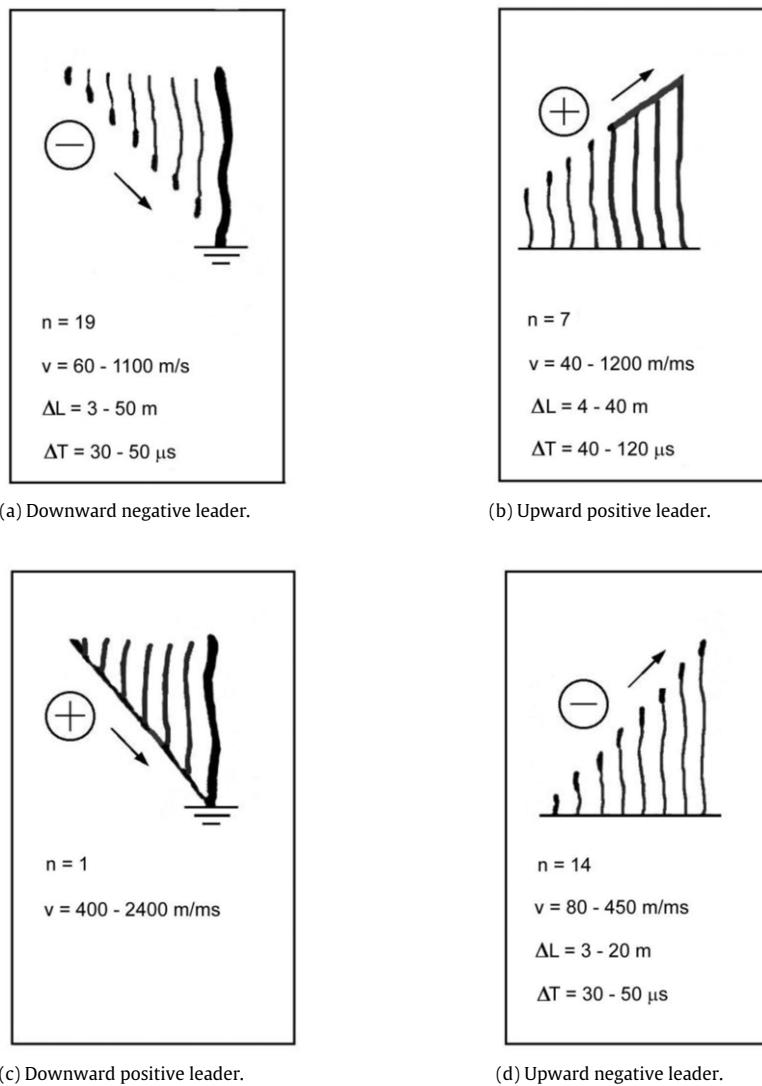


**Fig. 4.11.** Four different types of lightning leaders: (a) downward negative leader, (b) upward positive leader, (c) downward positive leader, and (d) upward negative leader. For each leader type, the polarity refers to that of the leader charge. Given for each type of leader are the sample size  $n$  and the range of propagation speeds  $v$ . Additionally given, for clearly stepped leaders, are the range for average step lengths  $\Delta L$  and the mean time interval steps  $\Delta T$ .  
Source: Adapted from Berger and Vogelsanger [159].

types of leaders takes place by different mechanisms, optically measured (in clear air) leader speeds, step lengths, and time between steps are remarkably similar for positive and negative leaders.

Berger and Vogelsanger [159] describe streak camera measurements of the four types of leaders illustrated in Fig. 1.2. Their observations are summarized in Fig. 4.11. Negative leaders, whether downward from the cloud or upward from the Swiss instrumented towers, were always found to be optically-stepped and to have similar characteristics. There is only one published streak photograph of a downward positive leader (see Fig. 4.11c), and it is reproduced in Fig. 4.12 from Berger and Vogelsanger [139]. Compare Fig. 4.12 to the streak photography of a negative downward stepped leader in Fig. 4.1. Fig. 4.13 shows a streak camera image of (a) an upward positive leader (b) a dart leader/return stroke sequence, (c) an M-component, and (d) a downward negative dart-stepped leader, all from triggered lightning. The differences in leader propagation modes are apparent.

Berger and Vogelsanger [139] reported that the positive leader shown in Fig. 4.12 had a downward speed that increased from  $3.6 \times 10^5$  to  $2.4 \times 10^6 \text{ m s}^{-1}$  as the leader approached ground. Based on this singular result, positive leader speeds had been generally viewed as being greater than negative leader speeds [e.g., [195,196]], until Saba et al. [193] compared high-speed video measurements of the speed of 39 positive leaders and 303 negative stepped leaders and showed both groups to be similar. The mean and median positive-leader 2-D speeds were  $2.5 \times 10^5$  and  $1.7 \times 10^5 \text{ m s}^{-1}$ , respectively, while the comparable negative values were  $3.0 \times 10^5$  and  $2.3 \times 10^5 \text{ m s}^{-1}$ . Saba et al. [193] consider the Berger and Vogelsanger [139]

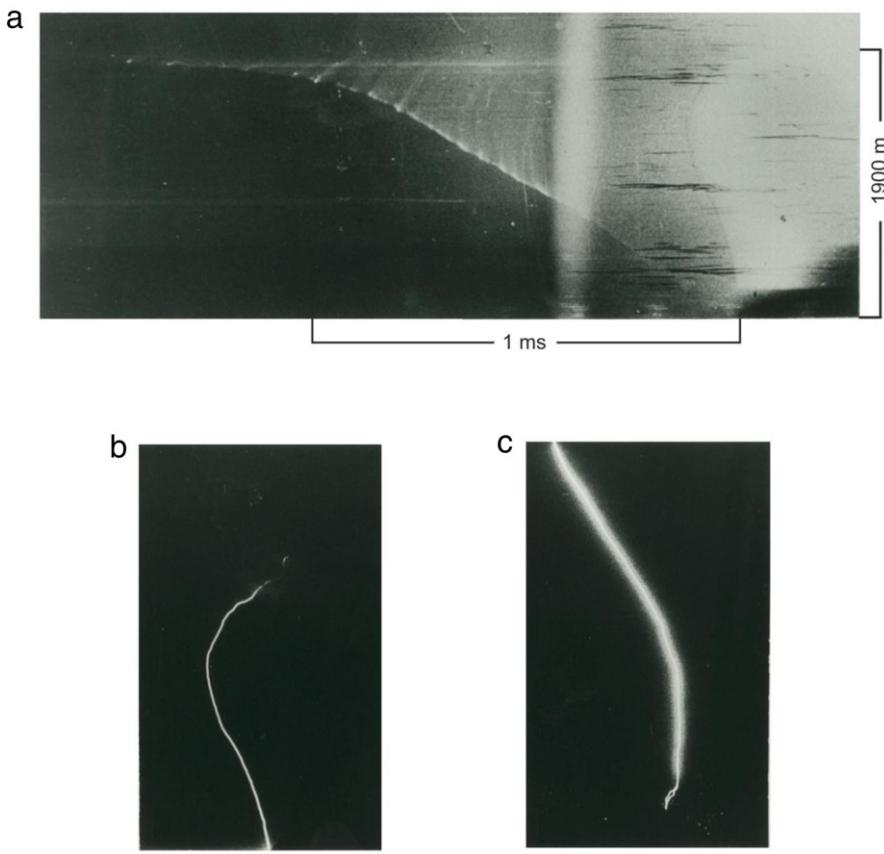


**Fig. 4.12.** (a) Streak photograph obtained from a range of 3.3 km of the last millisecond of a positive leader followed by a return stroke, (b) a still camera view from the same location, (c) a different still camera view showing the strike point on Lake Lugano, Switzerland and the “loop” at the bottom indicative of an upward connecting leader.

Source: Adapted from Berger and Vogelsanger [139].

positive leader to have been an extreme case. Saba et al. [193] show that positive leader speeds increase by a factor of 1.1–6.5 as the leaders move toward ground, whereas negative leader speed observed with the same instrumentation increased much less significantly as the negative stepped leaders approached the ground. Kong et al. [194], using high speed video and electric field measurements, found one 2-D positive leader speed that varied from  $0.1 \times 10^5$  to  $3.8 \times 10^5$  m s $^{-1}$ , with 26 electric-field leader pulses in the final 0.5 ms, and an average inter-pulse time of 17  $\mu$ s, the pulses being evidence of stepping. The intracloud process prior to this positive CG flash had a duration of 600 ms with channel branches developing horizontally at a speed of the order of  $10^4$  m s $^{-1}$ .

It is interesting to note that the speed of the upward positive leaders in triggered lightning in Florida, both initially and in later branches, for nine leaders was found by Hill et al. [197], using an LMA, to be generally between  $10^4$  and  $10^5$  m s $^{-1}$ . In previous triggered lightning studies Biagi et al. [161] found one upward positive leader to step with a constant average speed of  $5.6 \times 10^4$  m s $^{-1}$  over its initial 100 m, and Biagi et al. [198] report one case of leader speed increase from  $5.5 \times 10^4$  m s $^{-1}$  between the wire top of 123 m and 134 m to  $2.1 \times 10^5$  m s $^{-1}$  at 350 m altitude. These upward-positive-leader speeds are consistent with those reported by Fieux et al. [199], Laroche et al. [200], and Idone [160], whereas Yoshida et al. [201] measured, for the same leader as Biagi et al. [198], but using interferometry rather than optical measurements, a higher speed of  $3.3 \times 10^6$  m s $^{-1}$  at higher altitude, between 1.5 and 3.7 km, which was inside the visible cloud. In New Mexico, Edens et al. [202], using an LMA, found upward positive leader speeds along various branches of a triggered lightning to be  $1\text{--}3 \times 10^4$  m s $^{-1}$ , which they state is slower than found in other studies. However, a number of the 9 triggered lightning leaders studied by Hill et al. [197] (see above) have leader speeds in that range. Forty-five unconnected upward positive leaders initiated in response to nineteen downward negative leaders have been studied by Lu et al. [203] using high-speed video cameras. They report 2D upward speeds between  $5.8 \times 10^4$  and  $3.4 \times 10^5$  m s $^{-1}$  for lengths between 0.45 and 399 m, with 86% of the speeds being less than  $1.7 \times 10^5$  m s $^{-1}$ . Finally, upward positive leader characteristics have been measured with streak cameras by McEachron [204] on the Empire State Building and by Berger and Vogelsanger [139,159] on towers in Switzerland. McEachron [204] found upward leader speeds of  $5.2 \times 10^4$  to  $6.4 \times 10^5$  m s $^{-1}$  with a mean of  $2.5 \times 10^5$  m s $^{-1}$  while the Swiss data yielded a range from  $4 \times 10^4$  to  $1 \times 10^6$  m s $^{-1}$ . Step lengths and inter-step intervals were similar in the two studies, 4–40 m for step length and 20–120  $\mu$ s for interstep interval.

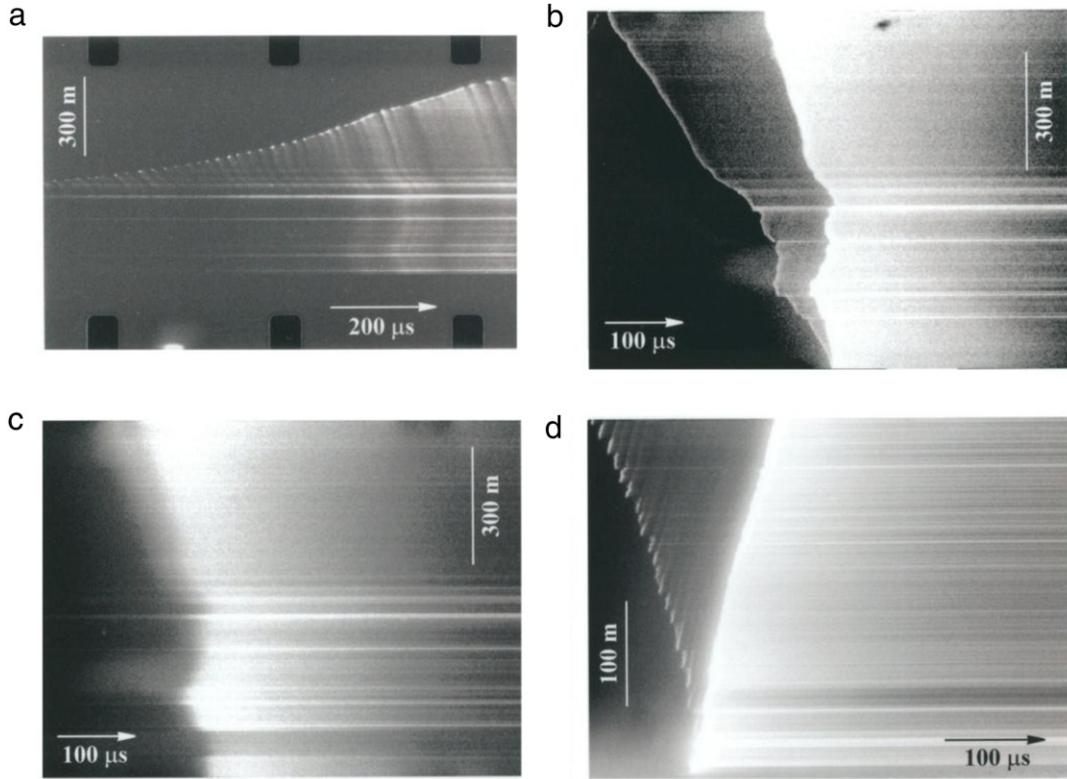


**Fig. 4.13.** a, b, c, d. Streak-camera records of (a) an upward positive leader, (b) and (d), two downward-negative subsequent-leader-return-stroke sequences, and (c) an M-component, in triggered lightning. Time advances from left to right. Records (a), (b), and (c) are from Kennedy Space Center (KSC) flash 8827; record (d) is from ICLRT flash 9734. Note the pronounced stepping evident in the upward positive and downward negative leaders of (a) and (d).

Source: All images courtesy of V.P. Idone, University of Albany, SUNY, and adapted from Rakov and Uman [5], Fig. 7.5.

We examine now the physics of the extension of positive leaders, as informed by one triggered lightning experiment and numerous laboratory long-spark studies. Biagi et al. [198] present high speed video images (3.3  $\mu$ s frame integration times) of an upward positive leader developing in “steps” from the 123-meter-high top of a grounded triggering wire. In the bottom 11 m there were 10 steps. The step lengths ranged from 0.4 to 2.2 m, the interstep time from 16.6 to 30.4  $\mu$ s. The initial upward speed was  $5.5 \times 10^4$  m s $^{-1}$ , as noted earlier. With each step there was a current pulse recorded at the bottom of the grounded wire. The peak step currents at the wire top were estimated to range from 10 to 89 A. From the current at the wire bottom, the positive charge per length on the leader was estimated as 51  $\mu$ C m $^{-1}$ , a value similar to that found in laboratory measurements of long positive leaders by Domens et al. [205] (50  $\mu$ C m $^{-1}$  in a 16.7 m spark gap). The triggered lightning upward leader is optically dark between steps, forms a new luminous step at the tip of the previous one with no evidence of a space stem or space leader, and propagates a wave of luminosity (and current) downward from each new step.

Other researchers, using streak photography, have observed that upward positive leaders in triggered lightning develop intermittently [e.g., [206,160,200]], but have not studied the first development from the triggering wire top coordinated precisely with wire-base current pulses. The luminosity waves that appear to propagate downward from the leader tip as reported by Biagi et al. [198] are consistent with similar reports by Refs. [160,207] from observations at higher altitude above the triggering wire. The currents determined for each leader step (on average 34 A) by Biagi et al. [198] are consistent with other reports of current pulses associated with the initiation of upward positive leaders [e.g., [161,200,208,209]], but are up to two orders of magnitude less than the peak currents (on average 1.6 kA) reported for individual steps in an upward positive leader at higher altitudes, between 300 and 500 m, by Rakov et al. [207]. The individual steps of the upward positive leader examined by Rakov et al. [207] transferred on average 31 mC of charge, or about a factor of 500 more than the average charge per step, 64  $\mu$ C, for the upward positive leader in Biagi et al. [198]. It is worth noting that Rakov et al. [207] defined a step as an “impulsive process that periodically illuminates the extending leader channel ...regardless of the mechanism involved”, and that the tip of the upward positive leader was not observed optically.

As noted earlier, Biagi et al. [198]’s upward-positive-leader speed of  $5.5 \times 10^4$  m s $^{-1}$  near the wire top had increased four-fold to  $2.1 \times 10^5$  m s $^{-1}$  when the leader tip reached a height of 350 m. These speeds are consistent with those reported by others (e.g., [160,161,199,200]) as noted earlier. Yoshida et al. [201], who presented a detailed description of the same

upward positive leader in Biagi et al. [198] using 3-D interferometric images, reported that the leader propagated from 1.5 to 3.7 km with a higher three-dimensional speed of  $3.3 \times 10^6 \text{ m s}^{-1}$ .

The lengths of the Biagi et al. [198]’s leader’s first steps between heights of 123 and 134 m (0.8 to 2.2 m), were smaller than those measured by Laroche et al. [200] (14 m) for a leader at a height of about 1 km. The mean inter-step time intervals for the upward positive leader in Biagi et al. [198] was about 21  $\mu\text{s}$ , which is consistent with the average inter-step time interval reported by Laroche et al. [200] of 20  $\mu\text{s}$ , but less than the average interstep time of 50  $\mu\text{s}$  that Rakov et al. [207] inferred from current and electric field records for an upward positive leader at a height of 300–500 m.

Both continuous and intermittent development of positive leaders have been observed in long laboratory sparks (e.g., [33, 40, 163, 205, 210–212]), as they have in Nature. In the laboratory, whether a positive leader propagates (1) continuously, (2) exhibits clear stepping via a mechanism different from negative stepped leaders, or (3) behaves in an intermediate manner is influenced by the applied gap voltage and its rate-of-rise and the ambient humidity. The humidity apparently effects positive streamer characteristics which determine the space charge injected into the gap ahead of the leader and other properties of the overall discharge. When positive high voltage is applied to the rod electrode, free electrons randomly found near the rod are accelerated toward it, avalanching and forming new electrons. This process leads to an initial impulse positive corona from the rod, also referred to as “fast corona” in the literature. The streamers converging at the rod heat the air there and form a conducting thermalized leader which elongates toward the grounded plane. In the case of continuous propagation, there is a steady group of positive corona streamers ahead of the continuously-moving leader tip. Domens et al. [205] studied this “continuous” type of propagation in a 16.7 m rod-plane gap and further described both a “restrike” type of intermittent, stepped propagation and an “oscillatory” type of propagation which was intermediary between the “continuous” and the “restrike” modes. According to Domens et al. [205], in the “restrike” mode, the discharge current and the discharge activity vanish during given time intervals as a result of the propagation-inhibiting effect of a high-space-charge electric field created by excessive corona activity. The halted leader then produced a new version of the “first corona” beneath it and propagation continues as it did from the rod. There appears to be a delicate balance of experimental conditions to produce the three types of positive leader propagation described by Domens et al. [205]. There is no indication in their paper that they are trying to simulate the types of propagation recorded in natural positive leaders, but it appears that they have, although there is no assurance that the qualitative mechanisms invoked to explain the stepping in the laboratory leader are the same mechanisms operative in the natural positive leader. This would not appear unreasonable, however. It is interesting to note that Bazelyan and Raizer [213] argue the continuously-moving positive leader in the laboratory would appear stepped if image with sufficient spatial and time resolution. McEachron [204, p. 191] had previously made a similar argument for the observed continuously-propagating upward positive leaders from the top of the Empire State Building.

Finally, there is only one report in the literature of X-ray emission from a positive leader and that report is not definitive in that the X-ray emission begins about 8 ms before the initiation of an upward positive leader in a Japanese winter storm, this early radiation being attributed to negative intracloud lightning, and continues through the positive leader initiation and upward propagation, during which time it is attributed to the upward positive leader [214]. As we have discussed, negative stepped, dart, dart-stepped, and chaotic leaders all produce X-rays [e.g., [169]], probably due to runaway electrons in the very high electric fields of negative streamers. The absence of the detection of X-rays in most experiments associated with positive leaders may be because downward positive leaders, due to their rarity, have not occurred near X-ray detectors; while upward positive leaders in triggered lightning, which are triggered at the ICLRT in the center of a network of X-ray detectors, are emitted at an altitude (generally the triggering wire extends higher than 200 m before initiating an upward positive leader) where the X-ray signals are significantly absorbed in the air path to the detectors. On the other hand, the positive streamers active in facilitating positive leader propagation just may not be producers of a significant flux of X-rays. Finally, we noted at the end of Section 4.2 that X-ray emissions have been reported from positive polarity laboratory sparks, but that it appears to be the negative streamers that produce the X-rays. The X-ray emissions from lightning and laboratory sparks will be discussed in more detail in Sections 5.3.1 and 5.3.2.

## 5. High energy atmospheric physics

### 5.1. Introduction

The field of High Energy Atmospheric Physics began in 1925 with the work of C.T.R Wilson on energetic electron production in our atmosphere [215]. Over the 75 years that followed, many researchers attempted to determine if thunderstorms or lightning produced such energetic radiation, with mixed results [e.g. [216–226], also see Refs. [227,228] for overviews of this earlier work]. In hindsight, it is likely that some of these observations were indeed detecting X-rays and gamma-rays from thunderclouds or lightning. However, as late as the year 2000, the existence of energetic radiation from thunderstorms and especially lightning was not widely accepted.

It is interesting and useful to look back at the state of the field in 2000, just before this research area underwent rapid and continuing growth. At that time, it was known that Terrestrial Gamma-ray Flashes (TGFs), intense bursts of gamma-rays seen from space, were produced in our atmosphere [229], but it was almost universally believed that they originated from high-altitude ( $\sim 70$  km) discharges called Sprites (Sections 1.3 and 7.1) by a process called runaway breakdown [177,230, 231]. There had been a few reports of X-ray emissions from thunderclouds [232–236], but these were viewed by many in the

field as a novelty, not central to the topics of interest in traditional atmospheric electricity. Finally, almost no one thought that lightning really emitted energetic radiation, or, at the very least, it had not been established that it did. At the time, Sprites seemed to be the one of the best examples of a source of energetic radiation in our atmosphere [120]. However, because Sprites occur in regions of the atmosphere with air densities about 20,000 times lower than at sea-level, it was not obvious if the intense energetic radiation observed was a consequence of the low-density environment and if the same processes could happen in deeper parts of our atmosphere.

Today, after over a decade of research, we now know that high-energy radiation is commonly produced in our atmosphere, including near the ground at sea-level. In addition, we know that Sprites are, in fact, not the source of Terrestrial Gamma-ray Flashes and apparently do not produce any detectable energetic radiation at all. Instead TGFs come from inside thunderclouds, deep within our atmosphere. This means that TGFs are much brighter near their source than originally thought. Indeed, it has been shown that TGFs may present a radiation hazard to individuals inside aircraft. It is also now known that some of the events originally identified as TGFs were in fact Terrestrial Electron Beams (TEBs) blasted out of the atmosphere by the intense gamma-ray emissions from thunderclouds. It has been established that natural and triggered lightning produce copious hard (hundreds of keV) X-rays, and the X-rays are usually produced in the high-field regions associated with the lightning leaders, often during the stepping process, as noted in Section 4.2. It has been established, as also noted in Section 4.2, that long, megavolt, laboratory sparks in air emit similar X-rays. Finally, it has been shown that the original runaway breakdown theory that had previously been used to model TGFs and Sprites, cannot alone explain either the X-ray emissions from lightning or TGFs. Instead, an old, previously discarded theory published in 1961, along with a new theory published in 2003, appear to best explain these phenomena.

In this section, we shall first introduce runaway electron theory and the mechanisms for generating large fluxes of energetic radiation in air. We shall then review recent observations of X-ray, gamma-rays and radio emissions within our atmosphere, elaborating on and justifying the statements in this section. Finally, we shall discuss some recent models that describe these observations.

## 5.2. Introduction to runaway electron physics

### 5.2.1. Wilson runaway electrons

Runaway electrons, the major component of high-energy atmospheric physics, were discovered by C.T.R. Wilson using cloud chamber measurements and were first described by him in 1925 [215]. It is interesting to note that C. T. R. Wilson, who is well known among particle physicists for his invention of the cloud chamber, and who won the Nobel Prize for this work, invented the cloud chamber because he was interested in atmospheric physics, i.e., interested in clouds. And so, it is fitting that a field that is a combination of particle physics and atmospheric physics was initiated by a man who made important fundamental contributions to both.

Runaway electrons occur when the average rate of energy loss in a medium is less than the average rate of energy gain due to an electric field, allowing them to reach high energies. For air at standard conditions, relativistic electrons below several tens of MeV lose energy predominately via ionization and atomic excitations. At higher energies, the energy losses from bremsstrahlung become important as well. For minimum ionizing electrons near 1 MeV, the energy loss per unit length is  $f_{min} = 2.18 \times 10^5 \text{ eV/m} \times n_{air}$  along the electron's path [237], with  $n_{air}$  being the density of air relative to that at sea-level at standard conditions. An electric field  $E_b = 2.18 \times 10^5 \text{ V/m} \times n_{air}$  thus produces an energy gain per unit length,  $eE_b$ , equal to the minimum ionizing energy loss. The electric field strength,  $E_b$ , is called the breakeven field and has historically served as a standard reference field when discussing runaway electrons. Because electric fields larger than  $E_b$  have been directly measured inside thunderclouds (see Section 3.3), it is immediately apparent that the effects of electric fields must be considered when describing energetic electrons (and positrons) in air.

Consider what happens when the electric field,  $E$ , is less than  $E_b$ . In this case, the change in energy is  $de = (eE - f_{min})dz < 0$  ( $eE$  is positive), so the electron loses energy and eventually slows down to the point where it is lost (i.e., it attaches to an air atom or recombines with a positive ion). Note that  $f_{min}$  can also be thought of as an effective frictional force, and so  $eE - f_{min}$  can be viewed as the total force in the direction of the electron's motion along the field line. In this case, the effective total force is negative, causing the electron to slow down. Because  $f_{min}$  is the minimum energy loss per unit length for energetic electrons in air,  $E > E_b$  will result in all energetic electrons losing their energies and eventually stopping. On the other hand, if  $E > E_b$ , then the change in energy is  $de = (eE - f_{min})dz > 0$  for minimum ionizing electrons, and these electrons will "run away", gaining energy from the field. How much energy they gain depends upon how large the field is. This is illustrated in Fig. 5.1, which shows the energy loss per unit length of an electron (or positron) in air as a function of kinetic energy,  $\varepsilon$ . The plot also shows the energy gain per unit length from a strong electric field (horizontal line). As can be seen, in order for an electron to run away, it must have an initial kinetic energy above the threshold,  $\varepsilon_{th}$ . Such energetic "seed" electrons, with kinetic energies above  $\varepsilon_{th}$ , may be provided from an external source such as cosmic-rays or radioactive decays. Note that the kinetic energy,  $\varepsilon_{th}$ , required for the seed particles decreases rapidly with increasing electric field. When the electric field is increased above the critical field,  $E_c$ , above the energy loss curve for all kinetic energies, then all free electrons may run away, and, in particular, the free thermal electron population created at low energies may run away. This mechanism is sometimes called "cold runaway", or "thermal runaway", and does not require any external seed particles [175,238]. In this paper, we shall refer to the production of runaway electron in such fields ( $E > E_c$ ) as "thermal runaway", because the source of the runaway electrons is the thermal electron population.

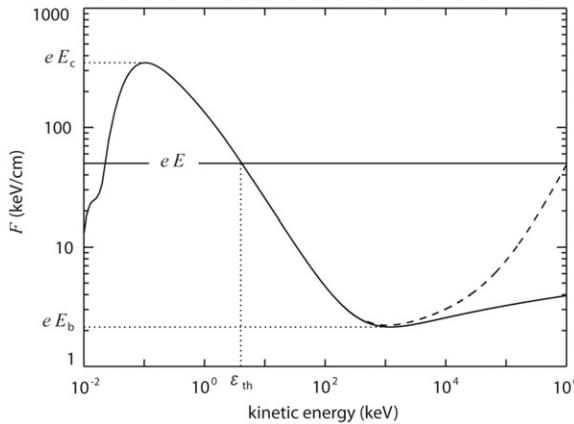


**Fig. 5.1.** The effective frictional force (energy loss per unit length) experienced by a free electron (or positron) moving through air at STP as a function of kinetic energy. The solid curve is due to inelastic scattering of the electron by air molecules, and the dashed curve indicates the effects of bremsstrahlung emission. The horizontal line shows the electric force from a  $5.0 \times 10^6$  V/m electric field. Runaway electrons occur for kinetic energies greater than the threshold energy,  $\varepsilon > \varepsilon_{th}$ . In the figure,  $E_c$  is the critical electric field strength for which low-energy thermal electrons will run away, and  $E_b$  is the so-called breakeven field.

Source: Figure from Ref. [172].

For fields below  $E_c$ , in order to create runaway electrons, energetic seed electrons with kinetic energies above  $\varepsilon_{th}$  must be supplied by some means. According to C.T.R Wilson, the runaway electron mechanism increases the energies of the seed electrons and increases their path lengths through air. For example, one might imagine atmospheric cosmic-ray electrons traversing a region of a thundercloud with a strong electric field, gaining energy and traveling farther than they would without the field. Strictly speaking, even electric fields below the  $E_b$  will cause energetic electrons to lose energy more slowly than if no field were present (assuming a favorable direction of the field), and so such weaker fields will also increase the path length of energetic electrons such as atmospheric cosmic-rays. The runaway electrons are therefore an extreme case, for which almost arbitrarily large energy gains and path lengths could be obtained.

More realistically, energetic electrons moving through air also experience elastic scattering, principally from atomic nuclei, with a smaller contribution coming from scattering with atomic electrons. Elastic scattering causes the path of the electrons to meander (straggle). Consequently, an electron moving from point A to B will almost always follow a longer path than the straight-line distance between the two points. This results in a larger energy loss than  $f_{min}$  applied over the straight-line distance between A and B. In particular, for electrons moving along an electric field line, the electrons will scatter off and on the field line, following the field line only on average. For minimum ionizing electrons, the extra path length due to elastic scattering produces an average energy loss per unit length of about  $f_d = 2.8 \times 10^5$  eV/m  $\times n_{air}$  along the field line. This means that an applied electric field of about  $E_d = 2.8 \times 10^5$  V/m  $\times n_{air}$  is needed to keep an electron moving without energy loss, which is about 30% larger than the breakeven field [239].

In addition, electrons lose much of their energy in air from electron-electron (Møller) scattering with atomic electrons [240]. The combination of many such scatterings, most involving small energy losses to the incident electron and a few involving large energy losses, results in the average energy loss per unit length discussed above. However, the statistical nature of the electron-electron (Møller) scattering has a dramatic effect on the runaway electrons, which we shall discuss in Section 5.2.3.

### 5.2.2. Thermal runaway electron production

For the Wilson runaway electron mechanism, because there is a one-to-one correspondence between the energetic seed electron injected and the runaway electron produced, the flux of runaway electrons will approximately equal the flux of injected electrons. Consequently, we would not expect very large enhancements in the number of energetic electrons or the X-rays and gamma-rays produced. As mentioned above, one way around this problem is to generate the seed electrons internally via the thermal runaway electron mechanism. Because the critical field,  $E_c \sim 3 \times 10^7$  V/m  $\times n_{air}$  is about ten times larger than the conventional breakdown field of air  $E_k = 3 \times 10^6$  V/m  $\times n_{air}$  [32], such a very high field cannot exist in air for very long, since conventional breakdown will rapidly discharge the field. It is conceivable that fields exceeding  $E_c$  could be briefly produced at, say, streamer tips in association with lightning leaders [176,241]. One might imagine a scenario in which a localized high-field is generated by lightning; runaway electrons are then produced via thermal runaway out of the free low-energy electron population; finally, these runaway electrons are energetic enough to continue to gain energy and run away (i.e., Wilson's runaway electron mechanism) in the lower field region in front of the lightning. This combination of thermal runaway electron production augmented by Wilson's runaway electron mechanism may be the dominant means for generating the X-rays observed from lightning leaders and laboratory sparks (Sections 5.3.1 and 5.3.2).

### 5.2.3. Relativistic runaway electron avalanches (RREAs)

In addition to external sources and thermal runaway, another way to generate seed runaway electrons (with  $\varepsilon > \varepsilon_{th}$ ) is via an avalanche process, first described in detail by Gurevich et al. [177]. For this mechanism, most commonly called the relativistic runaway electron avalanche (RREA) mechanism, energetic runaway electrons undergo electron-electron (Møller) scattering with atomic electrons in air [240]. Some of the scattered atomic electrons have kinetic energies with  $\varepsilon > \varepsilon_{th}$ , and so they also run away, along with the initial runaway electrons. The result is an avalanche of relativistic runaway electrons that increases exponentially with time and distance. Of course, to start the avalanche process an energetic seed electron is still needed. As a result, RREAs may greatly increase the flux of energetic electrons (e.g., by thousands), but the flux is still tied to the flux of the initial seed electrons injected into the avalanche region. The RREA is analogous to a low-energy electron avalanche (such as described in Section 2), except the length scale for avalanche multiplication is usually on the order of tens to hundreds of meters, rather than sub-millimeter in the low-energy case. Because low-energy electron avalanches alone are not considered a form of electrical breakdown (e.g., a normally operating gas-filled wire proportional counter is not considered to be in a state of electrical breakdown), the RREA also should not be considered a form of electrical breakdown [242,243]. An electrical breakdown is usually thought of as an internal state of the system producing a large self-sustaining electrical current that results in the rapid discharge of the system – a description that does not appear to apply to the RREA mechanism described by Gurevich et al. [177]. Nevertheless, the name “runaway breakdown” is sometimes used to describe such runaway electrons avalanches [120,244,245]. In this paper, we shall instead refer to an avalanche of relativistic runaway electrons by the descriptive name Relativistic Runaway Electron Avalanche (RREA). We refer the interested reader to Ref. [246] for a discussion of the early theoretical work on the RREA mechanism.

Examples of RREAs can be seen in Figs. 5.2 and 5.3. The figures show the output of a Monte Carlo code that simulates all the relevant physics of runaway electrons, positions and photons [77,242,247,248]. Fig. 5.2 shows the kinetic energy of the electrons moving under the influence of an electric field in air for a small segment of an avalanche. As can be seen, most of the electrons in the RREA do not runaway, instead quickly losing their energy. These intermediate energy electrons create additional ionization. The runaway electrons are the trajectories that steadily gain energy in the figure. The occasional sharp drops in energy are due to hard Møller scatterings and bremsstrahlung emissions. The horizontal dashed line is the average energy of the runaway electrons (7.3 MeV) [78,172,249]. As runaway electrons gain energy, eventually exceeding 7.3 MeV, additional runaway electrons are added at lower energies, maintaining the same average energy for all the runaway electrons.

Fig. 5.3 shows a whole avalanche, plotting the trajectories of runaway electrons moving through a uniform, vertically downward field (between the two horizontal dotted lines), with the field set equal to zero outside the avalanche region. As can be seen, the number of runaway electrons increases rapidly as they propagate upward. The meandering of the trajectories, which results in a lateral spreading of the avalanche, is mostly due to elastic scattering of the electrons with atomic air nuclei. At the top of the figure, the electrons leave the strong electric field (avalanche) region and slow down until they are reabsorbed by the air. Bremsstrahlung X-rays and gamma-rays are mostly emitted upward (not shown) and may travel up to a few kilometers at these altitudes before being absorbed [250].

Monte Carlo simulations show that the threshold electric field for avalanche multiplication is  $E_{th} = 2.84 \times 10^5 \text{ V/m} \times n_{air}$  [77,78]. Because runaway electrons will sometimes undergo a hard (Møller or Bremsstrahlung) scattering that results in a sudden energy loss, runaway electrons that have energies above the threshold energy ( $\varepsilon > \varepsilon_{th}$ ) may occasionally become lost due to such scattering, reducing the number of runaway electrons propagating. On the other hand, such Møller scattering will also occasionally generate new runaway electrons adding to the number of runaway electrons propagating. The threshold field  $E_{th} = 2.84 \times 10^5 \text{ V/m} \times n_{air}$  is the field where the two processes just balance and the avalanche length is infinite (i.e., the number of runaway electrons remains constant with time and distance).

### 5.2.4. Relativistic feedback mechanism

To recap, in 1925, Wilson introduced the runaway electron mechanism, which increases the energies and path lengths of energetic electrons, and in 1992, Gurevich et al. included the effects of Møller scattering to show that avalanches of runaway electrons result. In 2003, Dwyer introduced a new mechanism for generating runaway electrons, built upon this previous work. For this mechanism, illustrated in Fig. 5.4, positrons and energetic photons produce a positive feedback effect that exponentially increases the number of runaway electron avalanches, the inclusion of which results in a dramatic change of behavior that cannot be explained by the RREA mechanism alone [77,242]. In Fig. 5.4, avalanches of runaway electrons emit bremsstrahlung X-rays that may either Compton backscatter or pair-produce in air. If the backscattered photons propagate to the start of the avalanche region and produce other runaway electrons, either via Compton scattering or photoelectric absorption, then secondary avalanches are created. This mechanism is called X-ray feedback (also sometimes called gamma-ray or photon feedback).

Alternatively, the positrons created by pair-production of gamma-rays often turn around in the ambient electric field and run away in the opposite direction of the electrons. Because the positron annihilation cross-section decreases with energy and the positrons quickly accelerate to many ten of MeV, the positrons usually travel on the order of a kilometer at sea level before annihilating. When the positrons propagate to the start of the avalanche region they produce additional runaway electrons via hard elastic scattering with atomic electrons in the air (i.e., Bhabha scattering), thereby creating secondary avalanches. This mechanism is called positron feedback. These secondary avalanches, from X-ray and positron feedback, may

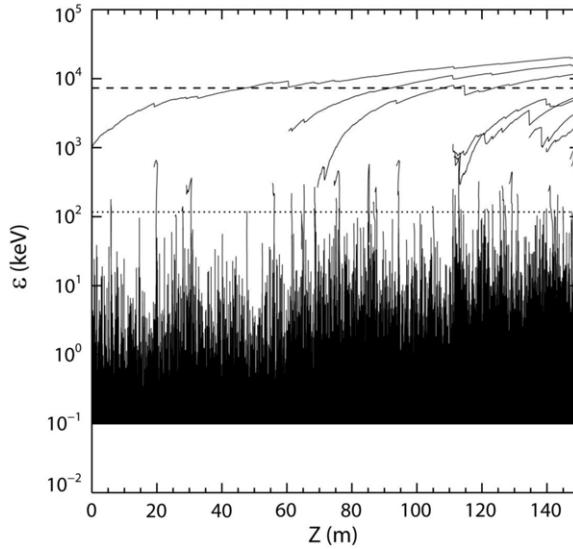


**Fig. 5.2.** Example of a Monte Carlo simulation of a relativistic runaway electron avalanche in air. Each line represents the trajectory of one electron, showing the kinetic energy of the electrons versus distance. The simulation is run at 1 atmosphere pressure and for a uniform, downward electric field of 430 kV/m. This avalanche was initiated by injecting one 1 MeV energetic electron at the left side of the figure. The minimum energy in this simulation,  $\varepsilon_{min} = 100. The runaway electron threshold energy,  $\varepsilon_{th}$ , is shown as a horizontal dotted line, and the average energy of the runaway electron, 7.3 MeV, is shown as a dashed line. As can be seen, due to the statistical nature of the process, not all electrons with kinetic energies above  $\varepsilon_{th}$  run away.$

Source: Figure from Ref. [239].

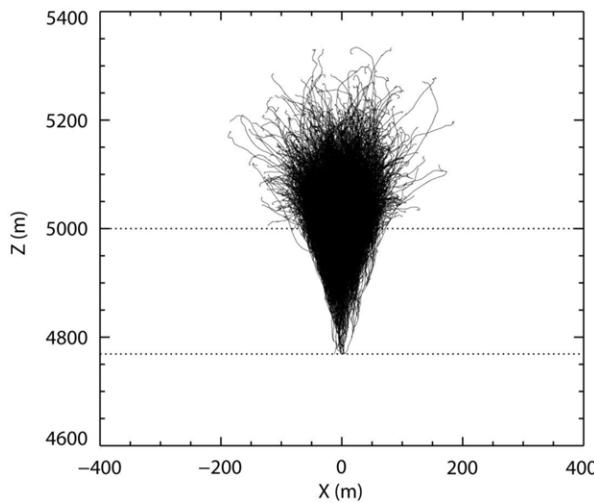


**Fig. 5.3.** Monte Carlo simulation showing runaway electron trajectories inside a thundercloud at 5 km altitude. The electric field is uniform in the region between the horizontal dotted lines and has a magnitude of 375 kV/m. Above and below the dotted lines the field is set to zero. The avalanche is initiated by 10 energetic electrons at the bottom of the high field region, which might correspond to the injection of energetic electrons by a lightning leader. The simulation calculates but does not plot the X-rays produced by bremsstrahlung emission. For a realistic thundercloud and lightning, the number of runaway electrons could, in principle, be 10<sup>14</sup> times larger than the number shown in the simulation.

Source: Figure from Ref. [259].

in turn emit more X-rays that Compton scatter or pair-produce, resulting in more feedback and more avalanches. As a result, the number of runaway electron avalanches can increase exponentially on a timescale measured in microseconds [77,251]. In addition to X-ray and positron feedback, secondary feedback mechanisms include feedback from annihilation gamma-rays and feedback from bremsstrahlung photons emitted by backward propagating positrons [242]. These secondary feedback mechanisms are usually small (e.g., <10%) compared with the primary X-ray and positron feedback mechanisms [242].

Because backscattered Compton photons have a shorter attenuation length than runaway positrons, X-ray feedback requires a shorter avalanche region than positron feedback in order to operate [77]. Indeed, Monte Carlo simulations show that X-ray feedback is usually important for higher electric field strengths (i.e.,  $E > 750 \text{ kV/m} \times n_{air}$ ), which have shorter avalanche lengths, and positron feedback dominates at lower field strengths.

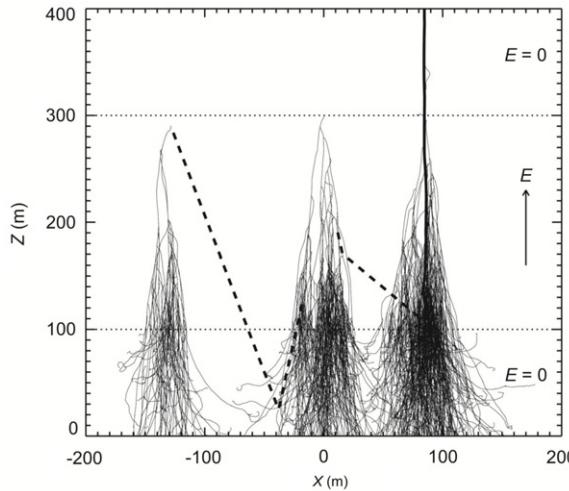


**Fig. 5.4.** Relativistic runaway electron avalanches (RREAs) and the relativistic feedback mechanism. Partial results of the Monte Carlo simulation are shown. The light tracks are the runaway electrons, the dashed lines are the X-rays and the dark track is a positron. The entire avalanche is initiated by one, 1 MeV, seed electron injected at the top of the high field region ( $x = 0$ ,  $z = 300$  m). The horizontal dotted lines show the boundaries of the electric field volume ( $E = 1000$  kV/m). For clarity, only a small fraction of the runaway electrons and X-rays produced by the avalanche are plotted. The avalanches on the left and right illustrate the X-ray feedback and positron feedback mechanisms, respectively.

Source: Figure from Ref. [77].

These feedback mechanisms described above are analogous to the feedback mechanisms that occur at low energies during a Townsend discharge. For example, in a Geiger counter, UV photon and ion collisions at the cathode generate a self-sustained breakdown, which terminates only when the voltage collapses. To distinguish the feedback mechanisms described here, which involve high-energy particles, from the low-energy feedback mechanisms occurring in ordinary Townsend discharges, these high-energy feedback mechanisms are jointly referred to as relativistic feedback [242].

Because relativistic feedback can create an exponentially growing number of runaway electron avalanches, the energetic electron production and gamma-ray emissions generated by this mechanism can be up to trillions of times more intense than for RREAs alone [242]. Consequently, relativistic feedback is a good candidate for explaining Terrestrial Gamma-ray Flashes.

### 5.3. Observations of energetic radiation produced within our atmosphere

#### 5.3.1. X-ray observations of lightning

As of 2001, little evidence existed that lightning emitted X-rays. Indeed, lightning had been seen to quench the emission of X-rays from thunderstorms [233,234], presumably by discharging the large-scale electric field that had been responsible for the emissions. From a theoretical point of view, there was also little reason to believe that X-rays should be observed from lightning. Unlike thundercloud, which can produce very large electric fields over many kilometers, thereby generating RREAs from the cosmic-ray background, the electric fields near lightning are not expected to result in significant RREA multiplication. The reason is that even though the fields may reach or even exceed the conventional breakdown field near the lightning channel, it falls off rather quickly on the scale of tens of meters or less and so not enough runaway electron avalanche lengths are present to significantly enhance the background flux of atmospheric cosmic-rays. X-rays also would not be expected to be produced in any measurable amount from thermal emission (not to be confused with thermal runaway electron emission) from the hot leader and return stroke channels. The hottest part of lightning occurs during the return stroke, at which time the channel heats up to about 30,000 K [252]. Although such a hot channel will emit copious visible and ultraviolet light (this is why lightning is so bright), it is far too cold to emit even soft X-rays. It had been suggested that perhaps the rarified return stroke channel could assist in the production of energetic electrons [226]. However, this idea has not been worked out in detail. Finally, the thermal runaway electron model had never been demonstrated to occur naturally in our atmosphere. It was also difficult to understand how the very high electric field needed for thermal runaway, which is ten times larger than the field needed to breakdown air, could occur. Altogether, in 2001, a compelling case could be made that lightning should not emit X-rays.

For this reason, it was all the more surprising when Moore et al. [170] reported intense energetic radiation during the stepped leader phase of negative natural cloud-to-ground lightning strikes on the mountains in New Mexico. Moore et al. used a NaI(Tl)/photomultiplier tube (PMT) detector and recorded large MeV pulses of energetic radiation for about 1–2 ms before the start of the return strokes for 3 nearby lightning strikes. A control detector with the same electronics but no NaI was also operated, and no detectable signals were recorded on the control during the 3 strikes, adding confidence that the

energetic radiation recorded by the NaI(Tl)/PMT detector was real and the signals were not due to lightning electromagnetic fields coupling to electronics or power systems.

Shortly thereafter, Dwyer et al. [171] investigated the emission of energetic radiation from rocket-triggered lightning at the International Center for Lightning Research and Testing (ICLRT) at Camp Blanding, Florida (see Section 1.4 for a description of this research facility). For these experiments, great care was taken to shield the detectors from sources that could possibly generate spurious signals that might be mistakenly taken for energetic radiation, such as light detected by the PMTs or electromagnetic noise picked up by the electronics. A 12.7 cm by 12.7 cm cylindrical NaI(Tl)/PMT detector along with an identical control detector with no NaI were placed inside a heavy aluminum box that formed a nearly perfect Faraday cage. The instrument was battery powered and fiber optics was used to transmit the analog signals from the PMTs to a shielded control room where the entire waveforms were recorded. The instrument was placed 25 m from the rocket launch tower (shown in Figs. 1.5–1.7) where the lightning was triggered.

It was found that rocket-triggered lightning makes intense bursts of energetic radiation during the dart (and dart-stepped) leader phases [253], similar to the results of Moore et al. Furthermore, it was found that detectable emission was recorded in 31 of the 37 leader/return stroke sequences, suggesting the emission of energetic radiation is a common feature of lightning. It was also found, in agreement with Moore et al., that the energetic radiation always ceased near the start of the return stroke, showing that the lightning leaders were producing the energetic radiation and not the rarified return stroke channel.

As noted in Section 1.3, rocket triggered lightning is very similar to the subsequent strokes of natural lightning. Furthermore, it was shown by later work that the small amount of metal vapor from the exploded triggering wire does not affect, nor is it responsible for the emissions of energetic radiation. Specifically, for multi-stroke flashes, there is no systematic difference between early strokes and later strokes. The energetic radiation originates from bremsstrahlung of electrons with energies of several hundred keV, which is unaffected by atomic processes. Finally, later TOA location determinations of X-rays (see below) show that the energetic radiation produced above the wire top is the same as for below the wire top. The advantage of rocket-triggered lightning over natural lightning is that it is known ahead of time where and when the lightning will strike, making it possible to make close-up and detailed measurements. The measurements can also be repeated, making the study of lightning an experimental science, rather than relying on intermittent observations.

After the work made in the summer of 2002, reported in Ref. [171], detailed investigations were carried out at the ICLRT to determine the properties of the energetic radiation emitted by lightning. In the summer of 2003, several new X-ray instruments recorded rocket-triggered lightning, using detectors shielded with varying thicknesses of bronze attenuators along with unattenuated NaI(Tl)/PMT detectors. It was found that the detected energetic radiation was in fact X-rays with energies up to about 250 keV [254]. It was also found that the X-rays were usually emitted in very short, sub-microsecond bursts during the dart leader and dart-stepped leader phases and possibly at the beginning of the return strokes of negative triggered lightning (See Fig. 5.5). Using collimators over NaI(Tl)/PMT detectors, it was also found that the X-rays originated from the bottom few hundred meters of the leader channel and that the source propagated downward with the leader as it approached the ground.

One challenge in measuring the energy spectrum of X-rays from lightning is the X-rays are emitted in very bright and very short pulses, with durations much less than a microsecond. Even fast plastic scintillators and fast LaBr<sub>3</sub> scintillators fail to resolve individual X-rays and instead measure many X-ray photons arriving at nearly the same time, producing pulse pile up. This can be seen in Fig. 5.5, where the deposited energy in the X-ray pulses is typically in the MeV range and yet the individual X-ray photons have energies around 100 keV. For this reason, attenuators are used at the ICLRT to distinguish the X-ray energies.

Dwyer [172], using the results of Ref. [254], compared the energy spectrum and intensity of the X-ray emissions with predictions by the RREA mechanism to show that the RREA mechanism could not be producing the X-ray emissions from triggered lightning. In particular, the energy of the X-rays (<250 keV) was much too soft to have been emitted by runaway electron avalanches, which have an average energy of 7.3 MeV. In that paper, it was suggested that, instead, the thermal (cold) runaway electron mechanism was responsible for the emission. Other theoretical work on thermal runaway electrons has since been done by Moss et al. [176] and Celestin and Pasko [255], who modeled the creation of thermal runaway electrons by streamers, showing that significant runaway electron production is plausible. Cooray et al. [256] also modeled thermal runaway electrons in the low-density, hot dart leader channel. Finally, Gurevich et al. [179] introduced an alternatively 2-step process for the production of runaway electrons in strong electric fields see comments by Ref. [246].

In 2004, two natural lightning strikes were recorded by the X-ray instruments at the ICLRT, both approximately 300 m from the instruments [173]. Comparing the X-ray measurements with electric field ( $dE/dt$ ) measurements, made with a flat-plate antenna, it was found that the X-ray emission recorded during the stepped leader phase was similar to those recorded from triggered lightning during the dart and dart stepped leader phases, with approximately the same X-rays energies. Furthermore, it was shown that the X-ray pulses were usually produced at the time of the step formation of the leader steps, connecting the production of X-rays with lightning propagation (see Fig. 4.9). This result was extended by Howard et al. [174]. This connection of the X-ray emission with the leader steps can be seen in Figs. 4.10 and 5.7, which show later measurements of triggered and natural lightning, respectively, in 2011 at the ICLRT [181].

After 2005, a new set of instruments were deployed at the ICLRT: The Thunderstorm Energetic Radiation Array (TERA) was designed to measure energetic radiation (X-rays, gamma rays and energetic charged particles) from thunderclouds, lightning and cosmic-ray extensive air showers (EASs). The TERA instruments are distributed at different stations across

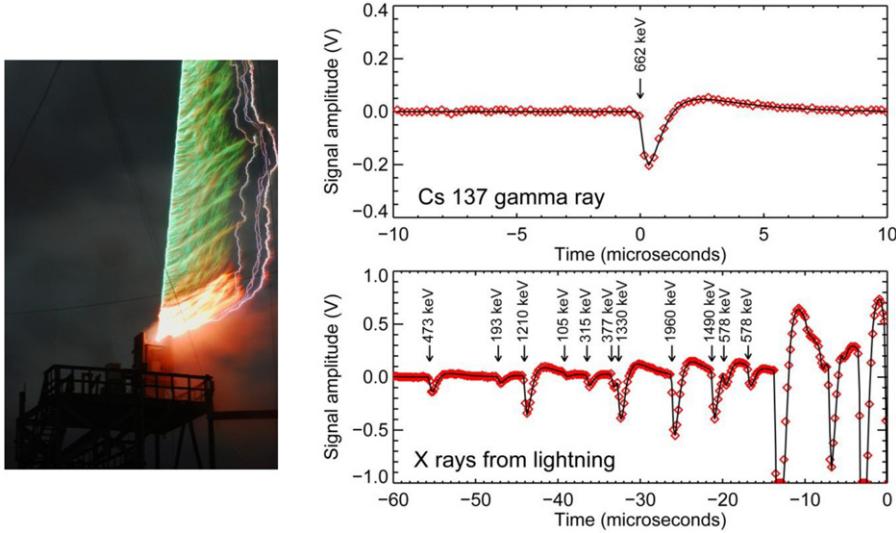


**Fig. 5.5.** Left: Photograph of rocket-triggered lightning at the ICLRT (courtesy Dustin Hill, UF). The illuminated straight triggering wire can be seen on the left. Four wind-blown leader/return stroke sequences are on the right. Top right: waveform from one of the NaI(Tl)/PMT detectors for a single 662 keV gamma-ray from a Cs-137 radioactive source placed temporarily on top of the instrument. The red diamonds show the data as recorded by the acquisition system, and the solid line shows the detector response as calculated from the NaI light decay-time and the RC-times in the front-end electronics. Bottom right: waveform for a time period just prior to a return stroke (at  $t = 0$ ) of triggered lightning. The detector response (solid line) is plotted over the measured data (red diamonds). The arrows indicate the times and deposited energies of the X-rays.

Source: The figure is from Ref. [254].

the  $\sim 1 \text{ km}^2$  ICLRT site. TERA is also part of an experiment called the MSE (Multiple Station Experiment). Besides the X-ray detectors, the MSE/TERA stations are equipped with instrumentation to measure electric fields and their derivatives as well as magnetic fields using flat plate antennas and loop antennas [257].

In a typical configuration, TERA is made up of 24 stations, composed of forty-five  $7.6 \text{ cm} \times 7.6 \text{ cm}$  cylindrical NaI(Tl)/Photomultiplier tube (PMT) detectors and two  $7.6 \text{ cm} \times 7.6 \text{ cm}$  cylindrical LaBr<sub>3</sub>(Ce)/PMT detectors, all contained in aluminum boxes to shield the instruments from moisture and light [185,258]. About half of the detectors were also enclosed in 0.32 cm thick lead attenuators. These lead attenuators absorb X-rays below  $\sim 300$  keV, thereby helping determine the energy spectrum by comparing the signals from the un-attenuated (with 30 keV cut-offs from the Al lids) and the attenuated detectors.

In addition, eight of the stations had detectors made of  $1 \text{ m}^2$  by 2 cm-thick plastic (BC-408, Pilot F) scintillators. The scintillators are shielded inside two (0.32 cm thick) aluminum light tight boxes and viewed by two PMT detectors. These plastic detectors, which were designed to primarily measure cosmic-ray air showers, also have sensitivity to X-ray and gamma-rays, but unlike the inorganic (NaI and LaBr<sub>3</sub>) scintillators they have poor energy resolution.

Saleh et al. [258] used TERA to make detailed measurements of the deposited X-ray energies versus radial distance from three triggered lightning channels. Monte Carlo simulations were compared with the measurements to infer properties of the energetic electrons created by the lightning that generated the X-rays. The X-ray emission was observed to occur during the dart-stepped leader phase of each stroke, just prior to the time of the return stroke. Significant X-rays were observed on all the detectors out to a distance of 500 m from the triggered lightning channel for times up to 200  $\mu\text{s}$  prior to the start of the return stroke. It was found that the energetic electrons that emit the X-rays had a characteristic energy of about 1 MeV for one particular dart-stepped leader event, which was larger than the 250 keV found by Ref. [254], but still much smaller than the 7.3 MeV that occurs during RREAs. The X-ray emission for all three events studied had a radial fall off most consistent with the energetic source electrons, on average, being emitted isotropically from the leader. However, Hill [181] found evidence that individual X-ray pulses often only illuminated a subset of detectors and so the emission may only be isotropic on average. It was also found that the X-ray and energetic electron luminosities of the leader channel increased as the leader approached the ground with a peak luminosity exceeding  $10^{16}$  electrons/s. This luminosity is large enough that the emission of X-rays from lightning is a good candidate for the RREA seed particles of Terrestrial Gamma-ray Flashes (TGFs) inside thunderclouds, possibly unifying the two phenomena [259] (see Section 5.4.8).

Howard et al. [149] discovered that a commonly occurring burst of  $dE/dt$  pulses immediately prior to the return stroke, called “leader burst pulses”, are one of the brightest sources of X-ray from lightning. Furthermore, Hill et al. [169] reported the first observations of X-ray emissions from chaotic dart leaders preceding triggered lightning return strokes. In four events, a relatively continuous and bright flux of X-rays was observed during the final 10–13  $\mu\text{s}$  of the descending leader from altitudes of several hundred meters, determined from  $dE/dt$  time-of-arrival (TOA) measurements.

Schaal et al. [260] analyzed TERA data for 28 leaders from 12 different triggered lightning flashes plus 2 leaders from 2 natural lightning strikes at the ICLRT. It was found that the natural lightning appeared to arise from an extended spatial

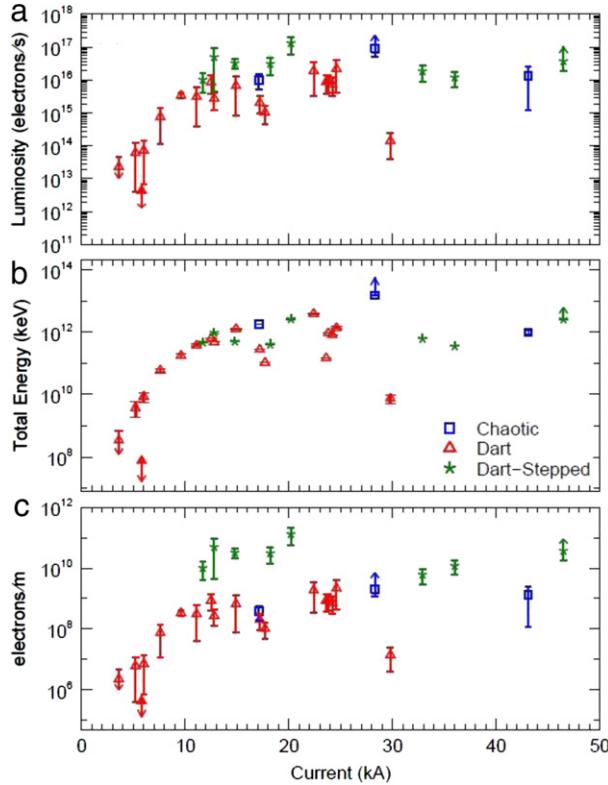


**Fig. 5.6.** (a) The electron luminosity versus the return stroke peak current. (b) The total X-ray energy versus the return stroke peak current. (c) The amount of energetic electrons per meter of downward propagation versus the return stroke peak current.  
Source: Figure from Schaal et al. [260].

source, consistent with several stepped leader branches emitting X-rays. For the triggered lightning it was found that M-components (current pulses occurring during a continuing current interval) do not emit any detectable X-rays. Furthermore, it was shown that properties of the X-ray emission correlated with the current of return stroke, and there appeared to be a threshold current of about 4 kA for there to be detectable X-rays. As the current increased, the intensity of the X-rays increased exponentially until about 10 kA, at which point the X-ray intensity saturated, with a maximum runaway electron luminosity between  $10^{16}$  and  $10^{17}$  electrons/s. This can be seen in Fig. 5.6. Because the X-rays are emitted by the descending leader before the return stroke, it is likely that the X-ray emission is in fact related to the charge density of the leader, perhaps explaining the correlation with the return stroke current.

Howard et al. [174] reported the first TOA measurements of the X-ray source locations (see discussion in Section 4.2). Using a subset of eight of the TERA NaI(Tl)/PMT detectors that were co-located with  $dE/dt$  flat-plate antennas, they located seven individual X-ray source locations and times, three were from a natural lightning flash in 2006 and four were from a triggered lightning flash in 2007. Howard et al. found that the X-rays were emitted within 50 m of the  $dE/dt$  source locations, and in all but one case, the X-ray locations were below the locations of the related  $dE/dt$  pulse. In addition, the X-ray emission times followed the emission times of the  $dE/dt$  source by 0.1 to 1.3  $\mu$ s. This meant that the X-rays were being emitted in coincidence with the electrostatic field change that occurred after fast step pulse. This time period of the electrostatic field change is usually identified as the time of the corona flash, in which many streamers propagate in the steamer zone in front of the new leader tip. The similar relationship of the  $dE/dt$  and X-ray sources for both stepped leader steps for natural lightning and dart-stepped leader steps for triggered lightning, suggests that the underlying physics of the two discharge processes are similar [181].

Using an improved TOA network of eight  $1 \text{ m}^2$  plastic scintillation detectors and two 7.6 cm LaBr<sub>3</sub>/PMT, Hill [181] extended the TOA work of Howard et al. for 7 dart stepped leaders from triggered lightning and 1 stepped leaders from natural lightning. Of these, 2 of the dart-stepped leaders and 1 stepped leader had measurable TOA X-ray locations, with a total of 30 X-ray source locations and times found. For the dart-stepped leaders from triggered lightning, the X-ray pulses could clearly been seen from well above the top of the exploded triggering wire, showing that the triggering wire did not affect the X-ray production other than steering the leader along the channel created by the wire. An example of the natural lightning data from Hill is shown in Figs. 5.7 and 5.8. Fig. 5.7 shows the  $dE/dt$  and X-ray data from a stepped leader from natural lightning that struck the ICLRT in 2011. The numbers indicate the pulses in which the TOA X-rays source reconstructions were possible using the arrival times of the TOA network. The association between the X-ray emissions and

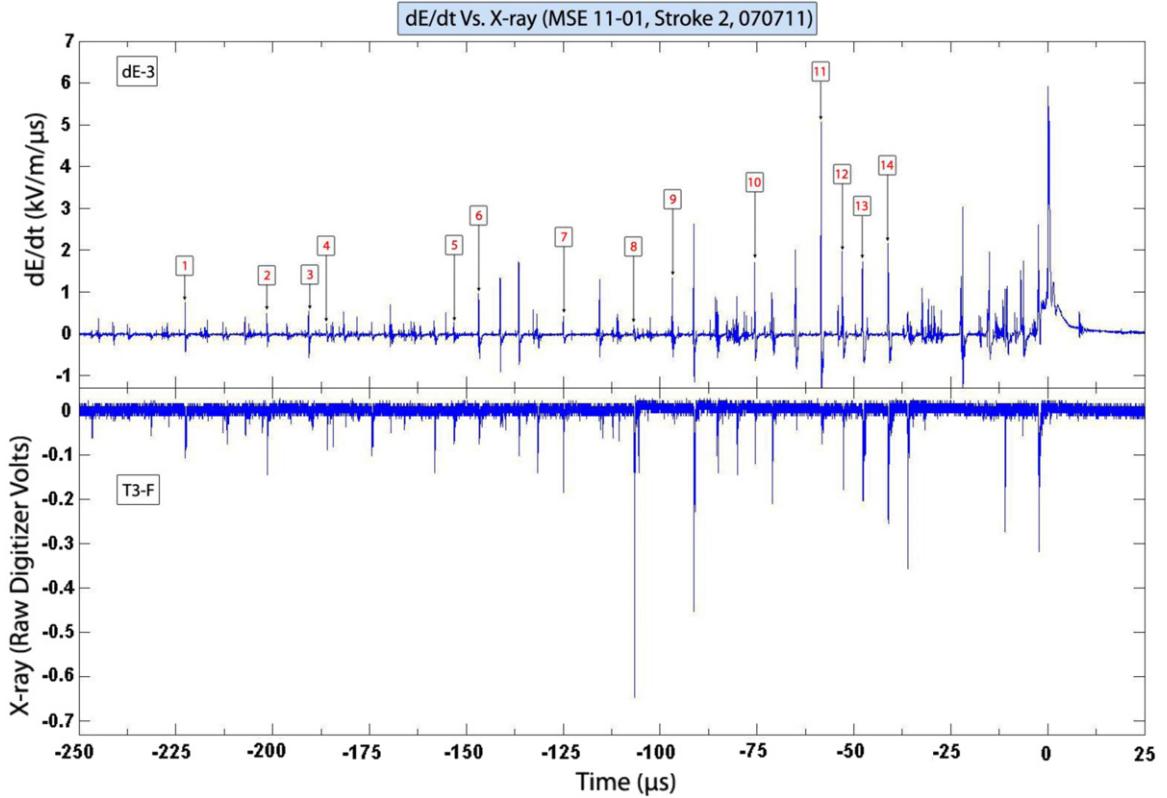


**Fig. 5.7.** In the bottom panel, a 275  $\mu\text{s}$  record of the X-ray emission recorded by the plastic scintillator at the ICLRT during the dart-stepped leader preceding the second stroke of natural flash. The corresponding  $dE/dt$  is shown in the top panel. There  $dE/dt$  pulses associated with the 14 located X-ray sources for this dart-stepped leader are annotated in the top panel with increasing integers.

Source: Figure from Hill [181].

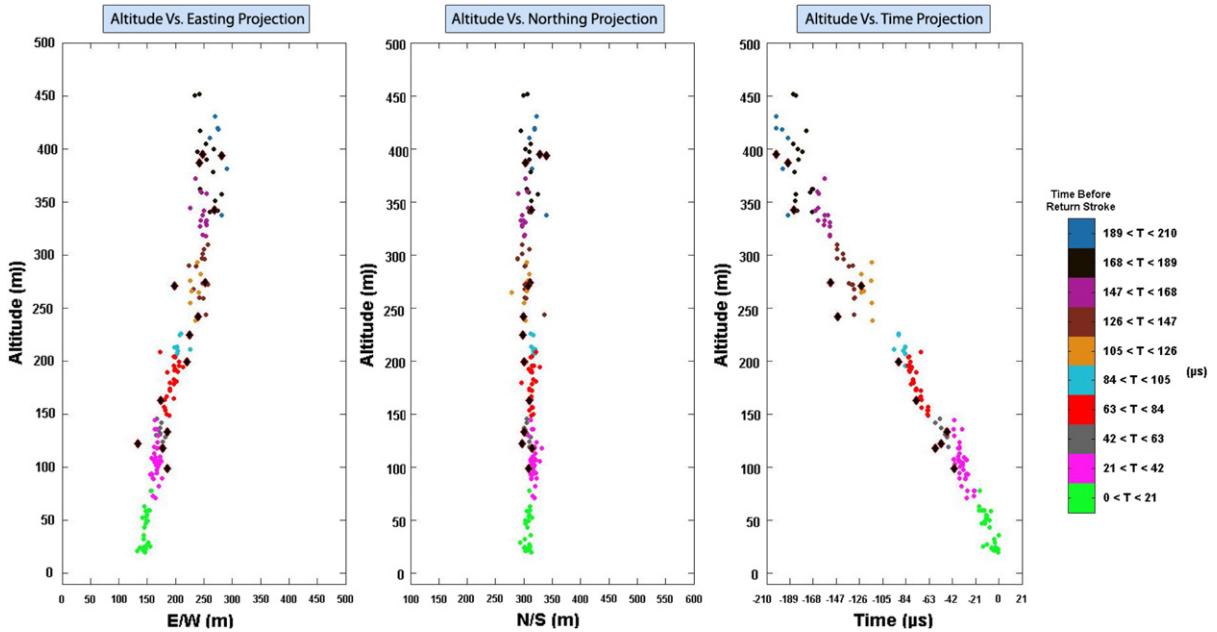
the leader steps ( $dE/dt$  pulses) that was first reported by Ref. [173] can easily be seen in the figure. It can also be seen that not every leader step produces detectable X-rays, a result also reported by Mallick et al. [261].

Fig. 5.8 shows the positions of the  $dE/dt$  sources and X-ray sources (black diamonds) for the stepped leader for the last 500 m above the ground. It was found that all the X-ray source locations generally agreed with the  $dE/dt$  positions to within about 10 m in the horizontal directions, and the X-ray sources were systematically below the  $dE/dt$  sources by roughly 20 m and occurred about 0.1  $\mu\text{s}$  afterwards, detailed data being given in Section 4.2, all in agreement with Howard et al. [174]. This picture is consistent with the X-rays being produced by the corona flash part of the stepping process. However, it should be pointed out that it is not well known exactly which part of the lightning leader step is producing the  $dE/dt$  pulse and so care must be taken when interpreting the relationship between the two measurements. See Section 4.2 for a discussion of TOA measurements of X-ray emission from triggered lightning.

The first high-time-resolution two-dimensional images of the X-ray emissions from triggered lightning were made at the ICLRT in 2010 [262]. The images of two chaotic dart leaders were recorded at a rate of 10 million frames per second using a new pinhole-type camera, located 44 m from the triggered lightning channel. In both events, as the chaotic dart leader approached the ground, the X-ray source was also seen to descend along the previous lightning channel. For the second event, the X-ray source exhibited a downward speed of  $4.5 \times 10^7 \text{ m s}^{-1}$ , in agreement with independent  $dE/dt$  time-of-arrival measurements of the speed of the leader front, demonstrating that the leader front was the source of the X-ray emission. Fig. 5.9 shows a sequence of X-ray images of one rocket triggered lightning leader as it approached the ground, showing that most of the X-ray emission originates from the tip of the descending leader. Because the background rate is very low, virtually all the non-black pixels seen in Fig. 5.9 correspond to X-rays emitted by the lightning leader.

Finally, other groups have also reported observations of X-rays from natural lightning. For example, Yoshida et al. [214] reported the detection of X-rays from a positive lightning leader, although this result has not been verified and no X-ray emissions have been detected so far from upward positive leaders during rocket triggered lightning at the ICLRT (see also discussion in Section 4.3). Chubenko et al. [263] and Antonova et al. [264] have reported observations of X-rays from natural lightning at the Tien Shan High-Altitude Scientific Station of the Physical Institute of the Academy of Sciences [see Ref. [246] for a discussion of this work].

In summary, it has been now firmly established that all types of negative leaders, including dart, dart-stepped, stepped, and chaotic leaders emit X-rays. X-ray emission has been well studied for both natural and rocket-triggered lightning. As



**Fig. 5.8.** Three projection views of the  $dE/dt$  and X-ray source locations for the dart-stepped leader preceding the second stroke of the flash shown in Fig. 5.7. At left, the altitude versus easting projection; at middle, the altitude versus northing projection; and at right, the altitude versus time projection.  $dE/dt$  sources are color-coded according to the key at right in 21  $\mu$ s windows. X-ray sources are plotted as black diamonds independent of emission time. Source: Figure from Hill [181].

found by TOA observations, the X-rays arrive in short sub-microsecond pulses that are closely associated spatially and temporally with leader steps, with the X-ray emission slightly following the  $dE/dt$  pulses generated by the leader step currents. X-ray images also show that the X-ray source propagates with the leader tip and that the X-ray source region is often compact, appearing as a bright spot near the leader tip. The energy spectrum of the X-rays is variable but usually implies runaway electron energies below about 1 MeV, which is inconsistent with RREAs being the dominate production mechanism. The luminosity of the X-ray is sensitive to the amplitude of the return stroke current, with the runaway electron luminosity increasing greatly up to return stroke currents of about 10 kA. Above that current, the runaway electron luminosity plateaus between  $10^{16}$  and  $10^{17}$  electrons/s. Put together, these observations support that bremsstrahlung emissions from runaway electrons produced by thermal runaway augmented with energy gain by Wilson runaway is the dominate mechanism for generating the runaway electrons. For dart-stepped and stepped leaders, the picture that the thermal runaway production is occurring at the negative streamer tips during the corona flash is plausible. For dart and chaotic dart leader, which do not produce clear steps, the picture is less clear, although it is possible that these leaders also step, but the steps are much shorter and hence difficult to discern.

Since it has now been definitively established that both natural and triggered lightning leaders commonly emit hard X-rays and hence produce runaway electrons as they propagate, one may ask whether or not runaway electrons are important to lightning processes. In our opinion there has been an exaggeration of the importance of runaway electrons, and especially RREAs, in lightning processes [120,244,245]. Although X-rays may be a useful tool for studying lightning, based upon more than a decade of detailed measurements of the X-ray emissions from lightning, we conclude that lightning can be mostly viewed as a conventional discharge and runaway electron physics is probably not needed in order to understand lightning propagation and attachment. For example, the current from the runaway electrons are not reasonable for generating the leader channels. In a sense, the runaway electron production can be viewed as an interesting side-effect of leaders and streamers in air. On the other hand, the presence of X-rays tells us that lightning is doing something unexpected. If we stipulate that negative streamer tips are likely to be the source of the runaway electrons, then the X-rays tell us that the electric fields in streamers often reach the critical field,  $E_c$ , ten times larger than the conventional breakdown field,  $E_k$ . It is not obvious that researchers would have known this without the X-ray observations. Furthermore, because the field at the streamer tip is sensitive to the ambient field through which it propagates, the presence of X-rays provides new information about the electric field and charge configuration of the lightning. Understanding streamer physics is important for many types of gas discharges in addition to lightning, and the electron phase space density is central to how streamers work. The X-ray observations show us that a high energy tail sufficient to allow runaway electron production is often present in this electron distribution, and so the runaway electrons can be viewed as an integral part of this larger picture.

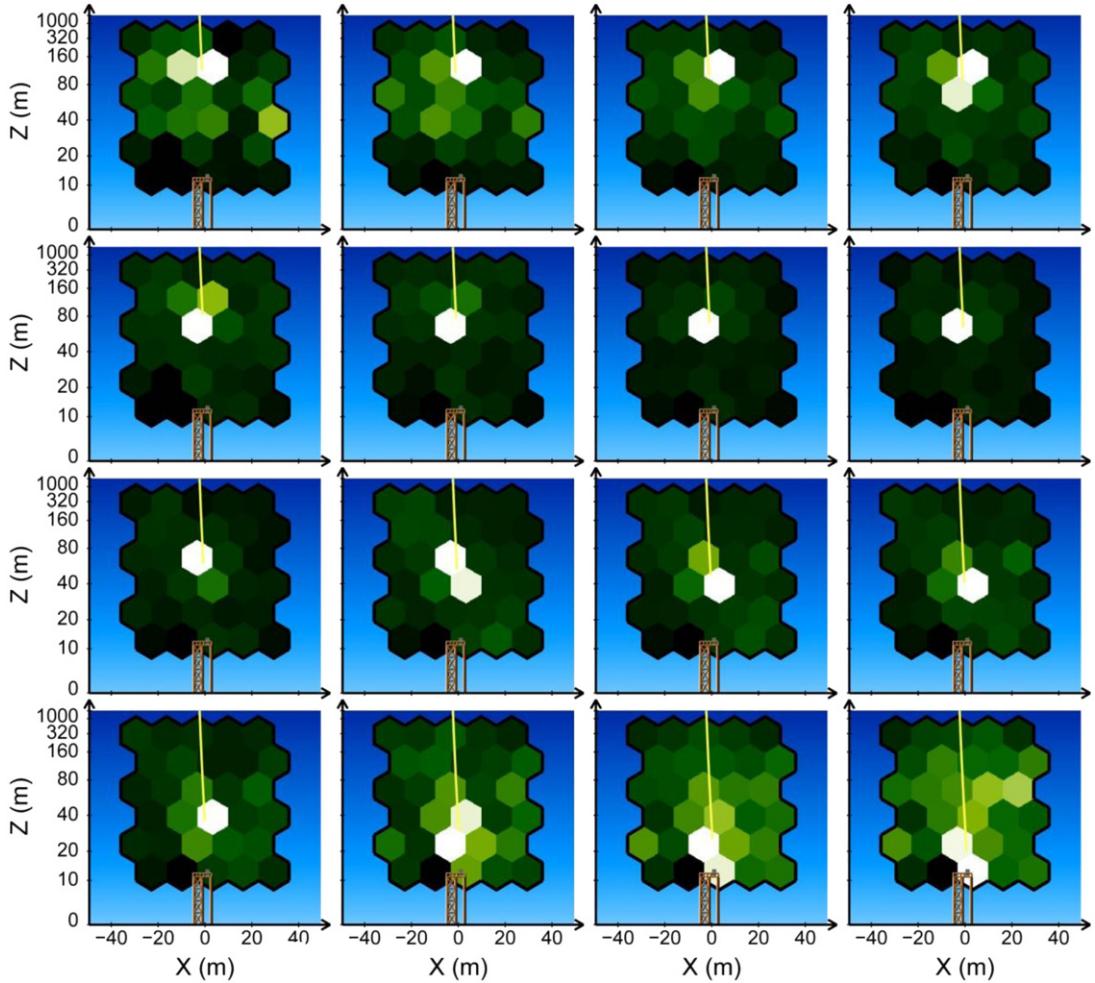


**Fig. 5.9.** Successive 0.1  $\mu$ s images of the X-ray emission from lightning, recorded on August 13, 2010 at the ICLRT. The first image is in the upper left corner and time progresses from left to right. The exposures cover the observation times from  $-1.53 \mu$ s to  $+0.07 \mu$ s relative to the return stroke. This corresponds to the emission times from  $-1.94 \mu$ s to  $-0.087 \mu$ s before the return stroke. The rocket launch tower is illustrated at the bottom along with the approximate location of the lightning channel. The color scale for each image has been adjusted so that the detector with the maximum deposited energy appears as white. This maximum deposited energy is 5.5 MeV in the first image, increases as the lightning approaches the ground, reaching a maximum of 28.2 MeV in the eleventh image, and then decreases to 16.6 MeV in the last image. Note that the deposited energy in each detector corresponds to the detection of multiple X-ray photons.

Source: From Ref. [262].

### 5.3.2. X-ray observations of long laboratory sparks

Insights into the X-ray emissions from lightning may be gained from long laboratory sparks in air. Using a 1.5 MV Marx generator, Dwyer et al. [182] discovered that long laboratory sparks in air at 1 atmosphere pressure emit X-rays similar in to those emitted by lightning. Fig. 5.10 shows an image of the 1.5 m long arc produced during this experiment. Specifically, it was found that both positive and negative polarity sparks, with lengths ranging from about 10 cm up to 2 m generated X-ray pulses in the hundred keV range, usually when either the voltage was near its peak value or the voltage in the gap was in the process of collapsing. While the former X-ray emission has been shown to originate from the spark gap, the later emission appeared to originate from outside the gap, perhaps by discharges induced on other objects in the room [185]. The emission of X-rays from long laboratory sparks has since been confirmed and expanded upon by several groups in different high voltage laboratories [186–189,265–270]. In particular, it has been found that X-ray emission is often linked to negative streamer onset at the cathode [186,271]. For positive sparks, the X-rays have been found to be emitted at the time the positive and negative streamers, emitted from the anode and cathode, respectively, meet in the air gap [184]. This is illustrated in Fig. 5.11, which shows a sequence of images of the streamers in the spark gap along with recorded properties of the discharge. This result may support the mechanism proposed by Cooray et al. [272], who suggested that the X-rays are emitted (via thermal runaway) in the high field region created when positive and negative streamer tips meet.

It has been shown that, similar to lightning leaders, RREAs cannot be responsible for the runaway electron production in laboratory sparks [273]. Theoretical work, using the thermal runaway electron mechanism, includes Gurevich [175],



**Fig. 5.10.** Image of a 1.5 m spark in air generated by a 1.5 MV Marx generator for which it was discovered that long laboratory spark in air produces X-rays similar to lightning [182].

Moss et al. [176], Gurevich et al. [179], Li et al. [274], Chanrion and Neubert [180,275], Colman et al. [276], and Celestin and Pasko [255]. This body of work supports the hypothesis that the strong electric fields produced during lightning and laboratory discharge are capable of generating runaway electrons, which result in the observed X-ray emissions. A review of earlier work involving the X-ray emission in small (<few cm), highly stressed gaps can be found in Babich [228].

### 5.3.3. Gamma-ray glows from thunderclouds

Gamma-ray glows from thunderclouds are defined to be second to minute long X-ray and gamma-ray emissions originating in or near thunderclouds [246]. Such emission appears to be distinct from the much shorter pulsed emissions that occur during Terrestrial Gamma-ray Flashes or from lightning leaders (see Sections 4.2, 5.3.4 and 5.3.1). Other names have been given to this kind of emission, depending upon where it has been measured. For example, Chilingarian et al. [277] refer to this emission as Thunderstorm Ground Enhancements (TGEs), since they were recorded on the ground (at mountain height). In this report, we shall follow Ref. [246] and refer to these emissions as gamma-ray glows, since this name refers to the properties at the thunderstorm source and not the observer.

When discussing ground based measurements, it is important to consider the effects of radon daughter product washout, which can cause a factor of a few enhancements in the background counts rates [227]. This enhancement, which correlates with rainfall, may be distinguished from gamma-ray emissions from RREAs, since unlike RREAs, radon daughter product washout exhibits line emission up to a few MeV and not the continuum spectrum up to tens of MeV as occurs for RREAs. Most successful ground based measurements of gamma-ray glows have been made either on high mountains [227,278–285] or in regions of Japan with thunderclouds with low charge centers [286–289]. For most gamma-ray glow observations, the enhancement of gamma-ray fluxes is on the order of 10% above background. Exceptions include Chilingarian et al. [284], who reported count rates at Aragats that more than doubled when a thundercloud was 100–200 m above the detector. Torii et al. [286] reported measurements made at the Monju nuclear reactor in Japan during a winter thunderstorm with enhancements up to 70 times the local background level. Modeling has shown that the many of the observed spectra are consistent with Bremsstrahlung emission from RREA [282–284,286–288,290–292]. We also note that the thunderstorm electric fields have been observed to either increase or decrease the flux of cosmic-ray secondary muons, depending on the sign of the field relative to the positive and negative muons [281,293,294].

Not surprisingly aircraft and balloon observations of gamma-ray glows, which make measurements inside or near thunderclouds, often record much larger enhancements than those seen on the ground. Parks et al. [232] and McCarthy and Parks [233] performed X-ray observations inside active thunderstorms using a NASA F-106 jet carrying NaI scintillation detectors. It was demonstrated that the X-rays emission, which lasted tens of seconds, extend to greater than 110 keV, and lightning generally terminated, rather than caused, the X-ray glows.

Eack et al. [234–236], flying scintillators and electric field sensors with balloons through and above active thunderstorms, measured hard X-ray glows up to 120 keV. Eack et al. [234] found that the X-ray emission occurred at the altitude (4 km) with the highest electric field and lasted throughout the passage of the balloon through the strong electric field region within the storm. However, the X-ray emission was interrupted and then restored by a pair of lightning flashes. Another balloon sounding found a similar high X-ray flux in an anvil at 14 km [236]. Eack et al. [235] recorded three shorter X-ray pulses, lasting about 1 s each, when the payload was at 15 km altitude, 3 km above the thundercloud.

Most recently, in 2009, the Airborne Detector for Energetic Lightning Emissions (ADELE) was flown on the Gulfstream V jet over and next to active thunderstorm cells in Florida. ADELE included 12.7 cm diameter by 12.7 cm long plastic and NaI scintillators for gamma-ray sensitivity above 10 MeV. ADELE observed one TGF during 37 h aloft [25] and observed 12 separate gamma-ray glows, lasting tens of seconds to more than a minute, during passes over or near the tops of active thunderstorms [295]. It was possible that the durations of the gamma-ray glows were limited by the passage of

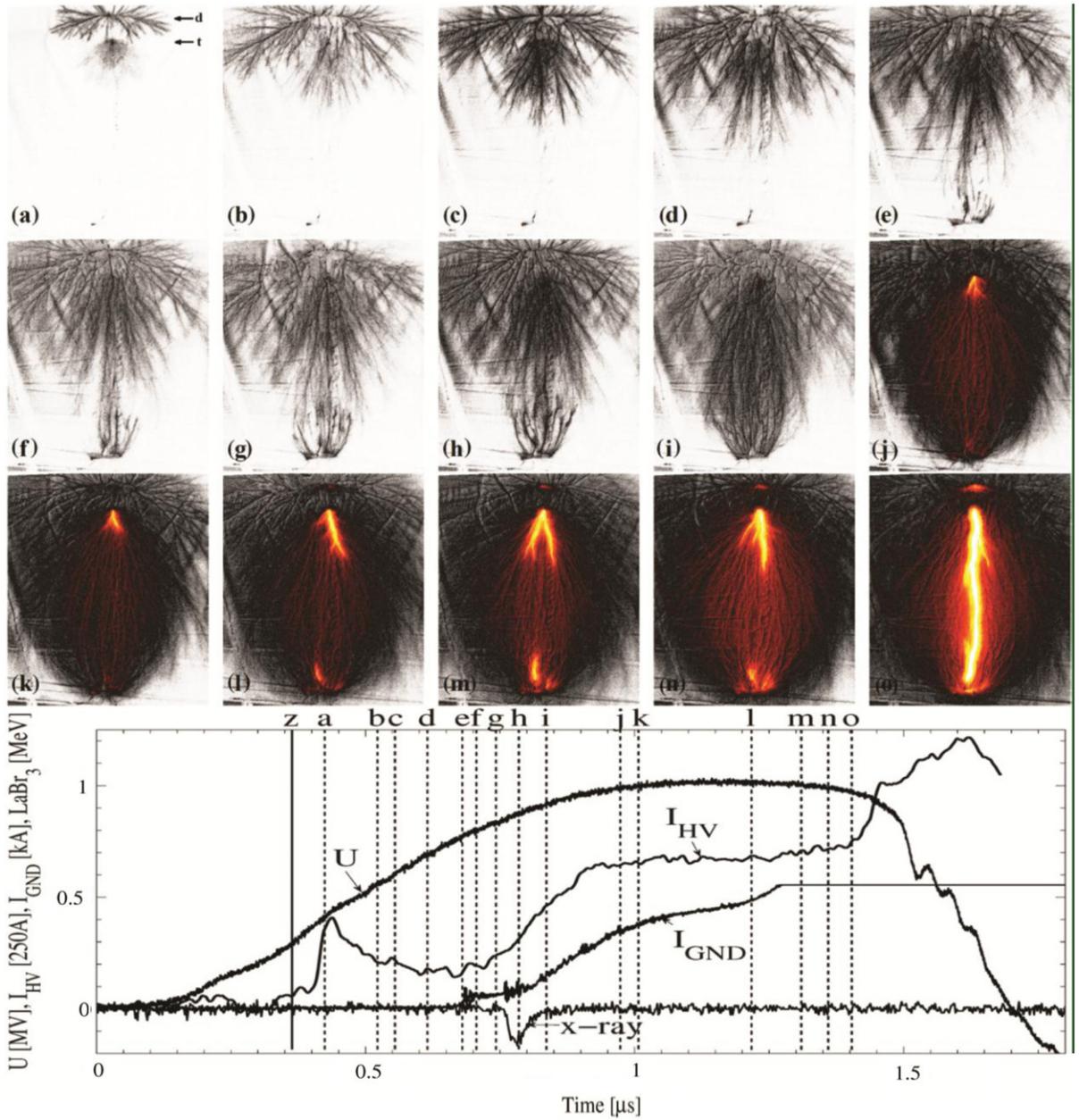


**Fig. 5.11.** A sequence of images showing the development of a 1 m long, 1 MV laboratory discharge in air. Each image is for a separate discharge. However, because the discharges are all very similar, combining the images gives a reasonable representation of how a single discharge progresses. The shutter always opens at  $t = 0.36 \mu\text{s}$  (solid line ( $z$ )), and the exposure time varies from 60 (a) to 1000 ns (o). The deposited X-ray energy, voltage, and cathode and anode currents are shown in the bottom plot (data from discharge (l)). The X-rays are detected when the downward positive streamers and upward negative counter-streamers meet as shown in (e)–(h).

Source: Figure from Ref. [184].

the aircraft near the thunderstorms and so the gamma-ray glows might actually have lasted longer than observed. It is reasonable that gamma-ray glows are the product of RREA emissions when the thunderstorms are in a highly charged state between lightning flashes. Because the discharge currents that result from the ionization by the runaway electrons might be substantial, it may be possible that the gamma-ray glows occur during a steady state when the thunderstorm charging is temporarily balanced by the runaway electron emission. For very active charging, relativistic feedback may become important, since very large runaway electron fluxes could be produced that would be able to counteract the growth in the electric field. Further research is needed in order to understand how gamma-ray glows are produced and what conditions are present inside the storms. For a more detailed discussion on gamma-ray glows we refer the reader to Ref. [246].

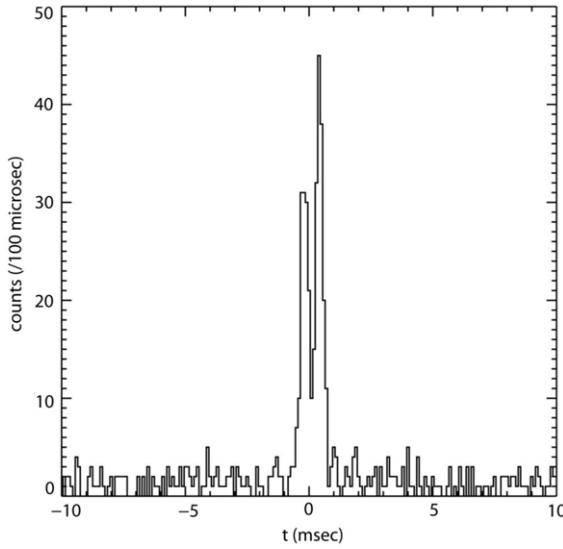


**Fig. 5.12.** Gamma-ray count rate for CGRO/BATSE TGF 106.

Source: Data courtesy Jerry Fishman.

### 5.3.4. Terrestrial gamma-ray flashes (TGFs)

Terrestrial Gamma-ray Flashes (TGFs) were discovered by Fishman et al. [229] using data from the BATSE instrument onboard the Compton Gamma Ray Observatory (CGRO), put in low-Earth orbit by the Space Shuttle in 1991. TGFs were originally assumed to originate from high-altitude discharges (i.e., Sprites), but it is now known that they originate from thundercloud altitudes, usually in association with IC lightning. The TGFs were first recorded by BATSE's 8 Large Area Detectors (LAD), each made of sheets of 1.27 cm thick NaI with 2025 cm<sup>2</sup> of effective area [296], and were identified as bright ms long pulses of gamma-rays originating from the Earth's atmosphere. TGFs were notably shorter and had harder energy spectra than cosmic gamma bursts, seen from other parts of the universe. Fig. 5.12 shows the count-rate versus time for the first TGF recorded by BATSE. As can be seen, the TGF had two peaks, which is common for BATSE TGFs. BATSE also recorded many single pulsed TGFs and several multi-pulsed TGF, some with as many as 6 separate gamma-ray pulses (see Fig. 5.27). Later space instruments have recorded single, double and even triple pulsed TGFs, but so far not TGFs with the large number of pulses seen by BATSE. When interpreting spacecraft data, it is important to understand whether or not the data acquisition requires an onboard trigger. For BATSE, TGFs were only recorded when the number of counts in a 64 ms window exceeded background by some level of significance. Because TGFs are usually less than 1 ms long, and there is a maximum count rate that BATSE can measure, most TGFs would not have triggered BATSE's data acquisition and thus were not seen. Instead, BATSE was severely biased towards longer TGFs, including multi-pulsed one, which over a 64 ms window will satisfy the trigger threshold. As a result, multi-pulsed TGFs are likely to be oversampled in the BATSE TGF data. Smaller detectors, on other spacecraft, may not be able to efficiently find the multi-pulsed TGFs since each pulse is usually not as bright as single pulsed TGFs.

Since the occurrence of BATSE TGFs followed the geographical pattern of thunderstorms on the Earth, it was immediately and correctly interpreted that TGF are associated with thunderstorms. Sprites, high altitude discharges associated with lightning, had been discovered a few years before [297]. Because gamma-rays are rapidly attenuated by the Earth's atmosphere, and since Sprites can extend up to about 80 km in altitude, the association of TGFs with thunderstorms was (incorrectly) interpreted as being an association with Sprites. Indeed, much theoretical work was devoted to explaining both TGFs and Sprites as byproducts of high altitude runaway electron beams [120].

The basic idea behind these models is the conductivity of the upper atmosphere above thunderclouds is relatively high and so as thunderstorms charge, the electric fields produced by these changes are expelled from the atmosphere above the thunderstorms by the accumulation of a screening charge layer (usually negative) on top of the cloud. When a large lightning discharge occurs, it can neutralize most of the charge within the cloud, but not the screening charge layer. This upper charge layer suddenly finds itself screening charges that no longer exists within the cloud, which results in an electric field above the storm that falls off as a dipole field, roughly as  $1/z^3$  with height,  $z$  (see Section 7 and Fig. 7.3). In contrast, the density of air decreases exponentially with height,  $n \approx \exp(-z/8.5 \text{ km})$ , and so both the runaway electron threshold field,  $E_{th} = 2.84 \times 10^5 \text{ V/m} \times n_{air}$  and the conventional breakdown field  $E_k = 3 \times 10^6 \text{ V/m} \times n_{air}$ , also decrease exponentially with height. Because the dipole field from the screening layer falls off with height more slowly than both  $E_{th}$  and  $E_k$ , for a large enough lightning discharge (e.g., with charge moment changes of several hundred C km), there will be altitudes at which  $E > E_{th}$  and  $E > E_k$ . The former could occur almost immediately above the thundercloud, and the latter usually occurs somewhere near 70 km altitude. High altitude runaway breakdown models of TGFs and Sprites assumed that both were

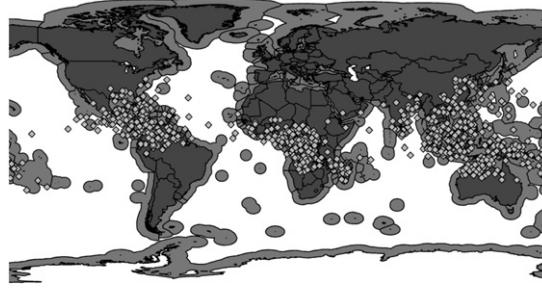


**Fig. 5.13.** Locations of 805 RHESSI TGFs on the planet (diamonds). Coastal regions are shown in gray.  
Source: Figure from Splitt et al. [299].

the manifestation of an intense upward beam of runaway electron generated after the lightning flash for altitudes with fields above the runaway avalanche threshold (note we use the name runaway breakdown here, since that was the term used at the time). In contrast, conventional discharge models of Sprites assumed that Sprites were streamer type discharges initiated in the high fields for which  $E > E_k$ .

Improved temporal and spatial resolution images (and movies) of Sprites, eventually lead to the consensus that Sprites are the result of conventional streamer type discharges [231] (see Section 7). Runaway breakdown models suffered from the problem that above about 40 km runaway electron beams follow the Earth's geomagnetic field, a behavior not seen in Sprites. Nevertheless, despite these difficulties, high altitude runaway electron models continued to be developed for many years and were the generally accepted as correct until about 2005.

Meanwhile, in 2003, while studying the X-ray emissions from rocket-triggered lightning at the ICLRT, a ground level gamma-ray flash was observed that had a similar energy spectrum and duration as satellite-observed TGFs [23]. This event was interpreted in that paper as originating from the overhead thundercloud and caused by charge motion from the triggered lightning. It was also then suggested that TGFs may share similar thundercloud origins.

The Reuven Ramaty High Energy Solar Spectroscopic Imager (RHESSI), a NASA Small Explorer spacecraft designed to study X-rays and gamma rays from solar flares, was launched on 5 February 2002. RHESSI's germanium detectors and orbit (inclination 38° and altitude 600 km) made it ideal for studying TGFs [298]. RHESSI also telemetered its photon data, so that ground searches of TGFs could be performed, greatly increasing the detection efficiency of TGFs over BATSE. Indeed, RHESSI recorded TGFs at an order of magnitude higher rate than BATSE. Fig. 5.13 shows the geographical occurrence of 805 RHESSI TGFs [299]. The predominance of TGFs at low geographic latitudes and in regions with large amounts of lightning such as south central Africa are apparent. TGFs are also noticeably absent from regions where Sprites are common such as the great plains of the United States.

Cummer et al. [300] measured 30 kHz and lower frequency radio emissions during 26 RHESSI TGFs and found that 13 of them occurred within several milliseconds of detectable positive polarity (those that transfer positive charge downward or negative charge upward) lightning processes. They also showed that the TGF-associated charge moment changes were 50–500 times too small to drive the RREA process at high altitudes, as had been assumed by most theoretical work up to that point [also see [301]].

Combining Monte Carlo simulations of RREAs with simulations of gamma-ray emission and propagation through the atmosphere, Dwyer and Smith [302] compared the average RHESSI TGF spectrum with model results for several source altitudes. They found that the RHESSI TGF spectrum was inconsistent with a source altitude above about 21 km and was consistent with spectra from 21 km down to 15 km, the lowest considered. This can be seen in Fig. 5.14.

As a result, around 2005, a paradigm shift occurred: TGFs are not caused by high altitude discharges and are not associated with Sprites. Instead, TGFs are produced either inside or just above thunderclouds. Further work confirmed and solidified this picture. In addition, many papers have used RHESSI TGF data to infer properties of the TGFs, including TGF beaming directions, geographical distributions, and the meteorology of thunderclouds associated with TGFs [303–309]. In particular, radio observations of lightning associated with TGFs found that most TGFs are associated with the early stage of positive intra-cloud (+IC: negative charge moving upward) lightning [310–312].

A consequence of a lower source altitude is that the luminosity of runaway electrons and gamma-rays at the source must be much larger than originally supposed due to the additional atmospheric attenuation of the gamma-rays. Model fits find that, on average, there are about  $10^{17}$  runaway electron for a 15 km source altitude [302,304]—an impressive number of high-energy electrons. Indeed, it has been shown that an aircraft directly struck by the runaway electron beam that makes a TGF would result in passengers inside the aircraft receiving a rather large radiation dose [259]. It is not clear how often, if ever, this actually occurs, but on average every commercial aircraft is struck by lightning once per year, and so aircraft often find themselves in thunderstorm conditions with strong electric fields, perhaps conducive to runaway electron production.

One problem with RHESSI is that its clock has a timing uncertainty of a few milliseconds, making it difficult to make detailed comparison of the TGFs with radio sferics. The Gamma-ray burst monitor (GBM) onboard the Fermi Spacecraft, which was launched in 2008, has also been recording a large number of TGFs [313]. Furthermore, GBM measures TGFs with

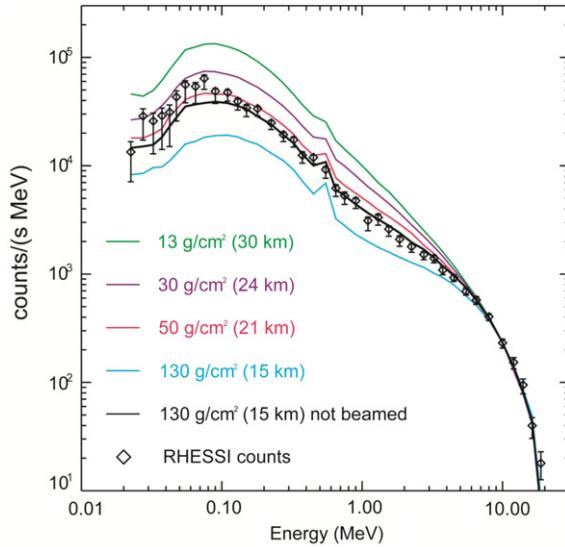


**Fig. 5.14.** Relativistic runaway electron avalanche (RREA) spectra at different altitudes compared to the RHESSI spectrum of 289 summed TGFs. The atmospheric depths from 13 to 130 g/cm<sup>2</sup> correspond to 30, 24, 21, and 15 km. Good agreement with the model spectra provide support that RREAs are involved in TGFs.

Source: Figure from Ref. [302].

microsecond scale absolute timing accuracy, and so it is making important measurements for the relationship between TGF gamma-rays and radio emissions (see Section 5.3.5).

A reanalysis of BATSE TGF data also found that BATSE suffered substantial dead-time due to the high count rates of the TGFs, and so TGFs are actually much brighter at the spacecraft than originally thought [314]. This dead-time produced instrumental effects that explained several previous results. For example, the combination of Compton scattering in the atmosphere and instrumental dead-time tends to artificially lengthen the duration of the measured TGF and causes a softening of the spectrum with time. It also contributed to erroneous high inferred source altitudes [315]. Using Fermi/GBM data, Fishman et al. [316] studied the widths of TGFs and reported the ( $T_{50}$ ) widths to range from  $\sim 50 \mu\text{s}$  up to about  $\sim 700 \mu\text{s}$ , with  $100 \mu\text{s}$  being the median pulse duration. Note that this is considerably shorter than the  $\sim 1 \text{ ms}$  duration originally reported by BATSE, the difference presumably caused by the large dead-time that BATSE experienced during TGFs.

Finally, AGILE (Astro rivelatore Gamma a Immagini LEggero), an Italian astrophysics mission, has been recording TGFs [317]. From AGILE data, Marisaldi et al. [318] found the geographical and diurnal distributions and the spectrum of TGFs are consistent with the RHESSI measurements. Because the MCAL on AGILE has a higher energy range than previous instruments used to study TGFs, individual photons up to 40 MeV were detected [also see [319]] Later, Tavani et al. [320] reported that the average energy spectrum measured by the AGILE spacecraft had a power-law tail that extended to 100 MeV, which is not consistent with the RREA mechanism. Given the success of RREAs at explaining most features of TGFs, further work is needed to establish if this high-energy tail is indeed real and what consequences it has on TGF theories [321].

### 5.3.5. Radio observations of TGFs

When TGFs were discovered it was recognized that their locations follow a similar geographical pattern as thunderstorms on the Earth. As a result, it was natural to assume that there would be some association of TGFs with lightning. One of the best ways to investigate this association is with the radio observations of thunderclouds associated with the TGF.

We distinguish two kinds of results related to the investigation of radio emissions associated with TGFs: The first kind involves the investigation, using radio observations, of the lightning environment near the time of the TGF, and, the second is the direct association of specific radio signatures from the TGF. The former was discussed in Section 5.3.4. Specifically, it has been established, primarily using RHESSI TGF data, that TGFs usually occur during the early stage of upward positive intracloud (IC) lightning, supporting the hypothesis that TGF originate from inside thunderclouds.

We next consider the radio signatures directly related to the TGF source, or at least interpreted as being directly related. Inan et al. [322] discovered that individual radio atmospherics (“sferics”), the signature of a lightning flash, were associated with TGFs. Specifically, they found that for two BATSE TGFs, from very low frequency (VLF) radio measurements, that lightning was occurring in storms beneath the satellite at the times of TGF detections. For one event, they found strong VLF emission occurred within 1.5 ms of the TGF, which was interpreted as CG lightning associated with the TGF.

Using RHESSI TGFs, Inan et al. [323] found that most events were associated in time with detectable sferics to within the several millisecond absolute timing uncertainty of RHESSI. These sferics showed that the radio emission resulted from relatively large peak currents compared with other lightning from the same storms, but also had relatively modest charge

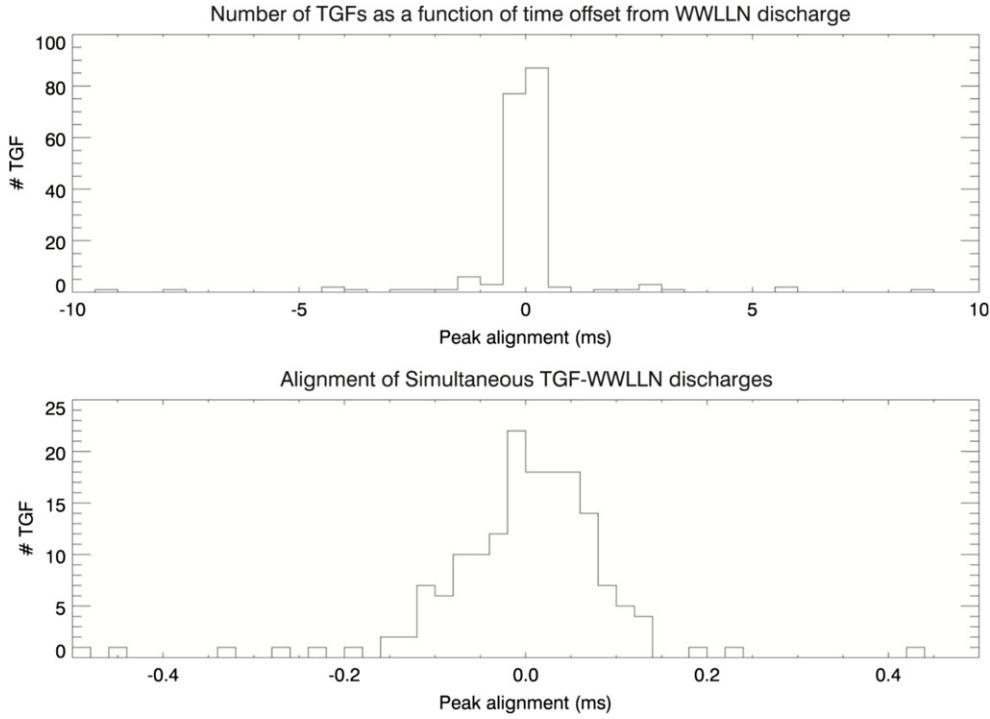


**Fig. 5.15.** Temporal alignment of Fermi/GBM TGFs and measured WWLLN discharge times.  
Source: Figure from Connaughton et al. [333].

moment changes, in agreement with Ref. [300]. Further close temporal associations between sferics and BATSE TGFs was reported by Cohen et al. [324]. Cohen et al. [325] used multi-station VLF measurements to geolocate the sferic source locations associated with 36 RHESSI TGFs and found that a majority matched the source of the RHESSI TGF to within the uncertainties associated with the RHESSI observations. In other words, for a majority of events, the radio emissions appeared to originate from the same location and time as the TGF. These results were supported by Lu et al. [326], who found that most (96%) of the 56 RHESSI TGFs studied occurred within several milliseconds of detectable VLF sferics.

At the time, all of the above observations were interpreted as a close association between the TGF production and lightning, the assumption being that normal lightning currents were generating the measured sferics. These results, along with the radio observations showing that TGFs are associated with the early stage of +IC lightning (see Section 5.3.4), appeared to constrain the source mechanism to ones that had a direct association between the runaway electron production and the lightning leader activity. In particular, it appeared to strongly favor the thermal runaway electron mechanism from lightning leaders, similar to the X-ray emissions from lightning seen near the ground.

This picture was strengthened by work by Connaughton et al. [327], who compared lightning location measurements made by the world wide lightning location network (WWLLN) [328,329] and 50 TGFs recorded by GBM onboard the Fermi spacecraft. Unlike RHESSI, which has an absolute timing uncertainty of a few ms, Fermi/GBM can determine the time of TGFs with microsecond-scale accuracy. They found that 15 of the 50 TGFs were associated with WWLLN lightning detections. When the propagation times of the gamma-rays and radio waves were included, it was found that of these 15 events, 13 had lightning times within a 40  $\mu$ s window of the TGF peak times at the source (Fig. 5.15).

Cummer et al. [330] made continuous (not triggered) 1–400 kHz radio measurements of 2 Fermi/GBM TGFs. The two TGFs were geolocated to within 2 km by National Lightning Detection Network (NLDN) [331] and both were found to be about 500 km for the Duke LF sensor located in Melbourne, FL. The geolocations allowed a timing comparison with approximately 15  $\mu$ s absolute uncertainty in each case. For both TGFs, a sequence of fast processes (a few tens of  $\mu$ s duration) were recorded, similar to previous observations [311,312,326]. However, these fast processes, which may be connected to lightning leader stepping, did not appear to be directly related to the TGF, since they did not exhibit a consistent time relationship to the TGF. On the other hand, for both TGFs, the LF signal from a much slower process (100–200  $\mu$ s duration) was found to closely match the gamma-ray profile of the TGF as measured by Fermi/GBM, with the radio source and gamma-ray source lining up to within about 10  $\mu$ s, thus, suggesting that the radio signature of the TGF-generating process itself was being recorded. This can be seen in Fig. 5.16, which shows the Fermi/GBM data and the LF signals.

The observations by Cummer et al. [330], led Dwyer [332] to investigate the electric currents generated by TGFs. In that work, it was found that TGFs produce current pulses with current moments of several tens of kA-km and the durations of these current pulses should put significant radio energy into the VLF and LF bands. Dwyer went on to predict that, although

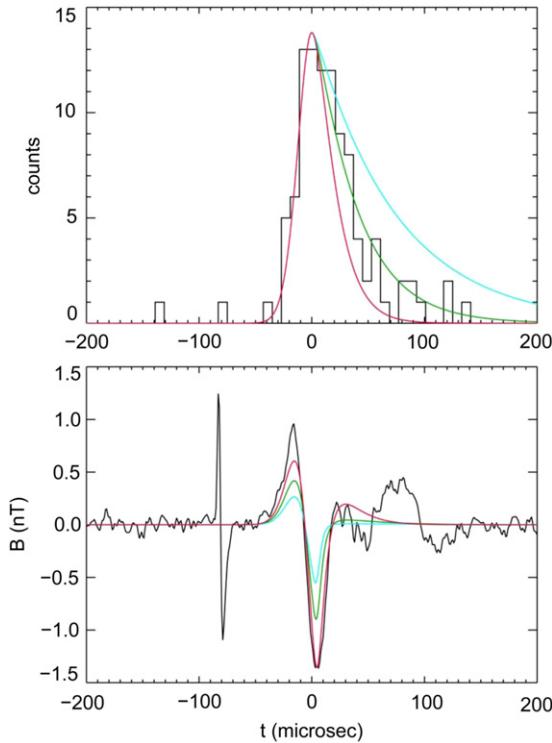


**Fig. 5.16.** *Top panel.* Fermi counts versus time for the August 3, 2010 TGF (black) as presented in Cummer et al. [326]. The smooth curves show different model fits to the gamma-ray data. Because of Compton scattering the source function may be most similar to the red curve. *Bottom panel.* The magnetic field measured by the Duke sensor in Melbourne, FL (black) for the same event [330]. The smooth curves show the predicted RF emissions based upon the sources shown in the top panel. The models include the effects of propagation and the antenna response.  
Source: Figure from Ref. [355].

IC lightning leaders may be present at the time of the TGF, the previous measurements of “lightning” sferics associated with the TGFs were not actually measuring currents from normal lightning processes. Instead they were directly recording the radio emission from the TGF itself, i.e., from the runaway electrons and associated currents produced by the low-energy electrons and ions (see Section 5.4.6). In addition, it was found that the TGF time-intensity profiles and hence the electric currents could naturally be explained by the relativistic feedback discharge mechanism. As a result, the close association of the sferics with the TGFs does not necessarily mean that lightning processes (e.g., thermal runaway electron production) are responsible for the TGFs.

Recently, Connaughton et al. [333] found that the rate of association between Fermi/GBM TGFs and VLF discharges detected by WWLLN depended strongly on the duration of the TGF, with the shortest TGFs having a match with associated WWLLN events over 50% of the time, and the longest TGFs having a match rate of less than 10%. This relationship can be seen in Fig. 5.17. WWLLN also measured some non-simultaneous (within 200  $\mu$ s) sferics, which could be interpreted as normal lightning processes occurring inside the thundercloud. However, the simultaneous events, which also exhibited the dependence on the TGF duration, were among the strongest measured by WWLLN. Connaughton et al. interpreted their results as showing the WWLLN radio sferics directly associated with TGFs were being produced by the runaway electrons (and accompanying low-energy electrons) supporting the hypothesis that TGFs are the source of the radio emissions.

It is still likely that many TGFs occur during the early stage of +IC lightning when positive leaders are crossing the gap between the main negative and positive charge regions. However, these new theoretical and observational results suggest that TGFs are then produced by very large discharges directly caused by the runaway electrons and their ionization. In addition to making the gamma-rays that are seen from space in the form of TGFs, these discharges may well make some of the largest electric current pulses in our atmosphere, rivaling lightning. It now appears that these TGF generating runaway electron pulses are an alternative way that thunderclouds can discharge themselves, since these discharges can happen faster than lightning. It is possible that previous radio observations of thunderclouds, independent of TGF observations, may also have been detecting TGFs instead of lightning and so may have been misinterpreted.

### 5.3.6. Terrestrial electron beams (TEBs)

When TGFs were thought to originate from high altitude runaway electrons, with discharges extending up to 80 km, it was natural to assume that many of the runaway electrons would subsequently escape to space where they could be detected. However, when it was later shown that TGFs are actually produced deep within the atmosphere, <20 km altitude,

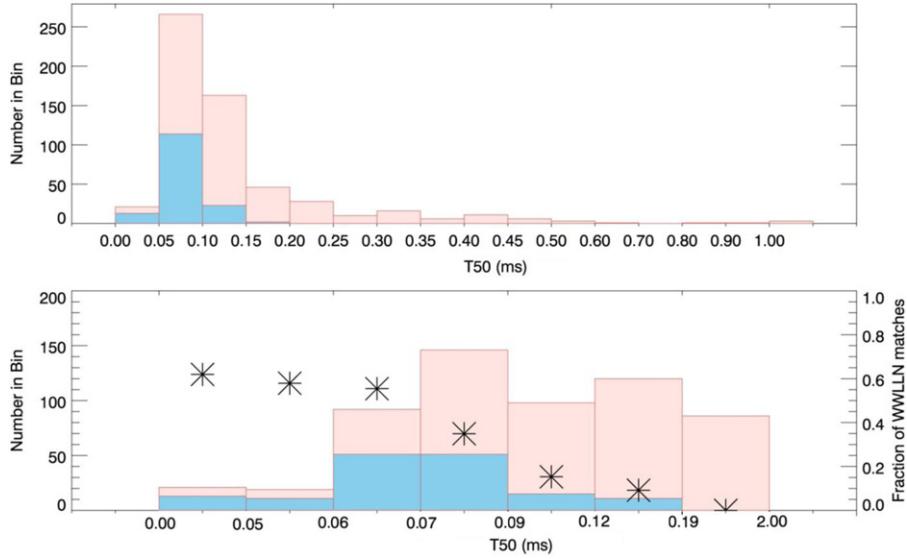


**Fig. 5.17.** Top panel: Histogram of 594 Fermi/GBM duration of TGFs (salmon) with the subset (blue) having a simultaneous match with WWLLN. Bottom panel: Same data rebinned so that at least 10 TGFs (blue) are in each time bin. The asterisks show the fraction of TGFs having a WWLLN match. As can be seen, the shortest TGFs have the highest WWLLN match rate. (For interpretation of the references to colour in this figure legend, the reader is referred to the web version of this article.)  
Source: Connaughton et al. [333].

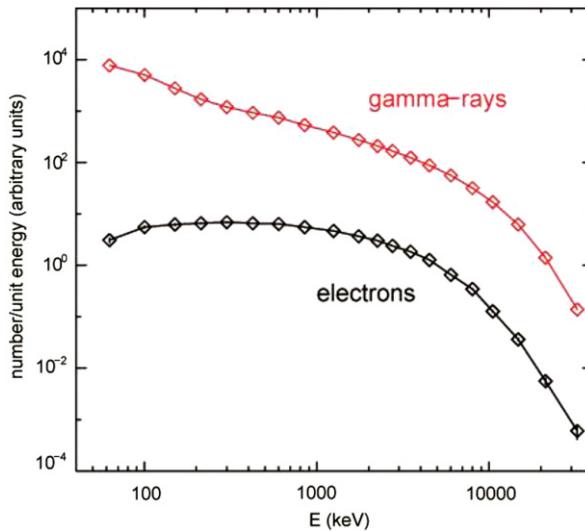


**Fig. 5.18.** Terrestrial gamma-ray flash (TGF) spectrum and terrestrial electron beam (TEB) spectrum. The electron (and positron) beam escapes the atmosphere and propagates into the inner magnetosphere where it can be detected by spacecraft thousands of km away.  
Source: Figure from Ref. [334].

it was found that it was impossible for the runaway electrons to escape to space, since they are rapidly absorbed by the atmosphere once they leave the strong electric field region of the thundercloud.

In 2004, RHESSI detected a bright event over the Sahara Desert that appeared to be an unusually long TGF (30 ms) with two widely spaced peaks. It was found from weather data that no thunderstorms were near the spacecraft at the time, but thunderstorms were present in south central Africa at the location of the geomagnetic foot-point that connected to the spacecraft. This led Dwyer et al. [334] to develop a new electron beam mechanism. In their model, the energetic electrons in space were not runaway electrons that escaped the atmosphere. Instead they are secondary electrons created primarily via Compton scattering and pair production of the gamma-rays in a TGF. At roughly 40 km altitude there is still enough air for the gamma-rays to readily interact, but not enough air to stop all of the energetic secondary electrons and positrons from escaping to space. Once created, the energetic secondary particles propagate along the Earth's magnetic field line, thus

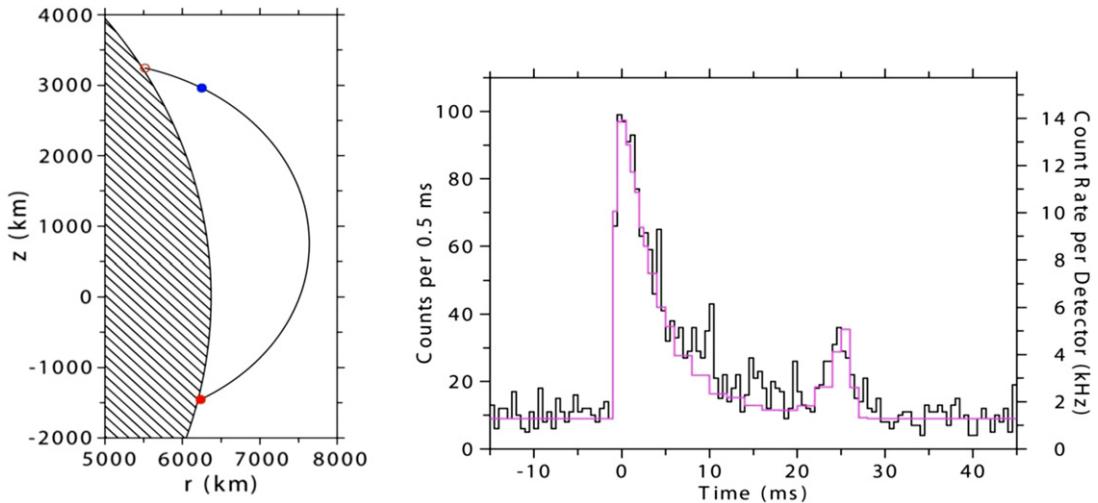


**Fig. 5.19.** Left: the geomagnetic field geometry for a terrestrial electron beam (TEB) event observed by the Fermi spacecraft. The shaded region represents the Earth and the solid line is the magnetic field line. The red dot shows the location of the TGF that created the TEB. The blue dot shows the location of Fermi. Right: Time intensity profile of the observed TEB (black). The red curve is the model prediction, including the magnetically mirrored component seen as the second pulse. (For interpretation of the references to colour in this figure legend, the reader is referred to the web version of this article.)  
Source: Figure courtesy Briggs et al. [335].

forming a beam of particles. This picture can be seen in Fig. 5.20, which shows an artist's impression of the TGF (pink) and TEB (yellow are electrons and green are positrons).

Monte Carlo simulations showed that the electron/positron beam had about 2% as many particles as the number of gamma-ray photons in the TGF [334]. Fig. 5.18 shows the energy spectra of the TGF and the TEB. As can be seen, the TEB has a hard spectrum, extending to several MeV, making TEBs some of the more energetic particles in the magnetosphere. Although the flux of TEBs is much smaller than that of TGFs at the top of the atmosphere, as the gamma-rays in the TGF continue to propagate to spacecraft altitudes (e.g., 500 km), their intensity falls off as  $1/r^2$ . In contrast, the charged electrons and positrons remain confined to the geomagnetic field line and so have roughly the same intensity as when they left the atmosphere. As a result, simulations show that at low-earth orbit altitudes, TEBs can have higher fluences than the TGFs by about a factor of 2.

For spacecraft in low earth orbit, such as CGRO, RHESSI and Fermi, TEBs may be observed as the beam propagates upwards away from the atmosphere. They also may be seen near the distant conjugate point, as a descending beam. Because the particles have a range of pitch angles, there will be a characteristic velocity dispersion in the arrival times, especially for observations near the distant foot-point. Furthermore, if the geomagnetic field is stronger below the spacecraft, some of the particles in the descending beam will "magnetic mirror" off of the stronger field, producing a second beam that strikes the spacecraft from the opposite direction. These results could naturally explain the RHESSI Sahara event with its two widely spaced peaks.

Reanalysis of the BATSE TGFs showed that 17% out of 36 BATSE "TGFs" available for study were likely to be high energy electron beams striking the CGRO spacecraft [334]. One such event was over the Sahara desert (BATSE TGF 2221). By modeling particle gyromotion along the Earth's magnetic field, the time profile of the event, including a second reflection peak 23 ms after the onset of the event, were well fit. Although the TEBs only strike the spacecraft about 0.01 times as often as TGFs, because the TEBs are often longer and brighter than normal TGFs, the BATSE triggering algorithm preferentially triggered on TEBs and so the set of events was heavily biased in favor of TEBs.

This scenario was confirmed by Briggs et al. [335], who reported several TEBs using the GBM instrument onboard the Fermi spacecraft. One such event was a measurement made when the spacecraft was over the Sahara Desert, similar to the TEB events recorded by BATSE and RHESSI. The Fermi TEB is shown in Fig. 5.19, which shows the magnetic field geometry line, which connected the spacecraft to a thunderstorm in south central Africa. In the figure, the count rate of the event, along with a model fit, are also shown. The second peak due to the reflection of the particles in the stronger magnetic field below the spacecraft can easily be seen and is well fit by the model. In addition, this and several other events showed remarkably large positron annihilation lines, indicating that a substantial fraction of the electrons in the beam were actually positrons. This is expected since pair production by TGF gamma-rays in the atmosphere plays a major role in the creation of the TEBs.

An additional study of the properties of TEBs appears in Refs. [336,337]. Finally, Cohen et al. [338] identified the radio signature from near the magnetic foot-point that was associated with a Fermi TEB. The charge moment change of this detected discharge was too small to produce high altitude runaway electron avalanches, providing further support for the model by Ref. [334].

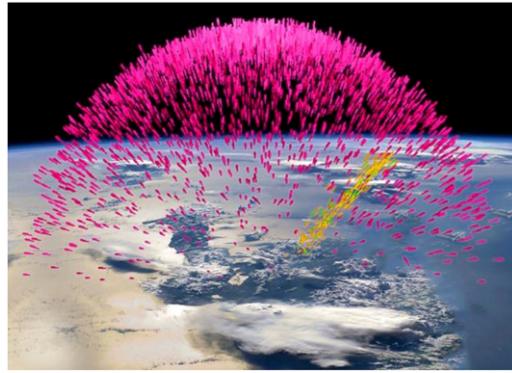


**Fig. 5.20.** Artist's conception of a TGF (pink) and TEB (electrons are yellow and positrons are green).  
Source: Image courtesy NASA.

### 5.3.7. Neutrons

Neutrons enhancements in association with thunderstorms and lightning have been measured by many research groups [284,339–346]. The most likely mechanism for producing neutrons is photo-production of neutrons when gamma-rays (e.g., from gamma-ray glows or TGFs) collide with air nuclei [342,347–352]. On the other hand, nuclear reactions have been shown to have negligibly small neutron yields, even for unrealistically high fields of 3 MV/m in lightning [347]. Because neutrons are likely to be a byproduct of gamma-rays from RREAs, they may provide additional information about how energetic particles are accelerated by thunderclouds. At this time, however, despite some previous inferences that neutrons might be associated with lightning, based upon the measured lightning X-ray spectra, it seems unlikely that lightning is a significant source of neutrons. We refer the reader to the review by Ref. [246] for more information.

## 5.4. Theory and modeling

### 5.4.1. RREA propagation

Let us now consider the relativistic runaway electron propagation. The number of runaway electrons in a RREA,  $N_{re}$ , passing through position  $z$  changes according to

$$\frac{dN_{re}}{dz} = \frac{N_{re}}{\lambda}, \quad (5.1)$$

where the e-folding length,  $\lambda$ , describes the avalanche length when  $\lambda > 0$  and the attenuation length when  $\lambda < 0$ . Eq. (5.1) is analogous to Eq. (2.6) for low-energy electrons. The avalanche and attenuation length are both approximately described by the empirical expression

$$\lambda = \frac{7.3 \times 10^6 \text{ V}}{(E - 2.76 \times 10^5 \text{ V/m} \times n_{air})}, \quad (5.2)$$

determined from fits to Monte Carlo simulation results [77,248,332]. Eq. (5.2) is valid as long as  $E$  is not too close to the threshold field,  $E_{th} = 2.84 \times 10^5 \text{ V/m} \times n_{air}$ . This simple empirical description of the avalanche length agrees well with other work [78,178,245,249,251,353,354]; see [246] for a detailed comparison.

If we consider an electric field pointed vertically downward,  $\vec{E} = -E(z) \hat{z}$ , then for one energetic seed electron injected at position  $z = 0$ , Eq. (5.1) may be integrated to give the number of runaway electrons at position  $z$  along the avalanche [242]

$$N_{re}(z) = \exp\left(\int_0^z \frac{dz}{\lambda(z)}\right), \quad (5.3)$$

where  $\lambda(z)$  is found from Eq. (5.2) using the specified  $E(z)$ . For a uniform electric field (and constant air density), Eq. (5.3) gives

$$N_{re}(z) = \exp\left(\frac{z}{\lambda}\right), \quad (5.4)$$

a simple exponential growth, similar to Eq. (2.7) for low-energy electrons.

Realistically, an electric field cannot remain constant forever, and there must be positions below and above the avalanche region where the electric field is smaller than the runaway electron avalanche threshold,  $E_{th}$ . In particular, beyond the end of the avalanche region, the number of runaway electron will steadily decrease according to Eqs. (5.2)–(5.4) with  $\lambda(z) < 0$ .

It is important to understand the behavior of the runaway electron avalanche near the end of the avalanche region because this is the location where most of the runaway electrons are produced and where most of the accompanying emissions (e.g., X-ray and radio) will be generated. To illustrate the behavior of the avalanche in this region consider an electric field strength that linearly decreases with height near the end of the avalanche region, that is  $E = E_{th} - \Gamma(z - L)$ , where  $\Gamma = |\frac{dE}{dz}|$  is evaluated at  $z = L$ , the end of the avalanche region [355]. Substituting this electric field into Eq. (5.2) and then doing the integration in Eq. (5.3) gives

$$N_{re}(z) = N_{max} \exp\left(\frac{-(z - L)^2}{2\kappa^2}\right), \quad (5.5)$$

where  $\kappa = \left(\frac{7.3 \times 10^6 \text{ V}}{\Gamma}\right)^{1/2}$  and  $N_{max} = \exp\left(\frac{z_0^2}{2\kappa^2}\right)$  is the maximum number of runaway electrons, at  $z = L$ . In other words, the number of runaway electrons near the end of the avalanche region, where the avalanche is largest, is approximately a Gaussian function of position.

The discussion above considers the total number of runaway electrons passing through a horizontal plane at position  $z$ , independent of the time. If instead we are interested in both where the runaway electrons are and when they are there, then we may use the diffusion-convection-type transport equation, similar to Eq. (2.1), to describe the density of runaway electrons (electrons per unit volume) as a function of position and time [120,356]:

$$\frac{\partial n_{re}}{\partial t} + \vec{v} \cdot (\vec{v} n_{re}) - \vec{\nabla} \cdot (\hat{D} \cdot \vec{\nabla} n_{re}) - \frac{n_{re}}{\tau_{re}} = S_{re}, \quad (5.6)$$

where  $\vec{v}$  is the average velocity of the runaway electrons. In Eq. (5.6),  $S_{re}$  is the source function describing the injection rate of seed energetic electrons, i.e., the number of seed particles per second per cubic meter. The second term on the left side describes the flow of the particles due to their motion in the electric field. The average speed of the avalanche was found in Ref. [248]. The speed changes slightly with electric field strength but is always fairly close to the value  $0.89c$ , which is in good agreement with the speed found in Ref. [357]. As a result,  $\vec{v} = -0.89c\vec{E}/E$ , where  $\vec{E}$  is the electric field vector. The third term on the left side describes diffusion of the runaway electrons, and the last term on the left describes avalanche multiplication, with  $\tau_{re}$  being the avalanche e-folding time. The avalanche e-folding time is  $\tau_{re} \approx \lambda/v$ . We note that Eq. (5.1) is obtained from Eq. (5.6) in the same manner as Eq. (2.6) was obtained from Eq. (2.1) with the use of the convective flux.

The spatial diffusion of the runaway electrons, which occurs in both the longitudinal (along the avalanche) and lateral directions is caused predominately by elastic scattering of the runaway electrons with atomic nuclei. The runaway electron diffusion coefficients have been calculated by Monte Carlo simulations in Refs. [35,357]. In particular, it has been shown that lateral diffusion causes considerable spreading of the avalanche, as can be seen in Fig. 5.3. Such spreading of the avalanche is problematic for the hypothesis that RREAs somehow result in the initiation of lightning via the creation of a hot channel by the runaway electrons [239,243,356,358,359]. In other words, it is difficult to understand how a large scale, diffuse runaway discharge could result in a hot ( $>5000$  K) channel, roughly a centimeter in diameter [243], as occurs with lightning.

As an illustration of the solution of Eq. (5.6), consider the injection of one seed particle at position and time,  $x_o, y_o, z_o$ , and  $t_o$ , i.e., a Dirac delta-function source in Eq. (5.6). Furthermore, let us consider a uniform field as was used for Eq. (5.4). The density of runaway electron in the avalanche is then

$$n_{re}(x, y, z, t; x_o, y_o, z_o, t_o) = \frac{1}{(4\pi(t - t_o))^{3/2} D_x^{1/2} D_y^{1/2} D_z^{1/2}} \exp\left(\frac{(t - t_o)}{\tau_{re}} - \frac{(x - x_o)^2}{4D_x(t - t_o)} - \frac{(y - y_o)^2}{4D_y(t - t_o)} - \frac{(v(t - t_o) - (z - z_o))^2}{4D_z(t - t_o)}\right) S(t - t_o), \quad (5.7)$$

where the step function,  $S$ , insures that only times,  $t > t_o$ , after the injection of the seed particles, are considered [35,360]. The step function is defined to be 0 for  $t < t_o$  and 1 otherwise.

Eq. (5.7) is the number density of runaway electrons. The convective flux,  $\vec{F}_{re}$ , (number per second per  $\text{m}^2$ ) of runaway electrons at any position is found by multiplying the density by the velocity of the runaway electron avalanche,  $\vec{v}$ . The electrical current density ( $\text{Amps}/\text{m}^2$ ) produced by the runaway electron avalanche is found by multiplying this flux by the charge of each electron,  $-e$ . As a result,

$$\vec{J}_{re}(x, y, z, t) = -e \vec{F}_{re}(x, y, z, t) = -e \vec{v} n_{re}(x, y, z, t). \quad (5.8)$$

Note that Eq. (5.8) is the electric current density from just the energetic runaway electrons and does not include electric currents produced by the low-energy electrons and ions that are created from ionization. Such currents will be discussed below.

The longitudinal diffusion coefficient  $D_z$  is generally small and so the spreading of the avalanche in the  $z$ -direction due to diffusion can often be ignored. Furthermore, we are often not interested in the lateral profile of the avalanche (e.g., a spreading of a few hundred meters will not affect gamma-ray observations seen 500 km away in space). As a result, for

some applications we may ignore the diffusion and set  $D_x = D_y = D_z = 0$ . In this approximation, and for simplicity setting  $x_0 = y_0 = z_0 = t_0 = 0$ , for  $t > 0$ , Eqs. (5.7) and (5.8) become

$$\vec{F}_{re} = \vec{v} \exp\left(\frac{z}{\lambda}\right) \delta(v t - z) \delta(x) \delta(y) \hat{z}. \quad (5.9)$$

If instead of a uniform electric field, we consider the linearly decreasing field above, the flux and electric current of the runaway electrons per seed runaway electron is given by [355,360]

$$\begin{aligned} \vec{F}_{re}(x, y, z, t) &= \vec{v} N_{max} \exp\left(\frac{-z^2}{2\kappa^2}\right) \delta(v t - z) \delta(x) \delta(y) \hat{z} \\ \vec{j}_{re} &= -e \vec{F}_{re}. \end{aligned} \quad (5.10)$$

For convenience, here, we have chosen our coordinate system such that the end of the avalanche occurs at  $x = y = z = 0$  and at  $t = 0$ . In summary, Eq. (5.10) is the approximate runaway electron flux and current for an avalanche resulting from the injection of one seed electron at the start of the avalanche region.

#### 5.4.2. Detailed runaway electron physics

Above a few hundred eV, the energy losses per unit length plotted in Fig. 5.1 can be described by the well-known Bethe equation [237]

$$\begin{aligned} f(\varepsilon) \equiv -\frac{d\varepsilon}{dx} &= \frac{2\pi N_a Z r_e^2 mc^2}{\beta^2} \\ &\times \left[ \ln\left(\frac{m^2 c^4 (\gamma^2 - 1)(\gamma - 1)}{I^2}\right) - \left(1 + \frac{2}{\gamma} - \frac{1}{\gamma^2}\right) \ln 2 + \frac{1}{\gamma^2} + \frac{(\gamma - 1)^2}{8\gamma^2} - \delta_{den}(\gamma) \right], \end{aligned} \quad (5.11)$$

where here  $N_a$  is the number density of the gas atoms ( $N_a = 5.39 \times 10^{25} \text{ m}^{-3}$  for air at sea level) and  $Z$  is the average atomic number of the gas atoms ( $Z = 7.26$  for air);  $r_e = 2.818 \times 10^{-15} \text{ m}$  is the classical electron radius;  $mc^2 = 511 \text{ keV}$  is the rest energy of an electron;  $\beta = v/c$ , which is a function of the kinetic energy of the electron,  $\varepsilon$ , and  $\gamma = 1/\sqrt{1 - \beta^2}$  is the Lorentz factor of the energetic electron;  $I$  is the effective ionization potential (e.g.  $I = 85.7 \text{ eV}$  for air) and  $\delta_{den}$  is a small correction due to the density effect. Eq. (5.11) is accurate above a few hundred eV and agrees with the curve in Fig. 5.1 for these energies.

As the energetic electrons move through air, some of the secondary electrons are produced with substantial energies. The production of secondary electrons is described by Møller scattering (electron-electron elastic scattering), given by the cross-section [240]

$$\frac{d\sigma_{Moller}}{d\varepsilon} = \frac{2\pi r_e^2 mc^2}{\beta'^2} \left[ \frac{(\gamma' - 1)^2 m^2 c^4}{\varepsilon^2 (mc^2(\gamma' - 1) - \varepsilon)^2} - \frac{(2\gamma'^2 + 2\gamma' - 1)}{\varepsilon (mc^2(\gamma' - 1) - \varepsilon)\gamma'^2} + \frac{1}{m^2 c^4 \gamma'^2} \right], \quad (5.12)$$

where  $\varepsilon$  is the kinetic energy of the scattered atomic electron and  $\beta'$  and  $\gamma'$  are the speed divided by  $c$  and Lorentz factor of the incident electron.

For energetic runaway electrons, the most important mechanism for generating energetic radiation is bremsstrahlung interactions with air atoms. Bremsstrahlung X-rays are mostly produced in the same direction as the incident energetic electron, with an angular width of about  $1/\gamma$ , the Lorentz factor of the incident electron [250]. For a mono-energetic beam of electrons, the energy spectrum of the bremsstrahlung X-rays is approximately  $1/\varepsilon_{ph}$  up to the energy of the incident electrons, where  $\varepsilon_{ph}$  is the photon energy. By increasing the energy and path length of the energetic electrons, the runaway electron mechanism also increases the amount of X-ray emission. Indeed, because runaway electrons may reach many tens of MeV in energy, there will be significant X-ray emission in the MeV range. We shall refer to such high-energy photons as gamma-rays, even though they are technically X-rays, since they are produced by energetic electrons and not nuclear processes. Once emitted, X-rays and gamma-rays will usually travel much farther than the energetic electrons that produced them. As a result, if runaway electrons are produced inside a thundercloud, for instance, it might be possible to measure enhancements in the X-rays and gamma-rays outside the storm. Indeed, such enhancements have been measured (see Section 5.3.3).

When photons are emitted via bremsstrahlung, the photon propagation involves four principle interactions: photoelectric absorption, Compton Scattering, pair-production and Rayleigh scattering [240].

For positrons, which are mostly created via pair production, the ionization energy loss equation (Eq. (5.11)) is modified slightly and the Møller scatter cross-section is replaced with the Bhabha scattering cross-section [240]. The energetic positron may run away exactly as the electrons do, but they will move in the opposite direction as the runaway electrons due to their opposite charge. Thus, an avalanche of runaway electrons moving, say, in the upward direction will occasionally result in runaway positrons moving in the downward direction. In practice, the propagation of the runaway positrons looks very similar to that of electrons, with the exception that avalanches of runaway positions are not produced like the

avalanches of electrons, and positron will eventually annihilate with atomic electrons. The runaway positrons are very energetic, reaching many tens of MeV and so the annihilation cross-section for the positrons is small [240], allowing the positrons to travel on the order of a kilometer at sea-level before annihilating [332]. This large propagation distance will often allow runaway positrons to reach the start of the avalanche region. When the positrons eventually do annihilate, two annihilation 511 keV gamma-rays are most often created. The positions also generate energetic secondary electrons (via Bhabha scattering) that spawn new runaway electron avalanches; this is the positron feedback process (see Section 5.2.4).

Elastic scattering of the runaway electrons (and runaway positrons) with atoms with atomic number  $Z$  may be calculated using the shielded-Coulomb potential

$$V(r) = \frac{Ze}{4\pi \varepsilon_0 r} \exp(-r/a), \quad (5.13)$$

where in this equation  $r$  is the spherical radius. This potential is an approximate expression for the potential derived from the Thomas–Fermi model of the atom when  $a = 183.8 \lambda Z^{-1/3}$  [361], where  $\lambda$  is the Compton wavelength. As already discussed, elastic scattering of the runaway electrons with the individual atomic electrons (Møller scattering) has already been considered above.

As derived in Ref. [242], the elastic scattering differential cross-section per solid angle is given by

$$\frac{d\sigma}{d\Omega} = \frac{1}{4} \left( \frac{Zr_e}{\beta^2 \gamma} \right)^2 \cdot \frac{(1 - \beta^2 \sin^2(\theta/2))}{\left( \sin^2(\theta/2) + \frac{\hbar^2}{4p^2 a^2} \right)^2}, \quad (5.14)$$

where all the symbols have their usual meaning. Accurately modeling this elastic scattering is very important, because it results in the electrons being scattered off the electric field lines, affecting the rate of energy gain, and it causes spatial diffusion of the runaway electrons as the avalanche propagates. The latter reduces the maximum conductivity produced by a runaway electron avalanche, affecting models of lightning initiation [35].

#### 5.4.3. Runaway electron energy spectrum

An important characteristic of runaway electron avalanches is their steady-state energy spectrum. After runaway electron avalanches move more than a few avalanche lengths, the energy spectrum approaches a steady state configuration. Although the number of runaway electrons grows exponentially, as the avalanche continues, the overall shape of the energy spectrum does not change. The reason is that as individual electrons gain energy, they always create new lower-energy electrons via Møller scattering, resulting in an exponential energy spectrum.

The steady state runaway electron energy distribution (spectrum) in an avalanche that grows exponentially with time may be described by the approximate equation [239]

$$\frac{f_{re}}{\tau_{re}} = -\frac{d}{d\varepsilon} (b(\varepsilon) f_{re}) + N_a Z \int_\varepsilon^\infty \frac{d\sigma_{Møller}}{d\varepsilon'} v' f_{re} d\varepsilon', \quad (5.15)$$

where  $b(\varepsilon) = d\varepsilon/dt$  is the average rate of change of the energy of the electrons;  $f(\varepsilon, t) = \frac{dN}{d\varepsilon}$  is the number of electrons per unit energy [362]; and  $\tau_{re}$  is the runaway electron avalanche time. The first term on the right side describes the rate of change in the number of electrons due to energy loss or gain. The second term on the right describes the creation of new electrons due to Møller scattering.

In Eq. (5.15), for  $\varepsilon \gg \varepsilon_{th}$ , the electrons run away in a direction opposite the applied electric field vector, resulting in a field-aligned beam. Therefore,  $b(\varepsilon) \approx v(eE - f_d)$ , where  $f_d$  is the average energy loss per unit length along the field line, which is approximately constant for relativistic particles. For relativistic electrons, Monte Carlo simulations find that  $f_d \approx 2.76 \times 10^5 \text{ eV/m} \times n_{air}$ , and  $v = 0.89c$ . If we consider energies that are high enough above  $\varepsilon_{th}$  so that most of the new electrons are injected below that energy, then Eq. (5.15) becomes

$$\frac{f_{re}}{\lambda} = -(eE - F_d) \frac{df_{re}}{d\varepsilon}, \quad (5.16)$$

where  $\lambda = v\tau_{re}$ . The solution to this equation is

$$f_{re} = f_o \exp \left( \frac{-\varepsilon}{(eE - F_d)\lambda} \right). \quad (5.17)$$

The avalanche length in Eq. (5.2) may be equivalently written

$$\lambda = \frac{7.3 \times 10^6 \text{ eV}}{(eE - 2.76 \times 10^5 \text{ eV/m} \times n_{air})}. \quad (5.18)$$

Substituting Eq. (5.18) into Eq. (5.17), we find the energy spectrum of runaway electrons to be

$$f_{re} = f_o \exp \left( \frac{-\varepsilon}{7.3 \text{ MeV}} \right), \quad (5.19)$$

independent of the electric field or the density of air.

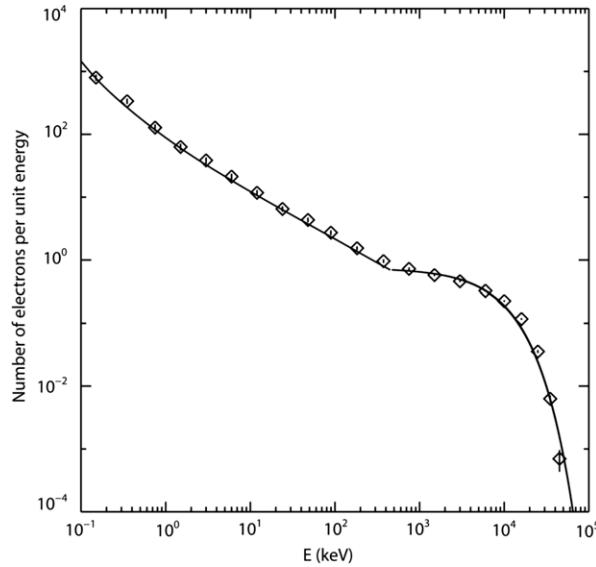


**Fig. 5.21.** Number of electrons per unit energy calculated by the full Monte Carlo simulations (diamonds), along with the simple model prediction of Eq. (5.15) (solid line). For the runaway electrons above a few hundred keV, the spectrum is exponential as given by Eq. (5.19).  
Source: Figure from Ref. [239].

**Fig. 5.21** shows the differential energy spectrum ( $f = dN/d\varepsilon$ ) for all electrons at time  $t = 5\tau$ , i.e., 5 avalanche e-folding times, along with the solutions to the simple calculation presented above for the runaway electrons. The energy spectrum of runaway electrons has been independently calculated by several groups [178,354] and found to be in good agreement [246]. A similar calculation may be done for the intermediate energy electrons (see [239,354]), the results of which are shown as the solid curve in the figure. The intermediate energy electrons, are the secondary electrons created by the runaway electrons that are below  $\varepsilon_{th}$ . These electrons will eventually lose all of their energy and attach to air atoms. The spectrum in **Fig. 5.21** is for the electric field  $E = 430 \text{ kV/m} \times n_{air}$ , which corresponds to and  $\tau_{re} = 1.8 \times 10^{-7} \text{ s}/n_{air}$ . The avalanche length  $\lambda = 48 \text{ m}/n_{air}$  for this field.

In contrast, the energy spectrum from the runaway electrons for the thermal runaway electron mechanism (such as from lightning leaders) does not possess any specific shape and may extend to much smaller energies (e.g., a few 100 keV) than the RREAs, depending upon the nature of the electric field. As a result, the observation of an X-ray (gamma-ray) spectrum that only extends into the 100 keV range, which is typical for lightning and laboratory sparks (see Sections 5.3.1 and 5.3.2), is a strong indication that thermal runaway plus Wilson runaway and not RREA is most important in the production of the runaway electrons.

Finally, a useful approximation for the bremsstrahlung X-ray spectrum produced by RREA is

$$f_{ph} \propto \frac{1}{\varepsilon_{ph}} \exp\left(\frac{-\varepsilon_{ph}}{7.3 \text{ MeV}}\right), \quad (5.20)$$

where  $\varepsilon_{ph}$  is the photon energy in MeV [246].

As can be seen in **Fig. 5.1**, given a high enough electric field strength with a large enough potential difference, runaway electron could reach extremely large energies, i.e.,  $>1 \text{ GeV}$ . In our atmosphere, the largest (large scale) electric fields occur inside thunderclouds. In situ electric fields measurements inside thunderclouds sometimes record fields well above  $E_{th}$  (see Section 3.3), so the production of runaway electrons by thundercloud fields is certain. The potential differences achieved by thunderclouds is not well measured, but estimates range from about 100 MV to about 1 GV [363], so very high maximum electron energies might possibly occur.

#### 5.4.4. Relativistic feedback calculations

Because the discharge currents generated by relativistic feedback grow exponentially on very short time scales, the electric field will be discharged very quickly, regardless of the charging currents. As a result, relativistic feedback describes a new internal state of the system, a self-sustained discharge that does not rely upon externally supplied particles. Once relativistic feedback starts and becomes self-sustaining, the electric field will almost always discharge, and so this process may be considered a novel form of electrical breakdown [242]. Indeed, large electric fields can be highly unstable due to relativistic feedback [77]. Relativistic feedback is important both because it may naturally explain very large fluxes of energetic electrons and gamma-rays, and because it also severely limits the electric field regimes in which alternative

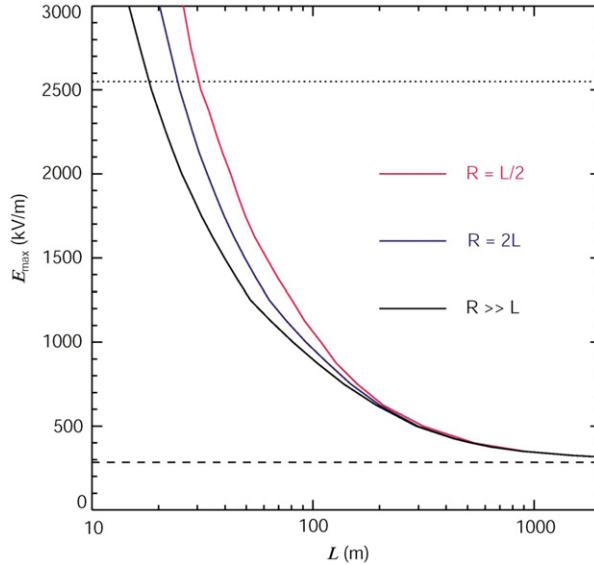


**Fig. 5.22.** The maximum static electric field strength achievable in air versus the length of the electric field region for the cases where the lateral radius of the high field region is  $R = L/2$ ,  $R = 2L$  and  $R \gg L$ . These lines satisfy the condition that the feedback factor  $\gamma = 1$ . The dotted line shows the conventional breakdown threshold and the dashed line shows the runaway avalanche threshold. For electric field configurations on the upper right side of the figure, the field is highly unstable and will quickly discharge until it drops below the feedback threshold, moving to the lower left side of the figure.

Source: Figure reprinted with permission from Ref. [242].

© 2007, AIP Publishing LLC.

mechanisms (i.e., runaway breakdown) may operate [247]. Fig. 5.22 illustrates the limit placed on the electric field in air by relativistic feedback for three different electric field configurations. On the right side of the curves, the field is highly unstable and will discharge rapidly.

The flux of runaway electrons from relativistic feedback was calculated and compared with results of the standard RREA model in Refs. [77,242,247,332] (also see Ref. [364]). Let  $F_o$  be the flux of external energetic seed particles that run away, e.g., the flux due to atmospheric cosmic-ray particles and radioactive decays. Depending upon the altitude and the geographic location,  $F_o$  is in the range  $100\text{--}10,000 \text{ m}^{-2} \text{ s}^{-1}$  [365]. If no feedback were occurring, then according to the RREA model, the flux of runaway electrons at the end of the avalanche region would be, according to Eq. (5.1),

$$F_{RREA} = F_o \exp(\xi), \quad \text{where } \xi = \int_0^L \frac{dz}{\lambda}. \quad (5.21)$$

In Eq. (5.21),  $\xi$  is the number of e-folding lengths and is equal to  $L/\lambda$  for a uniform field.

When relativistic feedback (RF) is considered, the number of individual REAs also changes with time. An important parameter for describing feedback is the feedback factor,  $\gamma$ , which is the ratio of the number of runaway electrons to that in the previous feedback cycle. The feedback time,  $\tau_{fb}$ , is the average time for the runaway electrons and backward propagating positrons (or X-rays) to complete one round trip within the avalanche region. The feedback factor,  $\gamma$ , is analogous to the second Townsend coefficient (times the total number of electrons in the avalanche), which describes a feedback process for low-energy electron avalanches.

Following the calculation in Ref. [242], for simplicity we shall assume that for time  $t > 0$  feedback is insignificant. For  $t > 0$ , the runaway electron flux at time  $t$  is the sum of all the feedback generations up until that time:

$$F_{RF} = \sum_{n=0}^{t/\tau_{fb}} F_n(t), \quad (5.22)$$

where  $F_n(t)$  stands for the flux of the  $(n+1)$ th runaway electron feedback generation and is given by the recursion relation

$$F_{n+1}(t) = \gamma \int_0^t D(t-t')F_n(t')dt', \quad (5.23)$$

where  $D(t-t')$  is the normalized transfer function that takes a particle at some location at time  $t'$  and gives the distribution of the next generation of particles at that same location, i.e., one feedback cycle later.

For the sake of illustration, if we ignore the time dispersion and use the approximation  $D(t-t') = \delta(t - \tau_{fb} - t')$ , where  $\delta$  is the Dirac delta function, then

$$F_n = \gamma^n S_o \exp(\xi) S(t - n\tau_{fb}), \quad (5.24)$$

where  $S$  is the step function. Inserting this expression into that for  $F_{RF}$  gives

$$F_{RF} = S_0 \exp(\xi) \sum_{n=0}^{t/\tau_{fb}} \gamma^n. \quad (5.25)$$

For the case  $t >> \tau_{fb}$ , Eq. (5.25), the flux of runaway electrons due to relativistic feedback, becomes

$$F_{RF} = \begin{cases} S_0 \exp(\xi) \exp(t/\tau')/(\gamma - 1), & \gamma > 1 \\ S_0(t/\tau) \exp(\xi), & \gamma = 1 \\ S_0 \exp(\xi)/(1 - \gamma), & \gamma < 1 \end{cases} \quad (5.26)$$

where

$$\tau' \equiv \tau_{fb}/\ln(\gamma) \quad (5.27)$$

is the e-folding time to increase the flux of runaway electrons due to feedback (assuming  $\gamma > 1$ ).

As can be seen in Eq. (5.26), if  $\gamma < 1$ , then the feedback process enhances the flux of runaway electrons in Eq. (5.21) by a simple multiplicative factor:

$$F_{RF} = \frac{F_0 \exp(\xi)}{1 - \gamma}, \quad \text{for } \gamma < 1, \quad (5.28)$$

valid for times  $t >> \tau_{fb}$ . In Eq. (5.28),  $F_0/(1 - \gamma)$  is the flux of seed runaway electrons from both external sources, e.g., cosmic-rays, and from relativistic feedback. Note that Eq. (5.21) is recovered in the limit  $\gamma \rightarrow 0$ , i.e.,  $F_{RF} \rightarrow F_{RREA}$  in this limit. On the other hand, if the avalanche multiplication is increased, for example from thundercloud charging, causing the feedback factor to increase and approach  $\gamma = 1$ , then the flux of seed runaway electrons in Eq. (5.28) will become very large (also see Eq. (5.26)), and relativistic feedback will dominate over external seed particles. However, even in this case, the flux of runaway electrons is tied to the external seed particles and would eventually stop if the external supply of seeds were removed. Because the behavior of the Eqs. (5.28) and (5.21) is dependent upon conditions external to the system, RREAs, even with the enhancement due to feedback, cannot be considered an electrical breakdown, which is an internal state of the system.

Nevertheless, even when  $\gamma < 1$ , large fluxes of runaway electrons may still be generated via relativistic feedback, according to Eq. (5.28). Indeed, as thunderclouds charge, these runaway electrons may produce a significant discharge current which may under some circumstances balance the charging currents, temporarily establishing an approximate steady-state electric field configuration. This scenario may explain the long lasting gamma-ray glows discussed in Section 5.3.3.

At first glance, it may seem impossible for  $\gamma$  to exceed 1, since the discharge currents would become very large as  $\gamma$  increases towards 1. However, Eqs. (5.26) and (5.28) are only valid after sufficient time has passed for the feedback process to reach the steady-state. For a sufficiently rapid growth of the electric field, it is possible to drive  $\gamma$  above 1 before the system can respond with a large discharge current. This may be accomplished through the large scale charging of the thundercloud or by charge motion during lightning. In addition, the currents resulting from the runaway electrons may drive the value of  $\gamma$  above 1 for some parts of the avalanche region while discharging other parts [356]. These processes are studied in detail with the model discussed in Section 5.4.9.

When  $\gamma > 1$ , then each feedback cycle increases the number of runaway electrons by a factor of  $\gamma$ . In a very short time, the flux of seed runaway electrons comes almost entirely from the feedback process, and the external source of seed particles becomes unimportant. Once relativistic feedback dominates the production of seed particles, the runaway electron flux at time  $t$  is given by

$$F_{RF} = S_0 \exp(\xi) \exp(t/\tau')/(\gamma - 1), \quad \text{for } \gamma > 1. \quad (5.29)$$

That is, the system is in a phase of exponential growth of runaway electron avalanches. This growth will continue until the electric field is reduced.

#### 5.4.5. Comparison of runaway electron mechanisms

**Table 5.1** summarizes the salient features of the four main runaway electron production mechanisms, along with potential applications. Wilson's runaway electron mechanism can be viewed as the low electric potential limit of the RREA mechanism. For the RREA mechanism, in order to increase the number of runaway electrons by 1 e-folding, there must be a minimum potential difference of 7.3 MV in the strong electric field region, with  $E > E_{th}$  [247]. As a result, a strong field region with a potential difference much less than 7.3 MV will produce runaway electrons but hardly any avalanche multiplication. Because the Wilson runaway electron mechanism does not involve avalanche multiplication, in order to produce significant fluxes of energetic radiation above the ambient background, there must be a large population of energetic seed particles, produced by some other means. Such a population may be provided by the thermal runaway mechanism, which accelerates electrons out of the low-energy thermal population. A distinguishing feature of the thermal runaway plus Wilson runaway mechanism is the runaway electrons will have a softer energy spectrum than for the RREA mechanism (Eq. (5.18)). We would

**Table 5.1**  
Runaway electron mechanisms.

Mechanism	Key reference	New feature	Runaway electrons	Applications
Wilson runaway electrons	Wilson [215]	Energy gained from an electric field can exceed energy losses in air	1 per seed particle	Lightning and laboratory sparks when combined with thermal runaway
RREA	Gurevich et al. [177]	Møller scatter produces avalanche multiplication	up to $\sim 10^5$ per seed particle	Gamma-ray glows, TGFs when combined with thermal runaway
Relativistic feedback	Dwyer [77]	Positron and X-ray feedback produce an exponentially growing number of avalanches	up to $\sim 10^{18}$ per seed particle	TGFs, gamma-ray glows, thundercloud discharging
Thermal runaway	Gurevich [175]	Electrons are accelerated directly from the free thermal electron population	up to $\sim 10^{11}$ per pulse	Lightning and laboratory sparks when combined with Wilson run away, TGFs when combined with RREA

expect the thermal runaway plus Wilson runaway mechanism to occur when there are large electric fields generated but not very large potential differences ( $< 7.3$  MV). Indeed, based upon X-ray observations, this combination of mechanisms appears to be operating for lightning and laboratory sparks (see Sections 5.3.1 and 5.3.2).

Similar to Wilson runaway electrons, the RREA mechanism may be viewed as the low electric potential limit of the relativistic feedback mechanism. For large enough potential differences in the strong electric field region, with  $E > E_{th}$ , the value of the feedback factor  $\gamma$  will be close to or above 1, resulting in very large numbers of runaway electron avalanches and thus very large fluxes of runaway electrons. For a given average electric field strength, as the potential is decreased (and hence the amount of avalanche multiplication is decreased), the feedback factor goes to zero, and the relativistic feedback mechanism becomes the same as the RREA mechanism. Conversely, the electric field cannot be increased without bound, since eventually the feedback threshold will be crossed causing the electric field to quickly collapse. For this reason, the amount of avalanche multiplication for the RREA mechanism is limited in most cases to the modest value of about  $10^5$  [242,247]. For RREAs seeded by atmospheric cosmic rays or radioactive decays, this usually produces only relatively small flux enhancements. Such enhancements might explain gamma-ray glows seen from thunderclouds (Section 5.3.3) but not TGFs (Section 5.3.4) [247]. On the other hand, like the thermal runaway plus Wilson runaway mechanism for lightning, thermal runaway electrons seeding RREAs could potentially account for the large fluxes seen for TGFs. Another possible application for which RREAs that may be important is the modification of high-energy extensive air showers by thundercloud electric fields. The RREA multiplication could greatly increase the size of the electromagnetic component of the shower, affecting properties of the shower. The resulting electric currents could also produce measurable radio frequency pulses (Section 5.4.7).

Finally, the relativistic feedback mechanism may produce up to  $10^{13}$  times more runaway electrons than the RREA mechanism alone, dramatically altering the behavior. Because the number of runaway electrons, and hence the number of gamma-rays, produced by relativistic feedback is only limited by the time it takes for the electric field to collapse, the study of relativistic feedback must be coupled to the discharge of the thundercloud that results. Consequently, a more descriptive name, in some cases, is the relativistic feedback discharge mechanism.

There are limits to the applicability of relativistic feedback. In particular, relativistic feedback requires large potential differences to operate. For example, potentials ranging from a few tens of MV, at very high field strengths, to a few hundreds of MV, at more moderate fields strengths, are required. There are some electric field geometries that are more favorable for relativistic feedback, especially electric fields configurations in which opposite avalanche regions can provide feedback X-rays and positrons to each other, either in a thundercloud field or around a lightning channel. Such configurations have been named cross-fire feedback [242]. Given the large potentials needed for feedback and based upon the X-ray energy spectra of lightning [172] it is very unlikely that relativistic feedback is involved in the production of X-rays from lightning and in particular is unlikely to be involved in the lightning stepping process as proposed by Babich et al. [251].

On the other hand, detailed simulations have shown that relativistic feedback discharges can naturally explain many of the observed properties of TGFs (Section 5.4.9). They also may generate large electric currents inside thunderstorms that rival those produced by lightning, producing some of the largest radio pulses from thunderclouds (Section 5.3.5). Such currents will partially discharge regions of the thundercloud more quickly than lightning. It is interesting that thunderclouds may have two distinct paths for rapid discharge: normal lightning and relativistic feedback discharges. The relativistic feedback discharge has also been called “dark lightning”, since it has been shown to produce little visible emission while producing large lightning-like electric currents [366]; also see [367].

We end this section with the comparison of the high-energy processes discussed in this section with the low-energy processes that occur in a conventional discharge, as discussed in Section 2. This comparison is summarized in Table 5.2.

At low-energies the basic unit of the discharge is the drifting low-energy (few eV) electron. At high-energies (keV to tens of MeV) the basic unit is the Wilson runaway electron. At both low and high energies, avalanches of electrons and runaway

**Table 5.2**

High-energy mechanisms and the analogous conventional low-energy discharge mechanisms.

High-energy mechanism	Conventional low-energy mechanism
Wilson runaway electrons	Drifting low-energy electrons
RREAs	Low-energy electron avalanches
Relativistic feedback discharge	Townsend discharge
Relativistic feedback streamer	Positive streamer

electrons may form, both require the injection of a seed electron usually supplied by an external source. At high energies these avalanches are called RREAs.

At low-energies, a self-sustained discharge, called a Townsend discharge, is produced by a positive feedback process involving backward propagating ions and UV photons. At high energies, a self-sustained discharge, called a relativistic feedback discharge, is produced by a positive feedback process involving backward propagating positrons and X-ray photons. For both the Townsend and relativistic feedback discharges, large numbers of electrons and runaway electrons are produced, respectively, often leading to the collapse of the electric field.

Positive streamers also have a high energy analog, called relativistic feedback streamers. A plot of one may be seen in Fig. 5.25, which is quite similar in structure to the positive streamer shown in Fig. 2.1. Finally, if we look for a low-energy analogy to thermal runaway electron production, it might be field emission of free electrons from sharp points, although unlike the cases above, in this case, the comparison is not exact. Another way of looking at this issue is that thermal runaway electron production occurs in the regime where the high and low energy discharge processes merge.

Altogether, it is interesting that the high and low energy regimes for atmospheric discharges are so similar even though they are separated in both energy and length scales by factors of about 1 million.

#### 5.4.6. Electric currents

As the runaway electrons propagate, they ionize the air, generating secondary electrons below the runaway threshold energy (see Fig. 5.2). These secondary electrons will very rapidly lose energy, further ionizing the air. The result is that each relativistic runaway electron in a RREA produces a total ionization of about  $\alpha_{re} \approx 8000 \text{ m}^{-1} \times n_{air}$ , which is the number of low-energy (few eV) electron-ion pairs per unit length traveled by the runaway electron [239]. As discussed in Section 5.4.6, the low-energy electrons and ions will drift in the electric field, creating additional electric currents.

Even though the low-energy electrons quickly attach to oxygen on a timescale,  $\tau_a$ , due to 2 and 3-body attachment processes, creating negative ions – at thundercloud altitudes,  $\tau_a$  is on the order of 1  $\mu\text{s}$  – the low-energy electrons greatly outnumber the runaway electrons that produced them, causing a substantial contribution to the charge density, conductivity, and current. Because the ions may drift for a long time (much greater than 1  $\mu\text{s}$ ), they often make important contributions to the transport of charge [247].

Let us consider the production of low-energy electron by the ionization created by runaway electrons, for electric fields low enough that low-energy electron ionization is negligible, i.e., the first Townsend coefficient,  $\alpha_e$ , is small. Ignoring the spatial variations in the low-energy electron density, we may modify Eq. (2.1) to give the number density of secondary low-energy electrons generated by the flux of runaway electrons

$$\frac{dn_e}{dt} = F_{re}\alpha_{re} - \frac{n_e}{\tau_a}. \quad (5.30)$$

The first term on the right describes the production of low-energy electrons by runaway electrons with convective flux  $F_{re}$  and the second term the loss due to attachment. Eq. (5.30) has the general solution

$$n_e(x, y, z, t) = \alpha_{re} \int_{-\infty}^{\infty} F_{re}(x, y, z, t') \exp(-(t - t')/\tau_a) S(t - t') dt'. \quad (5.31)$$

The electric current from the low-energy electrons is then

$$\vec{J}_e(x, y, z, t) = -e\mu_e \vec{E} n_e. \quad (5.32)$$

A similar expression for the number density of the ions and the ion current,  $\vec{J}_{ions}$ , can be found in Refs. [247,355].

We may insert Eqs. (5.9) or (5.10) into Eqs. (5.31) and (5.32) to find the low-energy electron density and current. For instance Eq. (5.10) gives

$$\vec{J}_e(x, y, z, t) = -eN_{max}\alpha_{re}\mu_e \vec{E} \exp\left(\frac{-z^2}{2\kappa^2}\right) \exp(-(vt - z)/v\tau_a) S(vt - z) \delta(x)\delta(y). \quad (5.33)$$

The low-energy electrons, thus, produce a current pulse that propagates with and trails behind the runaway electrons with a tail of length  $\sim v\tau_a$ . The total electric current from all sources is

$$\vec{J}(x, y, z, t) = \vec{J}_{re}(x, y, z, t) + \vec{J}_e(x, y, z, t) + \vec{J}_{ions}(x, y, z, t). \quad (5.34)$$

Inspecting Eqs. (5.10) and (5.33), we see that the electric current from the low-energy electrons is approximately  $\alpha_{re}\mu_e E\tau_a \approx 10\text{--}100$  times larger than the current from the runaway electrons alone. As a result, in practice, the current from the runaway electrons can usually be ignored. When investigating how the ionization from runaway electrons discharge the electric field, both the low-energy electron current and the ion current must be considered. This is especially important for relativistic feedback discharges. Alternatively, if we are instead interested in the radio frequency emissions from the runaway electrons and their ionization, then the ion contribution can usually be ignored. We shall discuss these radio frequency emissions more in the next section.

#### 5.4.7. Radio frequency emissions

Once the electric current is known, the magnetic field at position  $\vec{R}_o$  and time  $t$  is conveniently given by the equation [368,369]

$$\begin{aligned} \vec{B}(\vec{R}_o, t) &= \frac{1}{4\pi\varepsilon_0 c^2} \int d^3\vec{x}' \int dt' \frac{\vec{J}(x', y', z', t') \times \hat{R}}{R^2} \delta(t' - t + R/c) S(t - t') \\ &+ \frac{1}{4\pi\varepsilon_0 c^2} \frac{\partial}{\partial t} \int d^3\vec{x}' \int dt' \frac{\vec{J}(x', y', z', t') \times \hat{R}}{c R} \delta(t' - t + R/c) S(t - t'), \end{aligned} \quad (5.35)$$

where  $\vec{R} = \vec{R}_o - \vec{x}'$ . The first term in Eq. (5.35) is the so-called induction term and the second term is the radiation term. A similar expression can be written for the electric field, which in addition to the radiation and induction terms also includes a dipole moment change term [368]. With the current found above in Eqs. (5.33) and (5.34), Eq. (5.35) could be calculated exactly using numerical methods. However, if we make the simplifying assumption that  $v\tau_a \ll \kappa$ , i.e., the length of the low-energy electron tail is much smaller than the spatial scale of the runaway electron avalanche, then the electric current from both the runaway electrons and the low-energy electrons is obtained by multiplying Eq. (5.10) by the factor  $(1 + \alpha_{re}\mu_e E\tau_a)$ . If we define  $\vec{J}$  to be in the  $-z$  direction, the cross product is in the  $-\hat{\phi}$  direction. For  $N_0$  energetic seed electrons inject at once, the total number of runaway electrons is  $N_{max} = N_0 \exp(\xi)$ , where  $\xi$  is the number of avalanche lengths. The total magnetic field is then

$$\vec{B}(\vec{R}_o, t) = \frac{-\hat{\phi} e(1 + \alpha_{re}\mu_e E\tau_a)N_0 \exp(\xi) v \sin \theta}{4\pi\varepsilon_0 c^2 R_o (1 - \beta \cos \theta)} \left( \frac{1}{R_o} - \frac{(t - R_o/c)v^2}{c\kappa^2(1 - \beta \cos \theta)^2} \right) \exp\left(\frac{-(t - R_o/c)^2v^2}{2\kappa^2(1 - \beta \cos \theta)^2}\right). \quad (5.36)$$

[See Refs. [230,360] for other variations of this equation.] We note that the horizontal component of the magnetic field should be multiplied by an additional factor of 2 when measured near the conductive ground, due to the image currents.

For a wave propagating in the  $\hat{n} = \vec{R}_o/R_o$  direction, the radiation electric field can be found from the radiation magnetic field from

$$\vec{E}_{rad} = -c \hat{n} \times \vec{B}_{rad}. \quad (5.37)$$

Eqs. (5.36) and (5.37) could be applied to a cosmic ray extensive air shower (EAS) traversing a strong electric field region inside or above a thundercloud. In this case  $N_0$  is the number of particles in the air shower at that altitude.

Since 2002, several authors have calculated the radio-frequency emission from cosmic-ray extensive air showers and relativistic runaway electron avalanches [370–375]. A detailed investigation of the radio-frequency emission from runaway electron avalanches seeded by air showers, for a number of geometries, including for inclined air showers, can be found in Ref. [360]. It was also found that for reasonable thunderstorm conditions and air shower energies, relatively large radio-frequency pulses would be produced, which could be measured many kilometers from the location of the air shower core (see Fig. 5.23). These pulses are much larger than the radio emissions from air showers that is usually considered [376–381]. Previously, most models of these emissions involved so-called geo-synchrotron emission of electrons and positrons in the shower moving in the geomagnetic field [382]. The e-folding fall-off distance from the shower center of geo-synchrotron emission is expected to be about 100 m [383], which is much smaller than the fall-off seen in Fig. 5.23 when RREA multiplication is included.

To date there have been only limited reports of such RREA enhanced radio-frequency emission in association with extensive air showers [384], although several groups are currently searching for such emissions. Some researchers have interpreted narrow bipolar events (NBEs) in terms of this EAS-RREA mechanism. This topic is discussed in more detail in Section 6.5.

Instead of radio-frequency emission from an impulsive injection of seed particles, such as occurs from an air shower, we may consider the radio-frequency emission produced by a longer duration production of runaway electrons such as occurs during Terrestrial Gamma-ray Flashes (TGFs). TGFs last about 100  $\mu\text{s}$  and potentially may be produced by either relativistic feedback or a by the combination of a large number of thermal runaway electron injections by lightning leaders into a RREA region [247].

It has been found that many TGFs are measured by spacecraft to have an approximate Gaussian time intensity profile [316,385]. Some TGFs are found to have a longer fall time than rise time, but some of this effect may be due to Compton scattering in the atmosphere, which may be exaggerated due to instrumental dead time [314,315]. When investigating the

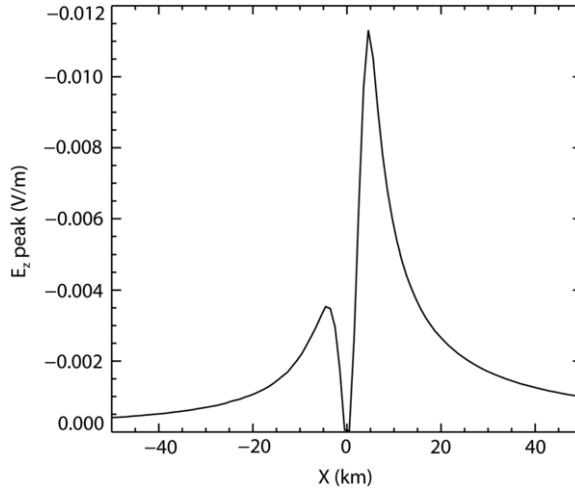


**Fig. 5.23.** Peak vertical RF electric field magnitude versus horizontal distance produced by the EAS/RREA mechanism. The simulation used a 375 kV/m upward electric field, ~300 m deep (10 avalanche lengths), traversed by a  $10^{17}$  e V air shower at  $45^\circ$  with respect to vertical. The air shower core strikes the ground at +5 km in the figure. The off axis maximum near +5 km is due to the relativistic motion of the air shower.  
Source: Figure from Ref. [360].

time-intensity profiles of the runaway electrons that produce the TGFs, it is especially useful to consider just the high-energy photons (e.g., > 1 MeV) which have been less affected by Compton scattering in the atmosphere. To illustrate the radio-frequency emission from a TGF we shall model the TGF as having a seed electron population that follows a Gaussian time profile. The flux of runaway electrons is then the convolution of Eq. (5.10) with this Gaussian, since Eq. (5.10) is for 1 seed electron.

In this case, a simplified version of Eq. (5.33) may be used, which depends only upon the electric current moment in the source region (Amp-meters). The magnitude of the radiation magnetic field in this case is simply [368]

$$B_{rad} = \frac{\sin \theta}{4\pi \epsilon_0 c^3 R_0} \frac{\partial I_{mom}}{\partial t}. \quad (5.38)$$

As above, if we define the direction of the current to be in the  $-z$  direction, the magnetic field is in the  $-\hat{\phi}$  direction.

For TGF durations that are long compared to the runaway propagation time in the avalanche region,  $\kappa/v$ , and the electron attachment time,  $\tau_a$ , it is found that the magnitude of the electric current moment from runaway electrons and the low-energy electrons is approximately equal to [332,333]

$$\vec{I}_{mom} = \int \vec{J} dV = \frac{-e\alpha_{re}\kappa \mu_e \vec{E} \tau_a N_{TGF}}{\sigma_{TGF}} \exp\left(\frac{-t^2}{2\sigma_{TGF}^2}\right), \quad (5.39)$$

where  $\sigma_{TGF}$  is the 1 sigma duration of the Gaussian shaped TGF and  $N_{TGF}$  is the total number of runaway electrons created by the TGF. It was found in Ref. [302] that  $N_{TGF}$  is about  $10^{17}$ . If we insert typical numbers for a TGF [332,333,355], it is found that  $I_{mom}$  can reach several tens of kA-km, which is comparable to the vertical current moments from lightning return strokes. As a result, TGFs can generate some of the largest current pulses inside thunderclouds, some of which might be mistaken for normal lightning.

Combining Eqs. (5.38) and (5.39), we find the magnitude of the radiation magnetic field

$$\vec{B}_{rad} = \frac{-\hat{\phi} \sin \theta}{4\pi \epsilon_0 c^3 R_0} \frac{e\alpha_{re}\kappa \mu_e E \tau_a N_{TGF}}{\sigma_{TGF}^3} t \exp\left(\frac{-t^2}{2\sigma_{TGF}^2}\right). \quad (5.40)$$

The peak magnitude magnetic field in Eq. (5.40) has maxima at  $t = \pm\sigma_{TGF}$ . Thus, the peak magnitude magnetic field in Eq. (5.40) is seen to be proportional to  $1/\sigma_{TGF}^2$ . As a result, shorter TGF have much larger magnetic field amplitudes than longer ones. Indeed, it has been found that shorter TGF have a much better chance of being detected in radio waves than longer ones, as was discussed in Section 5.3.5.

#### 5.4.8. TGF models

By comparing the flux and time structure of TGFs with various TGFs source models, when the limits imposed by relativistic feedback are included, it was argued in Ref. [247] that models that rely on atmospheric cosmic-ray particles seeding RREAs alone cannot explain TGFs. This conclusion applies to both the steady state atmospheric cosmic-ray background flux and the impulsive injection of runaway electron seed particles by cosmic-ray air showers. It was also found in Ref. [247] that the relativistic feedback mechanism and thermal runaway (e.g., from lightning leaders) augmented by additional RREA

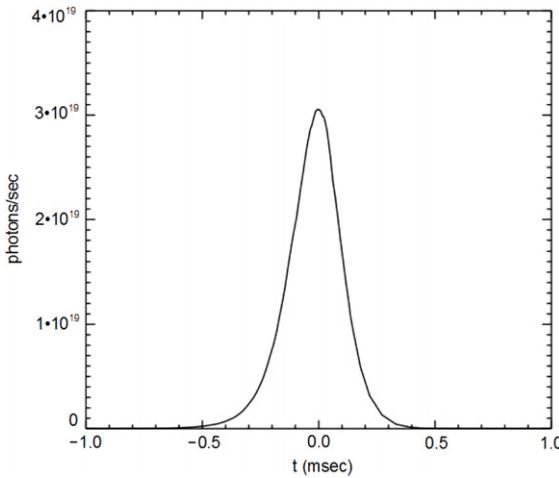


**Fig. 5.24.** Typical Gamma-ray flux at 15 km versus time produced by the RFD model.

Source: Figure from Ref. [332].

multiplication were the only two viable models of TGFs. Nevertheless, cosmic-ray models for which charge imbalances caused by lightning discharges generate large electric fields above the upper negative screening layer, producing large runaway electron avalanches seeded by atmospheric cosmic rays, have continued to be developed [e.g., [386,387], also see Ref. [121]].

Refs. [247,259] considered thermal runaway electron production by lightning leaders, similar to the process that makes the X-ray emissions from lightning recorded on the ground, enhanced by RREA multiplication by the large scale thundercloud field through which the lightning is propagating. Using runaway electron luminosities from lightning found by Saleh et al. [258], it was calculated that one such lightning leader propagating through a strong electric field region just below the relativistic feedback threshold could account for the number of runaway electrons needed to produce a TGF, i.e.,  $10^{17}$  runaway electrons [259]. Because lightning is routinely observed to produce X-ray near the ground, and thus produce runaway electrons, and because thunderclouds are known to have strong electric fields, sometimes above the RREA threshold, this model seems quite reasonable, given how ubiquitous lightning leaders are inside thunderclouds. A slight variation of this idea has been developed by several authors [179,255,321,388–391], in which the region with subsequent RREA development is provided by the lightning field and not the ambient thundercloud field [392]. Although these lightning leader models have made some limited progress in explaining TGFs, detailed models have only begun to be developed.

Alternatively, it has been shown that the intensities and durations of TGFs can be naturally explained by the relativistic feedback mechanism [247]. A detailed and self-consistent model of relativistic feedback discharges inside thunderclouds, which reproduces most of the observed properties of TGFs, is discussed in more detail in the next section.

#### 5.4.9. Results of the relativistic feedback discharge model

One of the most detailed models of TGF production to date can be found in Refs. [332,393]. For this model, as thunderclouds charge, the large-scale field approaches the relativistic feedback threshold. Positive intra-cloud (IC) lightning, which initiates in the high field region within the thundercloud, quickly forces the large-scale electric fields inside the thundercloud above the relativistic feedback threshold, causing the number of runaway electrons, and the resulting X-ray and gamma-ray emission, to grow exponentially, producing very large fluxes of energetic radiation. As the flux of runaway electrons increases, ionization eventually causes the electric field to discharge, bringing the field below the relativistic feedback threshold again and reducing the flux of runaway electrons. In this model, thermal runaway electron production from the lightning leaders is not included, and so the runaway electron fluxes arise just from the feedback processes.

In Refs. [332,393], these processes are modeled with a 2-D plus time (cylindrical symmetry) particle transport code that includes the production, propagation, diffusion and avalanche multiplication of runaway electrons, the production and propagation of X-rays and gamma-rays, and the production, propagation and annihilation of runaway positrons. In this model, referred to as the relativistic feedback discharge (RFD) model, the large-scale electric fields are calculated self-consistently from the charge motion of the drifting low-energy electrons and ions, produced from the ionization of air by the runaway electrons, including 2 and 3-body attachment and recombination. The runaway electrons and positrons are propagated according to Eq. (5.6), and parameters such as avalanche lengths and diffusion coefficients are found from Monte Carlo simulations. Simulation results show that when relativistic feedback is considered, bright gamma-ray flashes are a natural consequence of upward +IC lightning propagating in large-scale thundercloud fields. Furthermore, these flashes have the same time structures, including both single and multi-pulses, intensities, angular distributions, current-moments, and energy spectra as Terrestrial Gamma-ray Flashes (TGFs), and produce large current moments that should be observable in radio waves.

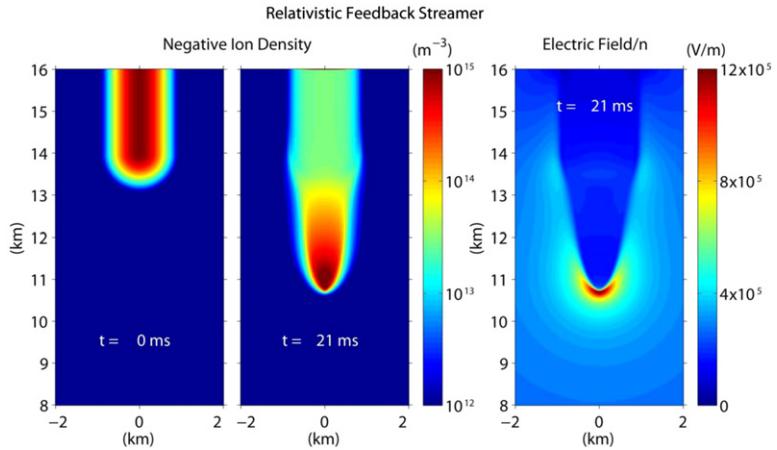


**Fig. 5.25.** Cross-sectional views of the low-energy ion density and electric field of a positive relativistic feedback streamer at thunderstorm altitudes. The relativistic feedback streamer was initiated from a conductive region ( $t = 0$  s) and propagates downward towards the bottom of the figure. Note the similarity of the structure of the relativistic feedback streamer with that of the low-energy positive streamer seen in Fig. 2.1, even though the length scales differ by a factor of 1 million.

Source: Figure from Ref. [393].

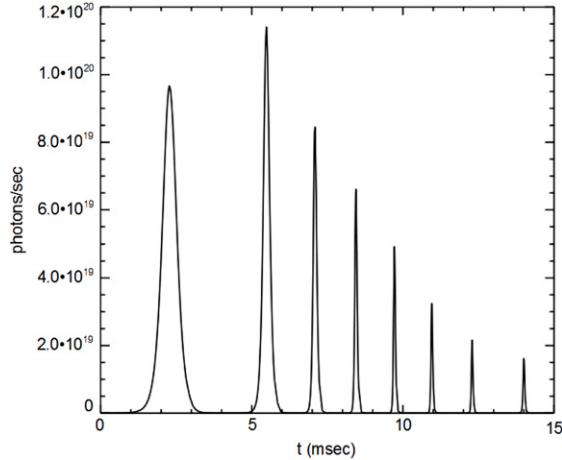


**Fig. 5.26.** RFD model calculations of the gamma-ray flux (at 15 km) versus time generated by a linearly decreasing sea level equivalent electric field with height.

Source: Figure from Ref. [332].

Examples of the simulation results are shown in Figs. 5.24–5.26. Fig. 5.24 shows the gamma-ray rate produced by the model, when IC lightning triggers the TGF. It is found that gamma-ray pulses with the same duration as is typical for TGFs are commonly produced by the model and the number of runaway electron is often around  $10^{17}$ , the same number found from TGF observations.

Fig. 5.25 is an example of the electric field and ion densities produced by the model of Ref. [393]. In this simulation the runaway electrons are propagating upward and the positrons downward. The dark area at the top of the left panel is the region discharged by the runaway electron and their ionization. As the number of runaway electrons increases, the region discharged propagates downward in the figure, similar to a conventional positive streamer, but on a much larger scale. In fact, the structure seen in Fig. 5.25 has been named a relativistic feedback streamer and has been found to propagate at a speed of about  $10^5$  m/s, discharging the field and generating intense pulses of runaway electrons and gamma-rays.

Interestingly, it was found that a relativistic feedback streamer produces multi-pulsed TGFs as seen in Fig. 5.26. The pulsing behavior of the relativistic feedback discharges in Fig. 5.26 comes about by the interplay between the low-energy electron and ion currents (see Section 5.4.6). Specifically, when the flux of runaway electron becomes large due to feedback, the low-energy electron current discharges the field at the end of the avalanche region, bring the feedback factor,  $\gamma$ , below 1 (the self-sustaining threshold). This terminates the runaway electron and hence the gamma-ray pulse. After the pulse, over some number of milliseconds, the current from the ions in the region beyond the avalanche region (i.e., in the discharge channel seen at the top of Fig. 5.25) increases the field in the avalanche region so that  $\gamma > 1$  again. The generation of

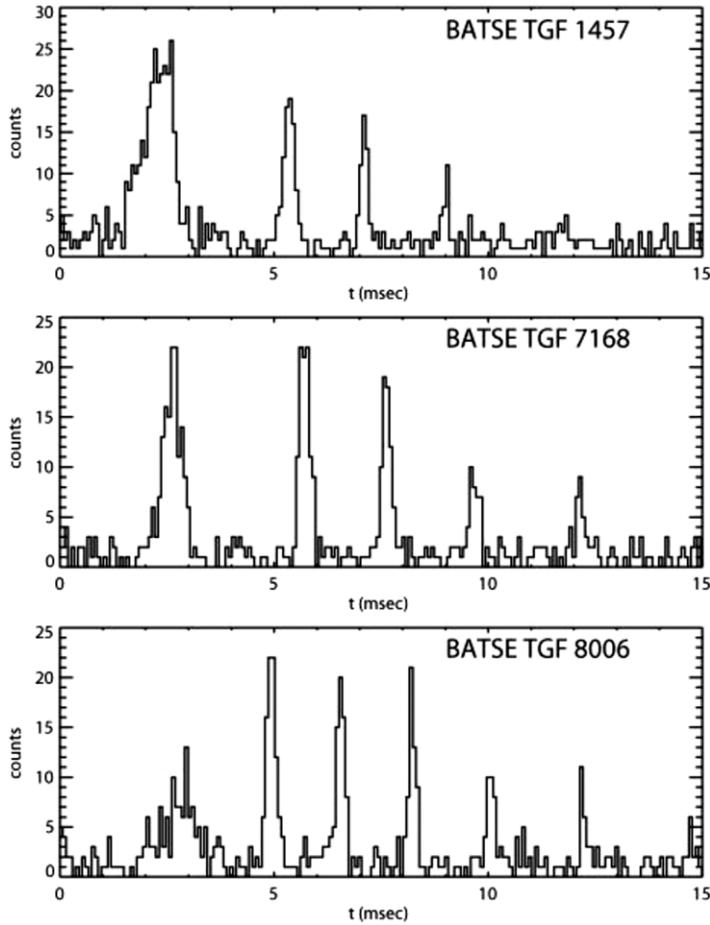


**Fig. 5.27.** Gamma-ray counts rates versus time as measured by CGRO/BATSE for three multi pulsed TGFs (TGFs 1457, 7168, and 8006).  
Source: Data courtesy Jerry Fishman. Figure from Ref. [332].

runaway electrons once again becomes self-sustaining and a second gamma-ray pulse is produced. These processes can repeat itself indefinitely until the strong electric field region is discharged.

Fig. 5.26 from the relativistic feedback discharge model may be compared with 3 TGFs measured by BATSE in Fig. 5.27. As can be seen, the model self-consistently reproduces many of the features seen in the real TGFs, including the wide first pulse, and decreasing and narrowing subsequent pulses.

#### 5.4.10. RREAs and cosmic-ray air showers

The idea of cosmic-ray extensive air showers causing lightning is frequently mentioned by the popular press. The idea being that somehow the conductive channel carved by the air shower assists the thundercloud in initiating lightning. By comparing the rate that lightning is produced by thunderclouds with the flux of cosmic-ray extensive air showers, it has been found that air showers with energies above  $10^{16}$  eV or so occur at a sufficiently high rate to account for lightning [394]. If correct, this idea connects lightning that we see on Earth with events in other parts of our galaxy, such as supernovae. Although, for some, this idea may be aesthetically appealing, unfortunately, there is currently almost no theoretical work to suggest that it is true, and almost no observational evidence to support it. A simple calculation shows that the conductivity of even the largest air shower is insufficient to significantly affect the thundercloud, and so the enhancement of the air shower via runaway electron avalanche multiplication has been considered. Gurevich et al. [358] introduced a model in which extensive air showers (EASs) traversing a strong electric field region inside a thunderstorm seed relativistic runaway electron avalanches (RREAs). In their model, the high conductivity generated by the runaway electron avalanche and the accompanying ionization locally enhances the field to the point that lightning can initiate. Later, it was shown that when lateral diffusion of the runaway electrons is properly taken into account [356], the avalanche and hence the discharge region is too wide and diffuse to substantially increase the conductivity of the air to the point where lightning initiates. Babich et al. [395] came to the same conclusion when they modeled, in more detail, the field enhancement generated by an air shower and RREA multiplication. The basic problem is that, even ignoring the lateral extent of the air shower, due to elastic scattering of runaway electrons with air atoms, the runaway electrons avalanches spread out laterally as the avalanche

propagate (seen in Fig. 5.3). This results in a very wide diffuse discharge. It is difficult to understand how such a discharge, hundreds of meters across, could result in a hot lightning leader just a centimeter or so across.

Worsening the discrepancy, extensive air showers also have considerable lateral widths. Although the core of the shower might be quite narrow, most of the charged particles that seed RREAs are electrons and positrons, which form a much wider distribution around the core. Combining the lateral width of the electromagnetic component of the air shower and the lateral spreading of the runaway electrons in the avalanche, the resulting field enhancements at the boundaries of the discharge region are usually only modest, again making it hard to understand how an air shower could lead to lightning initiation, even with the help of hydrometeors.

Gurevich et al. [396] reported the observation of an intracloud discharge in coincidence with an extensive air shower at the Tien-Shan Mountain Cosmic Ray Station, but the discharge that they reported was not IC lightning. (Note that although they did not claim that they were observing IC lightning, they did claim that they were observing “runaway breakdown”, which implies that an electrical breakdown was occurring.) Instead, they observed a decrease in the gamma-ray background rate at one detector at the time of the air shower and interpreted this decrease as being due to a discharge within the cloud. Such a decrease in gamma-ray flux is conceivable since the RREA production from the air shower could result in a localized reduction of the electric field, thereby reducing the amount of RREA production from the ambient atmospheric cosmic ray flux in that location. However, this observation is a long way from showing that cosmic-rays air showers are involved in lightning initiation.

In order to explain how lightning initiation from air showers might occur, one might consider larger electric fields inside the thunderstorms in order to magnify the amount of RREA multiplication. Similarly, one might consider higher energy showers, again to increase the number of runaway electrons. However, relativistic feedback places a strong limit on how much RREA multiplication is possible [247], and the frequency of EASs decreases rapidly with increasing energy [397], decreasing the fraction of lightning flashes that could potentially be explained by this mechanism.

Some authors have claimed that RREAs produce anomalously large conductivity increases, facilitating lightning initiation [358]. However, recent work has shown that standard ionization rates still apply to RREAs [239], and so the resulting conductivity increase from RREAs are too low to result in electrical breakdown, questioning the appropriateness of the name “runaway breakdown”. Furthermore, it was shown that for the largest air shower ever observed, in the most optimistic case, the maximum heating of the air caused by the EAS-RREA mechanism is only 0.1 K [243], far short of the several thousand degrees needed to form a leader channel. Altogether, Ref. [35] concluded that no compelling theoretical argument exists to suggest that cosmic-ray extensive air showers initiate lightning.

In order to observationally test the cosmic-ray lightning initiation hypothesis, one would need a way to identify the time and trajectory of extensive air showers, and a way to identify the approximate lightning initiation location and time. Operating a lightning mapping array (LMA) at a cosmic-ray air shower array such as the Pierre Auger Observatory, or at the ICLRT, would be one possibility [398]. One would then look for EASs that traverse the region of the thundercloud where and when lightning initiated. Unfortunately, such a study would be hampered by the lack of theoretical guidance. Firstly, it is not known what threshold energy of air showers is needed to initiate lightning, since how such initiation would proceed is not understood. If one considers low enough energy air showers, it will always be possible to find air showers traversing the region where lightning initiation occurs regardless of whether or not the showers were actually involved in the initiation process. Another challenge is when searching for coincidences of air showers with lightning, exactly what part of the lightning flash should be searched? Presumably, the very beginning of the flash or perhaps even before the flash, but, the exact instance of lightning initiation is still poorly understood, and so it is not known precisely when the very beginning actually occurs. As a result, a rather long time window is needed to search for coincidences, increasing the probability of accidental coincidences. Any such study would certainly be of a statistical nature and so it is likely that years of data collection would be necessary in order to establish a link between air showers and lightning if one indeed exists. We conclude with the remark that even if air showers do not initiate lightning, this does not mean that air showers seeding RREAs are uninteresting. For example, the radio pulses generated by air showers seeding RREAs should be quite large and should be measurable many kilometers away from the shower core. It is not clear if such radio pulses have been detected. Gurevich et al. [394] reported that the first radio emissions from lightning were short (few hundred ns wide) bipolar pulses that had widths and amplitudes in agreement with predictions of RREAs acting on air showers. Nag and Rakov [399] examined 2475 electric field records of lightning preliminary breakdown in attempted first cloud-to-ground leaders, i.e., preliminary breakdown that had the characteristics of negative cloud-to-ground discharges but were not followed by return strokes. In addition to the “classical” preliminary breakdown pulses (see Sections 3.2.3 and 4.1), they also observed that at the beginning and end of the pulse trains, much narrower pulses occurred, often having durations in the range of 1–2  $\mu$ s. Although longer than the pulses observed by Gurevich et al., these pulse durations are still within the range expected by air showers/RREA mechanism [360]. It has by no means been established that these short pulses are due to runaway electrons and not, say, leader steps, but the air showers/RREA mechanism seems viable.

If correct, such radio pulses may be of interest to the cosmic-ray community and may have applications as a remote observation tool for studying thunderstorm electric fields [360]. For the later, the RF pulse shape observed on the ground could, in principle, be used to infer the static electric field strength inside the thundercloud, an observation that is obviously important for understanding lightning initiation.

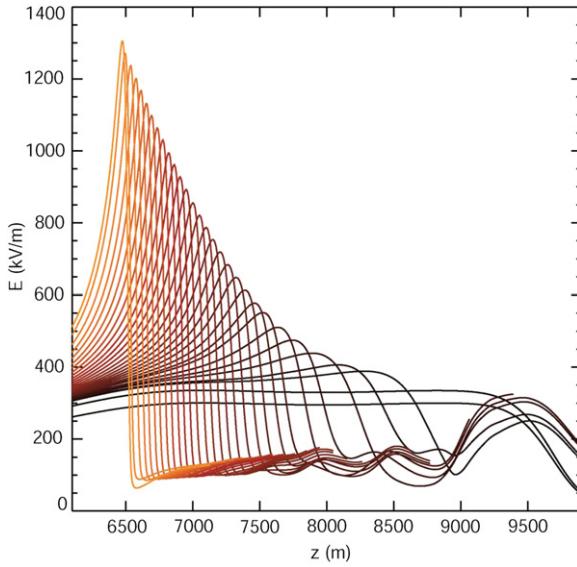


**Fig. 5.28.** Sea-level equivalent electric field strength versus height during a discharge produced by runaway electrons. The curves go from black to red to orange as time progresses. In the figure, the runaway electrons propagate from left to right, and the discharged region propagates from right to left, increasing the electric field. The field at the head of the discharge structure may reach values at which conventional breakdown may occur. Source: Figure from Ref. [356].

#### 5.4.11. Runaway electrons and field enhancements

Building upon earlier work by Gurevich et al. [177], Dwyer [356] developed a diffusion–convection type transport model of runaway electrons with parameters determined by Monte Carlo simulations. It was found that a charging thundercloud could produce enough RREA multiplication to discharge a localized volume at the end of the avalanche region. This discharge of the field produces a large dipole moment change in that region, enhancing the electric field at the boundaries of the discharge region. The larger electric field produced within the avalanche region increases the amount of avalanche multiplication, which causes the discharge region to extend. Often, as the discharge progresses, the relativistic feedback threshold is crossed, causing the whole process to rapidly accelerate. A self-propagating structure is formed that discharges the field in a wide channel and enhances the field at the head, very similar to a positive streamer, except this structure is hundreds of meters across and kilometers long (see Fig. 5.25) [332,393]. A sequence of electric field profiles produced by simulations of this propagating structure is shown in Fig. 5.28. As can be seen, the field can rapidly increase, perhaps to the point where lightning can initiate with the aid of hydrometeors. Babich et al. [395] performed similar modeling, but without including feedback effects, and found very similar field enhancements.

In summary, modeling work has shown that runaway electron production, either via a slow process (many seconds) without relativistic feedback, or via a faster process (few ms) with relativistic feedback, can create localized regions (e.g., 10–100 m across) within thunderclouds with very large electric fields. The electric field enhancements seen in Fig. 5.28 are reminiscent of the rapid field enhancements observed by Stolzenburg et al. [91], although no work has been done to directly compare these models to the observations. When combined with streamer emissions from hydrometeors, this may result in lightning initiation [107]. However, at this time, it is not clear how important this mechanism is for lightning initiation. An assumption in using these models to explain lightning initiation is that thunderstorms are incapable of generating such strong electric fields without the help of runaway electrons. Or, more precisely, they assume that it is more natural for thunderstorms to generate kilometer scale regions with moderate electric fields ( $E > E_{th}$ ), than to produce small regions with very strong electric fields. Balloon soundings show that the electric field profiles in regions with strong updrafts tend to be smoother with lower peak fields, than in regions outside the updraft [61], perhaps hinting at a tendency to produce kilometer scale regions with moderate electric fields in these updraft regions, but the issue has only begun to be addressed.

In Refs. [332,393], the relativistic feedback discharge model was refined and the propagation of such structures, referred to as relativistic feedback streamers, was investigated. It was found that not only do the fields enhance, as discussed above, the gamma-ray emissions agree well with the multi pulsed structures seen in some CGRO/BATSE TGFs [316]. This suggests a possible connection with TGFs and lightning initiation. Radio observations of TGFs shows that most TGFs occur after lightning has been initiated, during the initial stage of +IC lightning when an upward negative leader is traversing the region between the main negative and main positive charge regions [246,311,330]. These observations show that TGFs are not responsible for most lightning initiation, although they are produced not long after the initiation occurs, so perhaps TGFs provide information about the condition inside the thunderstorm that were present when lightning began.

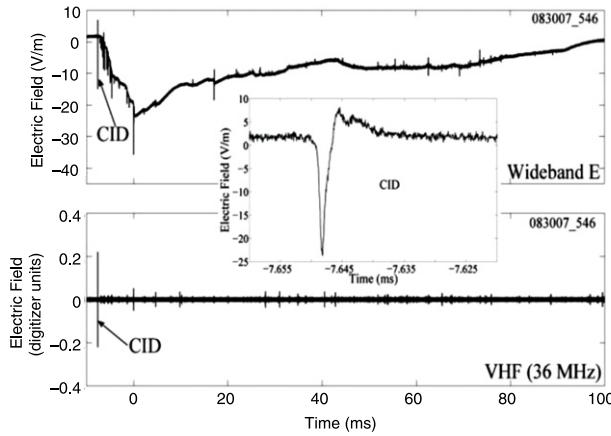


**Fig. 6.1.** A CID that occurs at the beginning of a normal IC flash. A close-up of the CID is seen in the inset.  
Source: Figure from Ref. [406].

## 6. Compact cloud discharges (CIDs)

### 6.1. Introduction

CIDs are interesting because they produce the most power natural radio bursts (in VHF, above  $\sim 30$  MHz) in the Earth environment, with peak powers for some events exceeding 1 MW, much more powerful than normal intracloud lightning or cloud-to-ground lightning return strokes. However, CIDs emit little visible light compared to normal lightning [400].

In 1980, Le Vine [74] discovered intense VHF emissions in a class of narrow bipolar events (NBEs), identifying these as a new phenomenon. Early on, these events were sometimes called Le Vine pulses. More commonly, they have been called Narrow bipolar pulses (NBPs) or Narrow bipolar events (NBEs), since they are observed as short bipolar radio pulses, with full widths of typically 10–30  $\mu$ s. When recorded at VLF/LF frequencies, such RF waveforms are sometimes called sferics. Based upon their short durations, the length of the assumed channel has been estimated to be a km or less, although this length is highly model dependent, hence the name Compact Intracloud Discharge or CID [401]. Furthermore, pairs of strong VHF pulses observed by satellites, called Trans-Ionospheric Pulse Pairs (TIPPs), have been linked to NBEs [402]. The HF-VHF emissions observed at ground level appear as random noise added on top of the slower field change waveform and are not just the higher frequency extension of the sferic [403]. The number of powerful VHF sources seen from space exceeds the number of NBEs observed on the ground [404], and the strength of the field change associated with the sferic observed on the ground does not seem to be correlated with the strength of the VHF emissions [74,404]. Moreover, not all NBEs are observed to produce strong VHF emissions. As a result, there may not be a one-to-one association between the powerful VHF emissions and the NBE sferics. The VHF emissions is usually thought to result from the breakdown of virgin air, e.g., via corona or streamer discharges. The field changes associated with the sferics may indicate that a hot channel has formed, allowing a larger current to flow, although this has not been shown to be true for CIDs. Indeed, the lack of detectable optical emissions constrains this picture. In this paper, we shall refer to the various phenomena discussed above as CIDs, keeping in mind that the relationships between them have not yet been fully worked out.

At the ground, most CIDs are recorded at large enough distances (e.g., > several tens of km) that the signal is dominated by the radiation component, although many CIDs have also been measured at closer distances allowing the dipole and induction components to be recorded as well [405,406]. The peak electric field recorded at the ground from CIDs is quite large, e.g., 10–100 V/m at a distance of 100 km, making them easily detectable (first return stroke peak fields at 100 km average 5–10 V/m). At large distances, the bipolar CID sferics always have a short, 1–2  $\mu$ s rise time, the leading pulse followed by a longer  $\sim 10$ –20  $\mu$ s trailing pulse of opposite polarity and lower amplitude (see Figs. 6.1 and 6.2). Because electromagnetic radiation seen on the ground at large distances is simply proportional to the derivative of the current moment, the current pulse that makes such bipolar radiation pulses is unipolar with a faster rise-time than fall-time. The polarity of CIDs may be either positive or negative, with positive CIDs having a current downward at the source and negative CIDs having a current upward at the source. Positive CIDs are more common than negative CIDs [407]. Figs. 6.1 and 6.2 show two examples of CIDs.

CIDs often appear as isolated pulses with little or no observable discharge activity either before or after. When they are accompanied by other pulses, those pulses almost always follow the CID and do not come before. In particular, when they are accompanied by a normal IC lightning flash, they are usually the initiator (first recorded pulse) of the flash [404,408]. As a result, CIDs are usually considered a type of preliminary breakdown (see Sections 3.2.3 and 4.1). Nag et al. [406] used wide-band electric field and electric and magnetic field derivatives, and narrowband VHF (36 MHz) data to study 157 positive CIDs. A range of events were recorded with some dominated by the radiation component and others the induction and electrostatic components. They found that about 24% of CIDs occurred prior to, during, or following normal

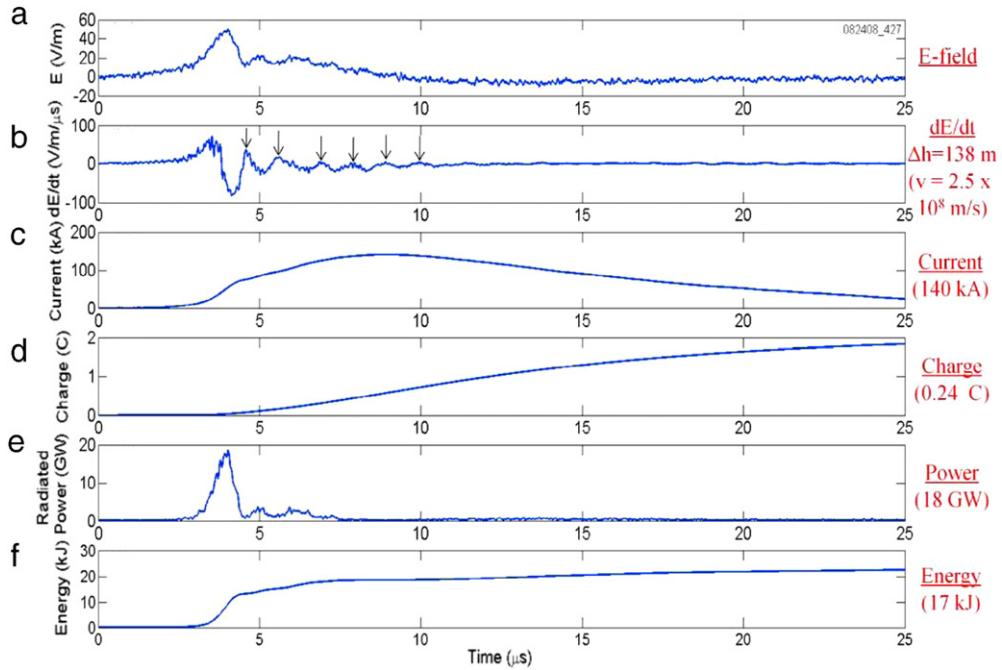


**Fig. 6.2.** Measured and inferred properties of a CID that occurred at a horizontal distance of 19 km, with an inferred height of 15 km, and had an inferred channel length of 138 m. (a) Measured electric field strength, (b) measured electric field derivative, (c) inferred electric current, (d) inferred charge transfer, (e) inferred radiated power, and (f) inferred radiated energy. The current and power values given in the parentheses are the peaks, and the charge and energy values are estimated at 5  $\mu$ s.

Source: Figure from Ref. [411].

lightning, and 72% occurring in isolation. About 6% appeared to be associated with cloud-to-ground lightning. In three cases, based on two CIDs that occurred within less than 200 ms of each other, a total of 4% of CIDs occurred in pairs. Wu et al. [407] studied a large number of CIDs using their VLF/LF lightning location network and found that for positive polarity CID, 11.7% of the CIDs preceded other discharge activity within 10 ms, but only 1.6% followed discharge activity within 10 ms. For negative polarity CIDs, the percentages were 4.4% and 1.7% respectively.

Fig. 6.1 shows an example of a CID that is followed by a normal IC flash. Note that in the wideband electric field data, the CID does not appear that remarkable. However, in terms of the VHF emission it clearly stands apart as a powerful VHF source. As mentioned above, the CIDs usually appear without any detectable breakdown processes preceding the event. In particular, the CIDs are unique in that the VHF and LF/VLF sferic (wide band) appear simultaneously, giving the impression that the hot channel (assuming that there is one) and the first detectable electrical breakdown occur at the same time.

Many models of CIDs assume a hot conductive channel exists through which the current that generates the sferic flows. From Eq. (5.38) it can be seen that the radiation electromagnetic field, when measured at large distances and at angles perpendicular to the current direction, is proportional to the time derivative of the current moment. As a result, integration of the electric field waveform with respect to time yields the current moment as a function of time. An additional integration gives the charge moment change. In this way it is found that the charge moment change associated with CIDs range between about 0.1 and 2 C km [405]. These charge moment changes are small when compared to those produced by CG lightning, which are often on the order of 100 C km and sometimes exceed 1000 C km. Because the RF emissions only provide information about the current moments and charge moments, in order to separately find the current or the length of the channel, a particular model must be assumed or additional information must be provided. For example, Hamlin et al. [409], found a small second peak in 133 NBEs located by the Los Alamos Sferic Array (LASA), which they interpreted as resulting from the reflection of the current pulse from the end of the conductive channel, similar to reflection from an impedance discontinuity along a transmission line. With this assumption they inferred that the channel lengths were less than 2 km. Similarly, Nag and Rakov [410,411] reported the observations of multiple oscillations, or ringing, in the electric field measurements of CIDs (see Fig. 6.2). Modeling these oscillations in terms of reflecting current pulses from both ends of a short conductive channel, they arrived at channel lengths for nine events of 108 m–142 m. With this channel length they were then able to find additional information about the CID, as is plotted in Fig. 6.2. Liu et al. [412] observed CIDs using VHF broadband interferometers and their measurement of the evolution of the VHF source heights confirms oscillating patterns reported in the earlier work.

In their model, Nag and Rakov [410] suggested that the HF and VHF emissions are produced by streamer emission from the two ends of the conductive channels, similar to the corona flash seen during the lightning stepped leader formation. This idea is similar to that discussed by Shao and Jacobson [413], who inferred a narrow discharge geometry of an assumed

corona region from studies of the polarization of FORTE VHF-intense TIPP events. They found that at least 40% are highly polarized, as compared to the concurrent background noise, implying that most of the selected TIPPs are well polarized at their sources. Other modeling work with different assumptions include Refs. [402,414,415].

## 6.2. Trans-ionospheric pulse pairs (TIPPs)

Beginning in 1993, the Blackbeard radio-frequency waveform recorders on the Alexis satellite recorded powerful HF/VHF noise pulses that arrived in pairs with a separation of tens of microseconds, named Trans-Ionospheric Pulse Pairs (TIPPs) [416]. Initially several explanations for the pulse pairs were considered, including an intracloud discharge followed by a second discharge in the mesosphere. Because of its limited sensitivity, Blackbeard only recorded the most powerful radio bursts, such as those reported by Le Vine [74]. Ground-based observations of dispersed HF pulse pairs similar to TIPPs, called Sub-Ionospheric Pulse Pairs (SIPPs) have also been reported [402], and appear to share a similar origin as TIPPs [402].

Later, the FORTE satellite demonstrated that the first TIPPs pulse was the radio emission that followed a direct path to the satellite and the second pulse was from a ground reflection of the radio waves from the same source [417,418]. The FORTE satellite was launched in 1997 with an approximately circular orbit with an 800 km altitude, and a 70° inclination (e.g., [408, 415]). It carried both optical and radio instruments. The dual-channel radio receiver has 25 MHz bandwidth, with a tunable central frequency in the VHF. For most reported work the low band was set to 26–51 MHz (called the “38 MHz band”), and a simultaneous high band was set to 118–143 MHz (called the “130 MHz band”). FORTE was much more sensitive than Blackbeard and so could be used to study much weaker radio emissions, such as stepped leader emissions in addition to the more powerful CIDs.

The vast majority of the intracloud radio pulses recorded by FORTE were coherent, polarized, and narrow pulses ( $\sim 0.05 \mu\text{s}$ ) that frequently appeared in pulse trains with irregular separations. These pulses appear to have characteristics similar to negative leader steps. In contrast, the more powerful TIPPs were composed of pulse pairs with pulse widths of several microseconds, e.g., typically  $4 \mu\text{s}$  envelopes in the 116–166 MHz pass band. It should be noted that in the literature TIPPs are sometimes taken to be synonymous with CID events. However, two classes of FORTE TIPPS were routinely seen: the “strong pulses”, which are the brightest RF signals recorded by FORTE, and the “coherent pulses”, which are two to three orders of magnitude weaker, narrower, coherent and perfectly linearly polarized, as noted above [404]. It is the “strong pulses” that are sometimes, but not always associated with CIDs. In the FORTE literature the two classes are usually divided by those with effective radiated powers (ERPs) above and below 40 kW [419].

The FORTE radio instrument could not identify the source of the discharge and so coincidences with the FORTE optical instrument and data from ground based networks such as NLDN and the Los Alamos array [420] were used. Knowing the geolocation allowed the Effective Radiated Power (ERP) to be determined, which could be used to discriminate the CIDs, the source of the TIPPs with strong pulses, from the larger set of stepped leaders.

Jacobson et al. [421] examined the multi-microsecond pulse-trains within individual TIPP pulses. The radio power envelope of some individual CID events shows emission persisting for  $\sim 10 \mu\text{s}$  in both bands, with the ERP at 130 MHz within a factor of  $\sim 3$  of the ERP at 38 MHz, indicating a very hard spectrum. Furthermore, the ERP envelope at 130 MHz consists of both random variations and quasi-discrete distinct peaks. There appeared to be no correlation between the peaks seen in the first and second pulses in the TIPP, which is puzzling given that both the first and second pulses are just different views of the same source. It should be noted that the peak power often quoted for CIDs is the maximum ERP within the events for the quasi-discrete distinct peaks. Ahmad [422] reported similar short nanosecond scale sub pulses within CIDs, which they suggest could be responsible for the HF/VHF emission.

## 6.3. CID optical emissions

CIDs produced no optical signal that could be measured by the FORTE satellite [423]. In particular, from the required luminosity to trigger the PDD optical photometer aboard the FORTE satellite, CIDs are found to be less luminous than ordinary lightning [408]. CIDs have an effective isotropic cloud top light output less than  $3 \times 10^8 \text{ W}$ . Integrating the pulse duration, the upper bound for CID's cloud-top radiance is about  $10^4 \text{ J}$ . In comparison, U-2 aircraft measurements of cloud-top effective radiated energies for normal lightning found values from  $10^5$  to  $10^6 \text{ J}$  [424], about an order of magnitude larger than the upper bound for NBEs.

When optical concurrence is observed by FORTE, it is almost always with the weaker “coherent pulses” and not the strong pulses associated with NBEs [404]. Interestingly, when the “strong pulses” are seen to initiate IC lightning flashes, if there is any optical concurrence, it tends to occur only for subsequent pulses and not the strong initiator pulse [404,406].

If we suppose that CIDs involve a hot channel similar to that of a CG return stroke, then using a channel length of rough 1 km, which is a typical length estimated for CIDs (e.g., [402] also see Section 6.5 below) and a luminosity per unit length of  $4 \times 10^5 \text{ W/m}$  typical of the subsequent strokes of natural CG lightning [425], then we arrive at a total luminosity at the source due to the incandescent channel of  $4 \times 10^8 \text{ W}$ , of which no more than half should exit the top of

the cloud, consistent with the  $3 \times 10^8 \text{ W}$  upper limit on the cloud top light output estimated by FORTE. As a result, based upon the FORTE upper limit, it is possible that CIDs do have a short hot channel.

#### 6.4. CID association with thunderclouds meteorology

It has been found that CIDs are often associated with strong convection within thunderstorms. Positive CIDs have been measured to have a source altitude between roughly 8 and 16 km, possibly corresponding to the region between the main negative and positive charge regions above. Negative CIDs have been measured to have a source altitude between 16 and 20 km, possibly corresponding to the region between the main positive and upper negative (screening) charge regions above [406,407,426]. Wu et al. [407] found that the fraction of negative CIDs relative to the positive ones appear to increase with convective strength.

Jacobson and Heavner [427] compared CIDs recorded by LASA with ordinary lightning and used infrared cloud imagery using GOES-East to infer that both were associated with severe convection. Similarly, Jacobson et al. [428] compared LASA and TRIMM satellite observations and found NBEs and ordinary lightning behave similarly with regards to their proximity to deep convective cores as measured by the TRIMM Microwave Imager. Other studies have found similar results that CIDs occur in the same general meteorological environment as ordinary lightning, within or near the convective cores of thunderstorms [402,429].

#### 6.5. RREA models of CIDs

One class of models for explaining CID are those involving the joint action of large cosmic-ray extensive air showers (EASs) with RREA multiplication [244,370–375]. These EAS-RREA models (also called EAS-RB models, with the RB standing for runaway breakdown) model the sferic of the CID as arising from the electric current produced by runaway electrons and resulting ionization impulsively seeded by an air shower traversing the strong electric field region of a thundercloud. As discussed in Section 5.4.7, such a mechanism could produce bipolar RF pulses with microsecond rise times similar to that seen in CIDs. There are a few difficulties with these models: (1) While the EAS-RREA could potentially reproduce some characteristics of the sferic, they do not address one of the defining features of CIDs, namely the incoherent VHF emission. (2) Detailed calculations have shown the amplitude of the sferic produced by the EAS-RREA mechanism may be too small to account for CIDs [360]. (3) Because the electron attachment times, even in the upper regions of thunderclouds, is less than a few microseconds [30], a continuous source of new ionization must be occurring to explain the total duration of the CID current. For example, the current pulse shown in Fig. 6.2 lasts at least 23  $\mu$ s (and probably longer judging from the rate the tail is decaying). If the source of the free electrons is the runaway electrons, then in this time these electrons would traverse a region of the storm more than 6 km deep. This seems to be a rather large distance for such a high field to exist, although it cannot be completely ruled out. Alternatively, this problem could be overcome if somehow the EAS-RREA creates a hot channel that allows the current to continue to flow after the runaway electrons are gone. Indeed, the EAS-RB mechanism has been invoked by Nag and Rakov [411] to explain how the hot conductive channel assumed in their bouncing current wave model could form so quickly (in less than 1  $\mu$ s). The bouncing current wave model can naturally explain the ringing pattern seen in the electric field data from several CIDs. However, this model requires that the channel be formed essentially instantaneously, i.e., at propagation speed of light. It is not easy to understand how this might happen with conventional discharge processes and so the EAS-RREA has been suggested. However, as was discussed earlier, it is not at all clear how a diffuse RREA discharge, even one seeded by a large EAS, measuring hundreds of meters across could result in a hot channel measuring centimeters across, as was discussed regarding EAS-RREAs and lightning initiation. Nevertheless, despite its difficulties, EAS-RREAs have continued to be discussed as a possible mechanism for explaining CIDs, largely because no viable alternative as yet been found. If it can indeed be shown that CIDs are produced by EAS-RREAs and a hot channel was created, then this would also provide a strong case that EAS-RREAs are also involved in lightning initiation.

### 7. Transient luminous events (TLEs)

TLEs are brief emissions of optical light from above thunderclouds in the stratosphere, mesosphere, and lower ionosphere, generated either by upward discharges or in response to in-cloud and cloud-to-ground lightning. There are several types of TLEs: Sprites (also called red Sprites), halos (also called Sprite halos), Elves, blue starters, blue jets, and gigantic jets, all of which involve electrical discharges in the upper atmosphere. Fig. 7.1 shows an artist's conception of several TLEs. Blue starters are not shown, but appear as a blue jet that extends to a lower altitude. In this section we shall give a cursory review of TLEs, pointing out a few interesting puzzles that are actively being pursued. We also refer the interested reader to the following reviews [231,430–433].

#### 7.1. Sprites and halos

Although TLEs had been anecdotally reported for at least 100 years, their existence was not established until 1990, when Franz et al. [297] accidentally recorded what would later become known as Sprites during tests of their low-light video camera. Sprites, which last for up to a few tens of ms, are comparable in optical intensity to moderately bright auroral arcs and are visible to dark adapted eyes [434]. Halos are brief descending ionization waves producing glows near the base of the

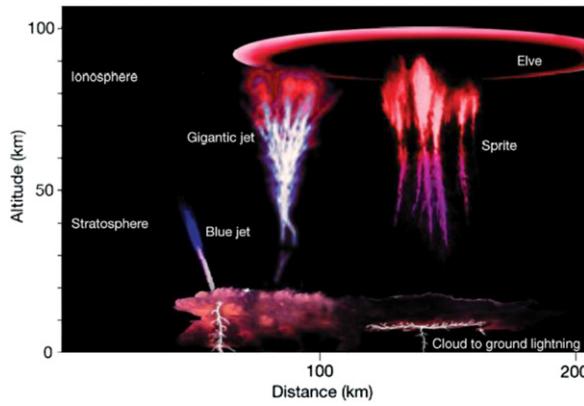


**Fig. 7.1.** Artist's conception of TLEs. From Pasko [465].  
Source: Reprinted from Ref. [484] with permission from *Nature*.

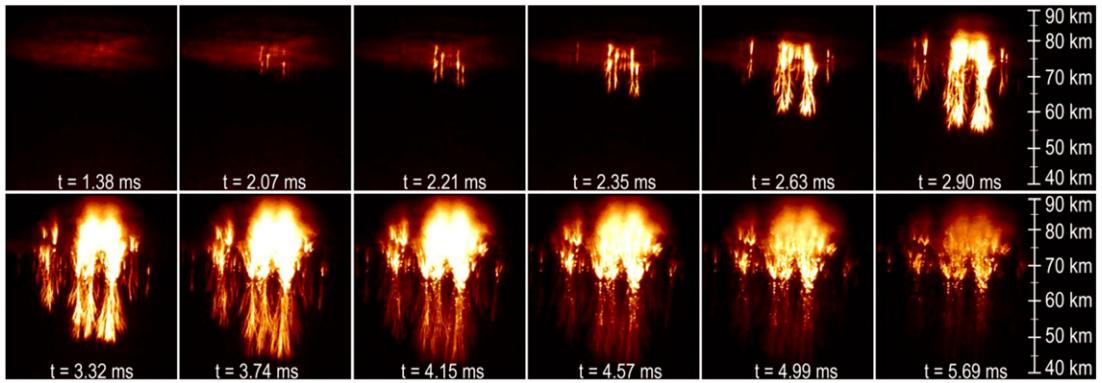


**Fig. 7.2.** The initiation and development of a large Sprite.  
Source: From Ref. [442]. Figure courtesy of Steve Cummer, Duke University.

ionosphere, with diameters less than 100 km, that sometime precede or accompany Sprites [435,436]. Halos are sometimes confused with Elves (discussed in Section 7.2).

The discovery of Sprites led to a great deal of research activity and much progress has been made over the two plus decades that followed [e.g., [437–444]]. Sprites have been found to come in a very large array of morphologies. High speed video images show that Sprites usually start with a streamer tip forming at about 80 km altitude [445]. These positive streamer tips, accelerate downward, brighten and move with an average speed between  $10^6$  and  $10^7$  m/s. At low frame rates, as is seen in Fig. 7.2, the propagating streamers appear as elongating columns. However, at higher frame rates, e.g., >10,000 fps, the streamers appear as propagating bright spots, corresponding to the luminous streamer tips. Longer lasting emission also appears in the channel following the streamer tip [446,447]. Events with just the downward propagating positive streamers are the Column or C-Sprites. In some cases, upward streamers follow, forming the so-called carrot Sprites. These upward streamers always appear to be initiated after and from lower altitudes than the initial positive streamers, and appear to start from existing structures in the Sprite. These properties of the upward negative streamers are consistent with the higher electric field strengths required for negative streamer initiation and propagation [37,448].

During the 1990s, one of the main hypotheses for Sprites was that Sprites were a manifestation of high altitude RREA discharges produced in response to large electric fields generated by lightning (e.g., [230,449–451]). According to this hypothesis, TGFs were produced by these same runaway electrons, and so Sprites and TGFs were assumed to be closely linked. This picture was challenged when detailed observations showed that Sprites are composed of filamentary streamers similar to seen during conventional breakdown [441]. Sprites also do not follow the geomagnetic fields as would be expected for runaway electron beams at high altitudes [452–454]. Fig. 7.2 shows a sequence of images of a Sprite. The filamentary positive streamers can be seen propagating downward as the images progress in time.

In contrast, work since 2005 has demonstrated that TGFs originate from thundercloud altitudes below about 21 km and are associated with lightning discharges with charge moment changes that are too small to initiate Sprites [300,302] (see Section 5). Furthermore, the global distribution of TGFs does not match that of Sprites [299,455,456]. Although it is possible that in response to lightning with large charge moment changes, some numbers of runaway electrons may be produced

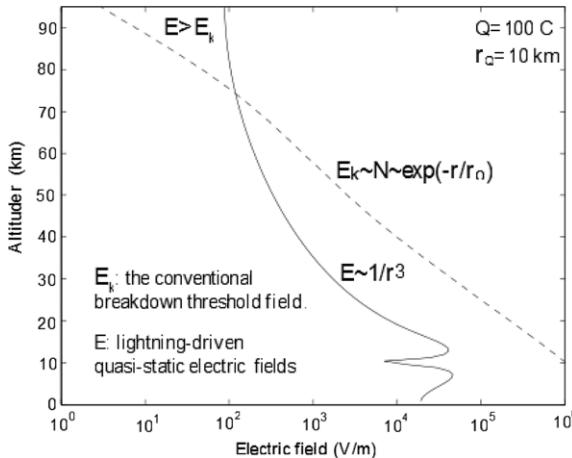


**Fig. 7.3.** Mechanism for producing a Sprite from a lightning discharge. The dipole electric field generated by the lightning,  $E$ , falls off less rapidly with height than the conventional breakdown field,  $E_k$ , allowing a discharge to develop between 70 and 80 km.  
Source: Figure from Ref. [465].

above the thundercloud, at present, it has not been established that any high altitude optical emissions are associated with runaway electron avalanche processes.

The currently accepted model of Sprites is that they are an entirely conventional discharge process, usually involving downward propagating positive streamers sometimes accompanied by an upward propagating more diffuse negative discharge (see Fig. 7.2) [31,446,457,458]. Sprites are most often initiated by the electrostatic field generated in response to large positive lightning cloud-to-ground discharges in and below the thundercloud [459]. Because of the high conductivity of the atmosphere above thunderstorms, as a thunderstorm charges, the electric fields in the space above are expelled and an upper screening charge layer is formed at the top of the cloud (see Section 3). Charge motion from lightning will produce a rapid dipole moment change within the troposphere. Because the electric field from the sudden appearance of this electric dipole is produced faster than the Maxwell relaxation time of the field in the upper atmosphere, an electric field is produced that extends up to the ionosphere, falling off with altitude approximately as the inverse cube of the height above the storm. Meanwhile, the conventional breakdown field scales linearly with the air density, which decreases exponentially with altitude. This is illustrated in Fig. 7.3. For a sufficiently large lightning flash, the local electric field created above the cloud will exceed the conventional breakdown field, often around about 70 km altitude. This electric field then initiates positive streamers which grow and branch, forming the Sprite. This basic picture was first proposed by C.T.R Wilson in 1925 [460], 65 years before Sprites were discovered.

Because positive CG lightning more often produces very large charge moment changes, e.g.,  $>$  few hundred C km, much larger than for most negative CG lightning, Sprites are usually initiated by large positive CG lightning flashes, typically with large continuing currents. Indeed, approximately 99% of all Sprites are generated by positive lightning. This fact helps explain the rarity of Sprites compared with lightning since the vast majority of CG lightning is negative. Indeed, it is estimated that there are about 1000 Sprites per day world-wide [461], compared with 4 million lightning flashes per day [462]. Furthermore, Sprites are often produced above the trailing stratiform region of mesoscale convection systems and complexes (MCCs and MCSs). Such large systems tend to be produced within continents, such as in the great plain region of the United States [445,463]. As a result, the global pattern of Sprites is different than that of all lightning (and TGFs). Sprites are almost always recorded at night, since they are primarily studied using low-light cameras that could not operate during the day. As a result, there is a strong observational bias with regards to the diurnal pattern of Sprites. However, because during the day, the ionosphere is lower, requiring Sprites to initiate at lower altitudes during the day, a larger lightning discharge is needed to produce daytime Sprites.

At the altitude range of Sprites, the discharges do not have sufficient time to heat the air to the point where a hot leader channel may form, and so Sprites and the upper parts of blue jets and gigantic jets are similar to a corona discharge, e.g., involving streamer discharges. When considering discharges on Mars, the atmospheric pressure at the surface of that planet is similar to the pressures found at the lower boundary of Sprite altitudes. It has been suggested that lightning may form on Mars from the triboelectric charging of dust, such as during dust devils and dust storms [464]. However, because at such low pressures, hot leaders and return strokes are unlikely to form, the discharges, if they exist, will probably be similar to Sprites. For this reason, the study of Sprites may give insight on Martian discharges. In addition, because Sprites are large, bright, and last a relatively long time (milliseconds), they are easily recorded with high speed video cameras. The study of Sprites is also the study of corona discharges and, in particular, the study of streamer discharges on a much larger scale than in the laboratory. Because they are initiated in air far from metal electrodes, Sprites allow us to test models of streamer initiation and propagation, topics that are important for understanding lightning initiation.

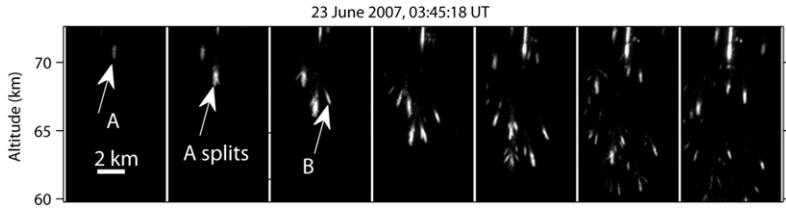


**Fig. 7.4.** Seven consecutive images of part of a Sprite viewed at 10,000 fps. The time between successive images is 100  $\mu$ s. A single streamer head is seen to enter the leftmost frame at an altitude of about 71 km. The streamers can be seen to undergo rapid branching, dividing into many separate streamers in the subsequent images.

Source: From Ref. [447].

Of particular interest is the issue of Sprite initiation. The picture due to C.T.R. Wilson described above and shown in Fig. 7.3 is quite compelling and indeed can explain much of the observed behavior of Sprites. One puzzle is when Sprites are observed, electromagnetic models of the fields in the upper atmosphere from the parent lightning discharge sometimes predict maximum fields that are considerably lower than the local conventional breakdown field, raising the issue of how the Sprite was initiated [465–468]. This problem is very similar to the lightning initiation problem discussed in Section 3. It has been suggested that conductive patches created by various processes in the lower ionosphere, e.g., meteors [469,470], may help locally enhance the field to the point where positive streamers may be initiated, similar to the role played by hydrometeors in lightning initiation inside thunderclouds. One possible difference between discharge processes at high altitude and low altitude is the role played by electron detachment, which is more important at Sprite altitudes than at thundercloud altitudes [468,471]. Recent modeling studies have demonstrated that localized conductive patches in subbreakdown fields of lightning are able to initiate Sprite streamers [37,448]. Research work is currently pursued to pinpoint which process is primarily responsible for the formation of such patches at ionospheric altitudes, such as local field enhancement created by the Sprite halo [435]. Because Sprite initiation and propagation models can be tested observationally, the study of Sprites may help test ideas about lightning initiation, which are difficult to directly test.

Another interesting topic is the dynamics of Sprite streamer propagation, which sometimes show interesting interactions between nearby streamers. For example, Sprite streamers are sometimes observed to collide, with streamer tips attracted to channels left behind by other streamers [442]. At the point of collision, a long persistent glow is observed, called a Sprite bead. Another issue is the branching of the streamer tips, which is found to be complex with single streamer tips sometimes spontaneously branching into many separate streamers [447]. Such branching, which is seen in Fig. 7.4, is important for understanding both Sprite and lightning propagation, and yet it has only begun to be modeled due to the challenge of implementing the necessary fully 3-D codes.

## 7.2. Elves

Elves were discovered by Boeck et al. [472] a year after the discovery of Sprites. Elves are rapidly expanding rings of light emission, up to about 300 km across, in the lower ionosphere. They are generated by the electromagnetic pulse (EMP) from lightning return strokes (see Fig. 7.1) [e.g., [473–478]]. The name Elves was originally an acronym for Emission of Light and Very Low Frequency perturbations due to Electromagnetic Pulse Sources, although few authors now mention this full name since both Elves and Sprites are also named for supernatural creatures. Elves are more common over oceans, presumably because lightning with large peak currents (e.g., >80 kA) are more common over the oceans than over land [456]. The EMP propagates as a spherical wave up from the base of the lightning channel. It intersects the lower ionosphere in a ring that expands outward faster than the speed of light. The electric field from the EMP is thought to produce heating of the free electrons, enhancing the collision induced excitations, ionization and the optical light emissions [433]. Based upon the ISUAL spacecraft observations, Elves are one of the most common TLEs, outnumbering Sprites 9 to 1 [456].

## 7.3. Blue starters blue jets, and gigantic jets

Blue starters and blue jets can be thought of as upward lightning that exits the tops of the thunderclouds and terminates in the upper atmosphere (e.g., [479–482]), reaching approximately 25 and 40 km altitudes, respectively. Blue jets propagate upward with speeds of about 10<sup>5</sup> m/s and have lifetimes of about 300 ms. Note that this long timescale does not match the sub-millisecond timescale of TGFs, suggesting the two phenomena are not related. Blue jets are bright enough to be seen by dark adapted eyes. Gigantic jets, which were the most recent to be discovered, are in some ways analogous to cloud-to-ground lightning, except that rather than propagating from the thundercloud down to the conductive ground, gigantic jets are lightning that propagates up to the conductive ionosphere at about 90 km (e.g., [483–487]).

Krehbiel et al. [134] modeled blue jets and gigantic jets as upward lightning. According to their model, blue jets begin as electrical breakdown between the main upper charge region and the upper screening layer, shortly after a CG or IC discharge produces a sudden charge imbalance in the storm, resulting in the upward propagating lightning that extends into the stratosphere. In contrast, they modeled gigantic jets as an upward analogy to negative bolts from the blue (see Fig. 1.8).

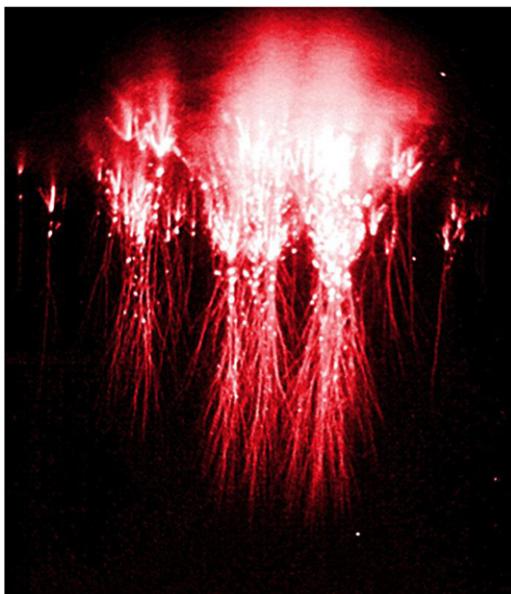


**Fig. 8.1.** Composite image of a Sprite. The black and white image was artificially colored to match the true color of Sprites.  
Source: Courtesy Steve Cummer, Duke University.

These start out as normal IC lightning discharges between the dominant mid-level charge and a screening-depleted upper level charge and continue to propagate up and out of the top of the storm.

## 8. Concluding remarks

We conclude this review with some thoughts about lightning physics and, more broadly, the atmospheric sciences. It is often pointed out, and widely agreed upon, that the oceans remain poorly explored. Indeed, a common mantra is that we know more about the surface of the moon than we do about the deep oceans [488]. A similar thought could be expressed about our atmosphere. Just as the deep oceans are difficult and dangerous to access and explore, so are the thunderstorms just a few thousand feet above our heads. Consider the image of a Sprite shown in Fig. 8.1. When viewed from a distance equal to the length of the state of Kansas, this Sprite would have an area 25 times larger than the full moon. Even though Sprites last about 1/1000 of a second, they are bright enough to see with the naked eye. It is incredible that something as large and impressive as this Sprite, and the ~300,000 others that occur over the skies of our planet each year, could go undetected until 1990. The equally impressive gigantic jets were discovered as recently as 2002. Similarly, it was only 8 years ago, in 2005, that it was realized that thunderclouds generate powerful flashes of gamma-rays, and it was only three years ago, in 2010, that we realized that thunderclouds can generate so many high-energy electrons that they present a potential radiation risk to individuals in aircraft. Indeed, aircraft measurements made directly inside thunderstorms often find a veritable zoo of energetic particle phenomena. One wonders what further exploration will find.

There is a new urgency to better understand our atmosphere. Because many of the physical processes involved are already familiar to physicists, lightning physics and especially high-energy atmospheric physics may provide a stepping stone to help those that are interested begin work in this important field.

## Acknowledgments

We thank Ningyu Liu and Waleta Newman for their assistance with this paper. This work has been primarily supported by DARPA grant HR0011-1-10-1-0061.

## References

- [1] D.J. Malan, Physics of Lightning, The English Universities Press, Ltd., London, 1963.
- [2] B.F.J. Schonland, The Flight of Thunderbolts, second ed., Oxford Univ. Press (Clarendon), London and New York, 1964.
- [3] M.A. Uman, Lightning, McGraw Hill, New York, 1969, 264 pages, revised paperback edition, Dover, New York, 1984.
- [4] M.A. Uman, The Lightning Discharge, Academic Press, London, 1987, 376 pages, revised paperback edition, Dover, New York, 2001.
- [5] V.A. Rakov, M.A. Uman, Lightning: Physics and Effects, Cambridge University Press, Cambridge, UK, 2003, 687 pages, paperback edition, Cambridge University Press, 2006.
- [6] in: V. Cooray (Ed.), The Lightning Flash, IEE Power & Energy Series, vol. 34, The Institute of Electrical Engineers, London, 2003.
- [7] H.D. Betz, U. Schumann, P. Laroche (Eds.), Lightning: Principles, Instruments and Applications, Springer Science+Business Media B.V., 2009.









- [217] B.F.J. Schonland, J.P.T. Viljoen, On penetrating radiation from thunderclouds, Proc. Roy. Soc. A 140 (1933) 314–333.
- [218] E.V. Appleton, E.G. Bowen, Source of atmospherics and penetrating radiation, Nature 132 (1933) 965.
- [219] W.A. Macky, An attempt to detect radiation in thunderclouds, Proc. Cambridge Philos. Soc. 30 (1934) 70–73.
- [220] E.C. Hallday, Thunder-storms and the penetrating radiation, Proc. Cambridge Philos. Soc. 30 (1934) 206–215.
- [221] E.C. Hallday, The thundercloud as a source of penetrating particles, Phys. Rev. 60 (1941) 101–106.
- [222] J. Clay, H.F. Jongen, A.J.J. Aarts, High energy electrons produced in a thundercloud, Physica 28 (1952) 801–808.
- [223] R.D. Hill, Investigation of electron runaway in lightning, J. Geophys. Res. 68 (1963) 6261–6266.
- [224] G.E. Shaw, Background cosmic count increases associated with thunderstorms, J. Geophys. Res. 72 (1967) 4623–4626.
- [225] D.P. Whitmire, Search for high-energy radiation near lightning strokes, Lettere Al Nuovo Cimento 26 (1979) 16, 497–501.
- [226] N. D'Angelo, On X-rays from thunderclouds, Ann. Geophys. Ser. B 5 (1987) 119–122.
- [227] D.M. Suszynsky, R. Roussel-Dupré, G. Shaw, Ground-based search for X rays generated by thunderstorms and lightning, J. Geophys. Res. 101 (1996) 23,505.
- [228] L.P. Babich, High-energy phenomena in electric discharges in dense gases, Futurepast, Inc. Arlington VA, 2003.
- [229] G.J. Fishman, et al., Discovery of intense gamma-ray flashes of atmospheric origin, Science 264 (1994) 1313.
- [230] R. Roussel-Dupré, A.V. Gurevich, On runaway breakdown and upward propagating discharges, J. Geophys. Res. 101 (1996) A2, 2297–2312.
- [231] V.P. Pasko, Recent advances in theory of transient luminous events, J. Geophys. Res. 115 (2010) A00E35.
- [232] G.K. Parks, B.H. Mauk, R. Spiger, J. Chin, X-ray enhancements detected during thunderstorm and lightning activities, Geophys. Res. Lett. 8 (1981) 1176–1179.
- [233] M. McCarthy, G.K. Parks, Further observations of X-rays inside thunderstorms, Geophys. Res. Lett. 12 (1985) 393–396.
- [234] K.B. Eack, W.H. Beasley, W.D. Rust, T.C. Marshall, M. Stolzenburg, Initial results from simultaneous observation of X rays and electric fields in a thunderstorm, J. Geophys. Res. 101 (1996) D23, 29637–29640.
- [235] K.B. Eack, W.H. Beasley, W.D. Rust, T.C. Marshall, M. Stolzenburg, X-ray pulses observed above a mesoscale convective system, Geophys. Res. Lett. 23 (1996) 21, 2915–2918.
- [236] K.B. Eack, D.M. Suszynsky, W.H. Beasley, R. Roussel-Dupré, E. Symbalisty, Gamma-ray emission observed in a thunderstorm anvil, Geophys. Res. Lett. 27 (2000) 185–188.
- [237] H.A. Bethe, J. Ashkin, Passage of radiation through matter, in: E. Segre (Ed.), Experimental Nuclear Physics, New York – London, Vol. 1, Part 2, 1953.
- [238] S.V. Sizikov, Runaway electron production rate in gaseous discharges, High Temperature 31 (1) (1993) 1–6.
- [239] J.R. Dwyer, L. Babich, Low-energy electron production by relativistic runaway electron avalanches in air, J. Geophys. Res. 116 (2011) A09301. <http://dx.doi.org/10.1029/2011JA016494>.
- [240] V.B. Berestetskii, E.M. Lifshitz, L.P. Pitaevskii, Quantum Electrodynamics, Pergamon Press, Oxford, 1982.
- [241] E.V. Oreshkin, S.A. Barengolts, S.A. Chaikovsky, V.I. Oreshkin, Simulation of the runaway electron beam formed in a discharge in air at atmospheric pressure, Phys. Plasmas 19 (2012) 043105.
- [242] J.R. Dwyer, Relativistic breakdown in planetary atmospheres, Physics of Plasmas 14 (4) (2007) 042901–042901–17.
- [243] J.R. Dwyer, L. Babich, Reply to comment by A. V. Gurevich et al. on Low-energy electron production by relativistic runaway electron avalanches in air, J. Geophys. Res. 117 (2012) A04303. <http://dx.doi.org/10.1029/2011JA017487>. 6 PP.
- [244] A.V. Gurevich, K.P. Zybin, Runaway Breakdown and the Mysteries of Lightning, Physics Today 58 (5) (2005) 37–43.
- [245] G. Milikh, R. Roussel-Dupré, Runaway breakdown and electrical discharges in thunderstorms, J. Geophys. Res. (2010) <http://dx.doi.org/10.1029/2009JA014818>.
- [246] J.R. Dwyer, D. Smith, S.A. Cummer, High energy atmospheric physics: terrestrial gamma-ray flashes and related phenomena, Space Science Rev., Space Sci. Rev. (2012) <http://dx.doi.org/10.1007/s11214-012-9894-0>.
- [247] J.R. Dwyer, The source mechanisms of Terrestrial Gamma-ray Flashes (TGFs), J. Geophys. Res. 113 (D10) (2008) CiteID D10103.
- [248] L.M. Coleman, J.R. Dwyer, The propagation speed of runaway electron avalanches, Geophys. Res. Lett. 33 (2006) L11810. <http://dx.doi.org/10.1029/2006GL025863>.
- [249] R. Roussel-Dupré, J.J. Colman, E. Symbalisty, D. Sentman, V.P. Pasko, Physical processes related to discharges in planetary atmospheres, Space Sci. Rev. 137 (2008) 51–82.
- [250] H.W. Koch, J.W. Motz, Bremsstrahlung cross-section formulas and related data, Rev. Modern Phys. 31 (1950) 4, 920.
- [251] L.P. Babich, E.N. Donskoy, I.M. Kutsyra, R. Roussel-Dupré, The feedback mechanism of runaway air breakdown, Geophys. Res. Lett. 32 (2005) L09809. <http://dx.doi.org/10.1029/2004GL021744>.
- [252] V.A. Rakov, M.A. Uman, Lightning: Physics and Effects, Cambridge University Press, Cambridge, UK, 2003, 687 pages, paperback edition, Cambridge University Press, 2006, p. 7.
- [253] P.E. Krider, Deciphering the Energetics of Lightning, Science 31 (2003) Vol. 299 no. 5607, 669–670.
- [254] J.R. Dwyer, M.A. Uman, H.K. Rassoul, V.A. Rakov, M. Al-Dayeh, E.L. Caraway, B. Wright, J. Jerauld, D.M. Jordan, K.J. Rambo, A. Chrest, C. Smyth, Measurements of X-ray emission from rocket-triggered lightning, Geophys. Res. Lett. 31 (2004) L05118. <http://dx.doi.org/10.1029/2003GL018770>.
- [255] S. Celestin, V. Pasko, Energy and fluxes of thermal runaway electrons produced by exponential growth of streamers during the stepping of lightning leaders and in transient luminous events, J. Geophys. Res. 116 (2011) A03315.
- [256] V. Cooray, J. Dwyer, V. Rakov, M. Rahman, On the mechanism of X-ray production by dart leaders of lightning flashes, J. Atmos. Solar-Terr. Phys. 72 (2010) 11,848–11,855.
- [257] J. Jerauld, Properties of natural Cloud-To-Ground lightning inferred from Multiple-Station measurements of close electric and magnetic fields and field derivatives, Ph.D. dissertation, UF, 2007.
- [258] Z. Saleh, J. Dwyer, J. Howard, M. Uman, M. Bakhtiari, D. Concha, M. Stapleton, D. Hill, C. Biagi, H. Rassoul, Properties of the X-ray emission from rocket-triggered lightning as measured by the Thunderstorm Energetic Radiation Array (TERA), J. Geophys. Res. 114 (2009) D17. <http://dx.doi.org/10.1029/2008JD011618>.
- [259] J.R. Dwyer, D.M. Smith, M.A. Uman, Z. Saleh, B. Grefenstette, B. Hazelton, H.K. Rassoul, Estimation of the fluence of high-energy electron bursts produced by thunderclouds and the resulting radiation doses received in aircraft, J. Geophys. Res. (2010) <http://dx.doi.org/10.1029/2009JD012039>.
- [260] M.M. Schaal, J.R. Dwyer, Z.H. Saleh, H.K. Rassoul, M.A. Uman, J.D. Hill, D.M. Jordan, Spatial Energy Spatial and energy distributions of X-ray emissions from leaders in natural and rocket triggered lightning, J. Geophys. Res. 117 (2012) D15201. <http://dx.doi.org/10.1029/2012JD017897>.
- [261] S. Mallick, V.A. Rakov, J.R. Dwyer, A study of x-ray emissions from thunderstorms with emphasis on subsequent strokes in natural lightning, J. Geophys. Res. (2013) <http://dx.doi.org/10.1029/2012JD017555>. in press.
- [262] J.R. Dwyer, M. Schaal, H.K. Rassoul, M.A. Uman, D.M. Jordan, D. Hill, H.K. Rassoul, High-speed x-ray images of triggered lightning dart leaders, J. Geophys. Res. 116 (2011) D20208.
- [263] A.P. Chubenko, et al., Energy spectrum of lightning gamma emission, Phys. Lett. A 373 (33) (2009) 2953–2958.
- [264] V.P. Antonova, L.I. Vildanova, A.V. Gurevich, K.P. Zybin, A.N. Karashtin, S.V. Kryukov, V.A. Ryabov, M.O. Ptitsyn, A.P. Chubenko, Yu.V. Shlyugaev, A.L. Schepetov, Influence of cosmic rays and the runaway-electron breakdowns on thunderstorm processes in the atmosphere, Radiophysics and Quantum Electronics 52 (9) (2009) 627–641.
- [265] I.D. Kostyrya, V.F. Tarasenko, A.N. Tkachev, S.I. Yakovlenko, X-ray radiation due to nanosecond volume discharges in air under atmospheric pressure, Techn. Phys. 51 (3) (2006) 356–361.
- [266] A.G. Rep'ev, P.B. Repin, Spatiotemporal parameters of the X-ray radiation from a diffuse atmospheric-pressure discharge, Techn. Phys. 53 (1) (2008) 73–80.
- [267] L.P. Babich, T.V. Loiko, Subnanosecond pulses of runaway electrons generated in atmosphere by high-voltage pulses of microsecond duration, Dokl. Phys. 54 (11) (2009) 479–482.
- [268] V. March, J. Montanyà, Influence of the voltage-time derivative in X-ray emission from laboratory sparks, Geophys. Res. Lett. 37 (19) (2010) L19801.

- [269] A.V. Gurevich, et al., Laboratory demonstration of runaway electron breakdown of air, *Phys. Lett. A* 375 (2011) 2845–2849.
- [270] V. March, J. Montanya, D. Romero, G. Sola, O. Van der Welde, X-rays from laboratory sparks in air: the relationship between runaway electrons and the electric field, in: International Conference on Lightning Protection, ICLP, 2012, pp. 1–7.
- [271] C.V. Nguyen, Experimental study on hard radiation from long laboratory spark discharges in air, Ph.D. Dissertation, Technische Universiteit Eindhoven, 2012.
- [272] V. Cooray, L. Arevalo, M. Rahman, J. Dwyer, H. Rassoul, On the possible origin of X-rays in long laboratory sparks, *J. Atmos. Solar-Terr. Phys.* (2009) <http://dx.doi.org/10.1016/j.jastp.2009.07.010>.
- [273] I.M. Kutsyk, L.P. Babich, E.N. Donskoii, E.I. Bochkov, Analysis of the results of a laboratory experiment on the observation of a runaway electron avalanche in air under high overvoltages, *Plasma Physics Reports* 38 (11) (2012) 891–898.
- [274] C. Li, U. Ebert, W. Hundsdorfer, 3D hybrid computations for streamer discharges and production of runaway electrons, *J. Phys. D: Appl. Phys.* 42 (2009) 202003.
- [275] O. Chantron, T. Neubert, A PIC-MCC code for simulation of streamer propagation in air, *J. Comput. Phys.* 227 (15) (2008) 7222–7245.
- [276] J.J. Colman, R.A. Roussel-Dupré, L. Triplett, Temporally self-similar electron distribution functions in atmospheric breakdown: The thermal runaway regime, *J. Geophys. Res.* 115 (2010) A00E16.
- [277] A. Chilingarian, H. Mkrtchyan, Role of the Lower Positive Charge Region (LPCR) in initiation of the Thunderstorm Ground Enhancements (TGEs), *Phys. Rev. D* 86 (2012) 072003.
- [278] M. Brunetti, S. Cecchini, M. Galli, G. Giovannini, A. Pagliarin, Gamma-ray bursts of atmospheric origin in the MeV energy range, *Geophys. Res. Lett.* 27 (2000) 1599–1602.
- [279] A.P. Chubenko, V.P. Antonova, S.Yu. Kryukov, V.V. Piskal, M.O. Ptitsyn, A.L. Shepetov, L.I. Vildanova, K.P. Zybin, A.V. Gurevich, Intense X-ray emission bursts during thunderstorms, *Phys. Lett. A* 275 (2000) 90–100.
- [280] A.P. Chubenko, et al., Effective growth of a number of cosmic ray electrons inside thundercloud, *Phys. Lett. A* 309 (2003) 90.
- [281] V.V. Alexeenko, N.S. Khaerdinov, A.S. Lidvansky, V.B. Petkov, Transient variations of secondary cosmic rays due to atmospheric electric field and evidence for pre-lightning particle acceleration, *Phys. Lett. A* 301 (2002) 299.
- [282] T. Torii, T. Sugita, S. Tanabe, Y. Kimura, M. Kamogawa, K. Yajima, H. Yasuda, Gradual increase of energetic radiation associated with thunderstorm activity at the top of Mt. Fuji, *Geophys. Res. Lett.* 36 (2009) L13804.
- [283] H. Tsuchiya, et al., Observation of an energetic radiation burst from mountain-top thunderclouds, *Phys. Rev. Lett.* 102 (2009) 255003.
- [284] A. Chilingarian, A. Daryan, K. Arakelyan, A. Hovhannisan, B. Mailyan, L. Melkumyan, G. Hovsepyan, S. Chilingaryan, A. Reymers, L. Vanyan, Ground-based observations of thunderstorm-correlated fluxes of high-energy electrons, gamma rays, and neutrons, *Phys. Rev. D* 82 (4) (2010) id. 043009.
- [285] A. Chilingarian, B. Mailyan, L. Vanyan, Recovering of the energy spectra of electrons and gamma rays coming from the thunderclouds, *Atmospheric Research* 114–115 (2012) 1–16.
- [286] T. Torii, T. M. Takeishi, T. Hosono, Observation of gamma-ray dose increase associated with winter thunderstorm and lightning activity, *J. Geophys. Res.* 107 (2002) 4324.
- [287] H. Tsuchiya, et al., Detection of high-energy gamma rays from winter thunderclouds, *Phys. Rev. Lett.* 99 (2007) 165002.
- [288] H. Tsuchiya, et al., Long-duration  $\gamma$  ray emissions from 2007 and 2008 winter thunderstorms, *J. Geophys. Res.* 116 (2011) D09113.
- [289] T. Torii, T. Sugita, M. Kamogawa, Y. Watanabe, K. Kusunoki, Migrating source of energetic radiation generated by thunderstorm activity, *Geophys. Res. Lett.* 38 (2011) <http://dx.doi.org/10.1029/2011GL049731>. L24801.
- [290] T. Torii, T. Nishijima, Z.-I. Kawasaki, T. Sugita, Downward emission of runaway electrons and bremsstrahlung photons in thunderstorm electric fields, *Geophys. Res. Lett.* 31 (2004) L05113.
- [291] L.P. Babich, E.I. Bochkov, E.N. Donskoii, I.M. Kutsyk, Source of prolonged bursts of high-energy gamma rays detected in thunderstorm atmosphere in Japan at the coastal area of the Sea of Japan and on high mountaintop, *J. Geophys. Res.* 115 (2010) A09317.
- [292] G.G. Karapetyan, Theoretical investigation of thunderstorm induced enhancements of cosmic ray fluxes, *Astropart. Phys.* 38 (2012) 46–52.
- [293] A.S. Lidvansky, The effect of the electric field of the atmosphere on cosmic rays, *J. Phys. G: Nucl. Part. Phys.* (2003) 29925–29937.
- [294] Y. Muraki, et al., Effects of atmospheric electric fields on cosmic rays, *Phys. Rev. D* 69 (2004) 123010.
- [295] N.A. Kelley, A. Lowell, D.M. Smith, J.R. Dwyer, S.A. Cummer, G. Lu, R. Blakeslee, Abstract AE11A-0332 presented at 2010 Fall Meeting, AGU, San Francisco, Calif., 2010, pp. 13–17.
- [296] G.J. Fishman, et al., in: W.N. Johnson, Proc. GRO Science Workshop, Greenbelt, NASA/GSFC, 1989, pp. 2–39.
- [297] R.C. Franz, R.J. Nemzek, J.R. Winckler, Television image of a large upward electric discharge above a thunderstorm system, *Science* 249 (1990) 48–51.
- [298] D.M. Smith, L.I. Lopez, R.P. Lin, C.P. Barrington-Leigh, Terrestrial gamma-ray flashes observed up to 20 MeV, *Science* 307 (2005) 1085–1088.
- [299] M.E. Splitt, S.M. Lazarus, D. Barnes, J.R. Dwyer, H.K. Rassoul, D.M. Smith, B.J. Hazelton, B.W. Grefenstette, Thunderstorm characteristics associated with RHESSI identified terrestrial gamma-ray flashes, *J. Geophys. Res.* 115 (2010) A00E38. <http://dx.doi.org/10.1029/2009JA014622>. 10 PP.
- [300] S.A. Cummer, Y. Zhai, W. Hu, D.M. Smith, L.I. Lopez, M.A. Stanley, Measurements and implications of the relationship between lightning and terrestrial gamma ray flashes, *Geophys. Res. Lett.* 32 (2005) L08811. <http://dx.doi.org/10.1029/2005GL022778>.
- [301] A. Kulak, J. Mlynarczyk, M. Ostrowski, J. Kubisz, A. Michalec, Analysis of ELF electromagnetic field pulses recorded by the Hylaty station coinciding with terrestrial gamma-ray flashes, *J. Geophys. Res.* 117 (2012) <http://dx.doi.org/10.1029/2012JD018205>.
- [302] J.R. Dwyer, D.M. Smith, A Comparison between Monte Carlo simulations of runaway breakdown and terrestrial gamma-ray flash observations, *Geophys. Res. Lett.* 32 (2005) L22804. <http://dx.doi.org/10.1029/2005GL023848>.
- [303] E. Williams, et al., Lightning flashes conducive to the production and escape of gamma radiation to space, *J. Geophys. Res. D* 111 (2006) D16209.
- [304] B. Carlson, N. Lehtinen, U. Inan, Constraints on terrestrial gamma-ray flash production derived from satellite observations, *Geophys. Res. Lett.* 34 (8) (2007) CitelID L08809.
- [305] T. Gjesteland, N. Østgaard, A.B. Collier, B.E. Carlson, C. Eyles, D.M. Smith, A new method reveals more TGFs in the RHESSI data, *Geophys. Res. Lett.* 39 (2012) L05102.
- [306] T. Gjesteland, N. Østgaard, A.B. Collier, B.E. Carlson, M.B. Cohen, N.G. Lehtinen, Confining the angular distribution of terrestrial gamma ray flash emission, *J. Geophys. Res.* 116 (2011) A11313. <http://dx.doi.org/10.1029/2011JA016716>.
- [307] B.E. Carlson, T. Gjesteland, N. Østgaard, Connecting the terrestrial gamma-ray flash source strength and observed fluence distributions, *J. Geophys. Res.* 117 (2012) A01314. <http://dx.doi.org/10.1029/2011JA017122>. 7 PP.
- [308] N. Østgaard, T. Gjesteland, R.S. Hansen, A.B. Collier, B. Carlson, The true fluence distribution of terrestrial gamma flashes at satellite altitude, *J. Geophys. Res.* 117 (2012) A03327. <http://dx.doi.org/10.1029/2011JA017365>. 8 PP.
- [309] M. Marisaldi, et al., Detection of terrestrial gamma ray flashes up to 40 MeV by the AGILE satellite, *J. Geophys. Res.* 115 (2010) A00E13. <http://dx.doi.org/10.1029/2009JA014502>.
- [310] M. Stanley, et al., Link between terrestrial gamma-ray flashes and intra-cloud lightning discharges, *Geophys. Res. Lett.* 33 (6) (2006) CitelID L06803.
- [311] G. Lu, R.J. Blakeslee, J. Li, D.M. Smith, X.-M. Shao, E.W. McCaul, D.E. Buechler, H.J. Christian, J.M. Hall, S.A. Cummer, Lightning mapping observation of a terrestrial gamma-ray flash, *Geophys. Res. Lett.* 37 (11) (2010) CitelID L11806.
- [312] X.-M. Shao, T. Hamlin, D.M. Smith, A closer examination of terrestrial gamma-ray flash-related lightning processes, *J. Geophys. Res.* 115 (9) (2010) CitelID A00E30.
- [313] M.S. Briggs, et al., First results on terrestrial gamma ray flashes from the Fermi Gamma-ray Burst Monitor, *J. Geophys. Res.* 115 (2010) A07323. <http://dx.doi.org/10.1029/2009JA015242>.
- [314] B.W. Grefenstette, D.M. Smith, J.R. Dwyer, G.J. Fishman, Time evolution of terrestrial gamma ray flashes, *Geophys. Res. Lett.* 35 (6) (2008) CitelID L06802.
- [315] T. Gjesteland, N. Østgaard, P.H. Connell, J. Stadsnes, G.J. Fishman, Effects of dead time losses on terrestrial gamma ray flash measurements with the Burst and Transient Source Experiment, *J. Geophys. Res.* 115 (3) (2010) A00E21.







- [457] N.Y. Liu, V.P. Pasko, H. Frey, S. Mende, H.-T. Su, A. Chen, R.R. Hsu, L.-C. Lee, Assessment of sprite initiating electric fields and quenching altitude of a1g state of N2 using sprite streamer modeling and ISUAL spectrophotometric measurements, *J. Geophys. Res.* 114 (2009) A00E02. <http://dx.doi.org/10.1029/2008JA013735>.
- [458] J. Qin, S. Celestin, V.P. Pasko, On the inception of streamers from sprite halo events produced by lightning discharges with positive and negative polarity, *J. Geophys. Res.* 116 (2011) A06305. <http://dx.doi.org/10.1029/2010JA016366>.
- [459] V.P. Pasko, U.S. Inan, T.F. Bell, Y.N. Taranenko, Sprites produced by quasi-electrostatic heating and ionization in the lower ionosphere, *J. Geophys. Res.* 102 (1997) 4529.
- [460] C.T.R. Wilson, The electric field of a thunderstorm and some of its effects, *Proc. Phys. Soc. Lond.* 37 (1925) 32D–37D.
- [461] C.L. Kuo, A.B. Chen, J.K. Chou, L.Y. Tsai, R.R. Hsu, H.T. Su, H.U. Frey, S.B. Mende, Y. Takahashi, L.C. Lee, Radiative emission and energy deposition in transient luminous events, *J. Phys. D Appl. Phys.* 41 (2008) 234014.
- [462] H. Christian, R. Blakeslee, D. Boccippio, W. Boeck, D. Buechler, K. Driscoll, S. Goodman, J. Hall, W. Koshak, D. Mach, M. Stewart, Global frequency and distribution of lightning as observed from space by the Optical Transient Detector, *J. Geophys. Res.* 108 (D1) (2003) 4005. <http://dx.doi.org/10.1029/2002JD002347>.
- [463] W.A. Lyons, M.A. Stanley, J.D. Meyer, T.E. Nelson, S.A. Rutledge, T. Lang, S.A. Cummer, The meteorological and electrical structure of TLE-producing convective storms, in: H. Betz, U. Schumann, P. Laroche (Eds.), *Lightning: Principles, Instruments and Applications*, Springer, Berlin, 2009, pp. 387–415.
- [464] P. Zarka, W. Farrell, G. Fischer, A. Konovalenko, Ground-based and space-based radio observations of planetary lightning, *Space Sci. Rev.* 137 (2008) 257–269. <http://dx.doi.org/10.1007/s11214-008-9366-8>.
- [465] V.P. Pasko, Red sprite discharges in the atmosphere at high altitude: the molecular physics and the similarity with laboratory discharges, *Plasma Sources Sci. Technol.* 16 (2007) S13–S29.
- [466] W.Y. Hu, S.A. Cummer, W.A. Lyons, Lightning charge moment changes for the initiation of sprites, *Geophys. Res. Lett.* 29 (2002) 120-1–120-4.
- [467] W. Hu, S.A. Cummer, W.A. Lyons, Testing sprite initiation theory using lightning measurements and modeled electromagnetic fields, *J. Geophys. Res.* 112 (2007) D13115. <http://dx.doi.org/10.1029/2006JD007939>.
- [468] N.Y. Liu, Multiple ion species fluid modeling of sprite halos and the role of electron detachment of O- in their dynamics, *J. Geophys. Res.* 117 (2012) A03308. <http://dx.doi.org/10.1029/2011JA017062>.
- [469] D.M. Suszynsky, R. Strabley, R. Roussel-Dupre, E.M.D. Symbalisty, R.A. Armstrong, W.A. Lyons, M. Taylor, Video and photometric observations of a sprite in coincidence with a meteor-triggered jet event, *J. Geophys. Res.* 104 (D24) (1999) <http://dx.doi.org/10.1029/1999JD900962>. 31,361–31,367.
- [470] N.A. Zabotin, J.W. Wright, Role of meteoric dust in sprite formation, *Geophys. Res. Lett.* 28 (2001) 2593–2596.
- [471] A. Luque, F.J. Gordillo-Vázquez, Mesospheric electric breakdown and delayed sprite ignition caused by electron detachment, *Nature Geosci.* 5 (2012) 22–25.
- [472] W.L. Boeck, O.H. Vaughan, R.J. Blakeslee, B. Vonnegut, M. Brook, Lightning induced brightening in the airglow layer, *Geophys. Res. Lett.* 19 (1992) 99–102.
- [473] U.S. Inan, T.F. Bell, J.V. Rodriguez, Heating and ionization of the lower ionosphere by lightning, *Geophys. Res. Lett.* 18 (4) (1991) 705–708.
- [474] H. Fukunishi, Y. Takahashi, M. Kubota, K. Sakanoi, U.S. Inan, W.A. Lyons, Elves: lightning-induced transient luminous events in the lower ionosphere, *Geophys. Res. Lett.* 23 (1996) 2157–2160.
- [475] U.S. Inan, C. Barrington-Leigh, S. Hansen, V.S. Glukhov, T.F. Bell, R. Rairden, Rapid lateral expansion of optical luminosity in lightning-induced ionospheric flashes referred to as ‘elves’, *Geophys. Res. Lett.* 24 (1997) 583–586.
- [476] S.B. Mende, H.U. Frey, R.R. Hsu, H.T. Su, A.B. Chen, L.C. Lee, D.D. Sentman, Y. Takahashi, H. Fukunishi, D region ionization by lightning-induced EMP, *J. Geophys. Res.* 110 (2005) A11312. <http://dx.doi.org/10.1029/2005JA011064>.
- [477] H.U. Frey, S.B. Mende, S.A. Cummer, A.B. Chen, R.R. Hsu, H.T. Su, Y.S. Chang, T. Adachi, H. Fukunishi, Y. Takahashi, Betatype stepped leader of elve-producing lightning, *Geophys. Res. Lett.* 32 (2005) L13824. <http://dx.doi.org/10.1029/2005GL023080>.
- [478] C.L. Kuo, et al., Modeling elves observed by FORMOSAT-2 satellite, *J. Geophys. Res.* 112 (2007) A11312. <http://dx.doi.org/10.1029/2007JA012407>.
- [479] E.M. Wescott, D. Sentman, D. Osborne, D. Hampton, M. Heavner, Preliminary results from the Sprites94 aircraft campaign: 2. Blue jets, *Geophys. Res. Lett.* 22 (1995) 1209–1212.
- [480] E.M. Wescott, D.D. Sentman, M.J. Heavner, D.L. Hampton, D. Osborne, O.H. Vaughan Jr., Blue starters: brief upward discharges from an intense Arkansas thunderstorm, *Geophys. Res. Lett.* 23 (1996) 2153–2156. <http://dx.doi.org/10.1029/96GL01969>.
- [481] W.L. Boeck, O.H. Vaughan, R.J. Blakeslee, B. Vonnegut, M. Brook, J. McKune, Observations of lightning in the stratosphere, *J. Geophys. Res.* 100 (1995) 1465–1475.
- [482] W.A. Lyons, T.E. Nelson, R.A. Armstrong, V.P. Pasko, M.A. Stanley, Upward electrical discharges from thunderstorm tops, *Bull. Am. Meteorol. Soc.* 84 (4) (2003) 445–454. <http://dx.doi.org/10.1175/BAMS-84-4-445>.
- [483] V.P. Pasko, M.A. Stanley, J.D. Matthews, U.S. Inan, T.G. Wood, Electrical discharge from a thundercloud top to the lower ionosphere, *Nature* 416 (2002) 152–154. <http://dx.doi.org/10.1038/416152a>.
- [484] V.P. Pasko, Electric jets, *Nature* 423 (2003) 927–929.
- [485] H.T. Su, R.R. Hsu, A.B. Chen, Y.C. Wang, W.S. Hsiao, W.C. Lai, L.C. Lee, M. Sato, H. Fukunishi, Gigantic jets between a thundercloud and the ionosphere, *Nature* 423 (2003) 974–976. <http://dx.doi.org/10.1038/nature01759>.
- [486] O.A. van der Velde, W.A. Lyons, T.E. Nelson, S.A. Cummer, J. Li, J. Bunnell, Analysis of the first gigantic jet recorded over continental North America, *J. Geophys. Res.* 112 (2007) D20104. <http://dx.doi.org/10.1029/2007JD008575>.
- [487] S.A. Cummer, J. Li, F. Han, G. Lu, N. Jaugey, W.A. Lyons, T.E. Nelson, Quantification of the troposphere-to-ionosphere charge transfer in a gigantic jet, *Nat. Geosci.* 2 (2009) 1–4. <http://dx.doi.org/10.1038/NGEO607>.
- [488] P. Snelgrove, A census of the ocean, Ted Talk, [http://www.ted.com/talks/paul\\_snelgrove\\_a\\_census\\_of\\_the\\_ocean.html?quote=1362](http://www.ted.com/talks/paul_snelgrove_a_census_of_the_ocean.html?quote=1362).
- [489] Encyclopedia Britannica Online, Lightning (2007) (see <http://search.eb.com/eb/article-9048228>).
- [490] K. Berger, Blitzstrom-Parameter von Aufwärtsblitzen, *Bull. Schweiz. Elektrotech. Ver.* 69 (1978) 353–360.
- [491] M. Uman, *The Art and Science of Lightning Protection*, 2008, Cambridge University Press, Cambridge, 2010.
- [492] J.D. Hill, J. Pilkey, M.A. Uman, D.M. Jordan, W. Rison, P.R. Krehbiel, M.I. Biggerstaff, P. Hyland, R. Blakeslee, Correlated lightning mapping array and radar observations of the initial stages of three sequential triggered florida lightning flashes, *J. Geophys. Res.* 118 (2013) <http://dx.doi.org/10.1002/jgrd.50660>. in press.